Relations structures propriétés à l'origine des comportements différés des bois : - de la compréhension des mécanismes à la détermination d'indicateurs prédictifs.

Tai-Yun Hsieh

THÈSE POUR OBTENIR LE GRADE DE DOCTEUR DE L'UNIVERSITÉ DE MONTPELLIER

École doctorale Informations Structures Systèmes (I2S - ED166)

Laboratoire de Mécanique et Génie Civil (LMGC)

Structure/properties relationships of time-dependent behavior of wood— from understanding mechanisms to determining predictive indicators

[Manuscript Provisional Record]

Présentée par Tai-Yun HSIEH
le 6 / 12 / 2022

Sous la direction de Sandrine BARDET
et encadrée par Cédric MONTERO

Devant le jury composé de :

Joseph GRIL, Directeur de Recherche	Université Clermont-Auvergne	Rapporteur
Robert LE ROY, Professeur	École Nationale Supérieure d'Architecture Paris Malaquais	Rapporteur
Frédéric DUBOIS, Professeur	Université de Limoges	Examinateur
Marianne PERRIN, Maîtresse de Conférences	Université Fédérale de Toulouse	Examinatrice
Stéphane CORN, Maître de Conférences	IMT Mines Alès	Examinateur
Bernard THIBAUT, Directeur de Recherche Émérite	Université de Montpellier	Examinateur
Sandrine BARDET, Maitresse de Conférences HDR	Université de Montpellier	Directrice de thèse
Cédric MONTERO, Maître de Conférences	Université de Montpellier	Encadrant

UNIVERSITÉ DE MONTPELLIER

Acknowledgements

This work was supported by the French National Research Agency (ANR) under the EFEUR5 project (ANR-15-CE08-0027) for investments in experimental equipment. Thanks to Laboratoire de Mécanique et Génie Civil (LMGC), Université de Montpellier, and Centre National de la Recherche Scientifique (CNRS) for providing this research and learning environment.

Grâce à des numéraux des personnes, j'ai finalement pu finir cette thèse.

J'aimerais dire un très grand merci à ma directrice de thèse : Sandrine Bardet et mon encadrant : Cédric Montero. C'était complexe de prendre soin d'une doctorante étrangère qui ne parlait pas français quand elle était arrivée. Ils m'ont supporté sur l'étude et le recherche, ainsi que la vie en France. Ils m'ont enseigné sur comment faire une étude, comment faire l'expérience, comme raconter bien une histoire, comment être une chercheuse.

Je remercie Tancrède Alméras de m'avoir aidé sur l'analyse de donnée, modélisation, et la structure de la soutenance. J'ai vraiment appris beaucoup de choses avec Tancrède. Je tiens à remercier Gille Camp et l'ensemble de l'équipe d'expérimentation et numérique du LMGC. Grand merci à Gille pour tous ses soutiens sur l'expérience, ainsi que m'avoir bien accompagné, discuté sur toutes les choses dans la vie. Je remercie Joseph Gril de m'avoir donné plein d'idées et de conseils, et de m'avoir toujours encouragé.

Je remercie l'équipe du bois au LMGC de m'avoir accompagné pendant ces trois ans, ainsi que les chercheurs et les doctorants au GDR science du bois d'avoir échangé avec moi. Je souhaite remercier les membres de jury : Joseph Gril, Rober Le Roy, Stéphane Corn, Marianne Perrin, Bernard Thibaut, Frédéric Dubois. Vous avez patiemment discuté avec moi et vous m'avez donné beaucoup de conseils.

Merci aux membres, docteurs et doctorants au LMGC. Merci à mes professeurs de français : Tiffany, Mikaël, Anthony, Julien et Sara. Merci à mes amis : Damien, Lucas et Audélie.

Je tiens à remercier mon chéri Rémi et ma belle–famille pour leur amour et soutien.

感謝我的同學胡顯琮告訴我這個來到法國深造的機會，以及協助我許多生活及學業障礙，一起抱怨各種事情，分享超市美食情報。我必需說，Tripes真的太好吃了。也感謝我的同學朴成赫，幫我翻譯了許多必需看懂的文件和必需搞懂的事情，還安排了幾趟很棒的旅行。謝謝陳家欣(茶欣)我的法文課同學，給了我許多過來人的建議與暖暖的陪伴，有你真好。感謝蔡明哲老師當初的全力支持，以及張豐丞老師的協助。感謝諸多來自遠方的精神支持：陸冠宇一家三口；子晴、詠祺和佩萱；池池和立立；突然早上七點打電話來叫我起床算材料力學的侯瑞瑜。感謝老爸老媽的無條件支持，也是真的只有父母會這樣。謝謝妹妹的陪伴，能有人可以討論所有事情真的很棒。最後謝謝我自己成功的存活了下來，完成了這本論文。

Abstract

Wood has been used as a structural material since ancient times, so we have always had to face the challenges of time and climate on wood and wood-based materials. In those situations, it expresses the creep behavior, a mechanical phenomenon in which the deformation increases with time at a constant level of load. The additional deformation would affect the feeling of use, and serviceability for users, and sometimes the security of the structure. When deformation reaches the mechanical limits of the material, it can lead to failure. The first scientific observation of the creep behavior of wood was published by Armstrong in the early 1950s. Since then, there have been successive studies on different species, different test methods, and experimental environment. Up to now, there is still no clear theory or common behavior law for the mechanism determining wood time-dependent behavior.

This study started from the overview of wood material and the construction of a database collecting wood creep measurements, representing the diversity of creep test methods and results from the literature. In the present study, experiments were focused on four species representative of the French resource : Douglas fir, Poplar, European Beech and European Oak. We chose a dedicated 4–point bending test for creep measurements associated with vibration procedure for pre-characterization of mechanical properties, as well as the physical measurements of density and dimensions. The clear wood samples were small (150 mm in the direction of the fibers) to avoid wood defects.

The vibration testing device has been designed at LMGC based on a system developed in Japanese wood laboratories. It allows us to measure the specific modulus, which is strongly correlated to the microfibril angle and the damping coefficient, in order to have a preliminary understanding of the mechanical characteristics of the samples. The density, specific modulus, damping coefficient, volume swelling coefficient, and grain angle of the specimens were measured and considered into an optimized sampling. The sampling method was developed to choose a specific property as a variable and control the variance of the other properties, so that the test results can focus on the effect of a given property. Thus, the influence of each property is tested separately from the others to determine the predictive indicators of creep.

Several series of creep tests were conducted to study the effect of each predictive indicators. All the experiments were conducted in controlled environment at temperature 20 °C and relative humidity 85% after a stabilization phase of the specimens, then the 4–point bending creep tests were conducted. A load of 650 g (10.52 MPa) was set on the specimens for a nominal duration of 10 days. There were 108 samples tested and considered in the modeling.

Creep behavior model can be expressed by an exponential function of time. Delayed compliance can be represented by a series of Kelvin elements, and the parameters of the elements (springs and dashpots) are

calculated numerically by fitting with the experimental data. Different from the traditional model, this study focuses on the relationship between the fitting parameters and the specimens characteristics. Three models are presented to estimate the fitting parameters of the creep function. The modeling suggests that the creep behavior of wood occurs in the cell wall rather than by sliding at the inter-cell zone, and the mechanism changes with time are shown in the modeling result. The effect of density decreases with the loading time, and the effect of specific modulus increases. It means that the deformation is transferred from the cell wall to other structure of wood, and the influence of microfibril angle increases during the loading process.

This study highlights the importance of microstructure on rheological behavior. Wood microstructure is influenced by age, growing environment and conditions, as well as wood extractive. The results of this study provide material properties to be considered in the mechanical grading assessment of construction materials.

Keywords: Experimental studies; Delayed behavior; Longevity; Rheology; Numerical modeling; Wood

Résumé

Le bois est utilisé comme matériau de construction depuis des temps très anciens. Tous les matériaux structurels doivent faire face aux défis du temps et du climat. Le comportement de fluage est un phénomène mécanique où la déformation augmente avec le temps, à niveau de chargement constant. Lorsque le fluage atteint les limites mécaniques du matériau (en déformation ou en contrainte), la rupture apparaît. La première observation scientifique du comportement de fluage du bois a été publiée par Armstrong au début des années 1950. Depuis lors, des études successives ont été menées sur différentes essences et différentes méthodes d'essai. Jusqu'à ces dernières années, il n'y a toujours pas de théorie claire sur le mécanisme du comportement de fluage du bois.

L'étude présentée dans ce manuscrit a commencé par un aperçu du matériau bois et la construction d'une base de données sur le fluage du bois qui présente une synthèse des méthodes et des résultats des essais de fluage de la littérature.

Dans les travaux réalisés pendant cette thèse, 4 essences ont été testées : le douglas, le peuplier, le hêtre européen et le chêne européen. Nous avons choisi l'essai de flexion 4 points pour les mesures en fluage et l'essai de vibration pour caractériser les propriétés mécaniques, ainsi que les mesures physiques de densité et de dimensions. Les échantillons sont de petite taille (150 mm dans le sens des fibres), pour éviter les défauts du bois. Une série de 10 jours d'essais de fluage en flexion 4 points a été réalisée sur la base des essais de vibration et d'un échantillonnage réalisé préalablement. Le dispositif d'essai de vibration a été conçu au LMGC depuis plusieurs années sur la base d'un système développé dans les laboratoires du bois japonais. Le test de vibration permet de mesurer le module spécifique, qui est fortement corrélé à l'angle des microfibrilles et le coefficient d'amortissement, pour avoir une compréhension générale des caractéristiques mécaniques des échantillons. La masse volumique, le module spécifique, le coefficient d'amortissement, le coefficient de gonflement en volume et l'angle de grain des échantillons ont été mesurés et considérés dans l'échantillonnage.

La stratégie d'échantillonnage a été conçue pour choisir une propriété spécifique comme variable et contrôler la variance d'autres propriétés, pour que le résultat du test puisse se concentrer sur l'effet d'une propriété donnée. Ainsi, l'influence de chaque propriété est testée séparément des autres afin de déterminer les indicateurs prédictifs du fluage. Les échantillons ont été stabilisés à une température de 20 °C et à une humidité relative de 85% avant d'être soumis à l'essai de fluage en flexion 4 points. Une charge de 650 g (10,52 MPa) a été appliquée en flexion 4 points pendant 10 jours. Cent-huit échantillons ont été testés et analysés dans la modélisation.

Le modèle de comportement de fluage représenté par une fonction exponentielle du temps. La complai-

sance différée peut être représentée par une série d'éléments de Kelvin, et les paramètres des éléments (ressorts et amortisseurs) sont calculés numériquement par comparaison avec les données expérimentales. Cette étude se concentre sur la relation entre les paramètres d'ajustement du modèle et les caractéristiques des échantillons mesurées expérimentalement. Trois modèles sont présentés pour estimer les paramètres d'ajustement de la fonction de fluage. La modélisation suggère que le comportement en fluage du bois se produit dans la paroi cellulaire plutôt que par glissement au niveau de la zone intercellulaire. Les résultats de la modélisation permettent de simuler les évolutions des mécanismes dans le temps. L'effet de la densité diminue avec le temps de chargement, et l'effet du module spécifique augmente. Cela signifie que la déformation est transférée de la paroi cellulaire à d'autres structures du bois, et que l'effet de l'angle des microfibrilles augmente pendant le processus de chargement.

Cette étude souligne l'importance de la microstructure sur le comportement rhéologique. La microstructure du bois est influencée par l'âge de l'arbre, l'environnement et les conditions de croissance, ainsi que par les extractibles du bois. Les résultats de cette étude fournissent des propriétés matérielles à considérer dans l'évaluation du classement mécanique des matériaux de construction.

Mots clés : Bois ; Comportement différé ; Modélisation ; Rhéologie ; Expérimental ; Longévité

Contents

List of Figures **9**

List of Tables **16**

List of Symbols **17**

1 Introduction **18**

1.1 Concerning wood and timber materials 18

1.1.1 Chemical composition of wood 19

1.1.2 Composition and structure of cell wall 21

1.1.3 Wood anatomy and mechanical properties 23

1.2 Creep behavior 25

1.2.1 What is creep behavior? 25

1.2.2 Why does it happen? 26

1.3 Creep behavior on wood 27

1.3.1 Effects of temperature 27

1.3.2 Effects of moisture 28

1.3.3 Effects of material properties 30

1.4 Summary 30

2 Wood Creep Database **31**

2.1 Importance of building a database 31

2.2 Toward a wood creep database 32

2.2.1 Describe of the database 33

2.2.2 Different testing method and loading 35

2.2.3 Different observed parameter 35

2.2.4 Digitalization and homogenize 38

2.3 Analysis of the database . . . 39
2.4 Summary . . . 48

3 Material Characterization and Sampling 49

3.1 Material: Small clear wood . . . 49
3.1.1 Introduction of the materials . . . 50
3.1.2 Specimens cutting . . . 54
3.1.3 Specimens characterization . . . 56
3.2 Vibration test . . . 60
3.2.1 Theory . . . 60
3.2.2 Testing method . . . 63
3.2.3 Results . . . 66
3.3 Sampling . . . 69
3.4 Summary . . . 85

4 Experimental study of creep in 4–point bending 86

4.1 Experimental method . . . 86
4.1.1 The *creep box*: an experimental system for creep behavior . . . 86
4.1.2 Loading of the specimens . . . 88
4.1.3 Testing environment . . . 88
4.1.4 Measurement of strain . . . 89
4.1.5 Loading process . . . 90
4.1.6 Data acquisition and strain calculation . . . 90
4.1.7 Loading time . . . 91
4.2 Creep test result . . . 93
4.2.1 Initial point value . . . 93
4.2.2 Original experimental data . . . 94
4.2.3 Creep compliance . . . 100
4.3 Data Analysis . . . 105

4.3.1 Elastic behavior . . . 105
4.3.2 Observation of creep compliance against the predictors . . . 106
4.4 Summary . . . 115

5 Modeling **116**

5.1 General model of creep behavior . . . 116
5.2 Observation of delayed compliance . . . 118
5.3 Two–mechanism model . . . 125
5.3.1 Potential predictor analysis: Density . . . 127
5.3.2 Potential predictor analysis: Specific modulus . . . 129
5.3.3 Comprehensive analysis: Creep factor . . . 131
5.3.4 Summary of two–mechanism model . . . 132
5.4 Discrete compliance model . . . 133
5.4.1 Correlation between J^*i and density . . . 135
5.4.2 Correlation between J^*i and specific modulus . . . 137
5.4.3 Summary of discrete compliance model . . . 139
5.5 Multiple regression model . . . 140
5.6 Summary . . . 143

6 Conclusions **144**

References **146**

A Multiple Regression Model Fitting Result **152**

List of Figures

1.1 Photography of temple Hōryū-ji in Japan 18

1.2 Photography of church Urnes Stave in Norway 19

1.3 Monomeric units in lignin (Popescu et al., 2006). 20

1.4 Multiscale structure of a softwood (Harrington, 1996, 2002). 22

1.5 Structure within a microfibril (Shmulsky and Jones, 2011). 23

1.6 Cell wall structure. 23

1.7 3 main directions in the wood: longitudinal (L), radial (R), tangential (T) direction. 24

1.8 Microscopic structure of (a) softwood and (b) hardwood (Richter, 2015). 24

1.9 Diagram of constant temperature creep behavior (Betten, 2008) 26

1.10 Evolution of compliance level at different temperature (left) and construction of a time/temperature equivalency(Sun and Frazier, 2007) 28

1.11 Schematics representation of mechano–sorptive creep over time (left) and moisture content (right) (Hunt, 1989) 29

1.12 Evolution of strain with time during a first phase of 35 hrs of creep followed by 20 hrs of relaxation obtained at various relative humidity environment (RH=28% on (a) and (b) results, 75% for (c) and 79% for (d) (Pittet, 1996) 29

1.13 Evolution of relative creep after 1 week at various relative humidity levels and for different values of specific modulus (GPa) indicated on each curve. (Matar, 2003) 30

1.14 The longitudinal tensile creep test of Sugi earlywood specimens with different microfibril angle (MFA) (Kojima and Yamamoto, 2004) 30

2.1 (a) Creep behavior (relative creep against time) for different testing method in beams (Granello and Palermo, 2019). (b) Creep test result (relative creep against time) of different direction on the same board (Schniewind and Barrett, 1972) 35

2.2 Examples of the creep tests result in literatures. 36

2.3 Wood creep database. 39

2.4 Wood creep data with different grain angle. 40

2.5 Grain angle effect (Schniewind and Barrett, 1972). 41

2.6 Microfibril angle effect (Kojima and Yamamoto, 2004). 42

2.7 Comparison of testing method. 43

2.8 Comparison of softwood and hardwood. 44

2.9 Comparison of different wood. 45

2.10 Wood creep bending test under different relative humidity. 46

2.11 Wood creep bending test under different temperature (Hermawan and Fujimoto, 2019). . . . 47

3.1 Douglas fir 50

3.2 Poplar 51

3.3 European Beech 52

3.4 European Oak 53

3.5 Different steps of specimens' cutting. (a) The end of the beam for outdoor long-term creep test; (b) Slicing into boards along the longitudinal direction with the thickness close to the width of the small specimen; (c) Cutting lengthwise into strips with the thickness close to the thickness of the small specimen; (d) Cutting into the length of the specimen; (e) The cross–section of the small specimen 54

3.6 The process of measuring the grain angle 56

3.7 The measuring result of grain angle 57

3.8 The distribution of dimension measurements. 59

3.9 Schematic diagram of amplitude decay. 61

3.10 Relationship between different testing method of internal friction 62

3.11 Results of vibration tests in references. 62

3.12 Vybris system 64

3.13 The record of weight, specific modulus and damping coefficient during the equilibrium process 65

3.14 Vibration test results 67

3.15 Relationship between specific modulus (GPa) and tanδ from literature. 68

3.16 Definition of delta Ono value 68

3.17 The sampling results of Douglas fir with maximum density variance. 71

3.18 The sampling results of Poplar with maximum density variance. 72

3.19 The sampling results of Beech with maximum density variance. 73

3.20 The sampling results of Oak with maximum density variance. 74

3.21 The sampling results of Douglas fir with maximum specific modulus variance. 75

3.22 The sampling results of Poplar with maximum specific modulus variance. 76

3.23 The sampling results of Beech with maximum specific modulus variance. 77

3.24 The sampling result of Oak with maximum specific modulus variance. 78

3.25 The sampling results of Douglas fir with maximum delta Ono variance. 79

3.26 The sampling results of Poplar with maximum delta Ono variance. 80

3.27 The sampling results of Beech with maximum delta Ono variance. 81

3.28 The sampling results of Oak with maximum delta Ono variance. 82

3.29 The sampling results for maximum density variance and specific modulus at 15.5 MPa. 83

3.30 The sampling results for maximum density variance and specific modulus at 22 MPa. 84

4.1 Creep Box. (a) The structure of a creep box. A specimen is supported by the supports on both sides, and the mass holder hangs on the specimen. The weight of the mass holder is about 50 g, and it holds a 600 g lead block. (b) Looking at the top of the sample, the gray part is the support of the creep box on both sides with the black marks to align the sample to make sure the longitudinal direction is perpendicular to the black marks indicated by the red arrow. (c) Top of the specimen with the mass holder. The dark gray bars are the loading point on the sample, and the light gray part is the lower part of the mass holder, which connects a thin metal bar to hang the lead block. There are two markers on the center point of the two dark gray bars to ensure that the lead block is hung in alignment with the center point of the sample. 87

4.2 Creep boxes in chamber before installing the specimens. The boxes are connected by C–clamps and fixed at the bottom of the chamber. 87

4.3 Relative creep values at different testing relative humidity (Matar, 2003) 89

4.4 Creep behavior at different testing temperature. (Morlier, 1994) 89

4.5 Calculation of creep strain and hygroscopic strain (Montero, 2011). 91

4.6 Relative compliance of 1 week creep test data at moisture content = 26% and predictive models toward 50 years (Montero and Gril, 2016). 92

4.7 Calculating starting point by extrapolation. 93

4.8 Creep test results, separated into creep strain (ε_c, $\mu\varepsilon$) and hygroscopic strain (ε_{hy}, $\mu\varepsilon$) of density group for each species. 95

4.9 Creep test results, separated into creep strain (ε_c, $\mu\varepsilon$) and hygroscopic strain (ε_{hy}, $\mu\varepsilon$) of specific modulus group for each species. 96

4.10 Creep test results, separated into creep strain (ε_c, $\mu\varepsilon$) and hygroscopic strain (ε_{hy}, $\mu\varepsilon$) of delta Ono group for each species. 97

4.11 Creep test result of the group with close specific modulus, mix species. 98

4.12 Sample condition after creep tests. Green: valid data; Orange: discontinuous data; White: untested specimens 98

4.13 Distribution of the specimens with discontinuous data 99

4.14 Creep compliance (GPa) against time (sec) of density group for each species. 101

4.15 Creep compliance (GPa) against time (sec) of specific modulus group for each species. 102

4.16 Creep compliance (GPa) against time (sec) of delta Ono group for each species. 103

4.17 Creep compliance of the group with close specific modulus 104

4.18 Relationship between dynamic Young's modulus and initial compliance (J_0) 105

4.19 Correlation between density at RH=85% and compliance. (a) initial compliance J_0. (b) compliance at 1^{st} minute J_{1m}. (c) compliance at 1^{st} hour J_{1h}. (d) compliance at 1^{st} day J_{1d}. 107

4.19 Correlation between density and compliance (continued). (e) compliance at 5^{th} day J_{5d}. (f) compliance at 7^{th} day J_{7d}. (g) compliance at 10^{th} day J_{10d}. 108

4.20 Correlation between dynamic Young's modulus and compliance. (a) initial compliance J_0. (b) compliance at 1^{st} minute J_{1m}. (c) compliance at 1^{st} hour J_{1h}. (d) compliance at 1^{st} day J_{1d}. 109

4.20 Correlation between dynamic Young's modulus and compliance (continued). (e) compliance at 5^{th} day J_{5d}. (f) compliance at 7^{th} day J_{7d}. (g) compliance at 10^{th} day J_{10d}. 110

4.21 Correlation between specific modulus and compliance. (a) initial compliance J_0. (b) compliance at 1^{st} minute J_{1m}. (c) compliance at 1^{st} hour J_{1h}. (d) compliance at 1^{st} day J_{1d}. 111

4.21 Correlation between specific modulus and compliance (continued). (e) compliance at 5^{th} day J_{5d}. (f) compliance at 7^{th} day J_{7d}. (g) compliance at 10^{th} day J_{10d}. 112

4.22 Correlation between delta Ono value and compliance. (a) initial compliance J_0. (b) compliance at 1^{st} minute J_{1m}. (c) compliance at 1^{st} hour J_{1h}. (d) compliance at 1^{st} day J_{1d}. 113

4.22 Correlation between delta Ono value and compliance (continued). (e) compliance at 5^{th} day J_{5d}. (f) compliance at 7^{th} day J_{7d}. (g) compliance at 10^{th} day J_{10d}. 114

5.1 Spring and dashpot elements (Bodig and Jayne, 1982). 116

5.2 The two basic combinations representing viscoelastic behavior (Bodig and Jayne, 1982). . . . 116

5.3 Creep function of Maxwell model (Banks et al., 2011). 117

5.4 Creep function of Kelvin model (Banks et al., 2011). 117

5.5 Calculation of delayed compliance 118

5.6 Delayed compliance results 119

5.7 Assumptions of creep behavior in the cell scale : deformation of the cell wall (1) and sliding between cells (2), proposition of a model to represent both phenomena. 120

5.8 Correlation between delayed compliance and density. (a) Compliance at 1^{st} minute minus initial compliance. (b) Compliance at 1^{st} hour minus initial compliance. (c) Compliance at 1^{st} day minus initial compliance. (d) Compliance at 5^{th} day minus initial compliance. 121

5.8 Correlation between delayed compliance and density (Continue). (e) Compliance at 7^{th} day minus initial compliance. (f) Compliance at 10^{th} day minus initial compliance. 122

5.9 Regression slope of delayed compliance and density. (a) The linear regression result from $J_{1m} - J_0$ to $J_{10d} - J_0$. (b) The linear regression result from $J_{1h} - J_0$ to $J_{7d} - J_0$. 122

5.10 Correlation between differences of compliance and density. (a) Compliance at 1^{st} minute minus initial compliance. (b) Compliance at 1^{st} hour minus 1^{st} minute. (c) Compliance at 1^{st} day minus 1^{st} hour. (d) Compliance at 5^{th} day minus 1^{st} day. 123

5.10 Correlation between difference of compliance and density (Continue). (e) Compliance at 7^{th} day minus 5^{th} day. (f) Compliance at 10^{th} day minus 7^{th} day. 124

5.11 Regression slope of difference of compliance and density. (a) The linear regression result from $J_{1m} - J_0$ to $J_{10d} - J_{7d}$. (b) The linear regression result from $J_{1h} - J_{1m}$ to $J_{7d} - J_{5d}$. 124

5.12 Schematic representation of the deformation and rate of deformation during the creep process showing 3 steps : primary, secondary and tertiary creep (Bodig and Jayne, 1982). 125

5.13 Experimental curves. 125

5.14 Primary and secondary creep calculation scheme for experimental data. 126

5.15 The relation between delayed compliance and density. (a) primary creep (b) secondary creep. $\times$: Douglas fir, $\bullet$: Poplar, $\star$: Oak, $+$: Beech, ——: 95% confidence region (CR), - - - -: 95% prediction band 127

5.16 The relation between specific compliance and density. (a) primary creep (b) secondary creep. ×: Douglas fir, •: Poplar, ⋆: Oak, +: Beech, ——: 95% confidence region (CR), - - - -: 95% prediction band 128

5.17 The relation between specific compliance and specific modulus. (a) primary creep (b) secondary creep. ×: Douglas fir, •: Poplar, ⋆: Oak, +: Beech, ——: 95% confidence region (CR), - - - -: 95% prediction band 129

5.18 The relation between adjusted relative compliance and specific modulus. (a) primary creep (b) secondary creep. ×: Douglas fir, •: Poplar, ⋆: Oak, +: Beech, ——: 95% confidence region (CR), - - - -: 95% prediction band 130

5.19 The relation between delayed compliance and creep factor. (a) primary creep (b) secondary creep. ×: Douglas fir, •: Poplar, ⋆: Oak, +: Beech, ——: 95% confidence region (CR), - - - -: 95% prediction band 131

5.20 Discrete compliance model. 133

5.21 Fitting process of compliance model for specimen DA046. (a) Black dotted lines are the curves from $J_1(t)$ to $J_5(t)$. Red dotted line is the experimental data of DA046. (b) Black dotted line is the fitting result, which is the sum of $J_1(t)$ to $J_5(t)$. 134

5.22 Linear regression result of J_i and density 135

5.23 Relationship between J^*i and density. (a) Correlation between J^*1 and density. (b) Correlation between J^*2 and density. (c) Correlation between J^*3 and density. (d) Correlation between J^*4 and density. (e) Correlation between J^*5 and density. ×: Douglas fir, •: Poplar, ⋆: Oak, +: Beech, ——: 95% confidence region (CR), - - - -: 95% prediction band 136

5.24 Linear regression result of J_i and specific modulus (E_s) 137

5.25 Relationship between J^*i and density. (a) Correlation between J^*1 and density. (b) Correlation between J^*2 and density. (c) Correlation between J^*3 and density. (d) Correlation between J^*4 and density. (e) Correlation between J^*5 and density. ×: Douglas fir, •: Poplar, ⋆: Oak, +: Beech, ——: 95% confidence region (CR), - - - -: 95% prediction band 138

5.26 Possible predicted function of J^*i 139

5.27 Multiple regression model 140

5.28 Fitting result of $b(\log \tau_i)$ and $c(\log \tau_i)$. 142

A.1 Multiple regression model fitting results of Douglas fir. 152

A.2 Multiple regression model fitting results of Douglas fir (Continue). 153

A.3 Multiple regression model fitting results of Douglas fir (Continue) 154
A.4 Multiple regression model fitting results of Douglas fir (Continue). 155
A.5 Multiple regression model fitting results of Poplar. 156
A.6 Multiple regression model fitting results of Poplar (Continue). 157
A.7 Multiple regression model fitting results of Poplar (Continue). 158
A.8 Multiple regression model fitting results of Poplar (Continue). 159
A.9 Multiple regression model fitting results of Beech. 160
A.10 Multiple regression model fitting results of Beech (Continue). 161
A.11 Multiple regression model fitting results of Beech (Continue). 162
A.12 Multiple regression model fitting results of Beech (Continue). 163
A.13 Multiple regression model fitting results of Oak. 164
A.14 Multiple regression model fitting results of Oak (Continue). 165
1 les résultat d'echantillonage ii
2 Système d'expérience iii
3 L'hypothèse principale iii
4 Modèle du fluage avec de nombreux éléments Kelvin iv
5 Le resultat de modelisation iv

List of Tables

2.1 References and testing information in the database. 34

3.1 The mechanical data from CIRAD Tropix 7 wood database [2] 54

3.2 Label system for samples. 55

3.3 The global and local grain angles (degree) for the four species. 57

3.4 Dimensions and density of the 4 species in dry and wet conditions. 60

3.5 The fitting parameters from the references for equation 3.9 66

3.6 The sampling parameters of Douglas fir with maximum density variance. 71

3.7 The sampling parameters of Poplar with maximum density variance. 72

3.8 The sampling parameters of Beech with maximum density variance. 73

3.9 The sampling parameters of Oak with maximum density variance. 74

3.10 The sampling parameters of Douglas fir with maximum specific modulus variance. 75

3.11 The sampling parameters of Poplar with maximum specific modulus variance. 76

3.12 The sampling parameters of Beech with maximum specific modulus variance. 77

3.13 The sampling parameters of Oak with maximum specific modulus variance. 78

3.14 The sampling parameters of Douglas fir with maximum delta Ono variance. 79

3.15 The sampling parameters of Poplar with maximum delta Ono variance. 80

3.16 The sampling parameters of Beech with maximum delta Ono variance. 81

3.17 The sampling parameters of Oak with maximum delta Ono variance. 82

3.18 The sampling parameters for maximum density variance and specific modulus at 15.5 MPa. . 83

3.19 The sampling parameters for maximum density variance and specific modulus at 22 MPa. . . 84

4.1 Creep boxes information 88

5.1 Best fitting parameters of multiple regression model. 142

List of Symbols

MFA	Microfibril angle
RH	Relative humidity
ρ	Density (g/cm^3)
α_V	Volume shrinkage coefficient
t	Time
F	Force
STD	Standard deviation
σ	Stress
J	Compliance
P	Load
L	Distance between the 2 supports of 4-point bending
l	Distance between the 2 loading points
b	Width of the specimen
h	Thickness of the specimen
E	Elastic modulus
ε	Strain
ε_c	Creep strain
ε_{hy}	Hygroscopic strain
η	Internal friction
λ	logarithmic decrement
$tan\delta$	Loss tangent
Q^{-1}	Quality factor
α	Temporal damping
Δf	Bandwidth at half-power of the peak
f_R	Resonance frequency
E'	dynamic Young's modulus
E_s	specific modulus (GPa)
$Grain_{AVG}$	Average local grain angle

Chapter 1

Introduction

1.1 Concerning wood and timber materials

The use of wood to make tools and shelters dates back to the earliest days of human history. It has also been used for transport and warfare, which has affected the human culture for thousands of years (Bodig and Jayne, 1982; Shmulsky and Jones, 2011). In addition, wood has been used in building construction since ancient times. For example, there is a series of small pile-dwelling wood houses built from around 5000 to 500 B.C. on the lakeside near the Alps.[1] There are still some structures, preserved until now, which testify the longevity of the construction. The oldest wood structure still standing nowadays is Hōryū-ji at Nara in Japan[2] (Wiedenhoeft and Miller, 2005). This wood temple was constructed during the Asuka Period, about 7^{th} century (figure 1.1).

Figure 1.1: Photography of temple Hōryū-ji in Japan

Another example in Europe is Urnes Stave wooden Church in Norway, which was built in the 12^{th} and 13^{th} centuries (figure 1.2). It is a traditional Scandinavian wooden architecture preserved and still standing today[1]. These are a few noteworthy examples of timber structures as a memorial proof of longevity.

Wood has always been an important raw material. During the 1970s in North America, wood products were used in construction more than any other structural materials. Therefore, the consumption of wood in the 1980s was even equal to the world's annual production of iron and steel (Bodig and Jayne, 1982).

[1] UNESCO World Heritage Conservation: https://whc.unesco.org/
[2] Horyoji: http://www.horyuji.or.jp/en/garan/

Figure 1.2: Photography of church Urnes Stave in Norway

According to 2005 statistics, the weight of wood used annually in the United States is almost equal to the weight of metal and plastic combined (Shmulsky and Jones, 2011).

Not only renewable after a few decades and low-energy recyclable, wood is also an important carbon storage resource. One cubic meter of new-growing wood can contain from 176 to 320 kg of carbon (Wiedenhoeft and Miller, 2005). Considering the energy consumption required to produce a cubic meter of material, wood is lower than many other construction materials like cement, plastic, steel, and aluminum (Blaß and Sandhaas, 2017). As a natural material, the physical properties of wood show a large diversity, regardless of species or even individually within a tree or a log. For example, the specific gravity of wood can be almost 10-fold different between species, 6-fold within a species and 3-fold within a year ring (Bodig and Jayne, 1982).

The plant that we normally call a "tree" is defined as a woody plant with a conventional height of regularly 4 to 6 meters and often even more (Shmulsky and Jones, 2011). Nowadays, the materials we commercially call "wood" are the trees of the Coniferales that produce softwood and Dicotyledons that produce hardwood (Kollmann and Côté, 1968). Softwoods have needle-like leaves that remain green almost year-round. Hardwoods, on the other hand, have broad leaves that usually change color and fall off in the fall. These two types of wood are not only different in appearance, but also in their chemical composition and cell structure.

To study mechanical behavior of wood, it is necessary to start from the chemical composition and the structure.

1.1.1 Chemical composition of wood

There are three main components in wood: cellulose, hemicellulose and lignin. They compose the main structure of the cell wall. Cellulose is a long linear molecule with high tensile strength that forms microfibrils

and is embedded in a matrix of lignin and hemicellulose. Lignin is a brittle matrix material. Hemicellulose helps to connect lignin and cellulose. Thus, these three components combine to act as the basic units of the cell wall (Wiedenhoeft and Miller, 2005; Bucur and Martin, 2011).

Cellulose

The monosaccharides that build the cell wall are made from carbon dioxide and water through photosynthesis. The two main components are glucose and fructose, which can be converted into each other by enzymatic action. These two compounds can be combined to form sucrose, which can be transported within the tree. Cellulose is a huge polymer composed of glucose. Glucose is bound by β linkages into a long linear polymer similar to starch, but cannot be hydrolyzed. The chemical formula of cellulose is $(C_6H_{10}O_5)_n$, with n exceeding 10000. The length of this macromolecule is 10 μm. It provides the main support for the entire structure (Shmulsky and Jones, 2011).

Hemicellulose

Hemicellulose is a polymer that is much smaller than cellulose. There are six different basic compounds to build hemicellulose, including glucose, fructose, mannose, galactose, xylose and arabinose. These simpler sugars are also made in the leaves. About hundreds to thousands of simple sugars build hemicellulose, which is a branched polymer. It acts as a binder within the cell wall structure (Shmulsky and Jones, 2011).

Lignin

Lignin is a kind of network polymer with benzene ring. There are three main compounds, including trans-*p*-coumaryl alcohol (*p*-hydroxyphenyl unit, H unit), trans-coniferyl alcohol (guaiacyl unit, G unit), and trans-sinapyl alcohol (syringyl unit, S unit) (Popescu et al., 2006). It acts as a matrix within and between the accumulations of cell walls. In addition, lignin has a characteristic that differs from cellulose and hemicellulose in that it is less hydrophilic. Therefore, it also has the function of reducing variation with humidity. It is a compound with a small amount of toxicity, so it makes wood more resistant to decay and prevents insect attacks (Shmulsky and Jones, 2011).

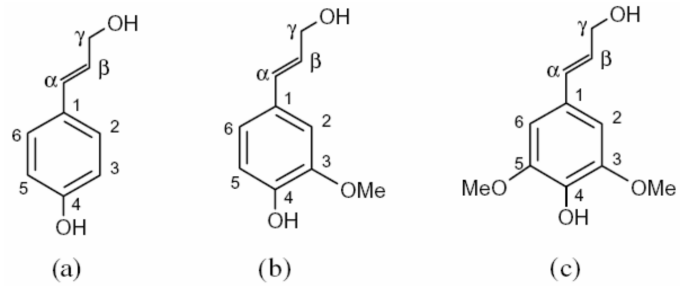

Figure 1.3: Monomeric units in lignin (Popescu et al., 2006).

Ash and Extractive

The main components of wood are the compounds mentioned earlier, and a little bit of inorganic compounds. These inorganic compounds remain after burning and are called ashes. Ash can contain several components, such as calcium, magnesium, manganese, potassium, and silicon. The percentage of these components is very low, about 0.3 to 0.5%. However, some tropical woods contain more than 2% by weight of ash (Shmulsky and Jones, 2011).

Extractives have a wide variety of wood compounds, including fats, fatty acids, fatty alcohols, phenols, terpenoids, steroids, resin acids, rosins, waxes and many other minor organic compounds. Most of them are categorized as secondary metabolites and can be extracted by solvents. They provide natural resistance to decay fungi, color and wood fragrance (Hon and Shiraishi, 2000; Wiedenhoeft and Miller, 2005; USDA Forest Service, 2021). In addition, they affect the loss tangent damping coefficient, which will be discussed in Chapter 3.

1.1.2 Composition and structure of cell wall

Wood is composed of the above-mentioned chemical components, and has a multiscale structure organization. Figure 1.4 provides a schematic representation of the different layers and scales of softwood. Based on cambium age, it can be classified as juvenile wood and mature wood. By location and function, it can be divided into heartwood and sapwood. After felling the wood, we make it into lumber. Different cuts cause differences in its physical and mechanical properties. Through the microscope, we can see that the wood material is made up of different types of cells, depending on their function. Wood cells are bound by an intermediate layer, and the cells are formed by several layers of cell walls. The cell walls can also be divided into several layers with different microfibril orientations. Thus, wood is a complex composite material with many scales of structure, each with natural differences.

Structure of microfibrils

Cellulose is a giant linear polymer of glucose that is the main component of the cell wall. Typically, 50-80 cellulose molecules are bound together to build "elementary fiber". Several elementary fibers, there are possible from 36 chains to 200 chains depending on organisms, links are connected by hydrogen bonds between their respective surfaces to become microfibrils (Bodig and Jayne, 1982; Delmer and Amor, 1995; Nilsson and Rowell, 2012). However, the cellulose molecules are bound by hydrogen bonds but are not perfectly aligned. Figure 1.5 shows crystalline region, semicrystalline region, and amorphous region within microfibril. It shows that there is still some potential for deformation within the microfibrils. Thus, microfibrils are the main units for building cell walls, which also play a decisive role in the mechanical properties of wood.

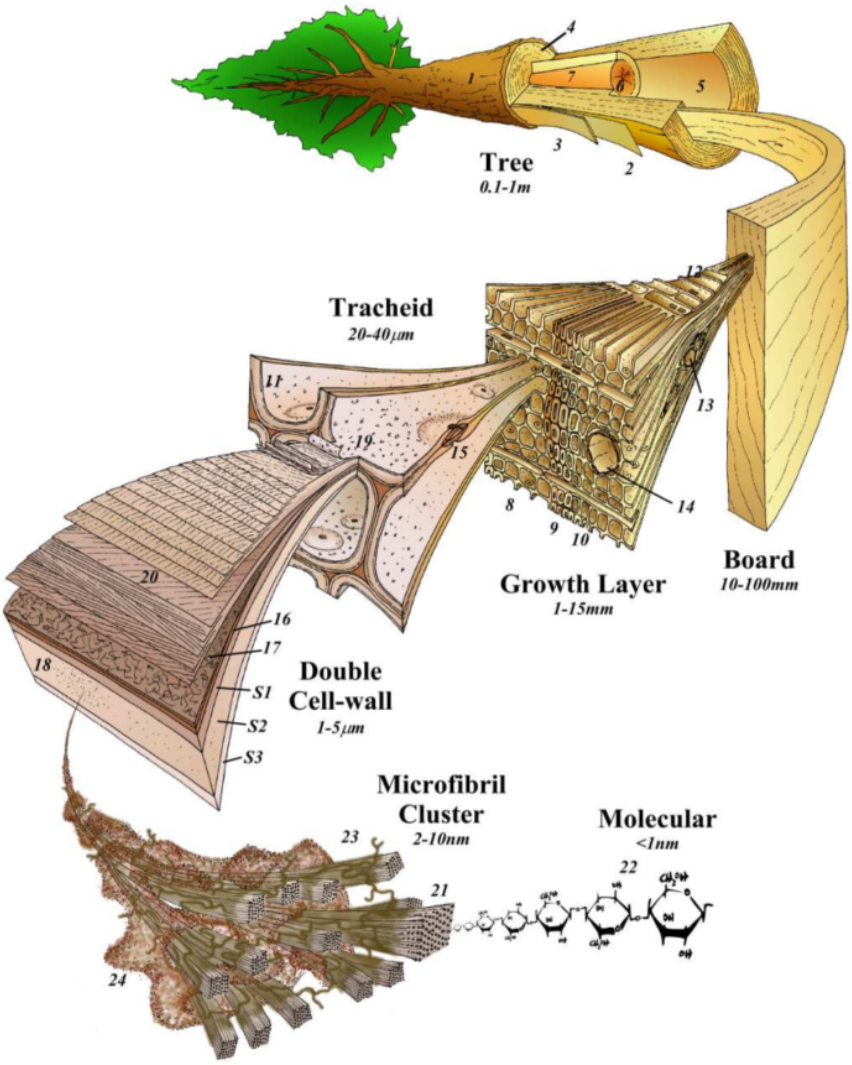

Figure 1.4: Multiscale structure of a softwood (Harrington, 1996, 2002).

The structure of cell wall

There are 3 layers that form the cell wall, which are middle lamina between cells, primary wall, and secondary wall from the outside to the inside of the cell. Some cells could also have the additional G-layer. Figure 1.6 (a) shows the structure of cell wall. Normally, the primary walls are formed by the complex of elementary fibrils and xylogucan (Hayashi, 1989). It determines the form of the cell and its direction of elongation. Microfibrils are then constructed by enzymes on the membrane and placed between the primary wall and the plasma membrane as a secondary wall, which is the thickest and gives the cell the greatest support.

The structure of secondary wall

The secondary wall is the thickest layer in the cell, and we can also divide it into three parts, called S1, S2 and S3 layers. Figure 1.6 (b) shows the structure and microfibril angle (MFA) of cell walls. Layer S1 is the first secondary wall formed, and the microfibers are wound around the layer at an oblique angle of 60 to 80

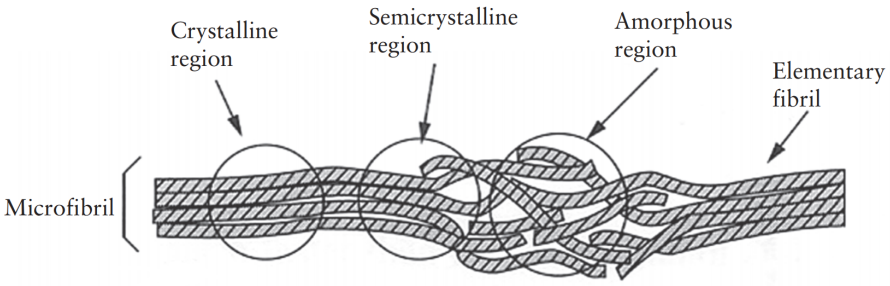

Figure 1.5: Structure within a microfibril (Shmulsky and Jones, 2011).

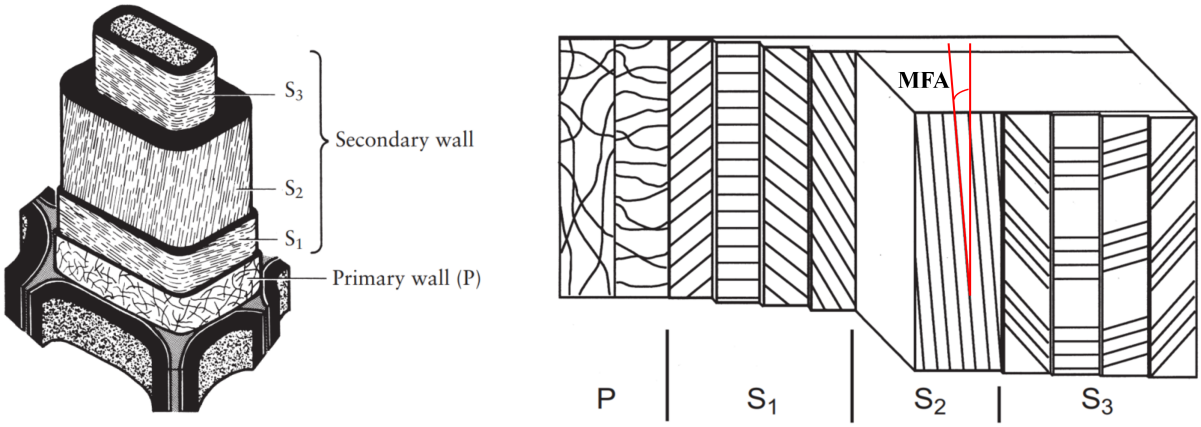

(a) Shmulsky and Jones (2011) (b) Abe and Funada (2005)

Figure 1.6: Cell wall structure.

degrees (Blaß and Sandhaas, 2017). The MFA of layer S1 gradually changes and then connects to layer S2. Layer S2 is the thickest of the three, it occupies about 60 to 80% of the cell wall (Astley et al., 1998). Layer S2 has the smallest MFA, which gives the greatest support to the cell wall, but the MFA is influenced by the growth conditions. According to the measurement of Kataoka et al. (1992), MFA of S2 layer is about 10 to 15 degrees. The microfibers in the S3 layer at a large angle of about 60 to 90 degrees, which is also the thinnest layer in the secondary wall (Abe and Funada, 2005; Blaß and Sandhaas, 2017). Therefore, the MFA of wood is mainly influenced by the thickest layer, the S2 layer, which plays an important role in the mechanical properties of the wood.

1.1.3 Wood anatomy and mechanical properties

The variation of mechanical properties within an individual wood element can be identified at 5 different scales: within the layers of cell wall, on the cell wall, cell level of organization, within the cells, and at the wood tissue with annual growth (Bodig and Jayne, 1982). In the previous section, changes at the cell wall level were shown. Wood is composed of different kinds of cells for different functions. Figure 1.8 shows the three cross-section at microscale. Figure 1.8 (a) shows the structure of softwood. The main cells in softwood are tracheids, which provide water transport and mechanical support. Figure 1.8 (b) shows the structure of hardwood. Hardwood microstructure is more complex than on softwood, including vessels, fibers, and

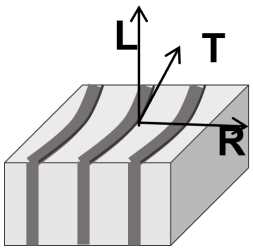

Figure 1.7: 3 main directions in the wood: longitudinal (L), radial (R), tangential (T) direction.

parenchyma cells (Richter, 2015; Schweingruber and Börner, 2018). Compared to softwoods, hardwoods have higher cellular variability and higher evolutionary level (Harrington, 1996). Wood structure influences the density, that is, the ratio between wood tissue and porosity. Softwood specific gravity is around 0.44, whereas hardwood specific gravity is around 0.57 (USDA Forest Service, 2021). Most cells are long and follow the same direction, so we can see there is a principal direction for the material (Kollmann and Côté, 1968). This anisotropy is a specific well-known characteristic of wood.

There are 3 main directions in the wood: longitudinal (L), radial (R), and tangential (T) direction (figure1.7). The fiber is oriented in the longitudinal direction. The tangential direction of the wood rings is the tangential direction. The direction perpendicular to the wood ring and starting from the pith is the radial direction. This also leads to variations in dimensional stability and mechanical properties. In consequence, the modulus of elasticity across the grain is much lower than along the grain (Kollmann and Côté, 1968), so $E_L \gg E_R > E_T$. According to USDA Forest Service (2021), E_T/E_L for hardwood is about 0.057, for softwood is about 0.054, E_R/E_L for hardwood is about 0.114, for softwood is about 0.093. The tensile strength of wood along the fiber direction is higher than its compressive strength. The bending strength, a combination of tensile and compressive strength, is between the two (USDA Forest Service, 2021).

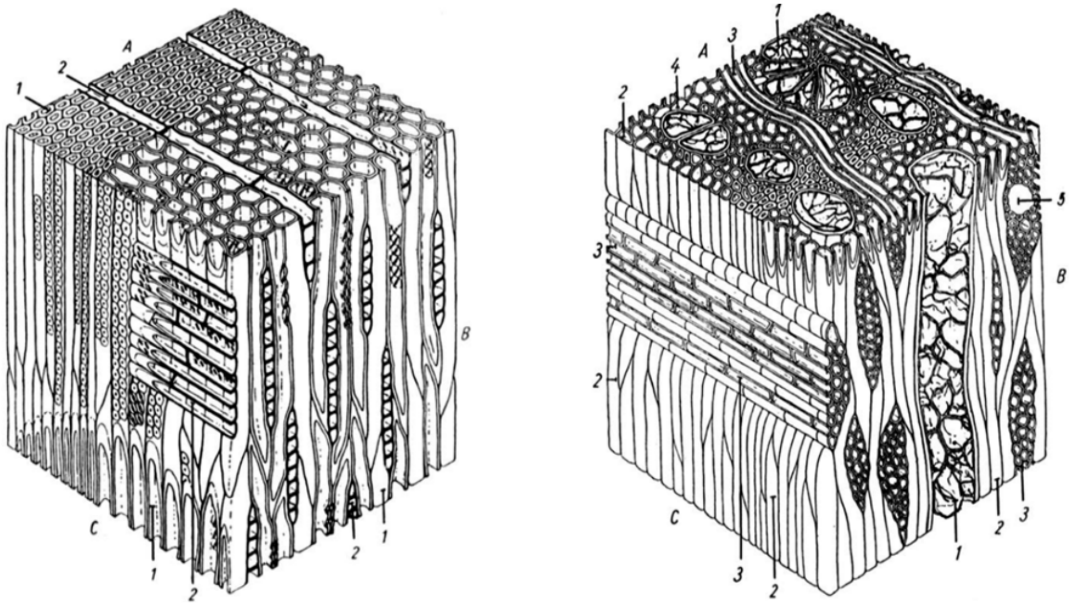

(a) (b)

Figure 1.8: Microscopic structure of (a) softwood and (b) hardwood (Richter, 2015).

1.2 Creep behavior

When materials are exposed for long-term time-scales, the effects of time need to be considered with caution, especially in the case of time-dependent materials. Two dual time-dependent behaviors can be discussed: creep and relaxation. Creep is the delayed deformation with time for a constant applied load. In contrast to this, relaxation is the decrease in stress with time for a constant deformation applied. Both behaviors can be observed on materials in service for structural applications. In this study, we mainly focus on creep behavior, which can be observed by changes in deformation (Slivker, 2007) for both its facility to experiment and to measure.

1.2.1 What is creep behavior?

Creep behavior is a phenomenon in which the deformation increases with time under a constant load. It had been mentioned in Leclerc and de Buffon (1740). In the mechanical experiment with wood, the authors found that a specimen that will hold a certain weight for a few minutes will not be able to hold the same weight for an hour. In addition, the specimens could not carry two–thirds of the load they had carried for one day for six months. There is also a record of this phenomenon on iron produced by Vicat in 1830 (Bell, 1989; Temesgen et al., 2020).

Creep behavior is widely observed in many materials like metals, plastics, rocks, concretes or glasses. It is considered to be part of solid mechanics and is intermediate between elastic and viscous behavior. When a stress is applied to an object, the structure of the object would rearrange inside the material. In reality, this rearrangement must take some time. If this process is short enough to be negligible, we consider the material to be purely viscous. The energy required to produce the deformation is dissipated in the form of heat. On the other hand, when the rearrangement of the material structure takes almost infinite time, we consider this material as a purely elastic material. In general, all materials are viscoelastic in between the two previously mentioned. Linear viscoelastic behavior means that the behavior of the material can be described by linear differential equations with constant coefficients, which plays an important role in modeling and prediction. (Tschoegl, 2012).

Studies of creep theory usually attempt to describe the interaction of strain-time relationships with load and temperature (Rusinko and Rusinko, 2011). Figure 1.9 shows a diagram of the creep behavior under constant temperature and load. The whole curve can be divided into three parts. Primary creep is the part where the creep rate decreases monotonically. Secondary creep is a long period, similar to plastic deformation. When the whole process enters tertiary creep, microscopic cracks appear at the grain boundaries, which eventually lead to the failure of the material and possibly of the structure (Betten, 2008; Guedes, 2011).

For design or manufacturing and even structural serviceability, it is important to understand the creep

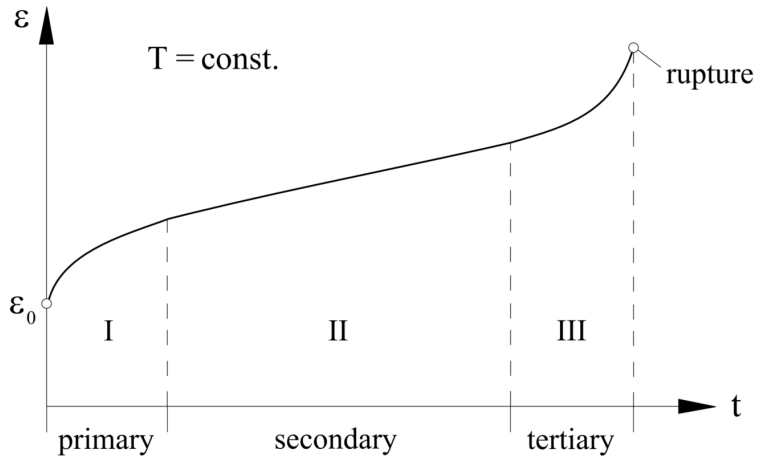

Figure 1.9: Diagram of constant temperature creep behavior (Betten, 2008)

behavior of the material because it will affect the structural stability or the performances of the desired product. In addition, creep must be considered carefully to prevent creep behavior from leading to failure at constant stresses below the tensile strength value (Guedes, 2011).

1.2.2 Why does it happen?

Until now, there is still no global creep theory which is suitable for all materials. In fact, it is impossible to develop such a theory without considering material microstructure and component interactions. (Rusinko and Rusinko, 2011). This is because the creep mechanisms are different for different materials. They can be divided into three levels: atomic, molecular and structure.

Metals

Metals are made up of strictly organized atoms directly. Even though alloys are made of a good mixture of different kinds of metals, they are connected to each other by metallic bonds, i.e. the atoms are arranged together. The mechanism of plasticity or creep is the dislocation movement that leads to grain slip. The creep behavior of metals can be modeled by slip or synthesis theory (Rusinko and Rusinko, 2011).

Polymers

Another widely used material is polymers, such as plastics. These are compounds that are connected by covalent bonds and are difficult to break and rebuild. However, huge polymers, whether linear or networked, have molecules that are connected to each other by hydrogen bonds, which can change the arrangement within the material (Bodig and Jayne, 1982).

Composites

Composites are another dimension of the problem. For example, in fiber-reinforced composites, there are more factors that influence the creep behavior, such as the behavior of the matrix, the elasticity and strength of the fibers, the arrangement of the fibers or the interfacial properties of the fibers with the matrix (Guedes, 2011). The increase in deformation may be caused by one or more of these factors.

1.3 Creep behavior on wood

The creep behavior of wood has been mentioned in the study of Grossman and Kingston (1954), Youngs (1957) and even earlier. In the studies conducted in the 1950s by Armstrong, this phenomenon was already being tested and discussed under the name "creep". In addition, there were some other studies, for example Norris and Kommers (1960), called this phenomenon as plastic flow. Compared with the materials mentioned before, wood is much complex composite with different levels of interactions and large variability. Therefore, building a nominal creep model for wood materials is not feasible and rather require a sophisticated and dedicated approach.

Under specific environmental conditions, such as a certain stress limit and a constant moisture content, wood can show linear viscoelastic behavior (Holzer et al., 1989). For example, Grossman and Kingston (1963) has mentioned that the linear viscoelastic behavior can be found in tensile creep tests performed on hoop pine at 50 °C parallel to the grain, with stresses of 75% of the static strength. Bhatnagar (1964) cited in Schniewind (1968) showed that the limit of the linear creep behavior is 50% of static strength for tensile test parallel to grain on Teak. This implies that the loading conditions affect the creep behavior, and similar findings have been found in compression and bending tests (Schniewind, 1968). Under high–stress condition, wood exhibits nonlinear behavior which is caused by structure changes, and it has been mentioned in Kollmann (1957) (Schniewind, 1968).

1.3.1 Effects of temperature

Like metals and plastics, the creep behavior of wood is influenced by the ambient temperature. Creep behavior can be accelerated by increasing the temperature. In previous studies, temperatures in the range of 20 °C to 70 °C have been tested and have been shown to have a significant effect (Holzer et al., 1989; Morlier, 1994). The results of Sun and Frazier (2007) present viscoelastic evolution of the compliance at multiple temperature levels, even leading to present a time/temperature equivalency.

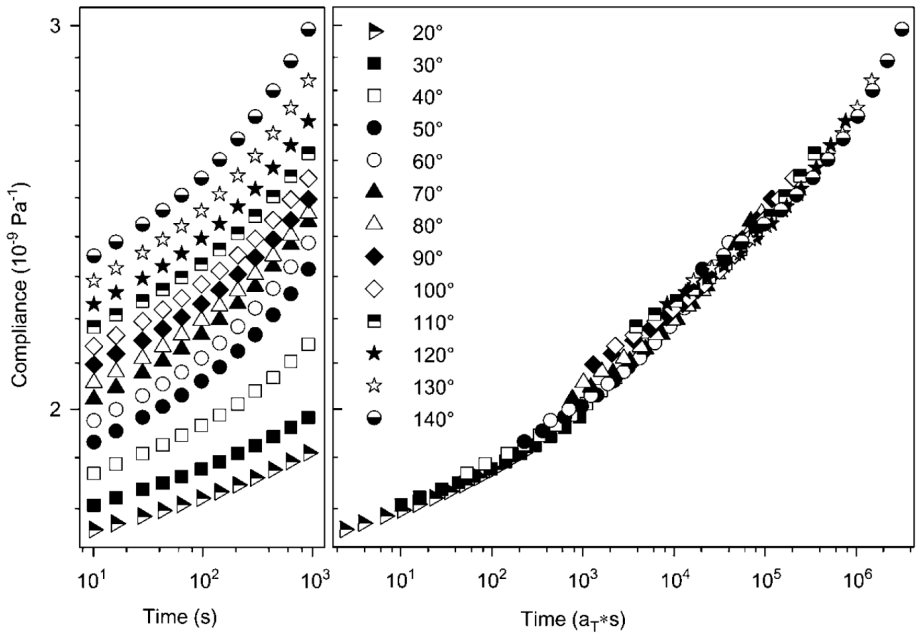

Figure 1.10: Evolution of compliance level at different temperature (left) and construction of a time/temperature equivalency(Sun and Frazier, 2007)

1.3.2 Effects of moisture

As a biological material, wood is more susceptible to environmental humidity than inorganic material. Both Armstrong and Kingston (1960) and Gibson (1965) have mentioned that a change in moisture content raises the creep deformation of the specimen. The effect of the interaction of moisture movement (drying and wetting) with the mechanical behavior of wood is commented on and is called mechano–sorptive behavior (Holzer et al., 1989). Because this phenomenon causes significant additional deformation that may directly affect the service life of the structure, there are many studies on this phenomenon that hope to model and estimate this behavior more accurately. For example, Mårtensson (1994) mentioned that creep tests conducted in an environment with cyclic changes in relative humidity had higher deformation than the group in a constant environment. In addition, the increment was associated with environmental conditions. Figure 1.11 in Hunt (1989) shows the schematic diagram of mechano–sorptive behavior. The total compliance of creep behavior can be presented by the sum of creep compliance at constant and cyclic moisture content.

However, in the basic definition of creep behavior for a hygroscopic material, the experimental hygrothermal environment should be constant, to prevent any hygroscopic and diffusion behavior from affecting the material. Under the premise that the relative humidity of the environment does not change during the experiment, Pittet (1996) has presented the creep phase followed by a relaxation phase with different relative humidity (figure 1.12). The results obtained with similar stress level to failure show the non–linearity of creep strain level according to hygroscopic environment.

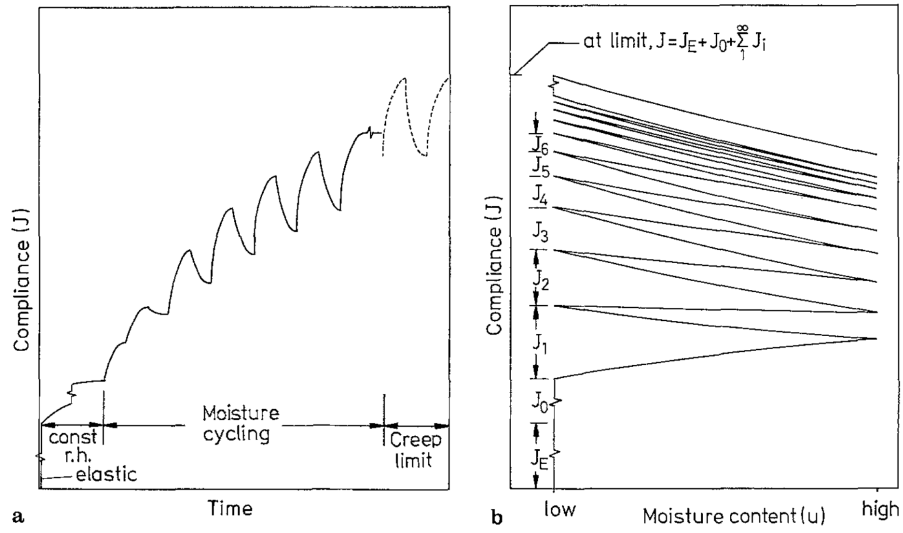

Figure 1.11: Schematics representation of mechano–sorptive creep over time (left) and moisture content (right) (Hunt, 1989)

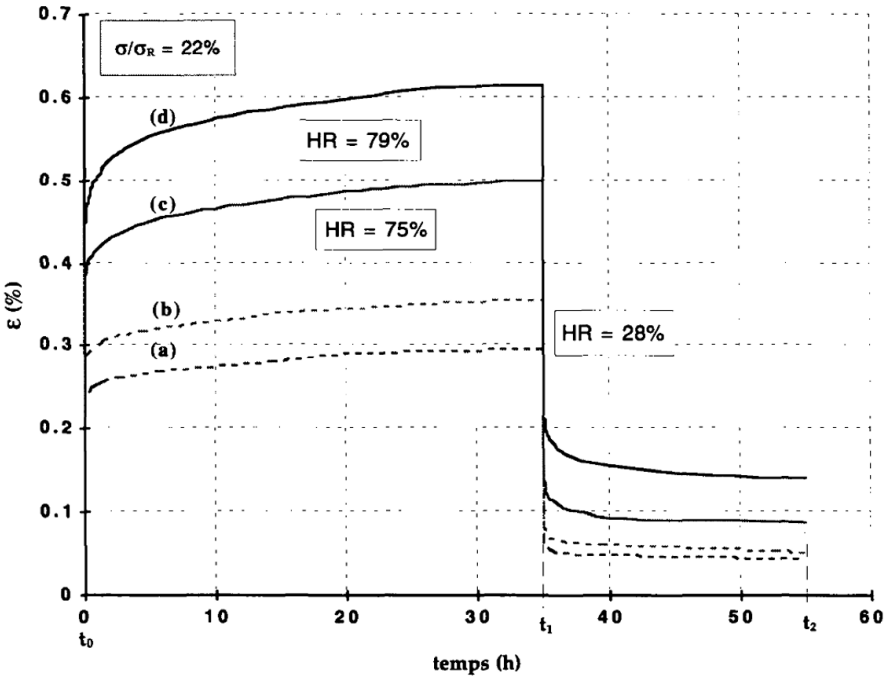

Figure 1.12: Evolution of strain with time during a first phase of 35 hrs of creep followed by 20 hrs of relaxation obtained at various relative humidity environment (RH=28% on (a) and (b) results, 75% for (c) and 79% for (d) (Pittet, 1996)

1.3.3 Effects of material properties

In addition to the effects of the experimental environment, wood properties also affect the creep behavior. Matar (2003) presents the creep test results for different specific moduli. Even with similar moisture content level and temperature, wood can express variability in creep deformation according to microstructural organization of the material and its specific density (figure 1.13). Additionally, the microstructure affects the creep behavior. Figure 1.14 shows the longitudinal tensile creep test results on Sugi with different microfibril angle (Kojima and Yamamoto, 2004). These two examples show that the properties of a material do have an effect on its creep behavior.

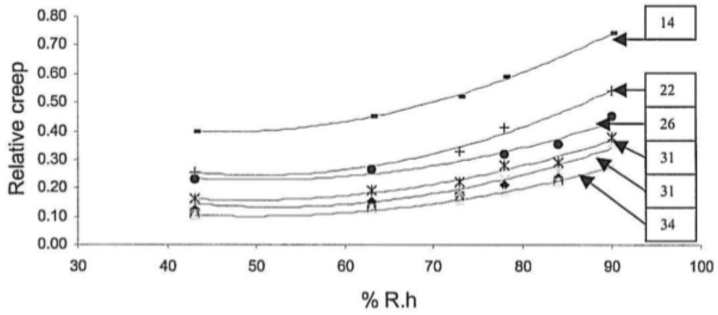

Figure 1.13: Evolution of relative creep after 1 week at various relative humidity levels and for different values of specific modulus (GPa) indicated on each curve. (Matar, 2003)

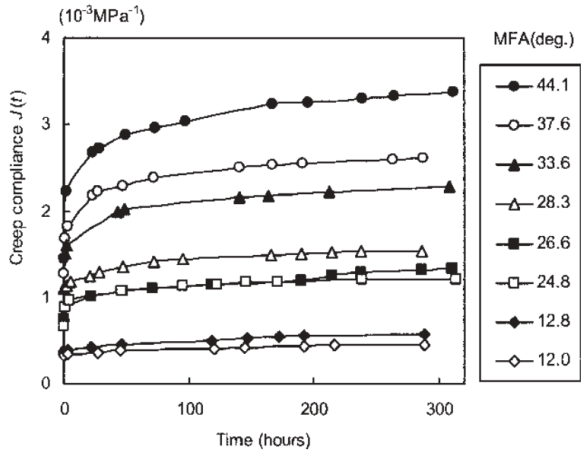

Figure 1.14: The longitudinal tensile creep test of Sugi earlywood specimens with different microfibril angle (MFA) (Kojima and Yamamoto, 2004)

1.4 Summary

Creep behavior of wood is a complex phenomenon that depends on temperature, moisture content and material properties. In order to better understand this phenomenon, this study started with the construction of a wood creep database. Considering the research objectives, we focused on the relationship between material properties and creep behavior under a constant hygrothermal environment. The wood creep database includes only the creep curves for constant environment.

Chapter 2

Wood Creep Database

In the first chapter, the time–dependent phenomenon of wood was presented. In the scientific literature, a variety of experimental results have been produced on different wood species, dimensions, moisture content and environments. In order to compare the results, the data were collected and digitized. After recalculation, they were organized in a database.

2.1 Importance of building a database

Building a database of materials' behavior could help to understand better its properties and also to predict its behavior or to compare the quality of materials between each others. It is a research method wildly used in many kinds of materials and come back in force with numerical developments. For example, the Inorganic Crystal Structure Database (ICSD) is published in 1913 provided by FIZ Karlsruhe. It is the largest database for completely determined inorganic crystal structures. This database is updated twice a year containing 262,242 entries and 184,968 types of structures. It is a well-organized database for all the researchers who work on crystallography domain (Zagorac et al., 2019; Karlsruhe, 1913). Also, several databases of additive manufacturing systems were created for the designers and practitioners, including materials, fabrication speed, machine parameters etc (Maidin et al., 2012). For the polymer industry, there are also the studies for the database of fiber reinforced polymers, collecting the mechanic properties of matrix and fibers for machine learning techniques (Liu et al., 2017; Huang et al., 2022).

As another example, the largest database of creep and shrinkage tests of concrete was built up since 1978 at Northwestern University (Hubler et al., 2015). It is a collaborative work by the researchers in different generations until today. This database contains 1400 sets of creep curves, which take into account different compositions, environments, shapes, and loading conditions (Tong et al., 2020). In Bazant and Baweja (2000), to compare and verify the accuracy of the creep and shrinkage model of concrete, the authors have used a large amount of data from the database. These examples demonstrate the importance of databases in the field of material science research.

2.2 Toward a wood creep database

Wood is a widely used biomaterial and many databases have been set up. There are many databases to collect the wood appearance features, mechanical properties, chemical compositions, etc. For example, the Wood Handbook, prepared by the United Stated Department of Agriculture Forest Service, collects data on the anatomical, physical and mechanical properties of commercial wood in North America (USDA Forest Service, 2021). It is a guide to the processing and use of wood that is updated every few years and includes a wood database with reference values for specific gravity, modulus of rupture, modulus of elasticity, Poisson's ratio, etc. In Guitard (1987) has also presented a wood mechanical database including specific gravity, modulus of elastic, and shear modulus.

There are a number of online wood databases available for reference. "InsideWood" is an online wood anatomy database constructed by North Carolina State University in collaboration with a number of researchers in the Netherlands, Belgium, the United Kingdom, Australia and Japan. This database is based on Chalk's dataset from the 1930s-1940s. Currently, the InsideWood database has a collection of over 36,000 micrographs, including over 3,000 species (InsideWood, 2004; Wheeler, 2011). There is also an online timber database, called "The Wood Database", built and maintained by Eric Meier. There are about 600 species searchable online. We can find photos of the wood, physical and mechanical data, and descriptions of the wood. The contents of the website are also published in a booklet (Meier, 2008). The website of the Timber Research and Development Association's website also includes a timber database with information on more than 150 commercial species. This database records information on the appearance, physical and mechanical properties of wood, the appearance of trees and the growing environment (TRADA, 1934).

Center for International Cooperation in Agricultural Research for Development (CIRAD) in France has a large and long-established collection of wood samples. The CIRAD wood collection has been existing for over 80 years and has collected 34,395 samples from a total of 8,385 species from 123 countries. A micro photo database with about 3,000 photos is based on this collection (Langbour et al., 2019). In addition, CIRAD wood database Tropix 7 is developed by Biomass, Wood, Energy, Bioproduct Research Unit (BioWooEB) in CIRAD. Tree characteristics, physical and mechanical properties, natural durability, and uses for 245 tropical and temperate forest species are included in the Tropix 7 database (CIRAD, 2017).

However, a comprehensive database on wood creep behavior does not yet exist. Tong et al. (2020) pointed out the importance of the wood creep database and gave us an idea. Building of a wood creep database will provide a powerful resource for predictive modeling, potentially provide a better understanding of the material and its rheological behavior, and be extended to a collaborative tool and further trendy methods of data mining techniques.

2.2.1 Describe of the database

Considering the objectives of this study, we focused on the relationship between material properties and creep behavior. In this study, 135 datasets of wood creep test under constant environment, which is about 20 °C and constant relative humidity, have been collected from 15 articles. Table 2.1 shows the references of the scientific article have been collected and the experimental conditions.

Table 2.1: References and testing information in the database.

Reference	Species	method	direction	grain angle (°)	RH (%)	T °C	Load/Stress	y unit	Subject
Schniewind and Barrett (1972)	Douglas fir	tensile	TL	***	50	22.2	16.55 MPa	relative creep %	grain angle: 0° & 90°
Schniewind and Barrett (1972)	Douglas fir	tensile	RL	***	50	22.2	16.55 MPa	relative creep %	grain angle: 0°, 15°, 30°, 45°, 60, 75°, 90°
Schniewind and Barrett (1972)	Douglas fir	tensile	TL	***	50	22.2	16.55 MPa	relative creep %	grain angle: 0°, 15°, 30°, 45°, 60, 75°, 90°
Nakai and Grossman (1983)	Eucalyptus	4pb	L	0	60	25	***	relative creep	Stress ratio: 17%, 33%, 50%, 67%
Nakai and Grossman (1983)	Eucalyptus	4pb	L	0	60	25	***	relative creep	Stress ratio: 17%, 33%, 50%, 67%
Nakai and Grossman (1983)	Hoop pine	4pb	L	0	60	25	***	relative creep	Stress ratio: 17%, 33%, 50%, 67%
Moosavi et al. (2016)	Hornbeam	4pb	L	0	65	20	***	Modulus of creep (MPa)	Growing altitudes: 400, 800, 1100 m
Moosavi et al. (2016)	Hornbeam	4pb	L	0	95	20	***	Modulus of creep (MPa)	Growing altitudes: 400, 800, 1100 m
Ozyhar et al. (2013)	European beech	tensile	***	0	65	20	26.2 MPa	strain %	L, T, R direction
Ozyhar et al. (2013)	European beech	comp.	***	0	65	20	11.9 MPa	strain %	L, T, R direction
Kojima and Yamamoto (2004)	Sugi	tensile	TL	***	100	20	14.2 MPa	compliance	MFA: 12, 12.8, 24.8, 26.6, 28.3, 33.6, 37.6, 44.1
Foudjet and Bremond (1989)	Movingui	feb	L	0	72	24	***	J $(MPa^{-1})\times10^{-5}$	Stress ratio: 24%, 28%, 33%, 41%
Foudjet and Bremond (1989)	Tali	feb	L	0	74	25	***	J $(MPa^{-1})\times10^{-5}$	Stress ratio: 28%, 34%, 41%
Foudjet and Bremond (1989)	Sapelli	feb	L	0	63	19	***	J $(MPa^{-1})\times10^{-5}$	Stress ratio: 26%, 30%, 35%, 42%
Foudjet and Bremond (1989)	Azobe	feb	L	0	63	20	***	J $(MPa^{-1})\times10^{-5}$	Stress ratio: 25%, 30%, 35%, 40%
Hermawan and Fujimoto (2019)	Sugi	Cantilever	T	90	***	20	1.86 N	J (GPa^{-1})	RH: 66%, 78%, 80%, 86%
Hermawan and Fujimoto (2019)	Sugi	Cantilever	R	90	***	20	2.15 N	J (GPa^{-1})	RH: 66%, 78%, 80%, 86%
Brian H. Bond (1993)	southern pine	***	L	0	65	20	22.06 MPa	J (Pa^{-1})	tensile, compression
Brian H. Bond (1993)	yellow poplar	***	L	0	65	20	22.06 MPa	J (Pa^{-1})	tensile, compression
Liu (1993)	scots pine	4pb	L	0	65	23	***	deflection (mm)	Stress ratio: 7.5%, 15%, 30%, 45%, 60%
Liu (1993)	scots pine	4pb	L	0	65	23	***	deflection (mm)	Stress ratio: 7.5%, 15%, 30%, 45%, 60%
Liu (1993)	scots pine	4pb	L	0	65	23	***	deflection (mm)	Stress ratio: 7.5%, 15%, 30%, 45%, 60%
Tissaoui (1996)	southern pine	***	L	0	65	20		J (Pa^{-1})	tensile, compression
Tissaoui (1996)	yellow poplar	***	L	0	65	20		J (Pa^{-1})	tensile, compression
Tissaoui (1996)	Douglas fir	comp.	L	0	65	20		J (Pa^{-1})	
Hoyle et al. (1985)	Douglas fir	4pb	L	0	65	21	***	relative creep %	Stress level: 1250, 1900, 2600, 3150 psi
Dong et al. (2021)	poplar	4pb	L	0	***	20	2.8 MPa	deflection (mm)	RH: 65%, 98%
Hering and Niemz (2012)	European beech	4pb	L	0	***	20		J (MPa^{-1})	RH: 35%, 80%, 95%
Moliński and Raczkowski (1988)	pine	4pb	L	0	40	20	52 N	relative creep	
Gnanaharan and Haygreen (1979)	basswood	3pb	L	0	***	22.22	155 N	relative creep	RH: 50%, 60%, 70%, 80%
Gnanaharan and Haygreen (1979)	basswood	3pb	L	90	***	22.22	9.1 N	relative creep	RH: 50%, 60%, 70%, 80%
Gnanaharan and Haygreen (1979)	basswood	tensile	L	90	***	22.22	9.1 N	deformation (10^{-4} inch)	RH: 50%, 60%, 70%, 80%
Gnanaharan and Haygreen (1979)	basswood	comp.	L	90	***	22.22	9.1 N	deformation (10^{-4} inch)	RH: 50%, 60%, 70%, 80%

***: Varies with test subject.
comp.: compression
3pb: 3-point bending
4pb: 4-point bending
feb: free end bending

2.2.2 Different testing method and loading

There is no standard testing method for the creep tests. Thus, every scientific study has designed a dedicated testing method for the subject which was focus on. The experimental methods which are usually used for wood creep test, including tensile test, compression test, 3–point bending test, and 4–point bending test. Figure 2.1 (a) shows a general relationship between different experimental methods (Granello and Palermo, 2019). In the database, there are also cantilever test and free end bending test, which has the similar effect to 3–point bending test and 4–point bending test but design the special shape for the study goal. However, different testing method reflect different wood mechanical properties. Classification is necessary before comparing. Figure 2.1 (b) shows the effect of loading direction. As we have mentioned in chapter 1, wood is an anisotropic material that different loading direction would have different behavior, as the curves in Schniewind and Barrett (1972).

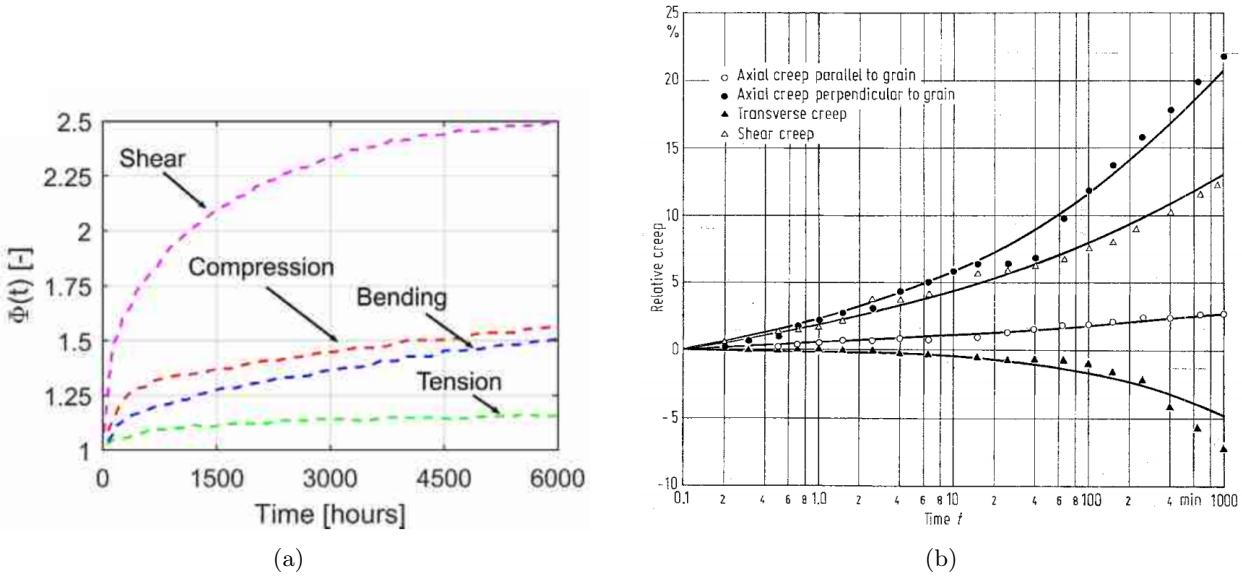

(a) (b)

Figure 2.1: (a) Creep behavior (relative creep against time) for different testing method in beams (Granello and Palermo, 2019). (b) Creep test result (relative creep against time) of different direction on the same board (Schniewind and Barrett, 1972)

2.2.3 Different observed parameter

Another factor has large variance is the observed parameter of the studies, that is, the timescale of x–axis and the y–axis unit of the experimental data. To understand the creep behavior, which is a time–dependent behavior, the record against time is necessary. There are two types of x–axis: linear and logarithm, presenting data based on demand. For the long–term experiment, the data is usually presented in logarithmic axis to have a global view (figure 2.1 b). Many types of time unit have been sued such as seconds, minutes, hours, and days depending on the experiment duration.

The variance of y–axis unit is more complex, and it is also one of the difficulty of constructing this

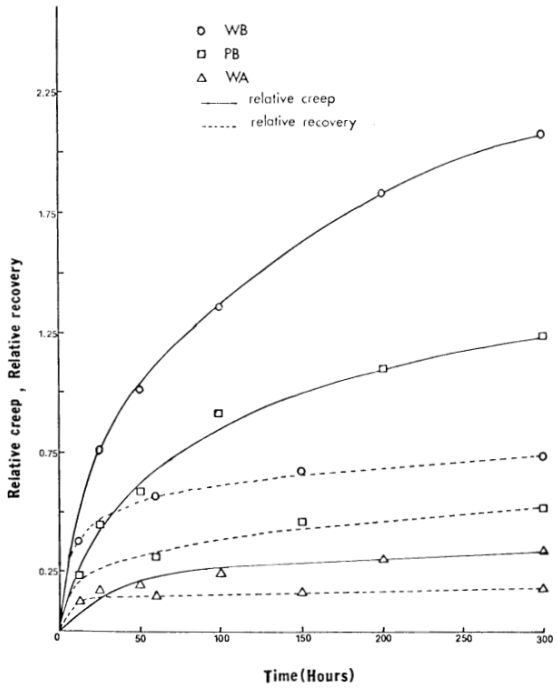

(a) Gnanaharan and Haygreen (1979)

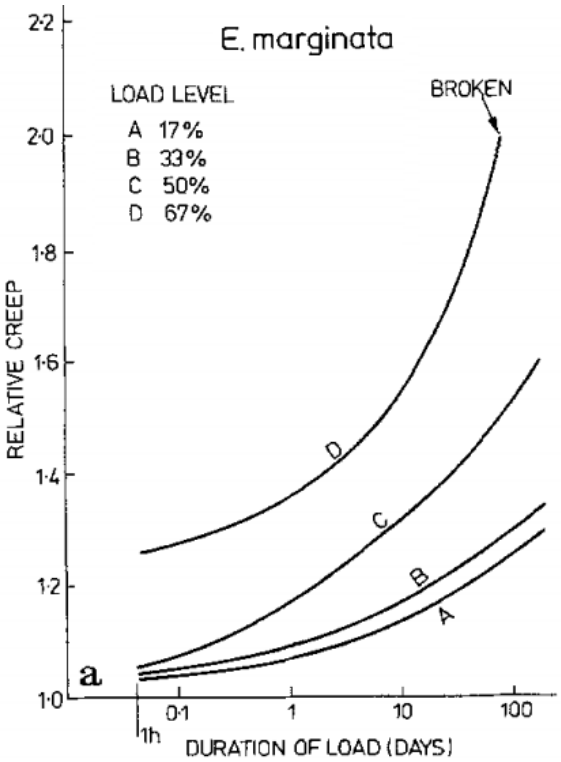

(b) Nakai and Grossman (1983)

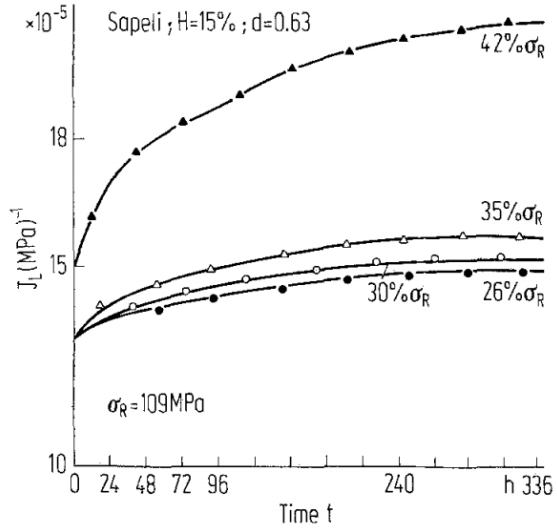

(c) Foudjet and Bremond (1989)

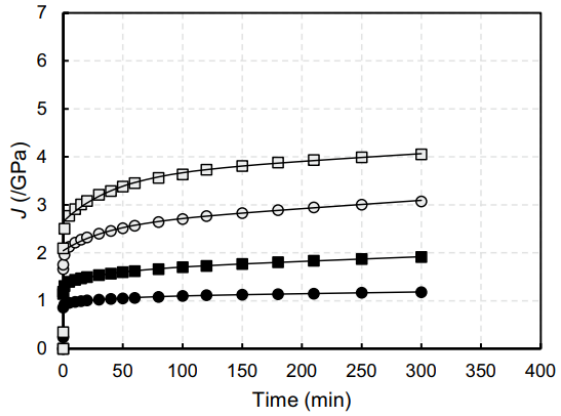

(d) Hermawan and Fujimoto (2019)

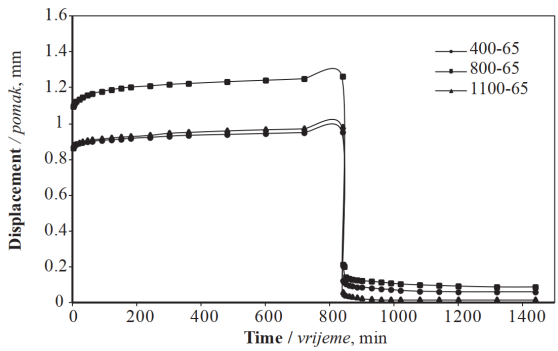

(e) Moosavi et al. (2016)

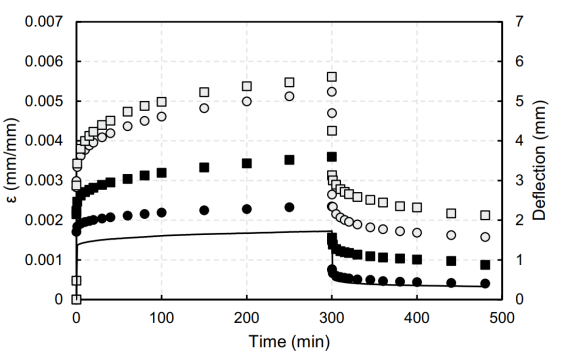

(f) Hermawan and Fujimoto (2019)

Figure 2.2: Examples of the creep tests result in literatures.

database. Figure 2.1 (b) and figure 2.2 show some examples of plotting creep test results.

Relative creep, which is shown in figure 2.1 (b), figure 2.2 (a) and (b), is generally defined as creep strain divided by initial strain. However, there are three different way of calculation present in different quantity levels in these three figures. Relative creep in figure 2.1 (b) is present with percentage and start from 0, it has been calculated as the deformation difference of creep strain and initial strain divided by initial strain times 100%. The value of relative creep in figure 2.2 (a) is also started from 0 but present without percentage. The relative creep in this case was calculated by the deformation difference of creep strain and initial strain divided by initial strain. Figure 2.2 (b) shows the third case that the relative creep value all start from 1, that is, the relative creep was calculated by creep strain divided by initial strain. These three cases present the complexity and no consensus in the definition of relative creep. There is another difficulty on data collecting in these cases that the experimental values were presented in the figures without the initial strain value. It would need the loading condition and the elastic modulus to calculate.

Figure 2.2 (c) to (f) present other kinds of y–axis unit. Figure 2.2 (e) shows the study of Moosavi et al. (2016) which discussing the relationship between the growing attitude of tree and wood creep behavior. The curves were plotted in displacement (mm) of 4–point bending test against time (minutes). It shows similar format to figure 2.2 (f), which present in creep strain. This figure from Hermawan and Fujimoto (2019) also shows that the two ways of presenting creep data show the same test results with different values and scales, but actually the same shape of the curves. Figure 2.2 (c) and (e) both plot the creep data as compliance, which is defined as strain divided by stress, but in different quantity levels. The unit of stress need to be considered when it was not present in International System of Units as pascal but in psi (pounds per square inch), the data would need to be converted.

In order to compare the data collected from different references, all the data are calculated to the same timescale as second and plot in logarithm scale. The y–axis value are converted to compliance in GPa^{-1}. For the data presented in strain (equation 2.1), it can be converted to compliance by the equation 2.2. For data presented in deflection, it can be calculated as strain value and then converted to compliance. There are two definitions for relative creep (equation 2.3, 2.4), using the initial compliance value to convert the data to compliance.

$$\varepsilon_c(t) = \frac{\Delta l}{l_0} = \frac{l(t) - l_0}{l_0} = \frac{12 \times \delta(t) \times h}{3L^2 - 4a^2} \tag{2.1}$$

$$J(t) = \frac{\varepsilon_c(t)}{\sigma} \tag{2.2}$$

$$Relative\ creep = \frac{J(t)}{J_0} \qquad J(t)\ or\ \varepsilon(t)\ or\ \Delta l(t) \tag{2.3}$$

$$Relative\ creep = \frac{J(t) - J_0}{J_0} = \frac{J(t)}{J_0} - 1 \tag{2.4}$$

2.2.4 Digitalization and homogenize

Data is stored in two parts in the database, including metadata and the creep curves. The first part is metadata, which is partially shown in table 2.1. The complete metadata includes the key number of the curve, reference information, the number of the figure in the literature, wood species, softwood or hardwood, density in g/cm^3, experimental method, loading direction, grain angle, dimension of the specimen, relative humidity and temperature of experimental environment, stress (MPa) or load (N) value, the x–axis and y–axis unit, and the calculation parameters. In order to make the numerical calculation easier, three calculation parameters were designed: to_second, $to\_compliance$, and $plus\_1$. The parameter to_second was designed for changing the timescale of x–axis. The original values time to_second is the time values with the unit of seconds. Conversion of creep compliance is in equation 2.5. The parameter $plus\_1$ was designed for the relative creep which is the deformation difference of creep strain and initial strain divided by initial strain. $plus\_1$ is equal to 1 in these cases. Other than that, $plus\_1$ is equal to 0. $to\_compliance$ is a value calculated from the experimental condition such as dimension of the specimen, initial creep strain, stress or stress, or the tenth power to change the scale. These three parameters were calculated for each curve and collected in the metadata in order to homogenize the creep data in the database of this study.

$$(Original\ Creep\ Data + plus\_1) \times to\_compliance = Creep\ Compliance\ Data\ in\ GPa^{-1} \tag{2.5}$$

For each piece of information, the metadata table has a key number which links to the creep data. Each piece of creep data is the x–y values of one curve in the figure of literature. The creep curves in the published articles were digitized by web tool WebPlotDigitizer[1] and saved as CSV files including time values and creep results. Published figures from the literature are screenshotted from PDF files and uploaded to the web tool. We can mark two points with the value to define an axis. 4 points were marked and given the value to have the x–axis and y–axis, and also defined the axes are linear or logarithm. Then, the experimental data was collected manually on the figure. The tool gives the value of the location of the data point according to the position and the value of the axes. The values of the curve were exported and saved as a CSV file, and it can be converted to the time unit of seconds and compliance in GPa^{-1} by the calculation parameters in metadata.

[1] WebPlotDigitizer: https://apps.automeris.io/wpd/

2.3 Analysis of the database

Figure 2.3 shows the data collected in this study. There is a large variance between the data.The creep data of Douglas fir and Basswood of tensile and compression test are over the others. However, all factors are mixed in this figure and it is difficult to say what is the main reason for this difference.

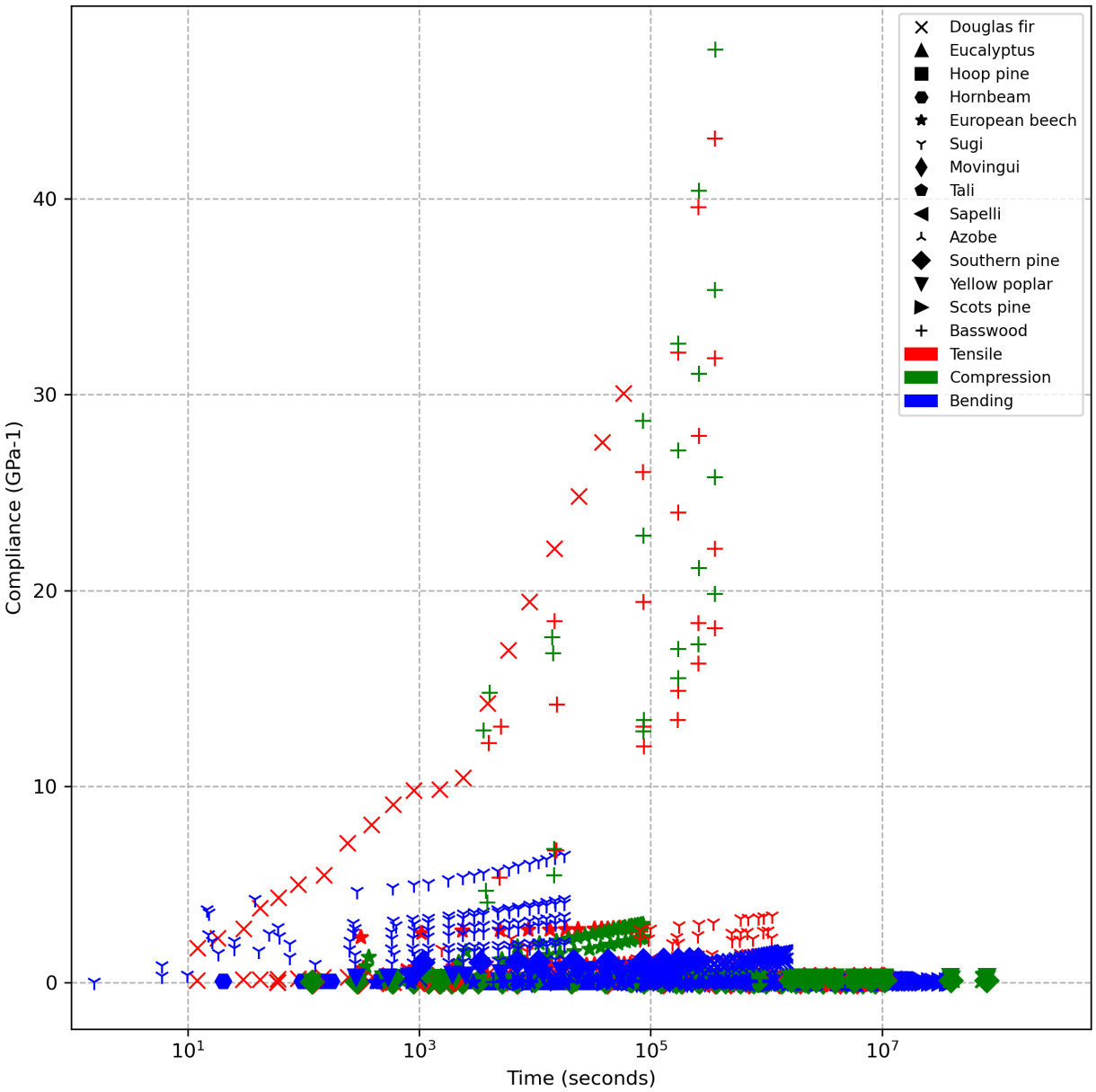

Figure 2.3: Wood creep database.

Figure 2.4 shows the main reason of this difference is caused by the grain angle. When the grain angle is perpendicular to loading direction, that is, wood fibers are torn apart. It is the weakest part of wood, so creep compliance is higher than the others. The results of Schniewind and Barrett (1972) show the grain angle effect (figure 2.5). The default specimens were made for tensile test along the grain direction. The grain angle in the figure is defined as the angle between wood grain and loading direction. This experiment confirms again that the grain angle affects the creep behavior. Another study which discuss about angle effect is Kojima and Yamamoto (2004) shown in figure 2.6. This study focus on the microfibril angle, which is a more microscopic structure. However, microfibril angle cannot be observed directly through the naked eye, it is needed to be measured by x-ray or represented by other mechanical properties.

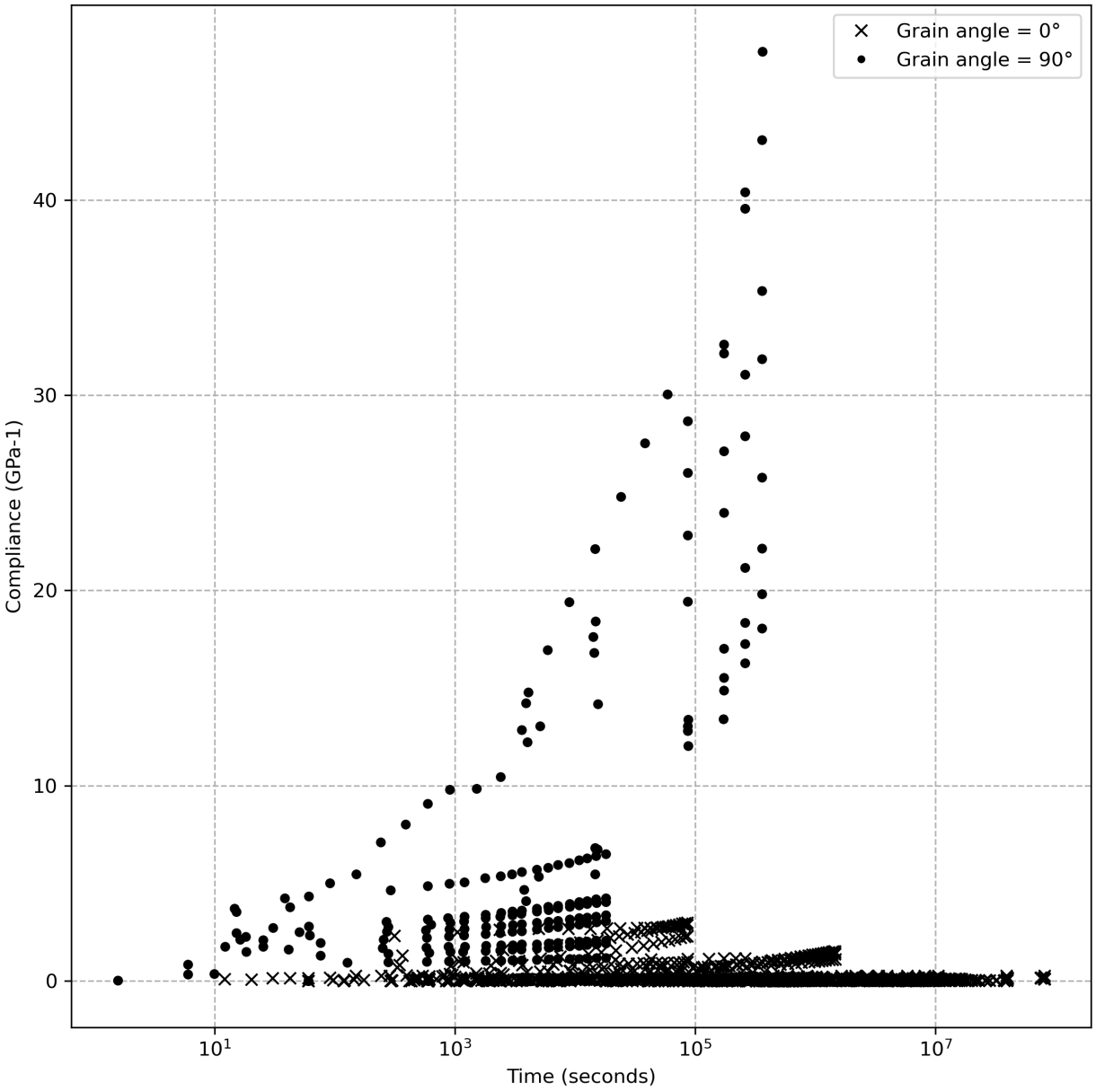

Figure 2.4: Wood creep data with different grain angle.

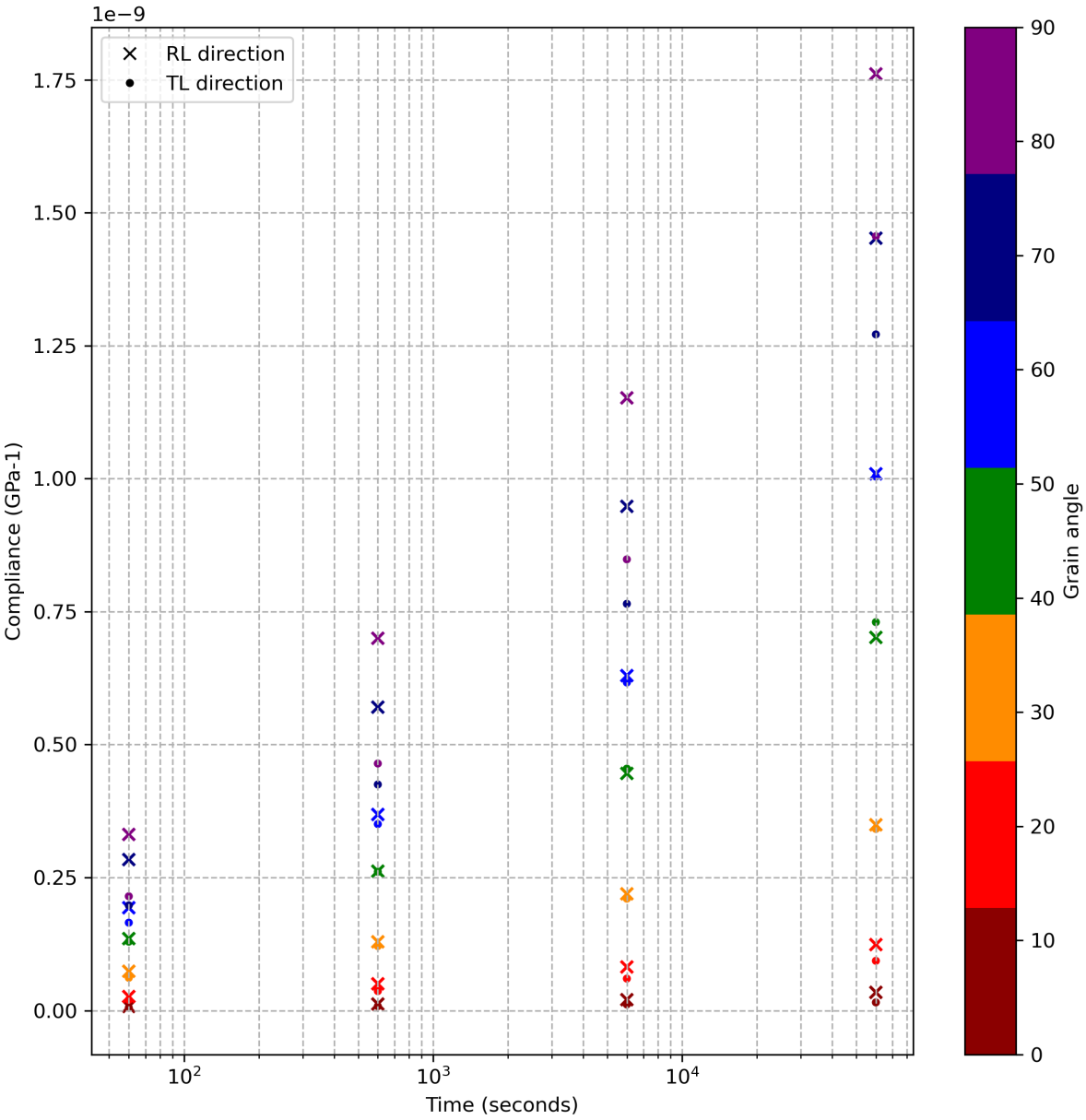

Figure 2.5: Grain angle effect (Schniewind and Barrett, 1972).

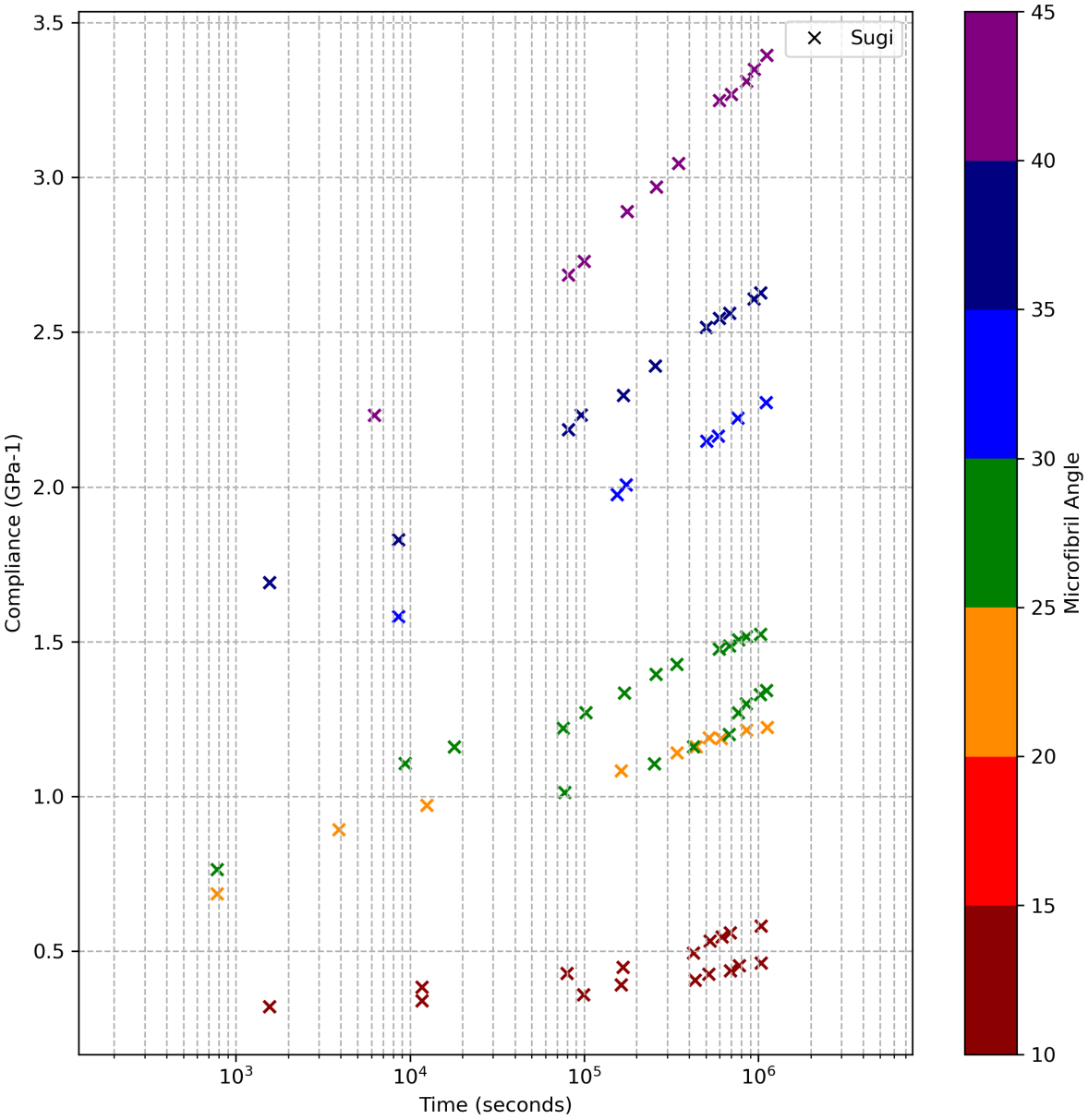

Figure 2.6: Microfibril angle effect (Kojima and Yamamoto, 2004).

To remove the grain angle effect, in figure 2.7, 2.8, and 2.9 consider only the data with grain angle equal to 0. Figure 2.7 shows the effect of testing method. Comparing the three types of testing method, tensile and compression tests show larger variance than bending test. Because wood material has directionality and vertical fiber direction is particularly fragile, tensile and compression test will magnify such weaknesses. Figure 2.8 shows the comparison of softwood and hardwood. There is no significant difference. Most of the creep test result has similar tendency and the compliance lower than 0.5. Comparing the species difference in figure 2.9, it can be inferred from this that the creep behavior may be independent to species. There is no significant concentration by the species of the curves. Depending on the test method, there are several extreme curves in each series.

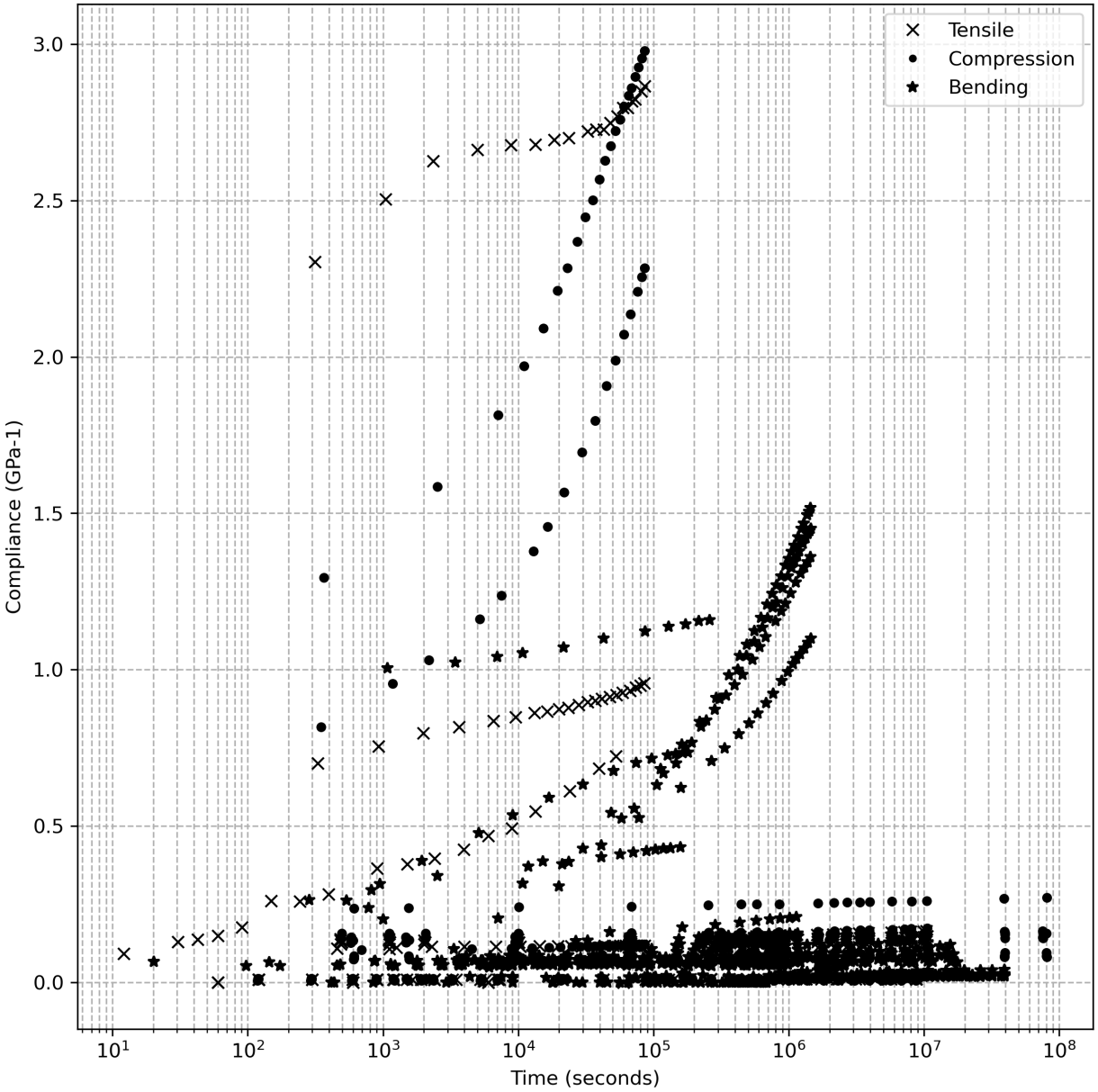

Figure 2.7: Comparison of testing method.

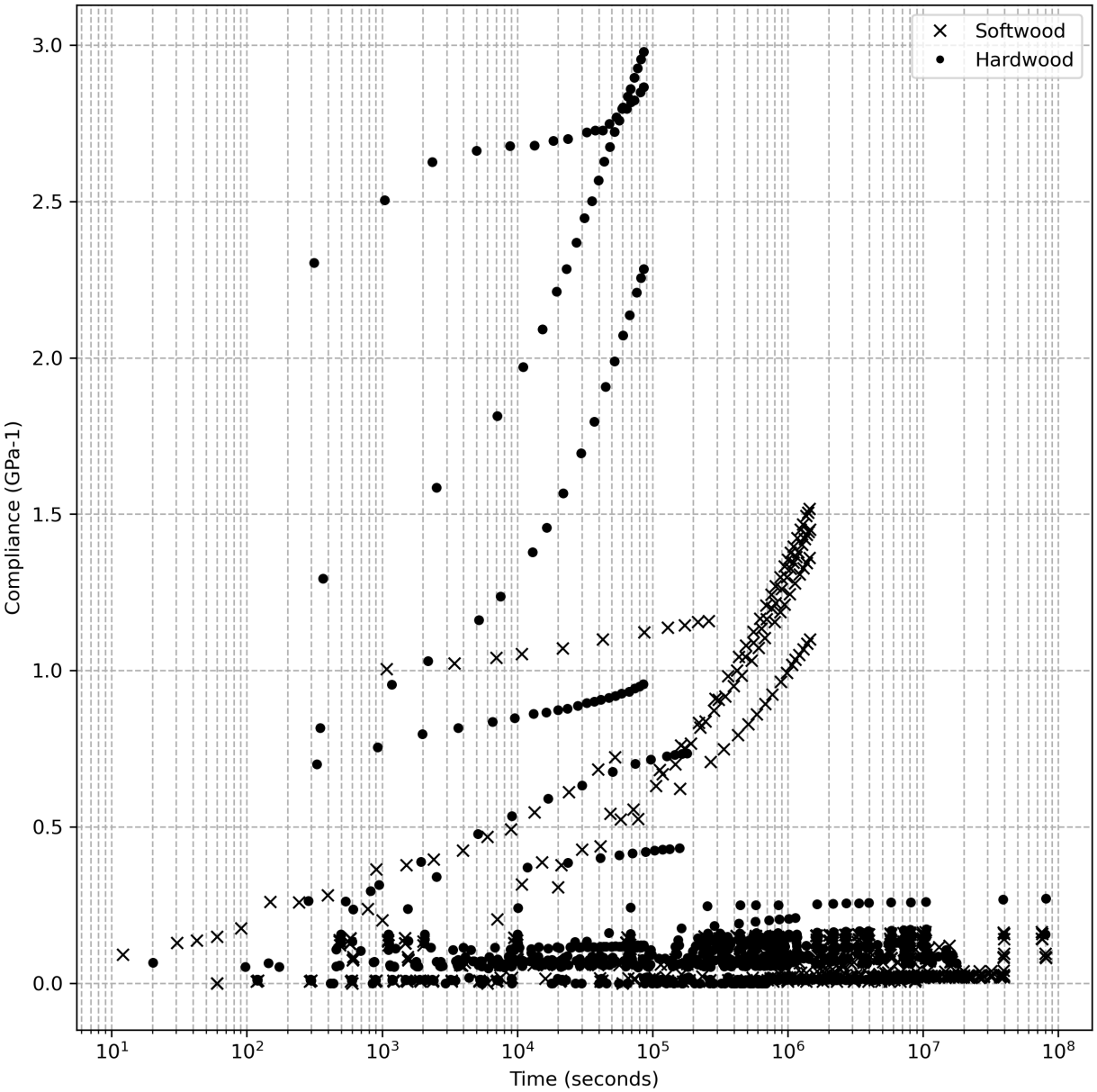

Figure 2.8: Comparison of softwood and hardwood.

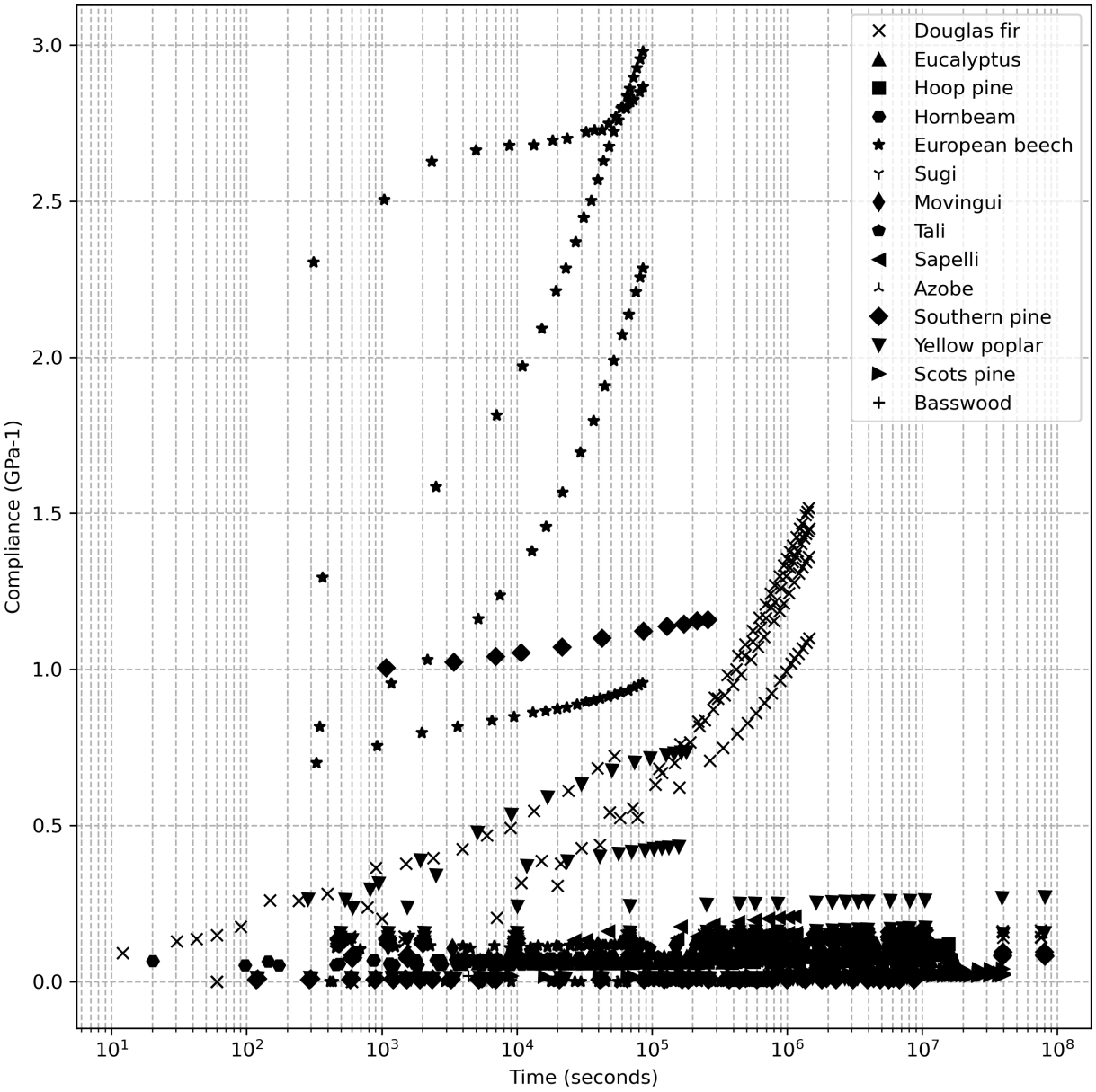

Figure 2.9: Comparison of different wood.

Figure 2.10 shows the creep curves tested by bending test. There is no clear relationship and difference between softwood and hardwood. The hardwood curves collected in this study show higher tolerance to bending creep. Mechanic properties of wood are strongly affected by moisture content, but this phenomenon is not perfectly present in figure 2.10. In the studies which work on the relative humidity effect, they do show the different result under different testing environment. However, when we consider other factors at the same time, the effect of moisture content is reduced.

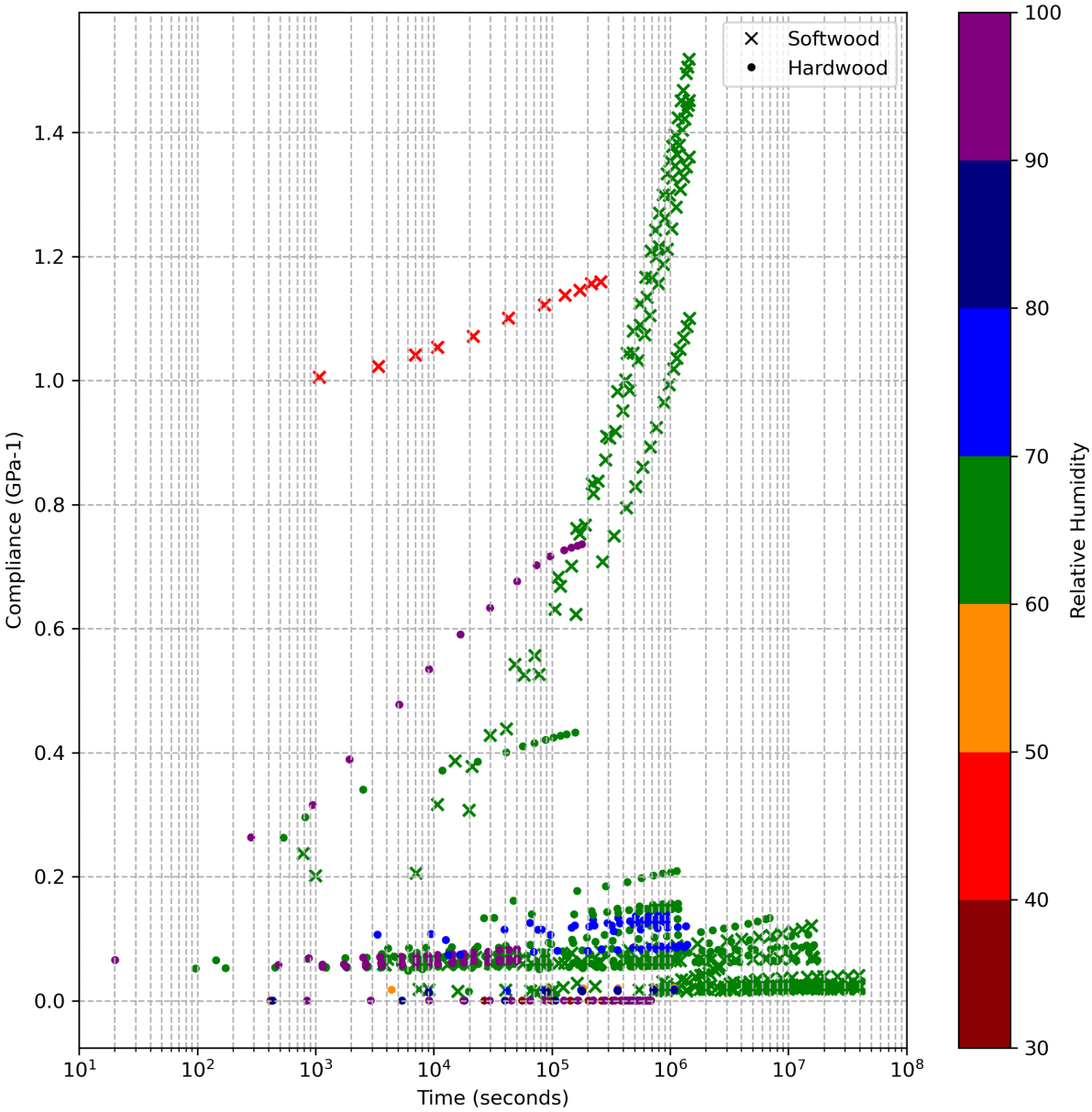

Figure 2.10: Wood creep bending test under different relative humidity.

Figure 2.11 shows the result of Hermawan and Fujimoto (2019), which is mainly discus about the temperature effect on wood creep. The tangential direction is more affected by creep behavior than the radial direction. Also, the specimens testing under higher temperature show higher creep compliance. The experimental result in this study is higher than the results in other studies (figure 2.3). That is because this test is the bending test vertical to the fiber direction. Compared with the strength of the fiber itself, the strength of the connection between the fibers is more tested. Along the radial direction, there is also the support of ray, so it shows better performance. However, the author tried to control the moisture content of wood specimens during the experimental process, but there were still the changes. The specimens in the group under the highest temperature were dried during the test, but the moisture content in the other groups were raising. It would also be another possibility that affect the result. This study presents the difficulty of temperature control in wood creep test.

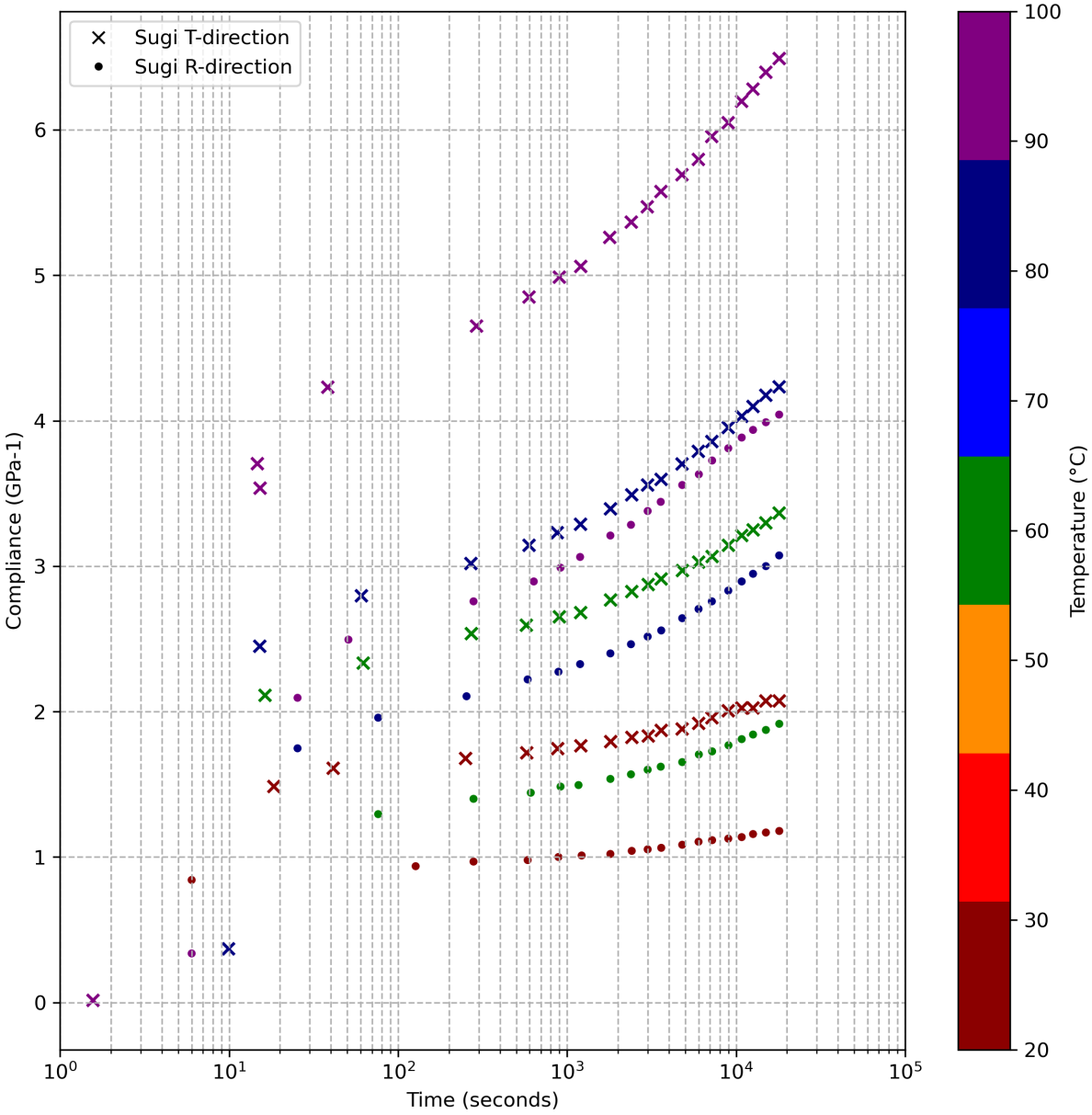

Figure 2.11: Wood creep bending test under different temperature (Hermawan and Fujimoto, 2019).

2.4 Summary

In the database of this study, we can observe a large variation in the behavior of wood creep for multiple reasons. It presents the complicity of wood in different scales for the microfibril angle to the grain direction. Also, we can see the reaction of wood material under different loading conditions and environment. This result highlights the characteristics of wood as a biological material. To understand such characteristics of the material, a creep test under constant environment and load was carried out in this study. In this study, material features such as density, elastic modulus and grain angle will be considered, and an attempt will be made to incorporate them into the prediction model.

Chapter 3

Material Characterization and Sampling

This chapter describes the preparation for the creep tests. Before the creep tests, the specimens characteristics were collected for sampling and modeling. The sampling method in this study attempts to select specimens for accurate and valid testing to achieve the main problem of this study, i.e. to determine a good indicator of long-term behavior.

3.1 Material: Small clear wood

Four kinds of wood have been used: Douglas fir (*Pseudotsuga menziesii*), European Beech (*Fagus sylvatica*), European Oak (*Quercus petraea*), and Poplar (*Populus spp.*). These four species are representative of the French forest. According to Memento FCBA (2020), there are 17.0 Mha of forest in France, which represent 30% of the total area of France. Of this total, 72% of the area is covered by hardwoods and 28% by softwoods. Oak occupies the largest area, 3808 kha (24%) and beech is the second largest with 1451 kha (9%). Douglas fir is a common wood, and is the 4th most common softwood in France. All these four kinds of wood are included in NFEN14081-1 (2016) appendix B. In parallel with this study, a series of long-term outdoor creep tests were carried out at LMGC, using beam-sized samples. It was related to a corporate research project including French institutes (GC2D Egletons, LERFOB Nancy, LERMAB Epinal, CRITT Epinal and LMGC Montpellier), named ANR EFEUR5. Some results are presented in Varnier (2019). The EFEUR5 project focused on these 4 species so that they were chosen for this study. The following are some basic information for each kind of wood.

3.1.1 Introduction of the materials

Douglas fir

Douglas fir is a kind of evergreen conifer native to western North America, and is now extensively planted in Europe and the United Kingdom. It is often used for reforestation in France. The color of Douglas fir wood is light brown with a little yellow or red, and the colors of heartwood and sapwood are clearly different. The grain is generally straight. The year ring is clear, too (figure 3.1). Although it is called "Fir", it belongs to the pine family. There are small to medium resin canals in this kind of wood. It has a moderate to low durability and can be machined easily, also it accepts stains, glues and finishes well. It is widely used for joinery, cladding, or structure.[1]

(a) The Wood Database

(b) TRADA

(c) Sample photo

Figure 3.1: Douglas fir

[1] Online wood databases that have been used:
The Wood Database: https://www.wood-database.com/
The Timber Research and Development Association (TRADA): https://www.trada.co.uk/
FrenchTimber: https://www.frenchtimber.com/en/

Poplar

Poplar, according to the classification of CIRAD, is a group that combines several kinds of plants in the genus *Populus* such as grey poplar (*P. canescens*), black poplar (*P. nigra*), aspen (*P. tremula*), white poplar (*P. alba*), Lombardy poplar (*P. italica*), black Italian poplar (*P. canadensis*), abele (*P. alba*), and robusta (*P. robusta*). It grows fast and easily. It spreads all over the Northern Hemisphere. The color of poplar wood is white to light brown (figure 3.2). It is a type of wood that is easy to work with hand and machine, but its surface presents a risk of peeling, so it needs to use sharp cutters for machining. Normally, it is used as a material of wood products such as plywood, boxes and crates, furniture.[1]

(a) The Wood Database

(b) TRADA

(c) Sample photo

Figure 3.2: Poplar

[1]Online wood databases that have been used:
The Wood Database: https://www.wood-database.com/
The Timber Research and Development Association (TRADA): https://www.trada.co.uk/
FrenchTimber: https://www.frenchtimber.com/en/

European Beech

European Beech can only be found in Europe by definition. It lives from southern Sweden to northern Sicily and from west Portugal and to northwest Turkey. It has been called the mother of the forest because of the strong shade prevention and easy growth. It can survive in difficult environments such as relative drought and lack of soil. The timber is reddish-brown, with a typically straight grain (figure 3.3). Generally, it has a good workability except for the red heart part. It is used for flooring, boat building, furniture, plywood, and also musical instruments. It is a hardwood which is widely used in Europe. It has good mechanical properties, and it can grow to a large size for applications that require large logs.[1]

(a) The Wood Database

(b) TRADA

(c) Sample photo

Figure 3.3: European Beech

[1] Online wood databases that have been used:
The Wood Database: https://www.wood-database.com/
The Timber Research and Development Association (TRADA): https://www.trada.co.uk/
FrenchTimber: https://www.frenchtimber.com/en/

European Oak

European Oak is an important resource in France. It is the most widespread hardwood in France, and France is the leading producer in Europe. The timber of Oak is light brown with a good durability (figure 3.4). The year ring is clear and there is a white silver grain figure on the surface of the quarter sawn surface. It is a high density wood with good mechanical properties and stability. On the other hand, it is relatively difficult to work and machine. It is used as structures, flooring, framework. Also, it plays an important role in the production of wine. Because there are tyloses that block the vessels, which makes it a well–known material for wine barrels.[1]

(a) The Wood Database

(b) TRADA

(c) Sample photo

Figure 3.4: European Oak

[1] Online wood databases that have been used:
The Wood Database: https://www.wood-database.com/
The Timber Research and Development Association (TRADA): https://www.trada.co.uk/
FrenchTimber: https://www.frenchtimber.com/en/

Table 3.1 gives the physical and mechanical data from CIRAD wood database for the four species of this study at 12% moisture content.

Table 3.1: The mechanical data from CIRAD Tropix 7 wood database [2]

	Douglas fir		Poplar		Beech		Oak	
	Average	STD	Average	STD	Average	STD	Average	STD
Specific gravity*	0.54	0.04	0.45	–	0.71	0.03	0.74	0.05
Static bending strength* (MPa)	91	6	62	–	111	9	105	15
Modulus of elastic in L direction* (GPa)	16.8	1.55	9.8	–	15.3	1.05	13.1	1.75
*: at 12% moisture content								

3.1.2 Specimens cutting

The wood samples came from the beams of the long-term outdoor creep tests. The end of the beam was cut and processed into small specimens (figure 3.5).

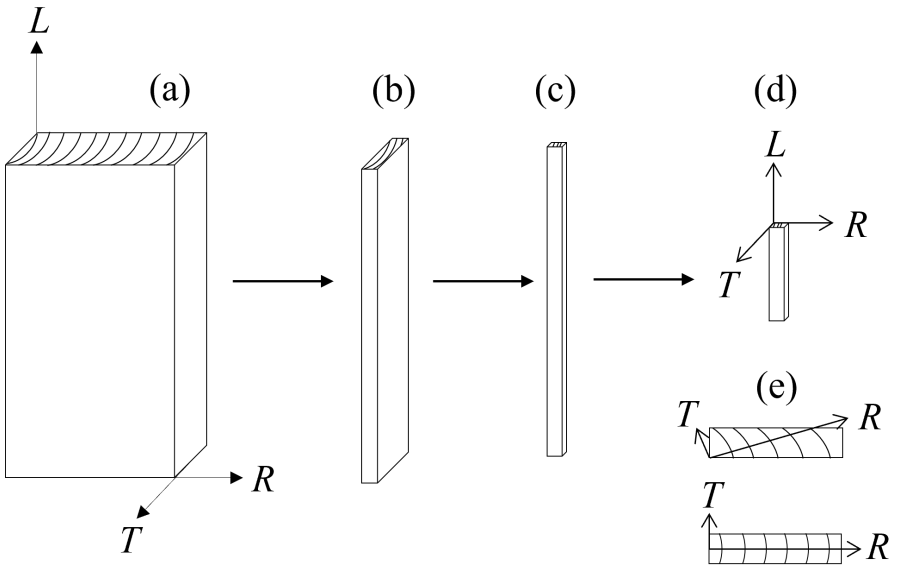

Figure 3.5: Different steps of specimens' cutting. (a) The end of the beam for outdoor long-term creep test; (b) Slicing into boards along the longitudinal direction with the thickness close to the width of the small specimen; (c) Cutting lengthwise into strips with the thickness close to the thickness of the small specimen; (d) Cutting into the length of the specimen; (e) The cross–section of the small specimen

All specimens were cut to the size of 150 mm (L) * 12 mm (b) * 2 mm (h). We tried to have the radial direction along the width (b), but sometimes it is not perfect (figure 3.5 e). The specimens were checked and selected, only those with no defaults were collected. There were 382 specimens in all, including 119 Douglas fir samples, 105 Poplar samples, 109 Beech sample, and 49 Oak samples. To mark the samples, a label system was designed and shown in table 3.2. A label is composed of one or two English codes and three digits. The first English code represents the wood species, D for Douglas Fir, P for Poplar, H for Beech and

[2]CIRAD wood database Tropix 7 is developed by Biomass, Wood, Energy, Bioproduct Research Unit (BioWooEB) in Center for International Cooperation in Agricultural Research for Development (CIRAD). The Tropix 7 database includes the technological characteristics of 245 kinds of tropical and temperate forest species. (https://tropix.cirad.fr/en/)

C for Oak. Two different Douglas-fir beams were taken for the experiment, so the Douglas-fir samples have codes A or B. The last three digits were used to number the specimens, and some specimens were used in other experiments, so the specimen numbers in this study are not consecutive. All the specimens were stored in the experimental room until equilibrium state before testing.

Table 3.2: Label system for samples.

Species	Beams	Number	Example
D: Douglas fir	A: Beam A	001–050	DA001
	B: Beam B	001–050 101–120	DB001
P: Poplar	(only one beam)	001–105	P001
H: Beech	(only one beam)	003–120	H003
C: Oak	(only one beam)	002–050	C002

3.1.3 Specimens characterization

Grain angle

All the specimens were scanned in room conditions and the grain angle was measured. Both global and local grain angle were measured by using the software ImageJ. The measuring process is shown in Fig.3.6. Two segments were drawn randomly along the width direction. Connecting the two middle points of the segments, we can have the middle line along the length direction of the sample as the reference line for measuring the grain angle. To measure the global grain angle, an entire year ring was chosen to measure the angle of the grain. The local grain angle value was obtained by the average of grain angle at 3 points, which were chosen randomly.

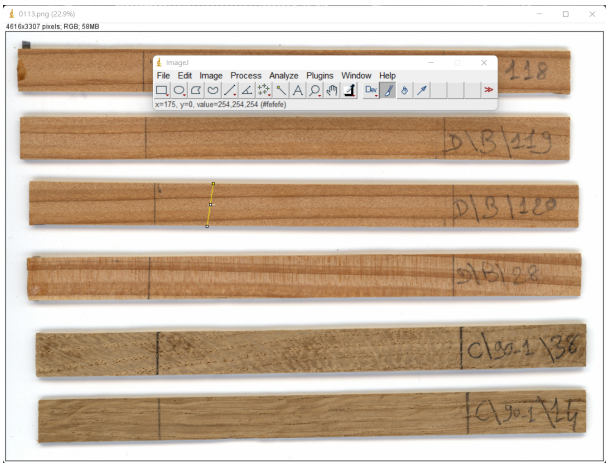

(a) A segment was made on the photo of the specimen along the width. The midpoint was displayed automatically, and it could be marked by the paint tool. Two midpoints define the middle line of the specimen

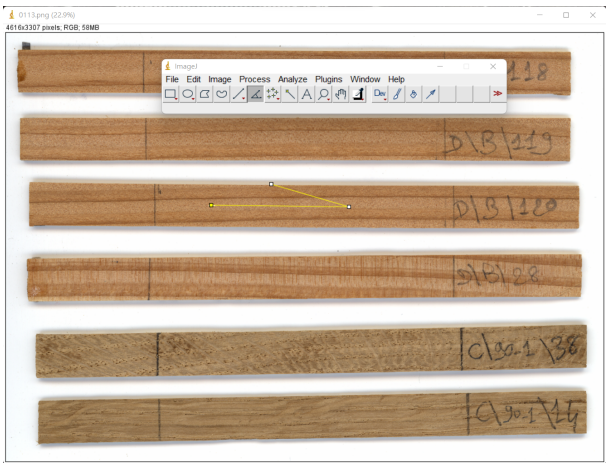

(b) The middle line was taken as the standard, and the angle tool was aligned to the middle line.

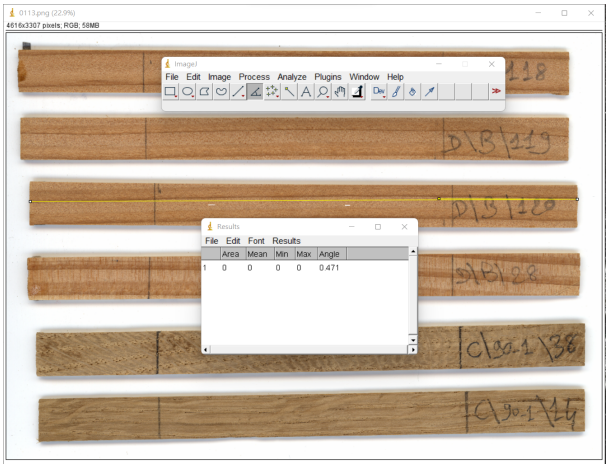

(c) To measure the global grain angle, an entire year ring was chosen. The endpoint (intersection) of the angle tool was set at the start of the year ring, and the other side of the angle tool was pulled to the end of the year ring. The function "measure" in the program gives the value of the angle directly.

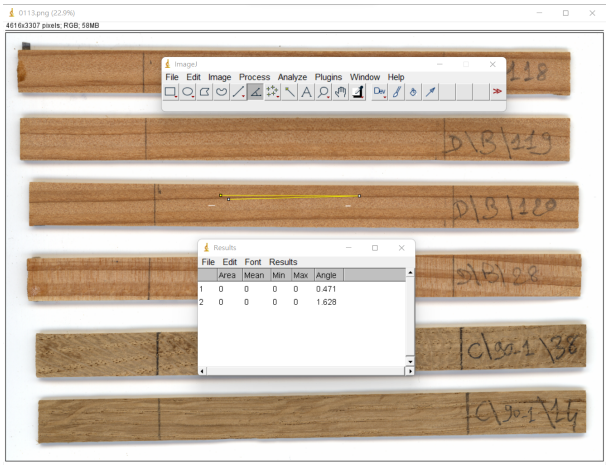

(d) To measure the local grain angle, 3 points were selected randomly to set the end point of the angle tool, and the other side of the angle tool was placed along the year ring to measure the angle. This figure shows only one point.

Figure 3.6: The process of measuring the grain angle

The average and standard deviation (STD) of the grain angle values are shown in table 3.3. The local grain angles were generally larger than the global grain angles for all the species. These results are consistent with the visual observations. Indeed, the grain of the wood was not straight, in the surface area of the sample we could see that the grain was curvilinear, so the local grain angles were larger than global grain angles. Figure 3.7 shows the distribution of both local and global grain angles. Most specimens had a grain angle of less than 5 degrees, either local or global. There were some extreme values greater than 5 degrees, including 18 specimens with an average local grain angle greater than 5 degrees and 4 specimens with a global grain angle higher than 5 degrees. The extreme values of the average local grain angle represent 2 Douglas fir samples, 13 Poplar samples, and 3 Oak samples. There were 2 outer values shown in figure 3.7 (a) which were both Poplar with the value of 24.1 and 10.2 degrees. For the results of global grain angle, the 4 outer data were 3 Poplar samples and 1 Oak sample. The maximum value was 8.7 degrees. It shows the within–individual variation of wood material at different scales in wood.

Table 3.3: The global and local grain angles (degree) for the four species.

	Douglas fir		Poplar		Beech		Oak	
	Average	STD	Average	STD	Average	STD	Average	STD
Global	1.3	0.9	2.0	1.5	1.6	0.9	1.1	1.3
Local	2.1	0.9	3.5	2.7	2.1	0.8	2.7	1.2

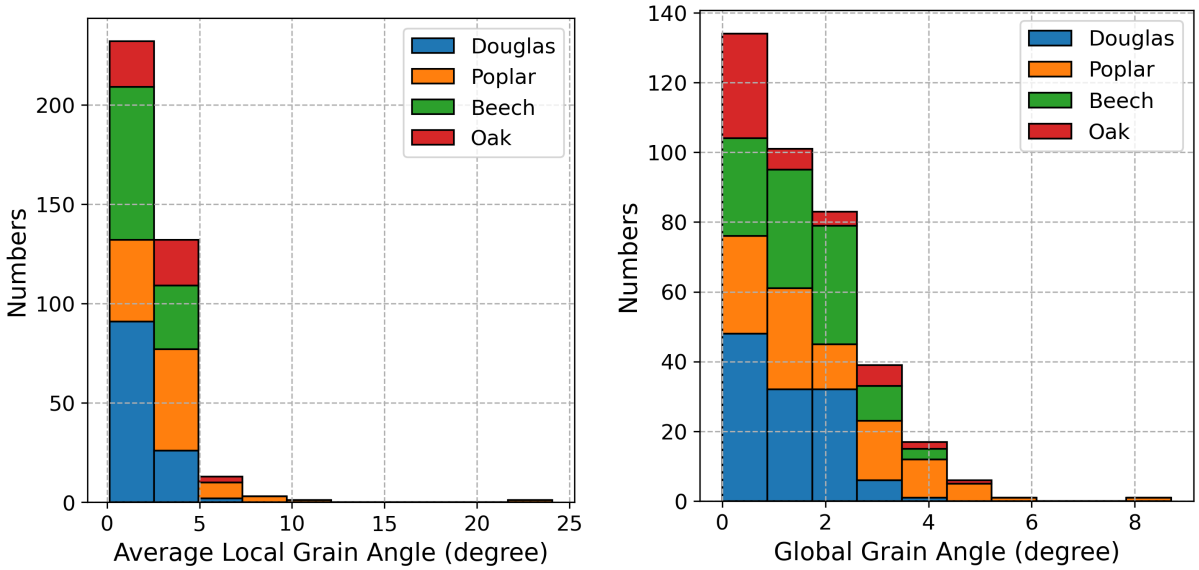

(a) The distribution of average grain angle

(b) The distribution of global grain angle

Figure 3.7: The measuring result of grain angle

Size, Weight and Density

After stabilization in the climate chamber Memmert HPP750 at 20 °C and 30% relative humidity (RH), the length, width, thickness, and weight of the specimens were measured inside the chamber. The length was measured by vernier caliper with accuracy of 0.01 mm. The width and thickness were measured by digital indicator calculation with accuracy of 0.001 mm. The weight was measured by the balance with accuracy of 0.0001 g. Density (ρ) is calculated as weight divided by volume and express in g/cm^3. Specific gravity is ρ/ρ_{water}. So that we can have the information on the specimens at low humidity environment. The first series of vibration tests are performed, then the climate chamber condition was adjusted to 20 °C and RH = 85%, and all the samples were stabilized in the chamber for 3 weeks. The weight and dimensions of the specimens were measured, and the vibration test were performed again after wet stabilization. By the dimensions in RH = 30% and 85%, the volume shrinkage coefficient was defined as equation 3.1 and 3.2.

$$\alpha_V = (1 + \alpha_L) \times (1 + \alpha_b) \times (1 + \alpha_h) - 1 \tag{3.1}$$

$$\alpha_{L,b,h} = \frac{(L, b, h_{RH=85\%} - L, b, h_{RH=30\%})}{L, b, h_{RH=85\%}} \tag{3.2}$$

According to NFEN14081-1 (2016), environmental conditions can be separated into 3 types:

- Class 1: the material has a moisture content corresponding to that obtained when the material is under an environment with a temperature of 20 °C and a relative humidity less than 65% for several weeks per year.
- Class 2: the material has a moisture content corresponding to that obtained when the material is under an environment with a temperature of 20 °C and a relative humidity less than 85% for several weeks per year.
- Class 3: the environmental conditions are worse than the class 2.

In order to have a larger creep behavior, the environmental condition has been set to reach the most extreme Class 2 event, that is 20 °C and RH = 85%. According to USDA Forest Service (2021), the wood specimens stabilized under these conditions would have a moisture content of 18%. Table 3.4 gives the average and STD value of the length (L), width (b), thickness (h), and density (ρ) of the specimens and figure 3.8 shows the distribution of the dimensions in both dry and wet conditions.

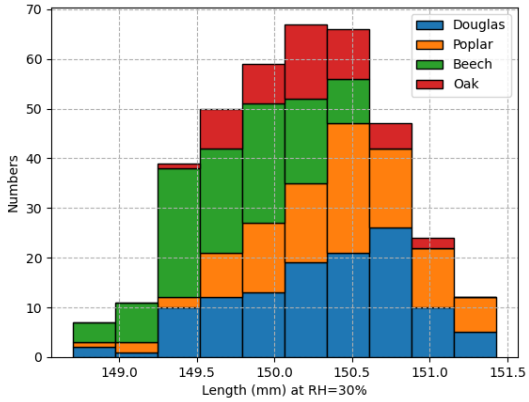

(a) Length at RH = 30%

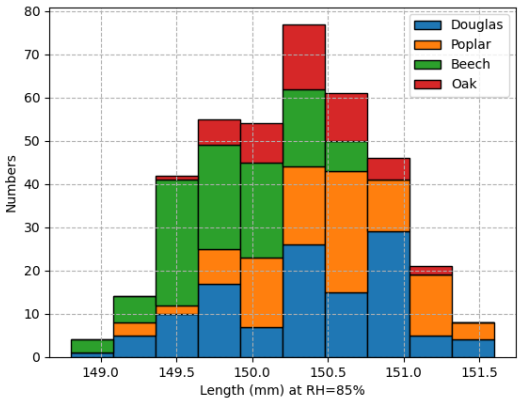

(b) Length at RH = 85%

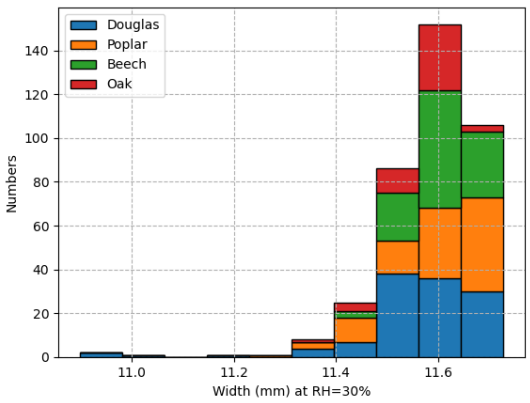

(c) Width at RH = 30%

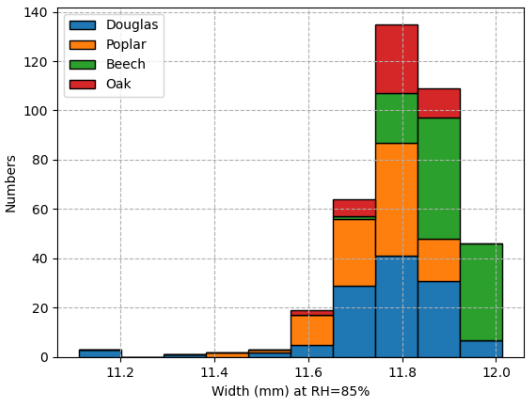

(d) Width at RH = 85%

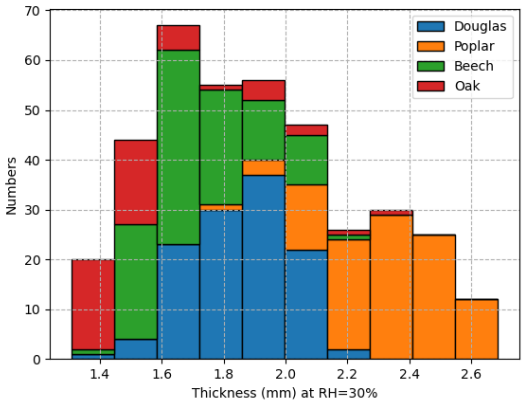

(e) Thickness at RH = 30%

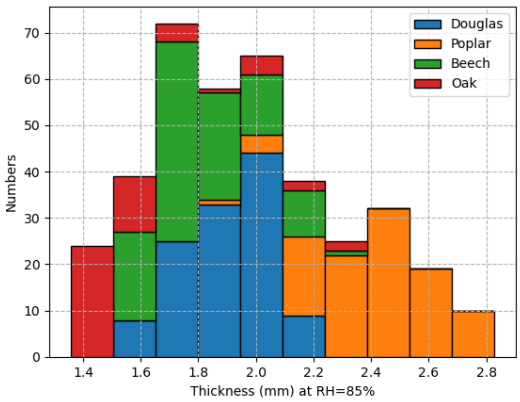

(f) Thickness at RH = 85%

Figure 3.8: The distribution of dimension measurements.

Table 3.4: Dimensions and density of the 4 species in dry and wet conditions.

		Douglas fir		Poplar		Beech		Oak	
	RH	Average	STD	Average	STD	Average	STD	Average	STD
L (mm)	30%	150.27	0.57	150.39	0.51	149.79	0.44	150.22	0.36
	85%	150.32	0.58	150.52	0.50	149.90	0.42	150.36	0.38
b (mm)	30%	11.56	0.14	11.60	0.09	11.59	0.07	11.58	0.06
	85%	11.77	0.14	11.75	0.09	11.88	0.07	11.79	0.06
h (mm)	30%	1.85	0.15	2.32	0.19	1.72	0.17	1.57	0.25
	85%	1.90	0.15	2.42	0.20	1.81	0.17	1.62	0.26
ρ (g/cm^3)	30%	0.52	0.03	0.44	0.02	0.72	0.02	0.62	0.02
	85%	0.54	0.03	0.45	0.02	0.73	0.02	0.63	0.02
α_V		0.045	0.011	0.054	0.008	0.074	0.007	0.052	0.010

3.2 Vibration test

Wood is a popular material for musical instruments. In ancient time, the selection of a suitable material for musical instruments depended heavily on the experience of the craftsmen. To better understand the relationship between wood characteristics and musical properties, vibration behavior has become a research issue (Fukada, 1950). In order to pre-estimate material properties, we measure by a vibrational method the specimens to perform a dedicated specimen selection for creep tests.

3.2.1 Theory

Assume that a perfectly elastic material is tested in an environment without friction, the vibration cycles would keep continuously, and the amplitude would never decrease. However, in reality, we can observe that the amplitude decreases even more rapidly than in the case where only the environmental friction is considered (schematic diagram as figure 3.9). It shows that there is always an internal friction (η) of the materials, which transforms mechanical energy to heat during the vibration cycles (Brancheriau et al., 2010). That is the damping behavior of the material. Equation 3.3 gives the relation between the initial amplitude (A_0) and the amplitude at the cycle n (A_n). The logarithmic decrement (λ) comes from the regression result of the peak amplitudes by time. The loss tangent ($\tan\delta$) is deduced from λ by equation 3.3 (Fukada, 1951; Brémaud et al., 2012).

$$\lambda = \pi \tan\delta = \frac{1}{n} \ln \frac{A_0}{A_n} \tag{3.3}$$

According to Brancheriau et al. (2010), the vibration test methods can be separated into 2 types: free-vibration device and forced-released bending vibration device. The free-vibration device is the system in which a single force is applied to the end of a specimen supported by 2 wires at the nodes. The specimen forms a wave naturally so that we can have the natural frequency. In the forced-released bending vibration

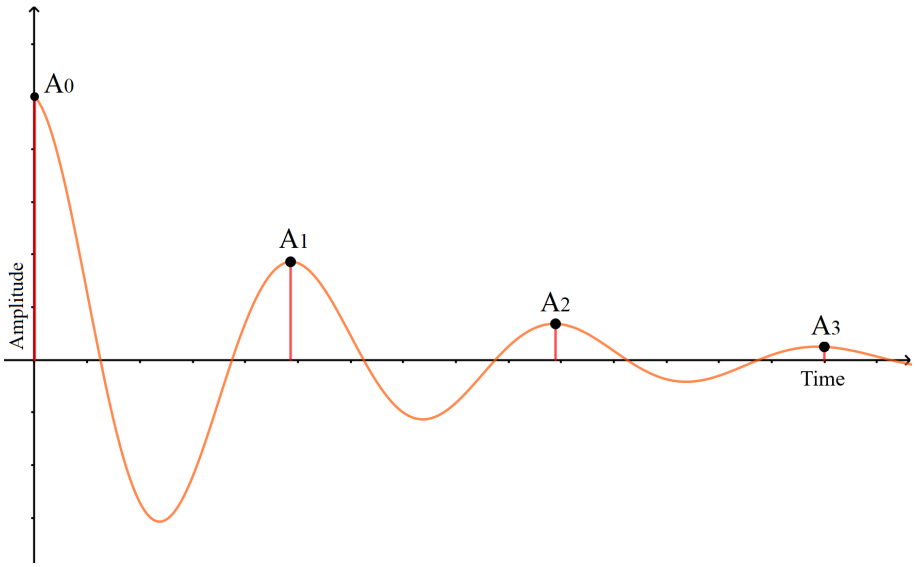

Figure 3.9: Schematic diagram of amplitude decay.

device, a series of frequencies is applied to the specimen. The frequency which has the maximum resonant amplitude is called the resonance frequency (f_R, f_1 in figure 3.10(b)). By different testing methods and expressions, there are several ways to present internal friction (η) including the quality factor (Q^{-1}), loss tangent (tanδ), and temporal damping (α). The figure 3.10(a) shows the typical curve of the forced-released bending vibration method, tanδ is calculated as the ratio between the bandwidth at half-power of the peak ($\Delta f = f_2 - f_1$) and the resonance frequency (f_R) (equation 3.4) (Vobolis and Aleksiejunas, 2003; Brémaud et al., 2012). According to Brémaud et al. (2012), the relationship between Q^{-1} and tanδ is almost y=x with a $R^2 = 0.989$. It means that in the normal cases, we can take Q^{-1} as tanδ. Figure 3.10(b) shows a good correlation between $\Delta f/f_1$ ($=Q^{-1}$) and α_1/f_{1flex} tested by free vibration device. The equation could be concluded as equation 3.5. Comparing with equation 3.6, we can say that the quality factor measured by the forced-released bending vibration device is equivalent to the internal friction of the material. At the same time, it is a determining factor for the damping behavior of materials. In this study, we chose the forced-released bending vibration device, and we use the Q^{-1} as tanδ to represent the damping parameter.

$$Q^{-1} \approx \tan\delta \approx \frac{\Delta f}{f_R} \tag{3.4}$$

$$\frac{\Delta f}{f_1} = \frac{\alpha_1}{\pi f_{1flex}} \tag{3.5}$$

$$\eta = \frac{\alpha}{\pi f} \tag{3.6}$$

Another feature that has been studied is the natural vibration phenomenon, which means that energy can be transferred between the equilibrium position by the mechanical wave without mass transfer. A wave with certain frequency would build up naturally between the nodes during the vibration process. This phenomenon

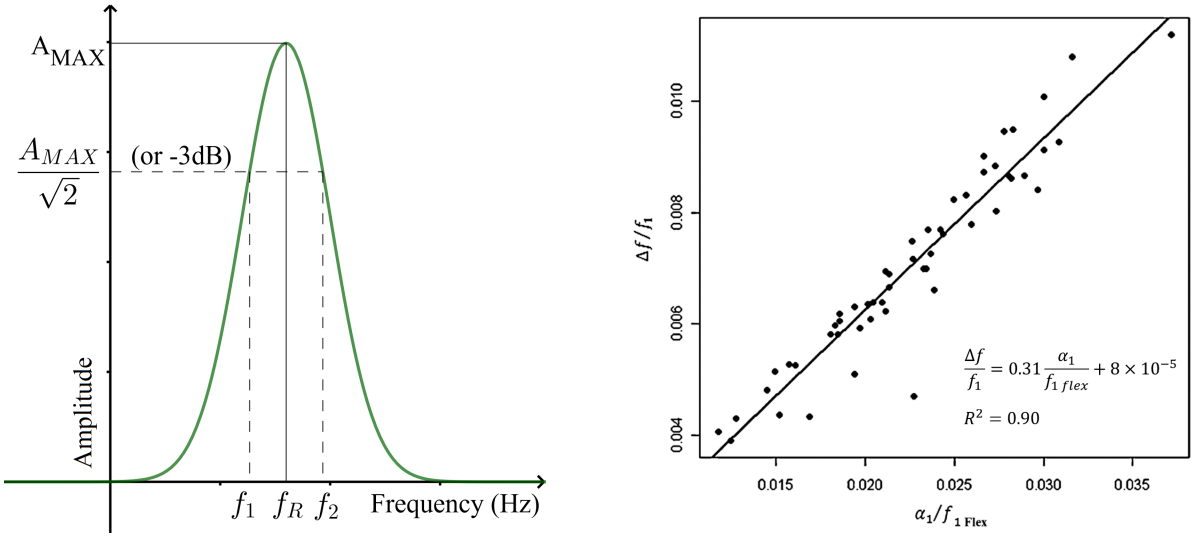

(a) Calculation method of $\Delta f/f_R$ by forced-vibration (b) Calculation method of $\Delta f/f_1$ by free-vibration Brancheriau et al. (2010)

Figure 3.10: Relationship between different testing method of internal friction

provides some experimental tools to analysis the mechanical properties of materials. Vibration tests become an efficient and simple way to understand the elastic behavior of materials (Brancheriau and Baillères, 2002). According to Kataoka and Ono (1975), the vibration tests have been used to study dynamic behavior for a long time, too. It is an efficient and non-destructive testing method. In Brancheriau and Baillères (2002) (figure 3.11 a), we could see a good correlation between the elastic modulus values obtained by different methods: 4–point bending test and vibration test. The modulus of elasticity is always an important information in structural calculation. It shows that through vibration testing, we can estimate the property of the material and simplify the measurement process. As a rapid test method, it can be widely used in wood science, which requires a large number of samples to study the variability of wood.

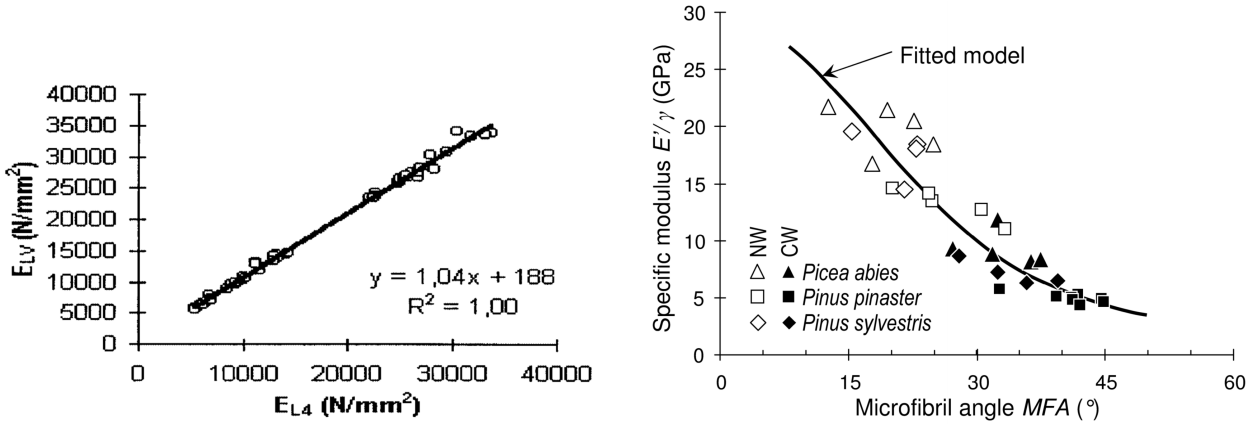

(a) Relationship between Young's modulus in 4–point bending (E_{L4}) and the longitudinal vibration modulus of elastic (E_{LV}) on clear wood samples (Brancheriau and Baillères, 2002).

(b) Relationship between microfibril angle (MFA) and specific modulus (Brémaud et al., 2013). Fitting equation is equation 3.8.

Figure 3.11: Results of vibration tests in references.

In this study, the system we used was the forced–released bending vibration device. By the vibration

test, we could have the f_R to calculate the dynamic Young's modulus (E') in L direction by the Equation 3.7 (Fukada, 1950; Kataoka and Ono, 1975; Brémaud et al., 2012). ρ is the density, l is the length, h is the thickness of the specimen, m is a constant. At normal testing condition, m = 4.73 (Kataoka and Ono, 1975).

$$E' = \frac{48\pi^2 \rho l^4 f_R^2}{m^4 h^2} \tag{3.7}$$

It is known that materials with a higher Young's modulus per specific gravity and lower internal friction are suitable for the soundboards of the musical instruments (Ono and Norimoto, 1983). By the vibration test, we can have the relationship between the Young's modulus by the vibration test, called dynamic Young's modulus, and the modulus of elasticity by 4–point bending test, called static Young's modulus. The specific modulus (E_s) is defined as the dynamic Young's modulus divided by density. But for convenience, the specific modulus is expressed in GPa like if it is dynamic Young's modulus divided by specific gravity (which has no unit). Therefore, in this study, specific modulus is calculated by dynamic Young's modulus divided by density but expressed in GPa. It is an important mechanical property of wood which is strongly correlated to microfibril angle (MFA, ϕ) (figure 3.11 b) (Brémaud et al., 2013). The relationship between specific modulus and MFA is shown in equation 3.8. Therefore, calculating the specific modulus is also a way to remove the effect of density (Brémaud et al., 2013).

$$Specific\ Modulus\ \frac{E'}{\rho} = \frac{1}{0.03426 \times \cos^4\phi + 0.2053 \times \cos^2\phi \sin^2\phi + 0.6797 \times \sin^4\phi} \tag{3.8}$$

3.2.2 Testing method

The vibration test system (Vybris system) was set up at LMGC, it is described in Figure 3.12 (Brémaud et al., 2012). The wood specimen is hanged up by 2 silk threads at 0.224 times of the specimen length from both ends to have a free-vibration condition. A laser-triangulation sensor points to the center of the specimen to collect the signal of vibration. The test is controlled and calculated by the control/acquisition card (National Instrument, Austin, TX, USA, NI PCI 6221, A/D conversion 16 bits) with a LabVIEW interface. It starts from a wide range scan from 150 to 750 Hz to find the resonance frequency (f_R). Then, the second scan from $0.98 \times f_R$ to $1.02 \times f_R$ allows a more precise measurement in order to have the bandwidth at the half-power (Δf). A series of frequencies is applied by the electromagnet at the metal piece at the end of the specimen. The weight of the metal piece is controlled, its average value is 1.17% (STD = 0.211%) of the wood specimen in air-dry condition. After pasting the metal piece at the end of the specimens, all the samples, the balance and the Vybris system are put inside the climate chamber in dry environment for 3 weeks. To low down the effect of the air circulation inside the climate chamber, a big plastic box is put inside the chamber and the Vybris system is settled up inside the box.

There was a pre-test to make sure the samples were stabilized, and the results are shown in figure 3.13. There were 2 specimens of each species, 8 specimens in sum, chosen to be measured during the equilibrium

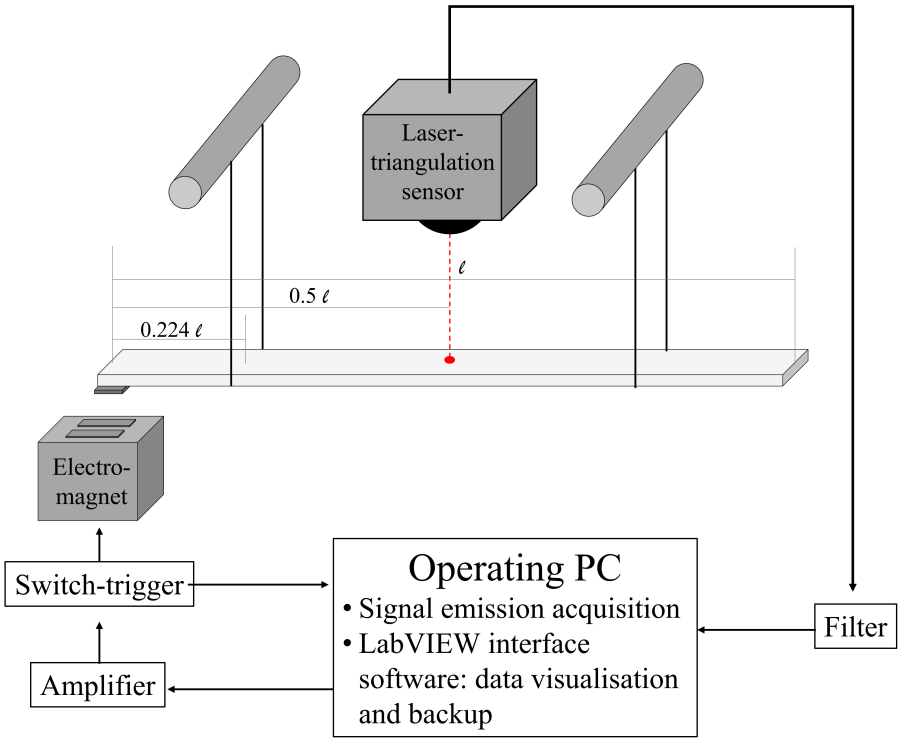

Figure 3.12: Vybris system

process to highlight the kinetics of the phenomenon. After the vibration test at 20 °C and RH = 30%, the environmental conditions were raised up to 20 °C and RH = 85%. The weight, specific modulus, and tanδ were measured during this 3-week equilibrium process. In figure 3.13 (a) and (b), we can see that the weight and specific modulus of the specimens were almost stable after 1 day. However, the evolution of tanδ takes longer time to stabilize and shows a different form. The curves of weight and specific modulus are reaching a limit smoothly, whereas the curves of tanδ show a maximum and declined after 1 day. It took about 3 weeks for tanδ to reach the stable state. So, we decided to wait 3 weeks before conducting creep tests after placing the samples in the chamber.

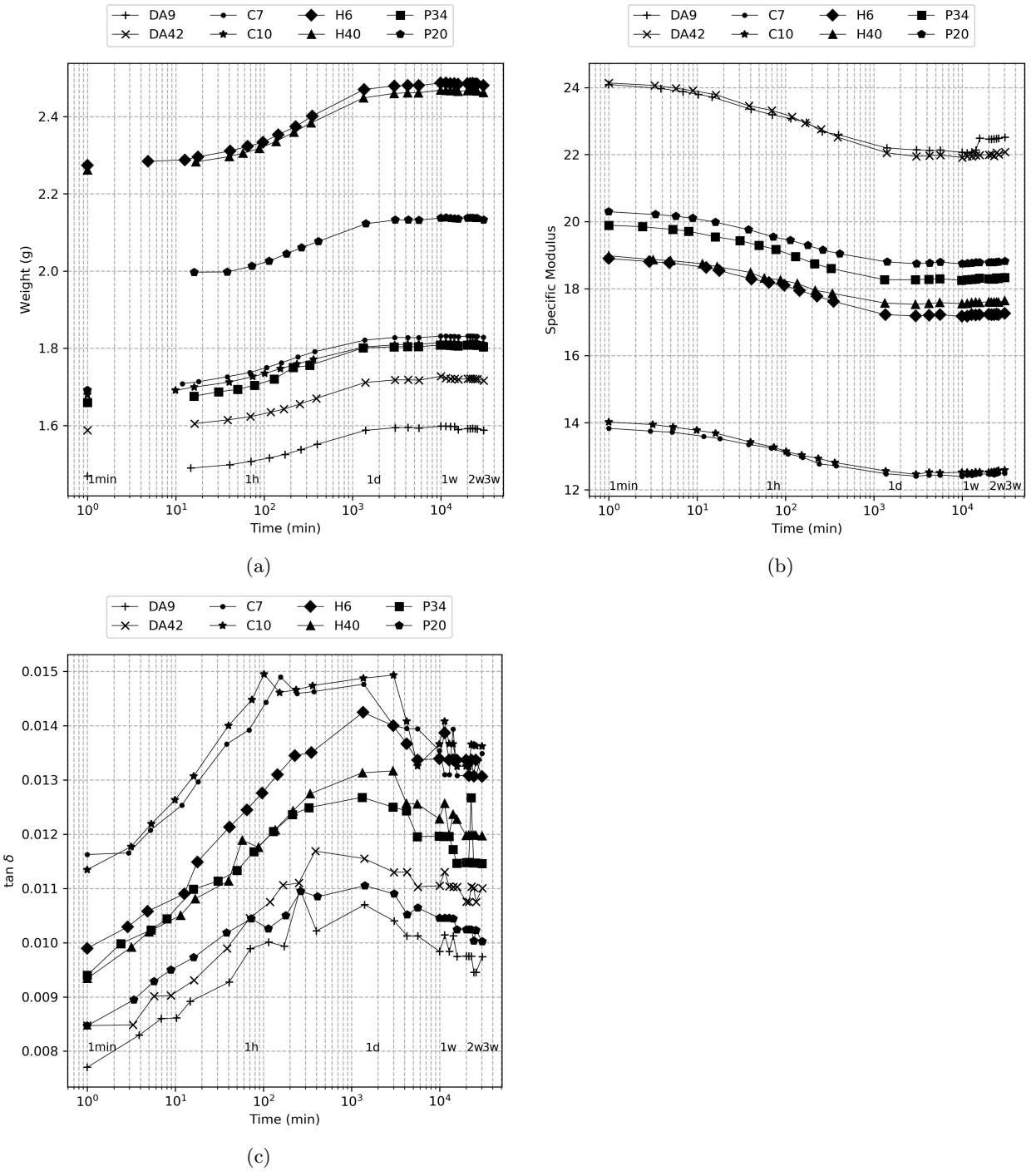

(a)

(b)

(c)

Figure 3.13: The record of weight, specific modulus and damping coefficient during the equilibrium process

3.2.3 Results

Figure 3.14 shows the results of the vibration test in both dry and wet conditions. By the vibration test, we can obtain the specific modulus and tanδ data to characterize each specimen. Figures 3.14 (a) and (b) show the relation between density and specific modulus. Because the specimens were cut from nearby material, the values of density show low variability for each species. Figures 3.14 (c) and (d) show the relationship between density and tanδ. Figures 3.14 (e) and (f) show the negative relation between specific modulus and tanδ as expected. Indeed, the tendency is the same as Brémaud et al. (2012) and Ono and Norimoto (1984) as shown in figure 3.15. The EC in the figure 3.15 (a) stands for the extractive content and γ is density. The results are separated into 2 groups: high extractive content and low extractive content (including softwood). Also, it shows the fitting result, which is also in Ono and Norimoto (1984). The fitting equation is defined as equation 3.9 and table 3.5 shows several fitting parameters. N is the number of specimens which are included in the fitting equation. ${R_1}^2$ is the coefficient of determination for the equation 3.10. ${R_2}^2$ is the coefficient of determination for the equation 3.11.

$$tan\delta = 10^{-A} \times (\frac{E'}{\rho})^{-B} \tag{3.9}$$

$$tan\delta = f(\frac{E'}{\rho}) \tag{3.10}$$

$$\frac{tan\delta}{E'/\rho} = f(\frac{E'}{\rho}) \tag{3.11}$$

The distance between the point and the fitting line represents the effect of extractive content of the sample (Brémaud et al., 2012). There is a factor called "delta Ono", which is the vertical distance of the point to the fitting line (figure 3.16). This factor is taken into account for sampling, and represents the influence of extractive in sampling. The fitting parameters considered in this study are A=1.23 and B=0.68, following (Brémaud et al., 2012).

Table 3.5: The fitting parameters from the references for equation 3.9

Data series	N	A	B	${R_1}^2$	${R_2}^2$
All samples in Brémaud et al. (2012)	1792	1.322	0.692	0.50	0.86
Softwood (Brémaud et al., 2012)	140	1.222	0.639	0.76	0.95
Hardwood with high extractive content (Brémaud et al., 2012)	1153	1.474	0.62	0.57	0.90
Hardwood with low extractive content (Brémaud et al., 2012)	221	1.231	0.677	0.73	0.94
Softwood (Ono and Norimoto, 1983)	1227	1.23	0.68		0.91
Hardwood (Ono and Norimoto, 1984)	118	1.34	0.62		0.83

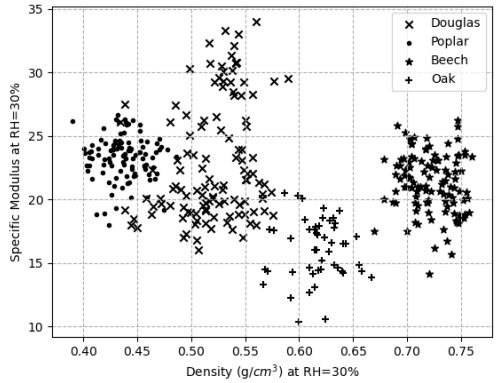

(a) Relationship between density (g/cm^3) and specific modulus (GPa) at RH=30%

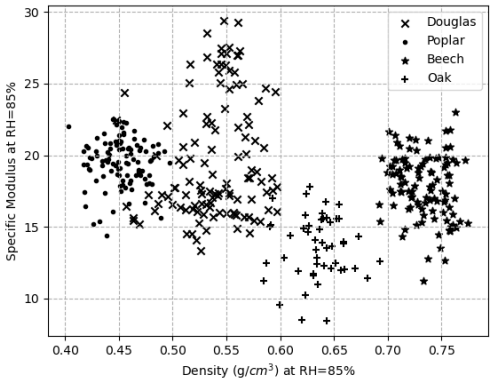

(b) Relationship between density (g/cm^3) and specific modulus (GPa) at RH=85%

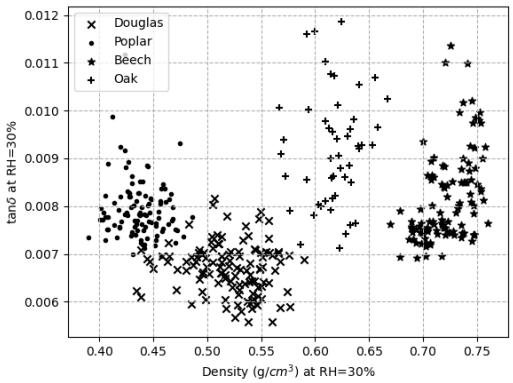

(c) Relationship between density (g/cm^3) and tanδ at RH=30%

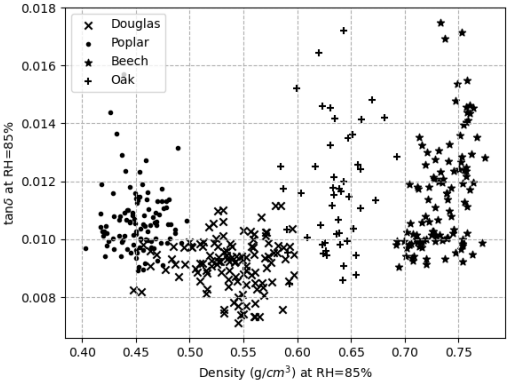

(d) Relationship between density (g/cm^3) and tanδ at RH=85%

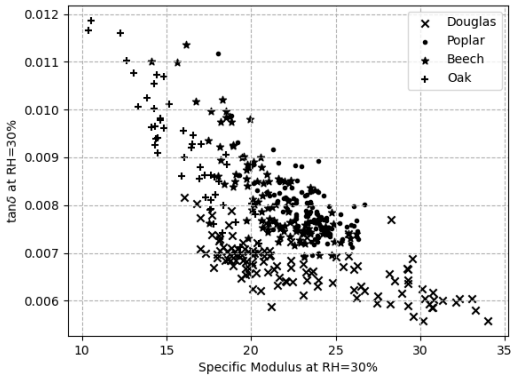

(e) Relationship between specific modulus (GPa) and tanδ at RH=30%

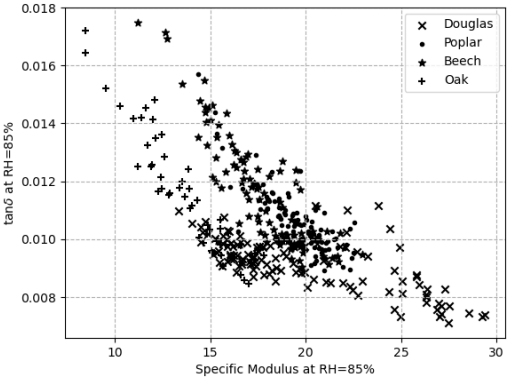

(f) Relationship between specific modulus (GPa) and tanδ at RH=85%

Figure 3.14: Vibration test results

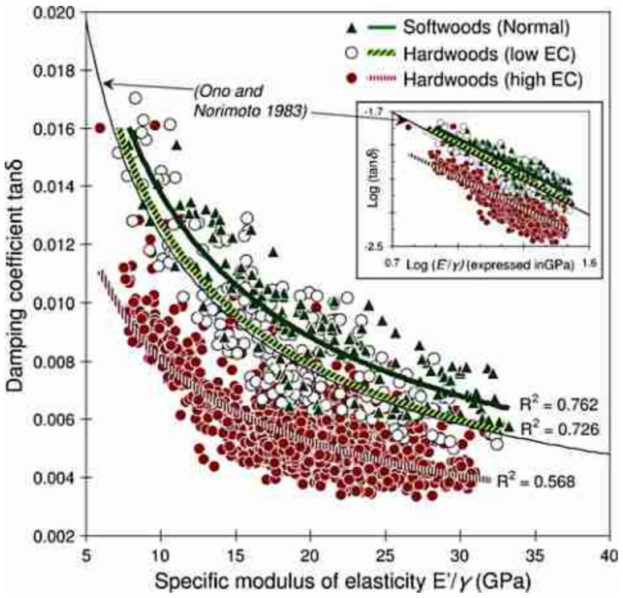

(a) Brémaud et al. (2012)

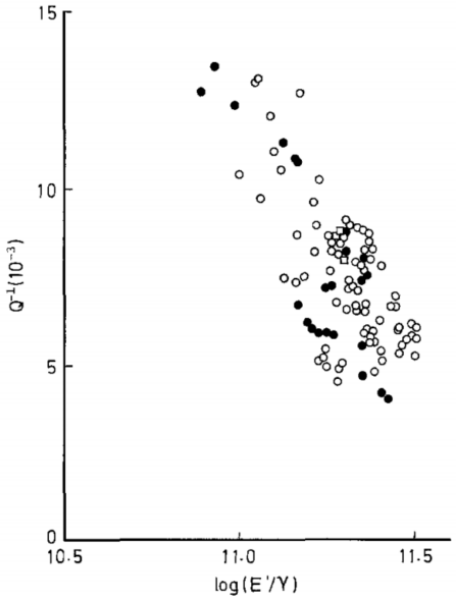

(b) Solid circles show ring-porous wood, open circles diffuse-porous wood.(Ono and Norimoto, 1984)

Figure 3.15: Relationship between specific modulus (GPa) and tanδ from literature.

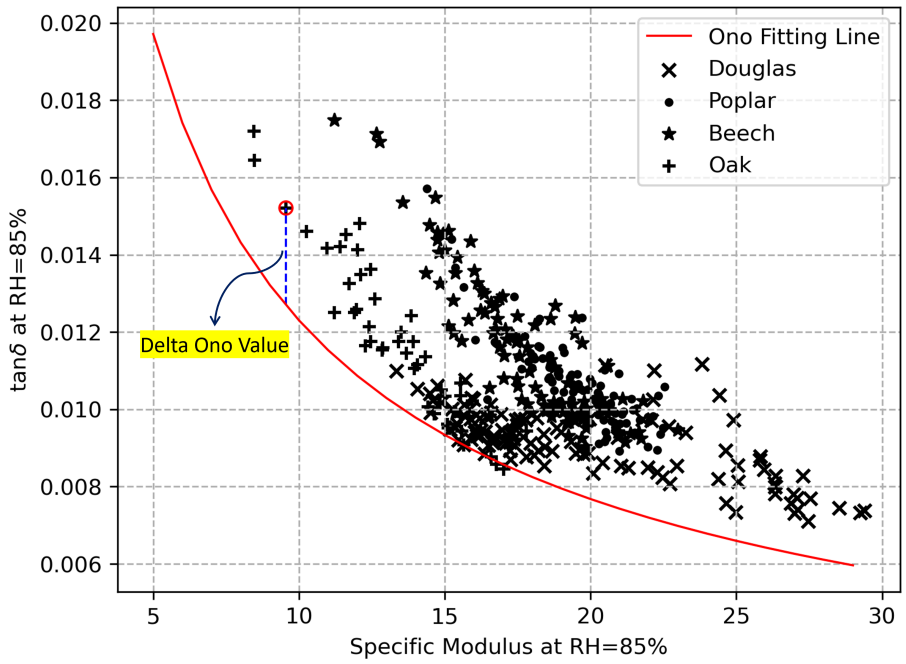

Figure 3.16: Definition of delta Ono value

3.3 Sampling

To identify the effect of a specific factor on wood creep, only one factor should have the maximum variability and the others should have the lowest variability as possible. To achieve this goal, we applied the following sampling method:

1. There are 6 parameters chosen for sampling: density, specific modulus at RH=85%, tanδ at RH=85%, average local grain angle, volume shrinkage coefficient, and ratio of specific modulus at RH=85% divided by specific modulus at RH=30%.
2. One parameter is decided as the target parameter to have the maximum variation. The others are control factors which have the minimum variation.
3. A weight parameter for each parameter is given that can be adjusted manually.
4. Standardized weight is calculated by equation 3.12, that is, the weight parameter decided manually divided by the standard deviation of all the samples included. Weighted selection variance is defined by equation 3.13.
5. Criterion is defined in equation 3.14. It is the variation target minus summations of variations control.

The maximum criterion means the variation of target factor reaches the highest value, and the other factors are controlled to the lowest value. Because the testing environment of creep test was set at 20 °C and 85% relative humidity, the values of density, specific modulus, and tangent delta at the same environment were selected as reference values. The average grain angle, the volume shrinkage coefficient and the ratio of specific modulus were also considered. The determination of optimal sampling was performed with a dedicated stochastic algorithm.

$$Standardized\ Weight = \frac{Weight\ parameter}{Sample\ Variance} \tag{3.12}$$

$$Weighted\ Selection\ Variance\ (WSV) = Standardized\ Weight \times Selection\ Variance \tag{3.13}$$

$$Criterion = WSV_{target} - \sum WSV_{controls} \tag{3.14}$$

In the first part of the creep test, the density was taken as the main factor, which had the largest variability. The control factors were specific modulus and tanδ at relative humidity 85%, average value of grain angle, volume shrinkage coefficient, and ratio of specific modulus between relative humidity 30% and 85%. The second part of the creep test focused on the specific modulus. Comparing the result of the first part, only density, specific modulus and a new factor delta Ono were considered. For this second part, the sampling

result leads to the maximum variance on specific modulus and minimum on the others. Even though the grain angle was not counted, the extreme value was avoided. The third part considered the factor delta Ono to have the most variance and low down the others. There were also two independent tests which considered all the species and selected the samples had different density and selected the samples with the same specific modulus. Two values chosen are 15.5 GPa and 22 GPa (figure 3.29 and 3.30). All specimens were tested only once, if a specimen was already chosen in the previous experiment, the sample number would be increased to choose a new sample. The followings tables and figures summarize the sampling parameters and the results.

The parameters are noted as follows:

1. density: $\rho(g/cm^3)$
2. specific modulus at RH = 85% : E_s (GPa)
3. average local grain angle : $Grain_{AVG}$ (°)
4. volume shrinkage coefficient: α_V
5. ratio of specific modulus at RH = 85% divided by specific modulus at RH = 30%: Ratio E_s

Table 3.6: The sampling parameters of Douglas fir with maximum density variance.

Factors	ρ (g/cm^3)	E_s (GPa)	tanδ	$Grain_{AVG}$	α_V	$Ratio_{E_s}$
Weight of Parameters	0.1	7	10	0.015	1	5
Sample Variance	3.49E-03	2.05E+01	1.48E-06	8.48E-01	1.39E-04	9.52E-04
Selection Variance	2.50E-03	2.06E-01	7.74E-09	3.95E+00	9.79E-06	8.85E-06
Variance Ratio	7.16E-01	1.01E-02	5.21E-03	4.65E+00	7.03E-02	9.29E-03
Standardized Weight	2.87E+01	3.42E-01	6.74E+06	1.77E-02	7.17E+03	5.25E+03
Weighted Selection Variance	7.16E-02	7.05E-02	5.21E-02	6.98E-02	7.03E-02	4.65E-02
Criterion	-2.37E-01					

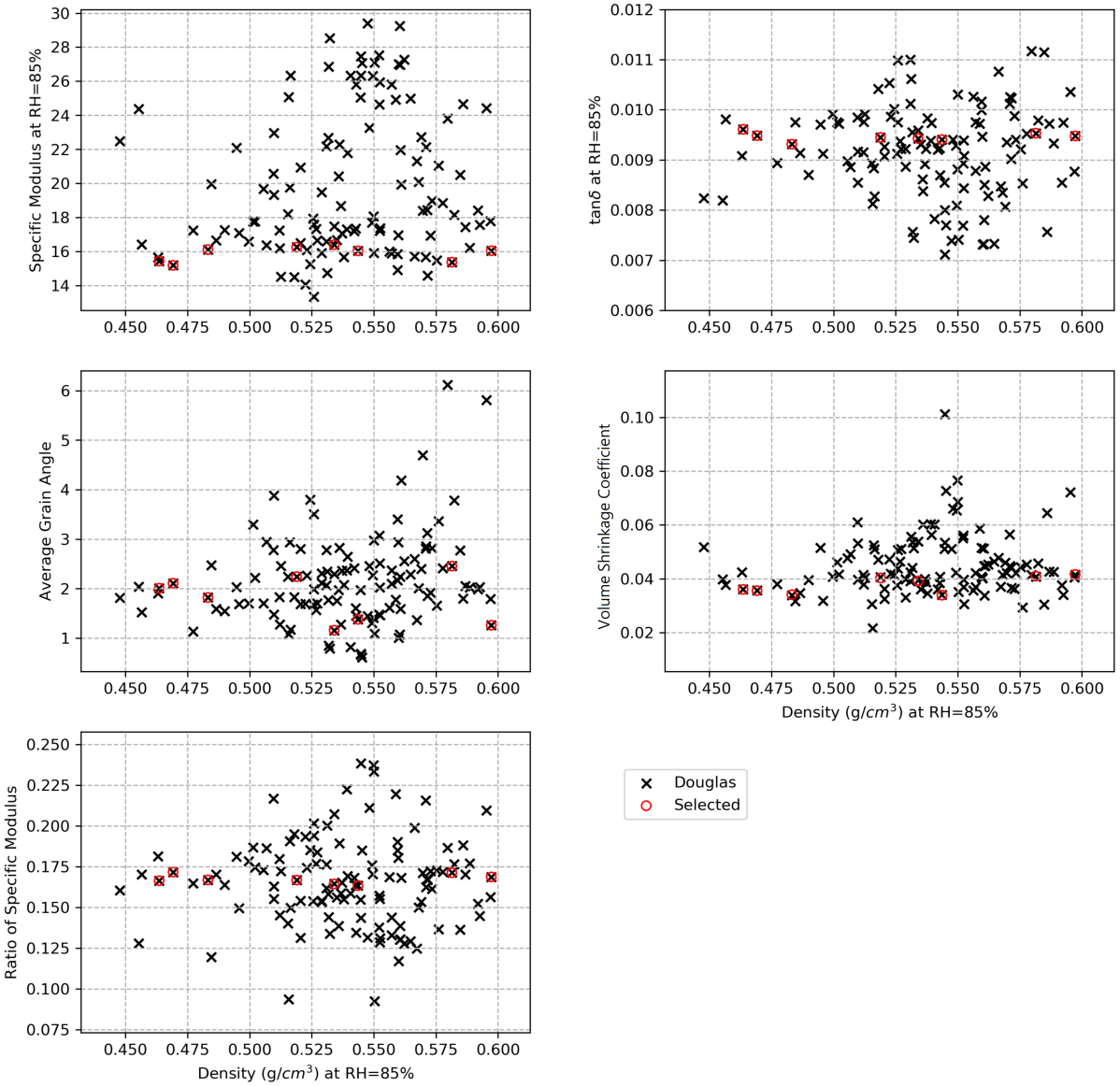

Figure 3.17: The sampling results of Douglas fir with maximum density variance.

Table 3.7: The sampling parameters of Poplar with maximum density variance.

Factors	ρ (g/cm^3)	E_s (GPa)	tanδ	$Grain_{AVG}$	α_V	$Ratio_{E_s}$
Weight of Parameters	0.1	7	10	0.1	1	5
Sample Variance	3.77E-04	2.63E+00	1.22E-06	7.39E+00	6.98E-05	6.35E-04
Selection Variance	5.13E-04	5.96E-02	2.33E-08	7.33E+00	9.98E-06	2.88E-05
Variance Ratio	1.36E+00	2.26E-02	1.91E-02	9.92E-01	1.43E-01	4.53E-02
Standardized Weight	2.66E+02	2.66E+00	8.19E+06	1.35E-02	1.43E+04	7.87E+03
Weighted Selection Variance	1.36E-01	1.59E-01	1.91E-01	9.92E-02	1.43E-01	2.26E-01
Criterion	-6.82E-01					

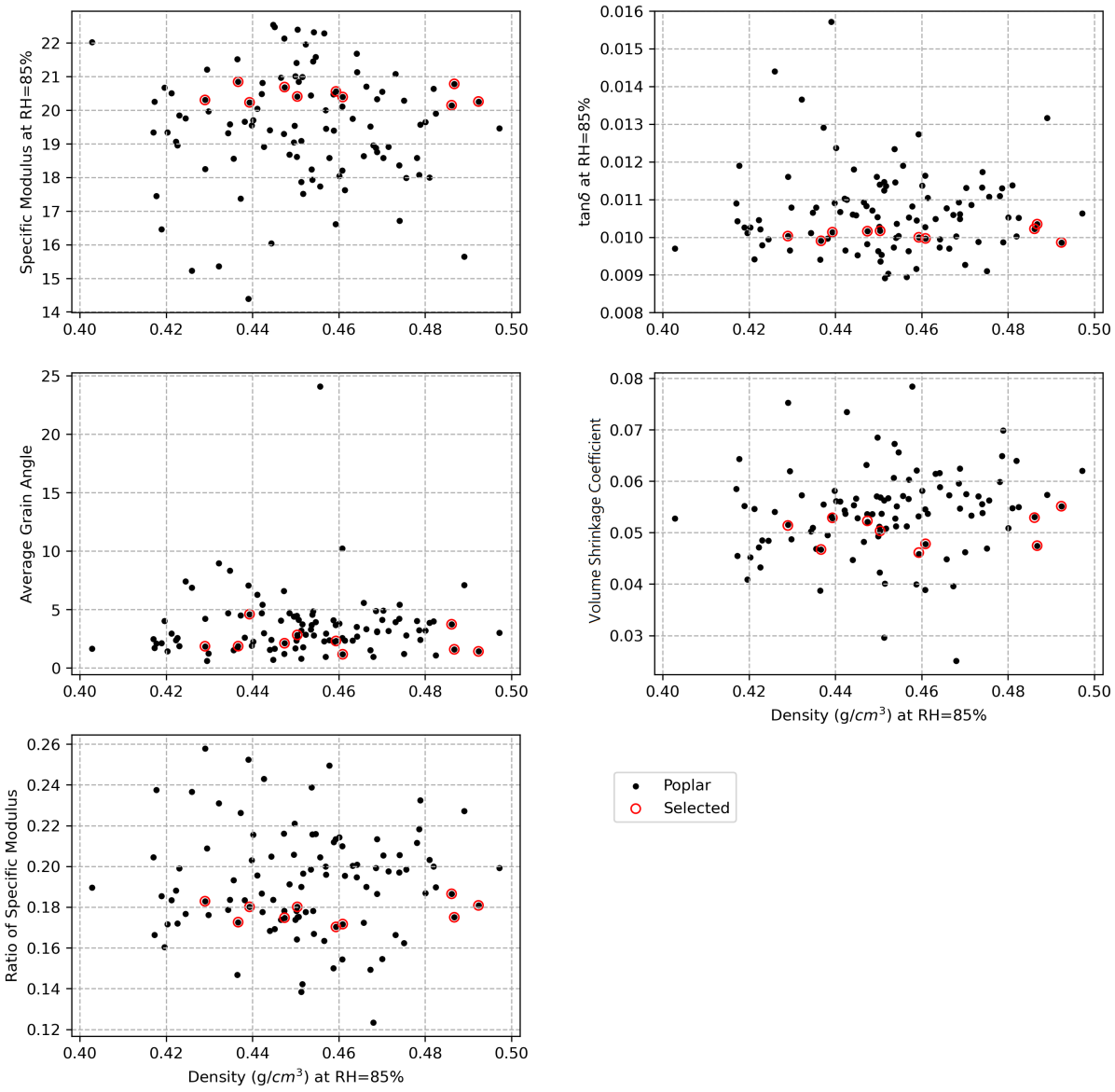

Figure 3.18: The sampling results of Poplar with maximum density variance.

Table 3.8: The sampling parameters of Beech with maximum density variance.

Factors	ρ (g/cm^3)	E_s (GPa)	tanδ	$Grain_{AVG}$	α_V	$Ratio_{E_s}$
Weight of Parameters	0.1	1	8	0.01	1	5
Sample Variance	4.30E-04	4.95E+00	3.58E-06	6.58E-01	5.56E-05	9.53E-04
Selection Variance	1.80E-04	2.72E-01	2.70E-08	2.77E+00	2.90E-06	6.74E-06
Variance Ratio	4.19E-01	5.49E-02	7.56E-03	4.20E+00	5.21E-02	7.07E-03
Standardized Weight	2.33E+02	2.02E-01	2.24E+06	1.52E-02	1.80E+04	5.25E+03
Weighted Selection Variance	4.19E-02	5.49E-02	6.05E-02	4.20E-02	5.21E-02	3.54E-02
Criterion	-2.03E-01					

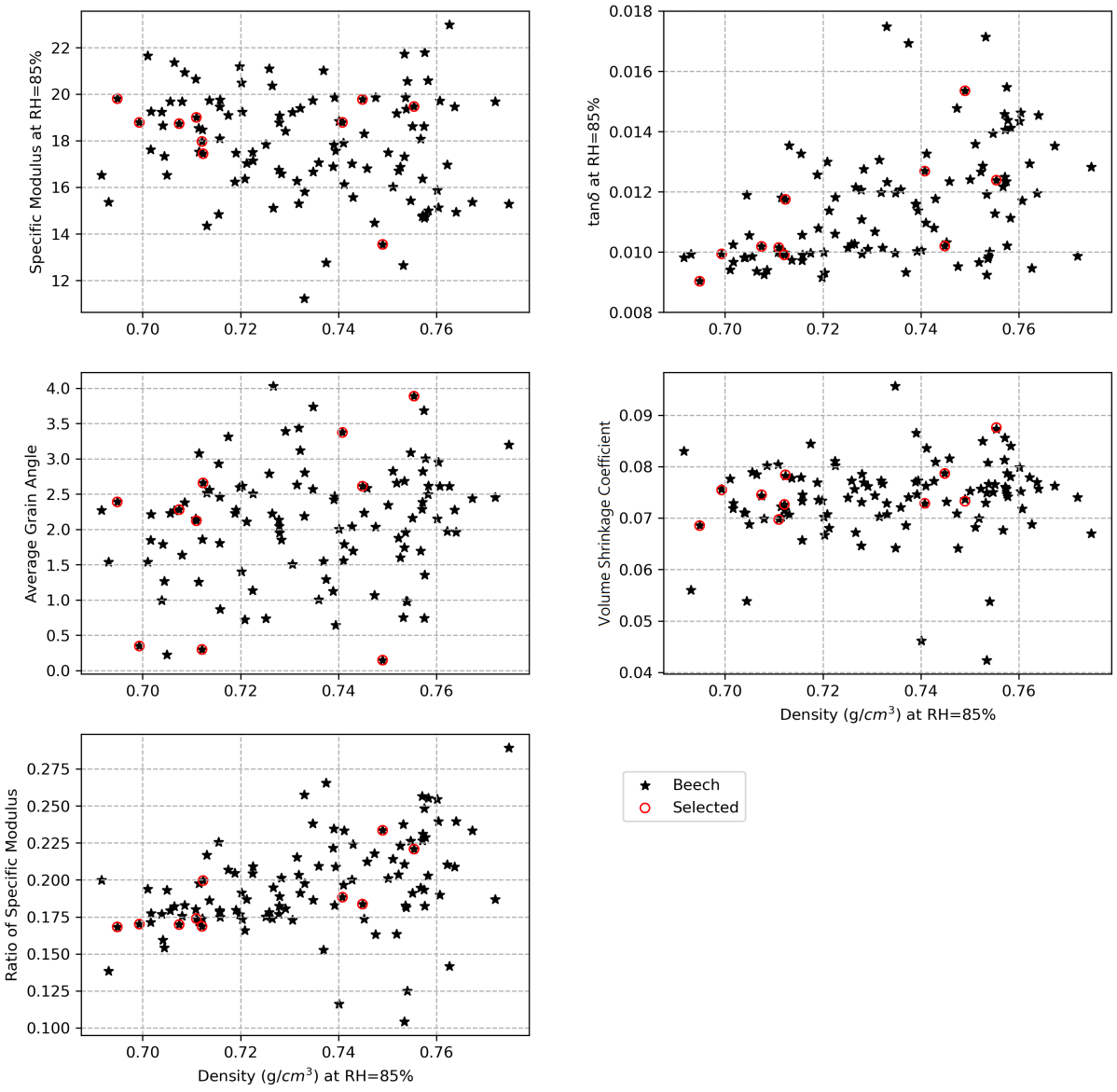

Figure 3.19: The sampling results of Beech with maximum density variance.

Table 3.9: The sampling parameters of Oak with maximum density variance.

Factors	ρ (g/cm^3)	E_s (GPa)	tanδ	$Grain_{AVG}$	α_V	$Ratio_{E_s}$
Weight of Parameters	0.1	2	3	0.04	1	2
Sample Variance	5.70E-04	4.86E+00	4.39E-06	1.51E+00	9.51E-05	1.08E-03
Selection Variance	4.74E-04	2.33E-01	1.66E-07	4.01E+00	7.14E-06	5.14E-05
Variance Ratio	8.33E-01	4.79E-02	3.78E-02	2.64E+00	7.51E-02	4.75E-02
Standardized Weight	1.76E+02	4.12E-01	6.83E+05	2.64E-02	1.05E+04	1.85E+03
Weighted Selection Variance	8.33E-02	9.59E-02	1.14E-01	1.06E-01	7.51E-02	9.50E-02
Criterion	-4.02E-01					

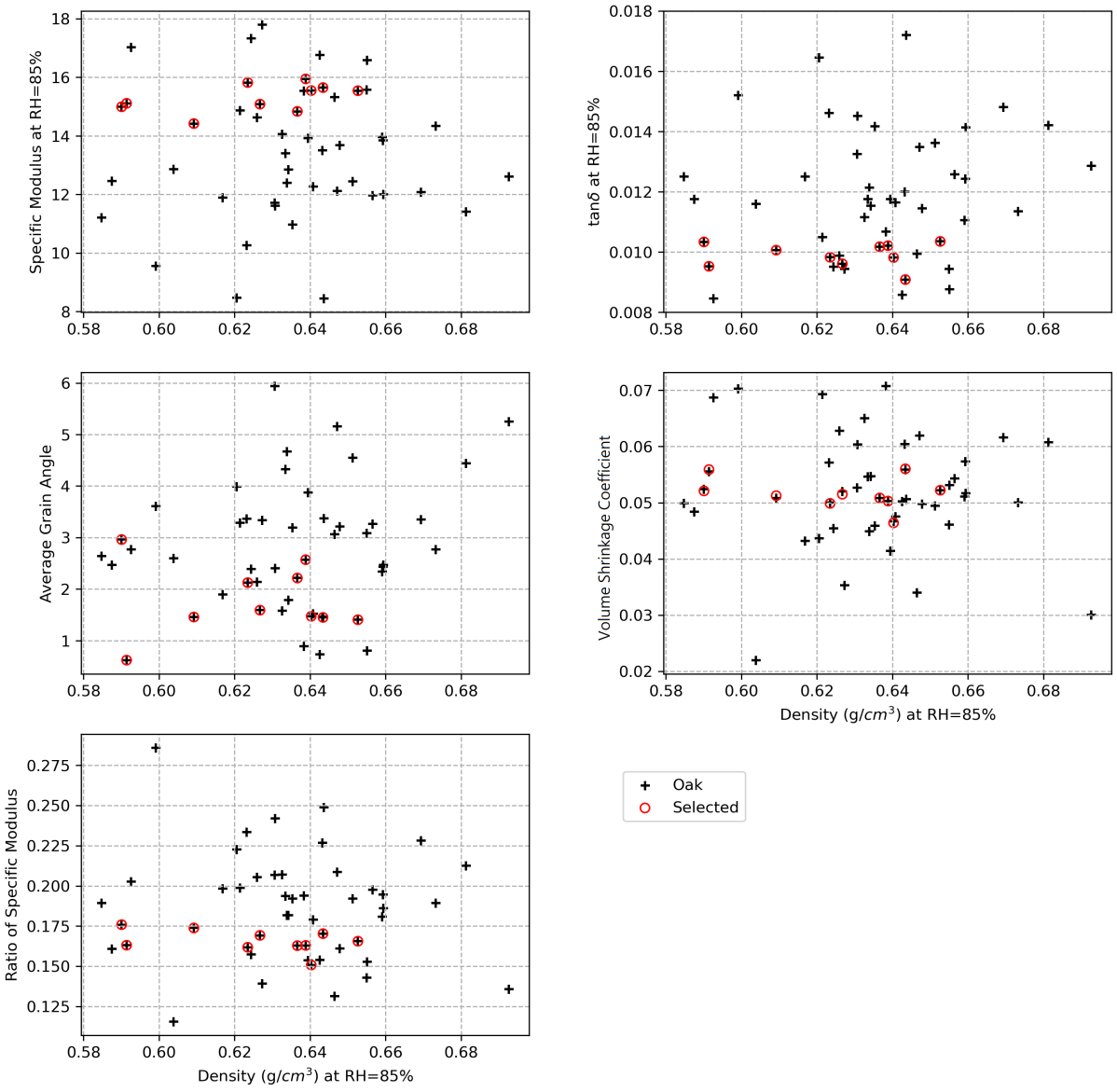

Figure 3.20: The sampling results of Oak with maximum density variance.

Table 3.10: The sampling parameters of Douglas fir with maximum specific modulus variance.

Factors	ρ (g/cm^3)	E_s (GPa)	ΔOno	$Grain_{AVG}$	α_V	$Ratio_{E_s}$
Weight of Parameters	5	0.1	5	0	0	0
Sample Variance	3.49E-03	2.05E+01	6.28E-07	8.48E-01	1.39E-04	9.52E-04
Selection Variance	6.74E-05	3.35E+01	1.03E-08	5.20E+00	8.11E-05	1.06E-03
Variance Ratio	1.93E-02	1.64E+00	1.64E-02	6.13E+00	5.82E-01	1.11E+00
Standardized Weight	1.43E+03	4.89E-03	7.96E+06	0.00E+00	0.00E+00	0.00E+00
Weighted Selection Variance	9.65E-02	1.64E-01	8.18E-02	0.00E+00	0.00E+00	0.00E+00
Criterion	-1.46E-02					

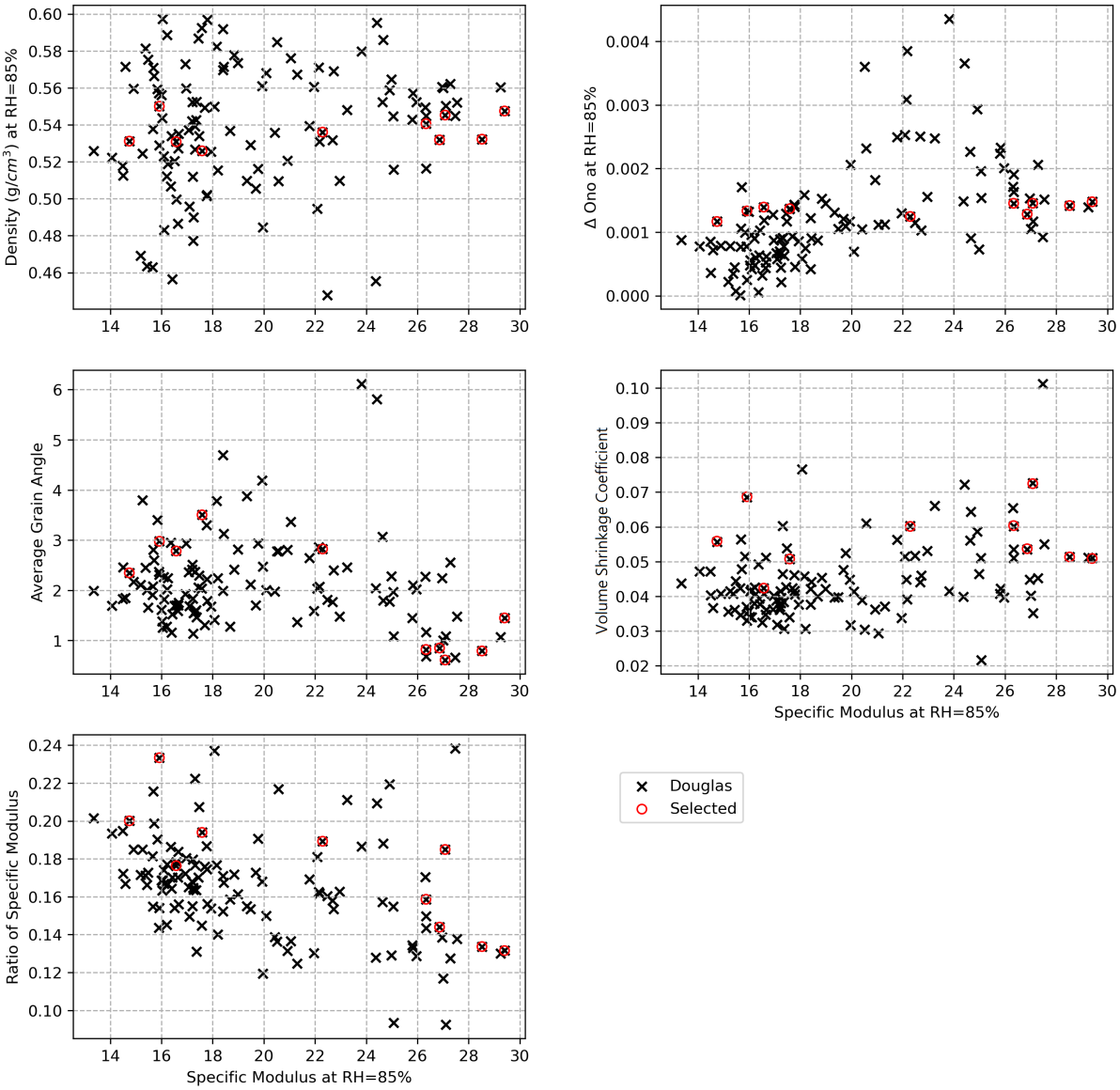

Figure 3.21: The sampling results of Douglas fir with maximum specific modulus variance.

Table 3.11: The sampling parameters of Poplar with maximum specific modulus variance.

Factors	ρ (g/cm^3)	E_s (GPa)	ΔOno	$Grain_{AVG}$	α_V	$Ratio_{E_s}$
Weight of Parameters	6	0.1	4	0	0	0
Sample Variance	3.77E-04	2.63E+00	5.33E-07	7.39E+00	6.98E-05	6.35E-04
Selection Variance	7.03E-06	3.42E+00	1.80E-08	1.21E+01	1.08E-04	6.04E-04
Variance Ratio	1.87E-02	1.30E+00	3.37E-02	1.63E+00	1.55E+00	9.50E-01
Standardized Weight	1.59E+04	3.80E-02	7.50E+06	0.00E+00	0.00E+00	0.00E+00
Weighted Selection Variance	1.12E-01	1.30E-01	1.35E-01	0.00E+00	0.00E+00	0.00E+00
Criterion	-1.17E-01					

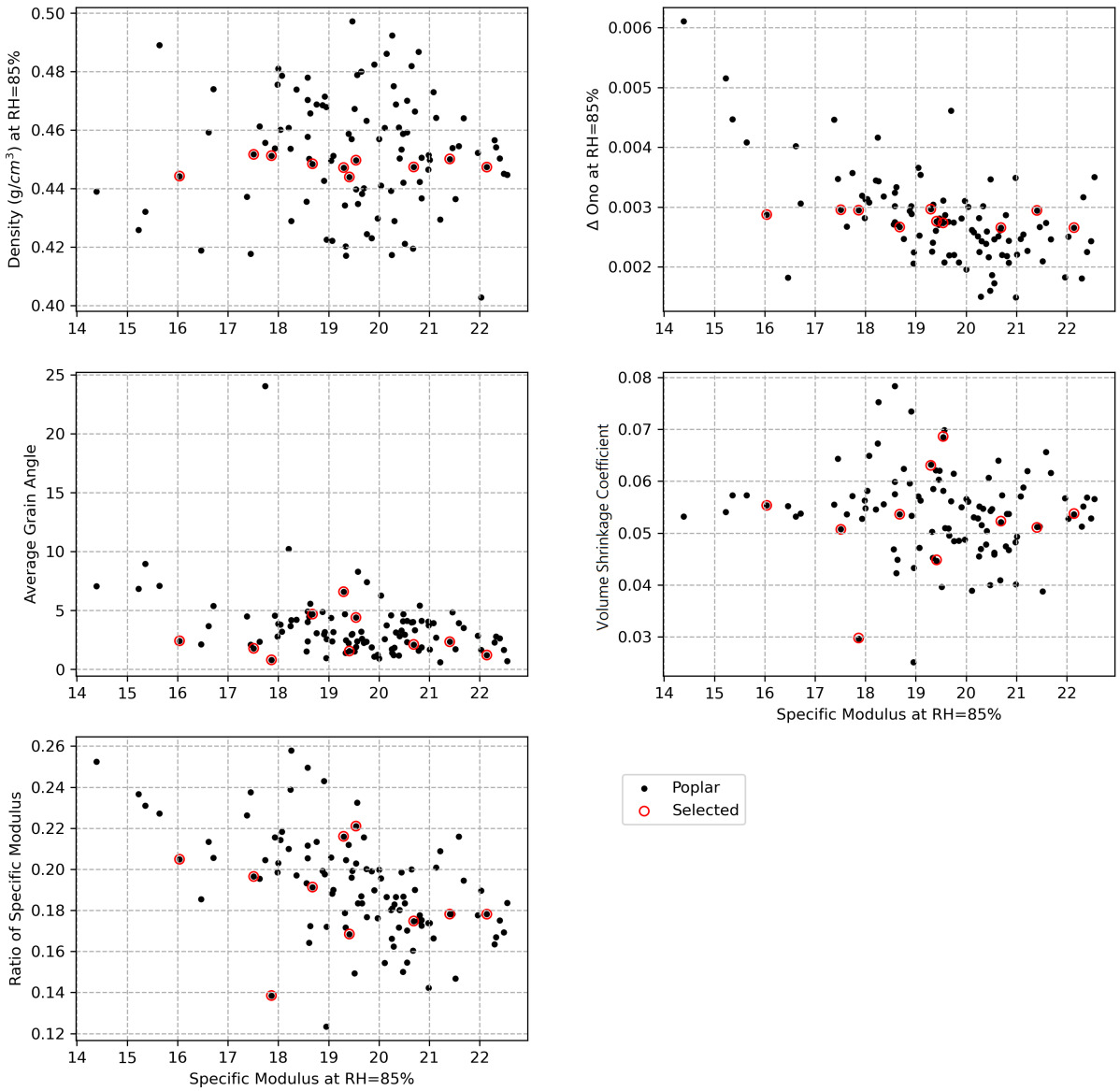

Figure 3.22: The sampling results of Poplar with maximum specific modulus variance.

Table 3.12: The sampling parameters of Beech with maximum specific modulus variance.

Factors	ρ (g/cm^3)	E_s (GPa)	ΔOno	$Grain_{AVG}$	α_V	$Ratio_{E_s}$
Weight of Parameters	3	0.1	5	0	0	0
Sample Variance	4.30E-04	4.95E+00	1.62E-06	6.58E-01	5.56E-05	9.53E-04
Selection Variance	1.43E-05	4.42E+00	6.77E-08	7.82E+00	2.57E-05	1.66E-04
Variance Ratio	3.33E-02	8.94E-01	4.18E-02	1.19E+01	4.62E-01	1.74E-01
Standardized Weight	6.98E+03	2.02E-02	3.09E+06	0.00E+00	0.00E+00	0.00E+00
Weighted Selection Variance	9.99E-02	8.94E-02	2.09E-01	0.00E+00	0.00E+00	0.00E+00
Criterion	-2.19E-01					

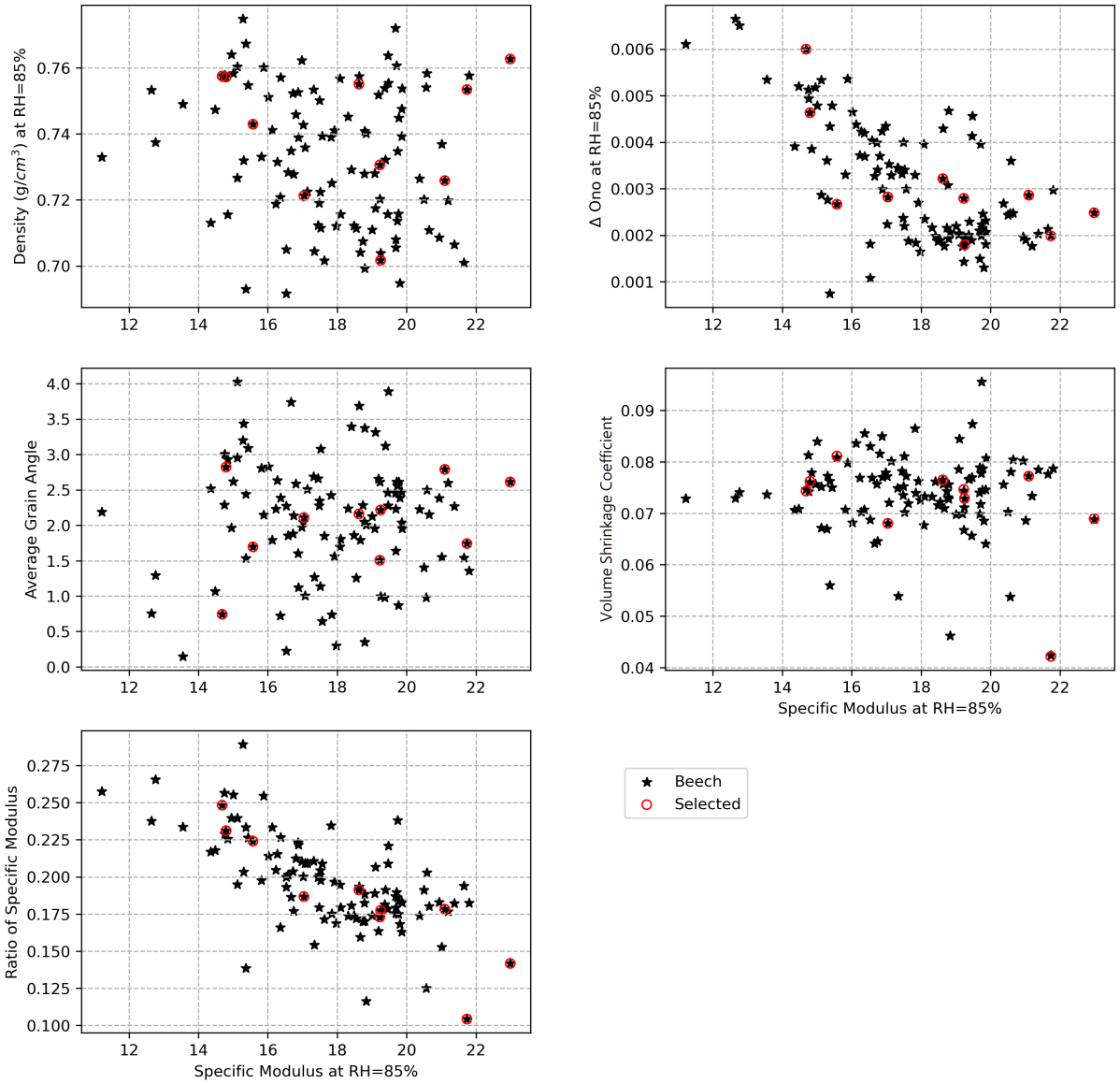

Figure 3.23: The sampling results of Beech with maximum specific modulus variance.

Table 3.13: The sampling parameters of Oak with maximum specific modulus variance.

Factors	ρ (g/cm^3)	E_s (GPa)	ΔOno	$Grain_{AVG}$	α_V	$Ratio_{E_s}$
Weight of Parameters	5	0.5	1.5	0	0	0
Sample Variance	5.70E-04	4.86E+00	1.04E-06	1.51E+00	9.51E-05	1.08E-03
Selection Variance	4.32E-05	6.96E+00	3.76E-07	1.24E+01	1.04E-04	7.15E-04
Variance Ratio	7.59E-02	1.43E+00	3.60E-01	8.18E+00	1.09E+00	6.60E-01
Standardized Weight	8.78E+03	1.03E-01	1.44E+06	0.00E+00	0.00E+00	0.00E+00
Weighted Selection Variance	3.79E-01	7.16E-01	5.40E-01	0.00E+00	0.00E+00	0.00E+00
Criterion	-2.04E-01					

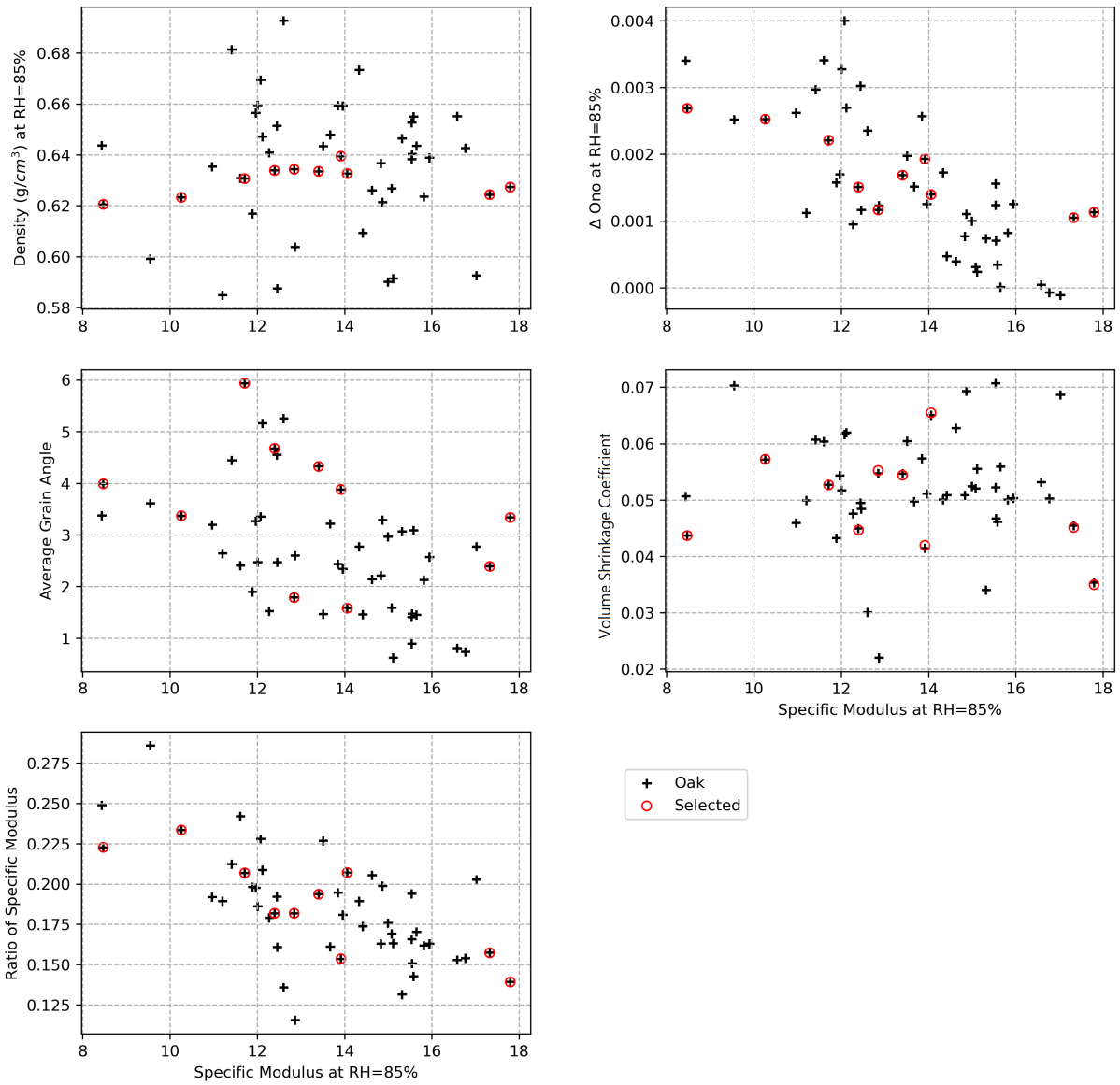

Figure 3.24: The sampling result of Oak with maximum specific modulus variance.

Table 3.14: The sampling parameters of Douglas fir with maximum delta Ono variance.

Factors	ρ (g/cm^3)	E_s (GPa)	ΔOno	$Grain_{AVG}$	α_V	$Ratio_{E_s}$
Weight of Parameters	10	2	0.5	0.0085	0	0
Sample Variance	3.49E-03	2.05E+01	6.28E-07	8.48E-01	1.39E-04	9.52E-04
Selection Variance	1.11E-04	2.90E+00	1.85E-06	1.13E+01	1.79E-04	1.07E-03
Variance Ratio	3.17E-02	1.42E-01	2.94E+00	1.33E+01	1.29E+00	1.13E+00
Standardized Weight	2.87E+03	9.78E-02	7.96E+05	1.00E-02	0.00E+00	0.00E+00
Weighted Selection Variance	3.17E-01	2.84E-01	1.47E+00	1.13E-01	0.00E+00	0.00E+00
Criterion	7.59E-01					

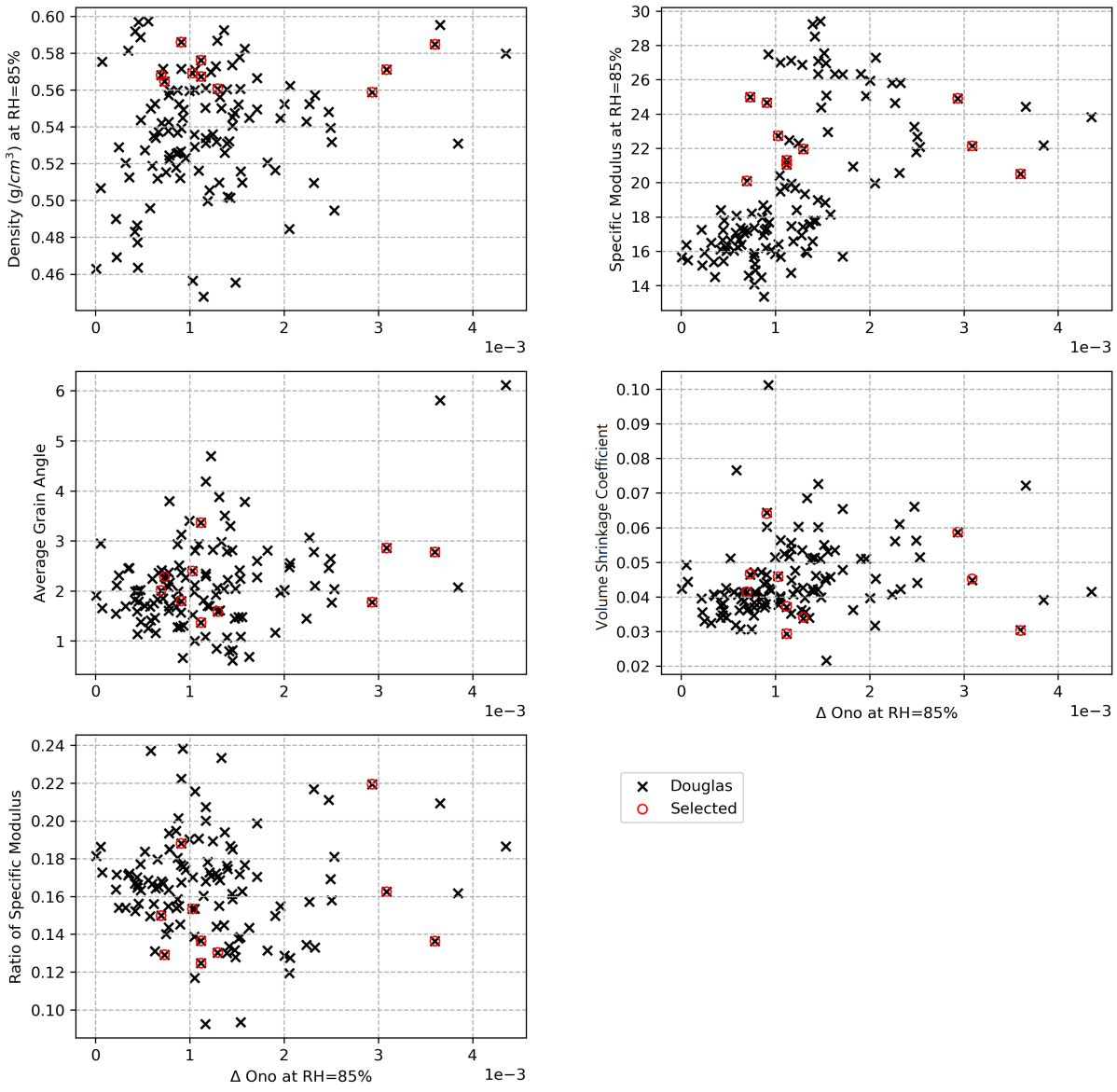

Figure 3.25: The sampling results of Douglas fir with maximum delta Ono variance.

Table 3.15: The sampling parameters of Poplar with maximum delta Ono variance.

Factors	ρ (g/cm^3)	E_s (GPa)	ΔOno	$Grain_{AVG}$	α_V	$Ratio_{E_s}$
Weight of Parameters	10	2	0.5	0.0085	0	0
Sample Variance	3.77E-04	2.63E+00	5.33E-07	7.39E+00	6.98E-05	6.35E-04
Selection Variance	1.58E-05	5.49E-01	6.90E-07	1.72E+01	4.77E-05	4.67E-04
Variance Ratio	4.20E-02	2.09E-01	1.29E+00	2.32E+00	6.83E-01	7.35E-01
Standardized Weight	2.66E+04	7.60E-01	9.38E+05	1.15E-03	0.00E+00	0.00E+00
Weighted Selection Variance	4.20E-01	4.17E-01	6.47E-01	1.97E-02	0.00E+00	0.00E+00
Criterion	-2.11E-01					

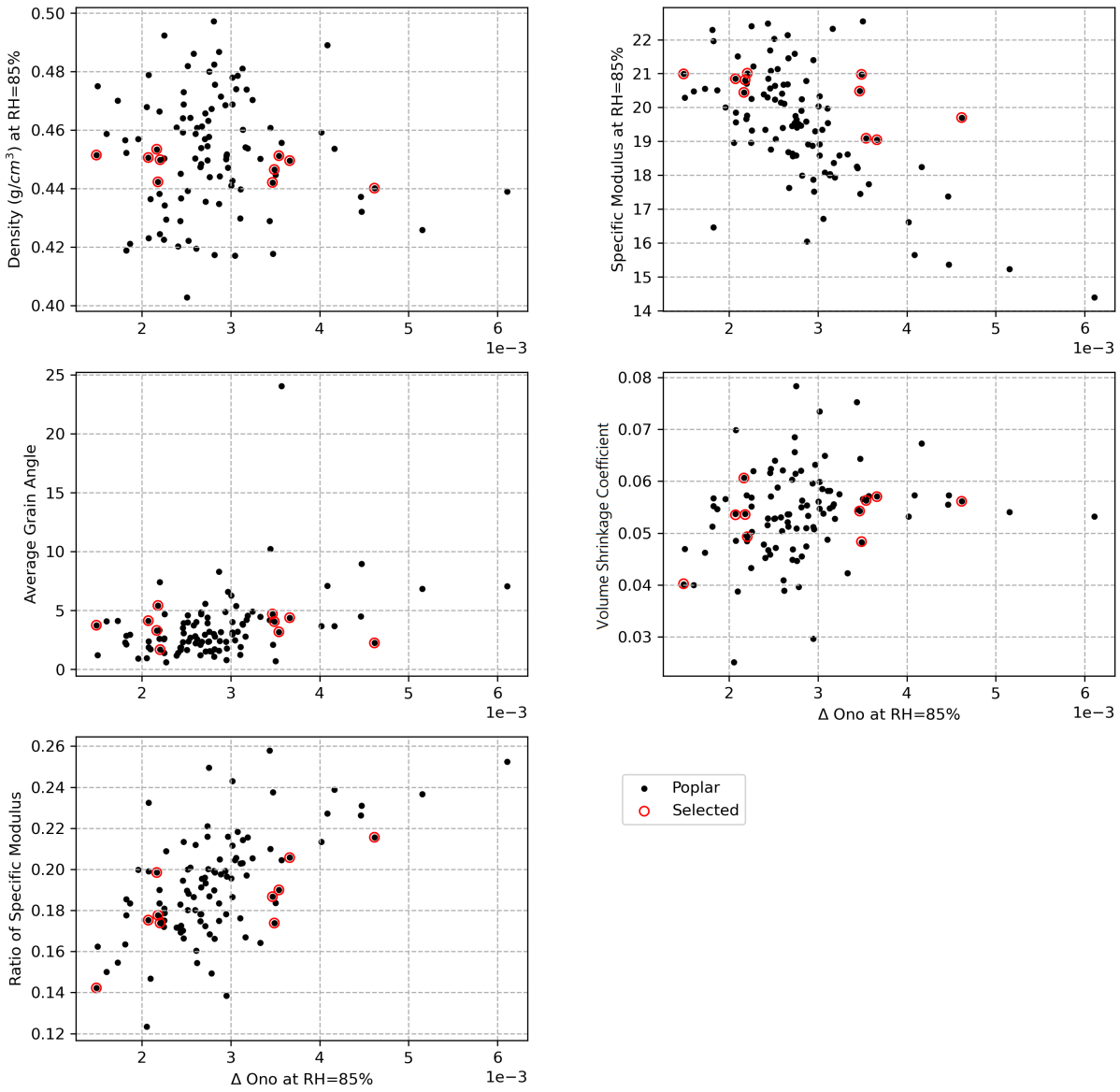

Figure 3.26: The sampling results of Poplar with maximum delta Ono variance.

Table 3.16: The sampling parameters of Beech with maximum delta Ono variance.

Factors	ρ (g/cm^3)	E_s (GPa)	ΔOno	$Grain_{AVG}$	α_V	$Ratio_{E_s}$
Weight of Parameters	10	2	0.5	0.01	0	0
Sample Variance	4.30E-04	4.95E+00	1.62E-06	6.58E-01	5.56E-05	9.53E-04
Selection Variance	8.14E-06	7.50E-01	7.54E-07	4.54E+00	1.11E-04	1.09E-03
Variance Ratio	1.89E-02	1.52E-01	4.66E-01	6.90E+00	2.00E+00	1.15E+00
Standardized Weight	2.33E+04	4.04E-01	3.09E+05	1.52E-02	0.00E+00	0.00E+00
Weighted Selection Variance	1.89E-01	3.03E-01	2.33E-01	6.90E-02	0.00E+00	0.00E+00
Criterion	-3.29E-01					

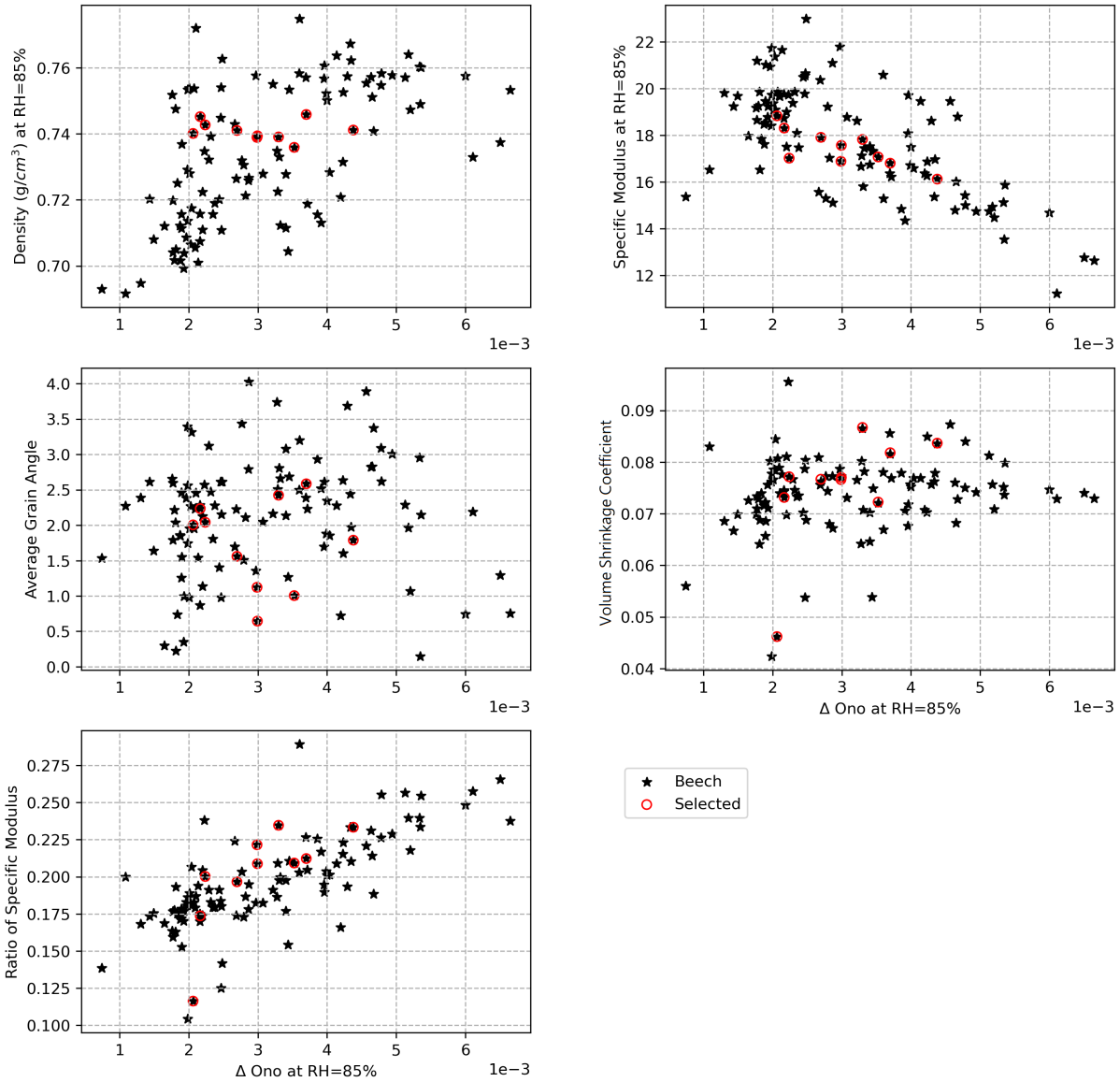

Figure 3.27: The sampling results of Beech with maximum delta Ono variance.

Table 3.17: The sampling parameters of Oak with maximum delta Ono variance.

Factors	ρ (g/cm^3)	E_s (GPa)	ΔOno	$Grain_{AVG}$	α_V	$Ratio_{E_s}$
Weight of Parameters	10	2	0.5	0.01	0	0
Sample Variance	5.70E-04	4.86E+00	1.04E-06	1.51E+00	9.51E-05	1.08E-03
Selection Variance	7.03E-05	2.63E+00	8.15E-07	9.39E+00	7.30E-05	6.73E-04
Variance Ratio	1.23E-01	5.41E-01	7.81E-01	6.20E+00	7.68E-01	6.22E-01
Standardized Weight	1.76E+04	4.12E-01	4.79E+05	6.60E-03	0.00E+00	0.00E+00
Weighted Selection Variance	1.23E+00	1.08E+00	3.91E-01	6.20E-02	0.00E+00	0.00E+00
Criterion	-1.99E+00					

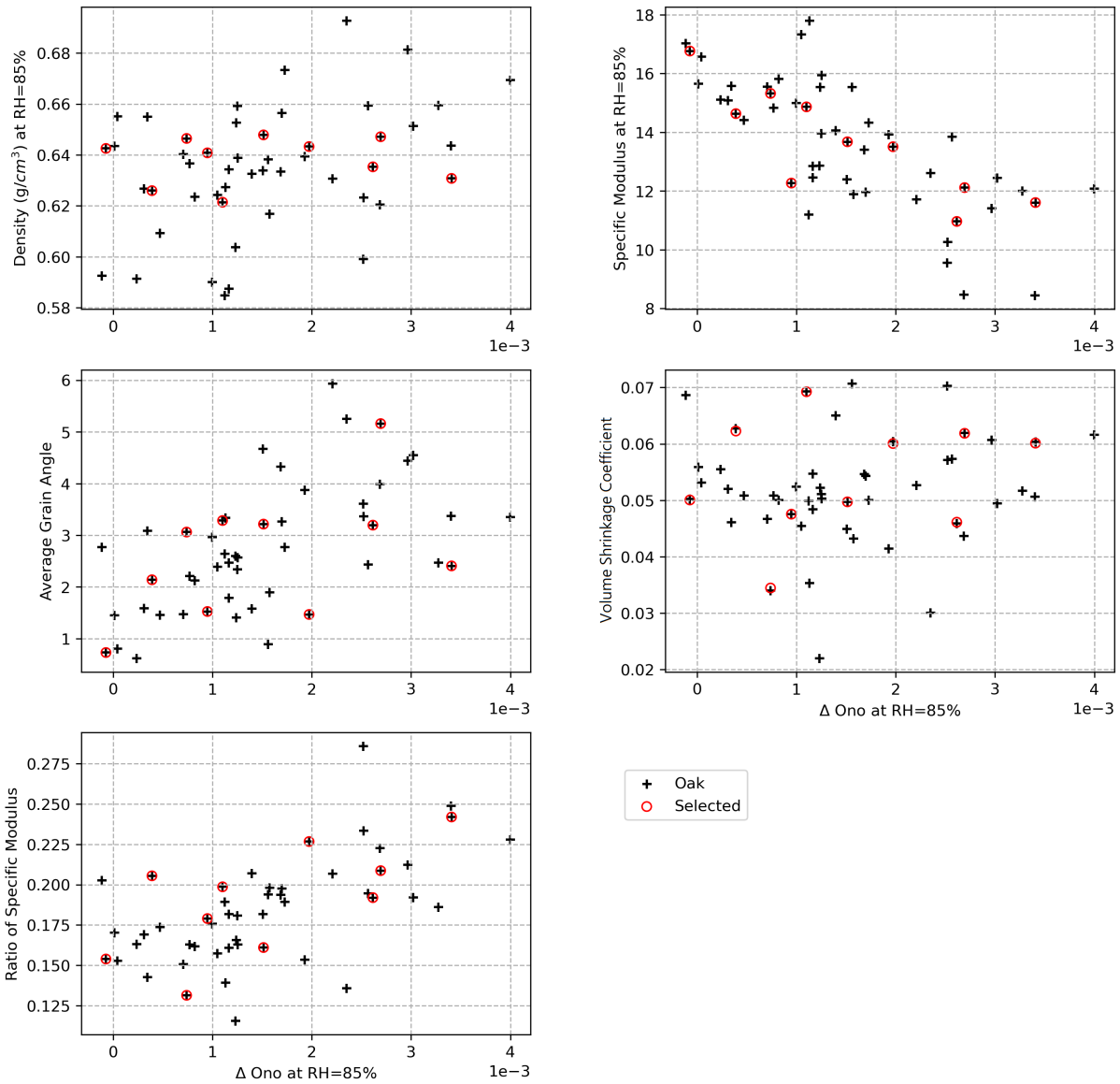

Figure 3.28: The sampling results of Oak with maximum delta Ono variance.

Table 3.18: The sampling parameters for maximum density variance and specific modulus at 15.5 MPa.

Factors	ρ (g/cm^3)	E_s (GPa)	tanδ	$Grain_{AVG}$	α_V	$Ratio_{E_s}$
Weight of Parameters	0.01	6	0	0	0	0
Sample Variance	1.37E-02	1.29E+01	3.44E-06	3.03E+00	2.26E-04	1.05E-03
Selection Variance	1.32E-02	2.03E-02	3.43E-06	1.40E+01	1.99E-04	1.57E-03
Variance Ratio	9.66E-01	1.57E-03	9.98E-01	4.62E+00	8.81E-01	1.49E+00
Standardized Weight	7.31E-01	4.64E-01	0.00E+00	0.00E+00	0.00E+00	0.00E+00
Weighted Selection Variance	9.66E-03	9.40E-03	0.00E+00	0.00E+00	0.00E+00	0.00E+00
Criterion	2.60E-04					

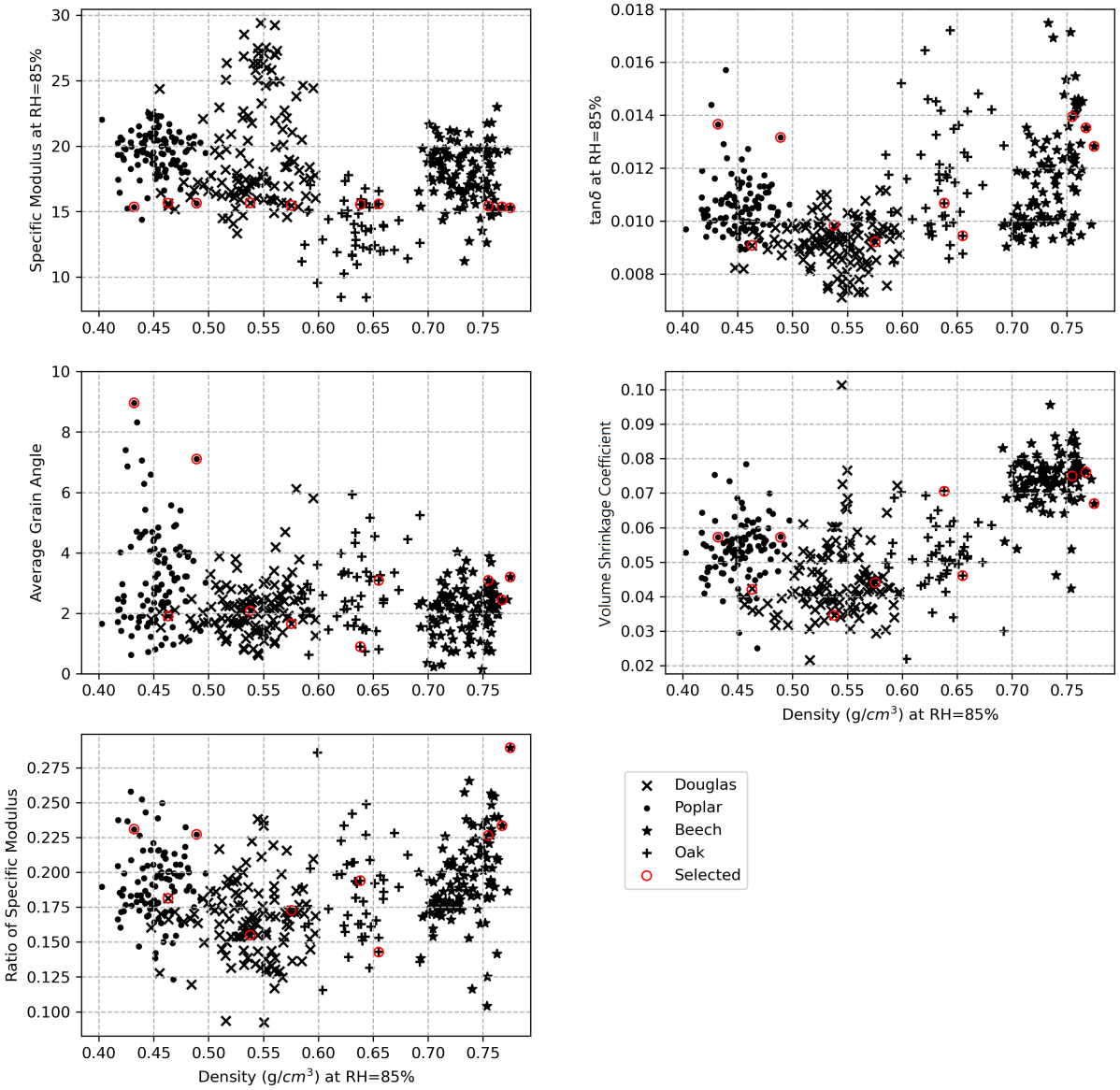

Figure 3.29: The sampling results for maximum density variance and specific modulus at 15.5 MPa.

Table 3.19: The sampling parameters for maximum density variance and specific modulus at 22 MPa.

Factors	ρ (g/cm^3)	E_s (GPa)	tanδ	$Grain_{AVG}$	α_V	$Ratio_{E_s}$
Weight of Parameters	2	0.5	1.5	0	0	0
Sample Variance	1.37E-02	1.29E+01	3.44E-06	3.03E+00	2.26E-04	1.05E-03
Selection Variance	1.61E-02	2.52E+01	4.79E-06	9.04E+00	1.55E-04	7.10E-04
Variance Ratio	1.17E+00	1.94E+00	1.39E+00	2.98E+00	6.83E-01	6.74E-01
Standardized Weight	1.46E+02	3.87E-02	4.36E+05	0.00E+00	0.00E+00	0.00E+00
Weighted Selection Variance	2.35E+00	9.72E-01	2.09E+00	0.00E+00	0.00E+00	0.00E+00
Criterion	-7.11E-01					

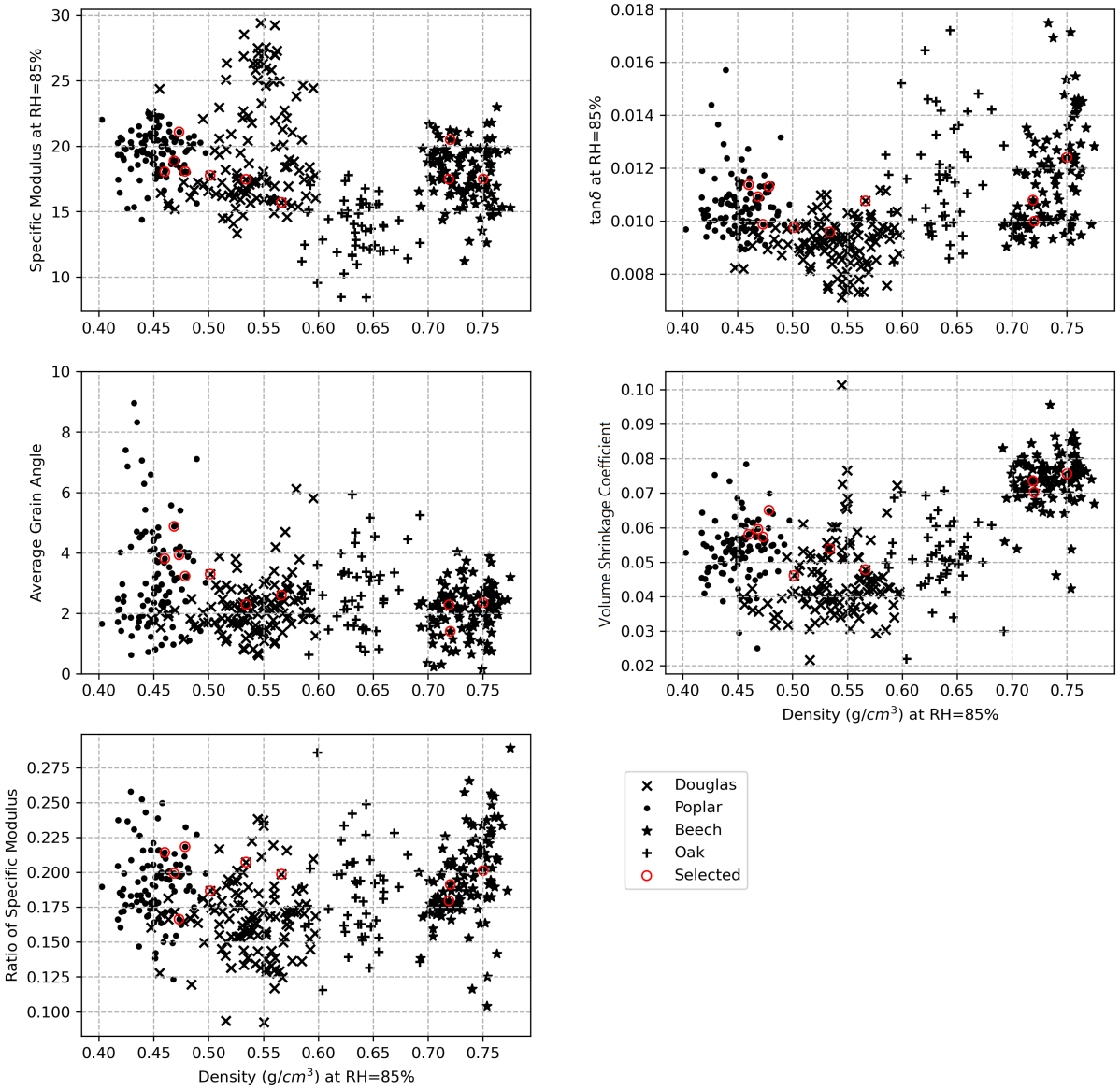

Figure 3.30: The sampling results for maximum density variance and specific modulus at 22 MPa.

3.4 Summary

In this chapter, we have an overview of the 4 kinds of wood which have been used in this study. To measure the mechanical and physical characteristics of the wood studied, the size and weight of the specimens were measured, and vibration tests were performed. Through the measurement, density, specific modulus and size data were collected as sampling parameters.

The strategy of sampling is to focus on a specific factor and low down the effect of other parameters. A criterion value was defined to have the maximum variance of the target factor and minimize the variance of the others. By the sampling technique, we can have the group of samples with the largest variance of each parameter to perform the creep test.

Finally, this sampling leads to 14 different creep tests:

- 3 "factor" groups, 12 tests in sum: test on only 1 species, 10 specimens, 1 variable factor (density, specific modulus, or delta Ono)
- 2 "individual" tests: 4 species were tested at the same time with the same specific modulus ($\approx 15.5GPa$ and $\approx 22GPa$) and maximum variance of density.

Chapter 4

Experimental study of creep in 4–point bending

This chapter describes the creep test design, procedure, measurements, calculations, and results obtained. Some series of 4–point bending creep tests were carried out based on the sampling procedure described in chapter 3. All the tests were carried out under a constant environment at 20 °C and RH=85% inside the climatic chamber and lasted 10 days.

4.1 Experimental method

4.1.1 The *creep box*: an experimental system for creep behavior

Figure 4.1 (a) shows the design of a *creep box*. The original shape was designed by LMGC during the Master internship of Sylvain Conte in 2019. Initially, the creep box was designed to perform 4–point bending test in a hermetically sealable environment. The specimen is set up between two supports with an outer span of 110 mm. The specimen is slid into the mass holder and the distance between the 2 loading bars is 60 mm of inner span. A 598 (± 1.3) g lead block was hanged in the middle of the support. Each box was 190 mm in length, 145 mm in high, 85 mm in depth, and weight 1827 g. A total of 10 creep boxes, including mass supports and lead blocks, were placed in the climate chamber, as shown in the figure 4.2, with five boxes per row and a total of two layers. All boxes were held together by C–clamps to reduce vibration from the machine fan or from user-operated contact. Each box was marked with 6 markers to help the user to set up the specimens and the loads accurately. There were 4 marks on the cantilever supports, shown in figure 4.1 (b) with the red arrows, to make sure the middle line of the sample was parallel to the cantilevers. The gray parts are the support of the creep box at both sides with the black marks to align the specimen to make sure the length direction is vertical to the black marks. The other two marks were located in the center of the loading bar to align the midline of the specimen (figure 4.1 c). The dark gray bars are the loading point of on the specimen, and the light gray part is the lower part of the mass holder which connects a metal thin bar to hang the lead block. The two marks on the central point of both the dark gray bars to make sure the lead block is hanged align the central point of the specimen.

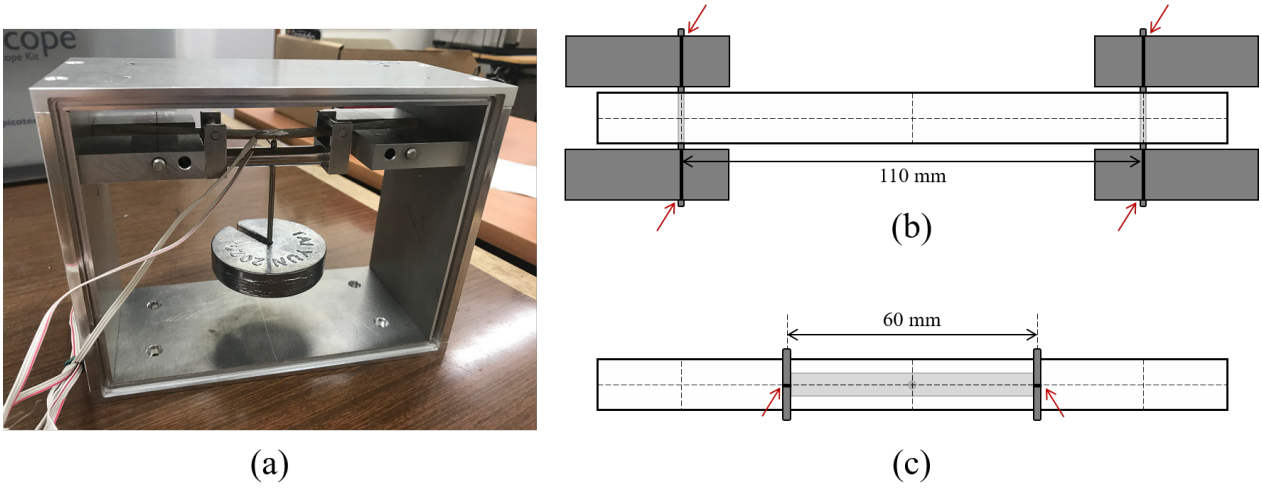

Figure 4.1: Creep Box. (a) The structure of a creep box. A specimen is supported by the supports on both sides, and the mass holder hangs on the specimen. The weight of the mass holder is about 50 g, and it holds a 600 g lead block. (b) Looking at the top of the sample, the gray part is the support of the creep box on both sides with the black marks to align the sample to make sure the longitudinal direction is perpendicular to the black marks indicated by the red arrow. (c) Top of the specimen with the mass holder. The dark gray bars are the loading point on the sample, and the light gray part is the lower part of the mass holder, which connects a thin metal bar to hang the lead block. There are two markers on the center point of the two dark gray bars to ensure that the lead block is hung in alignment with the center point of the sample.

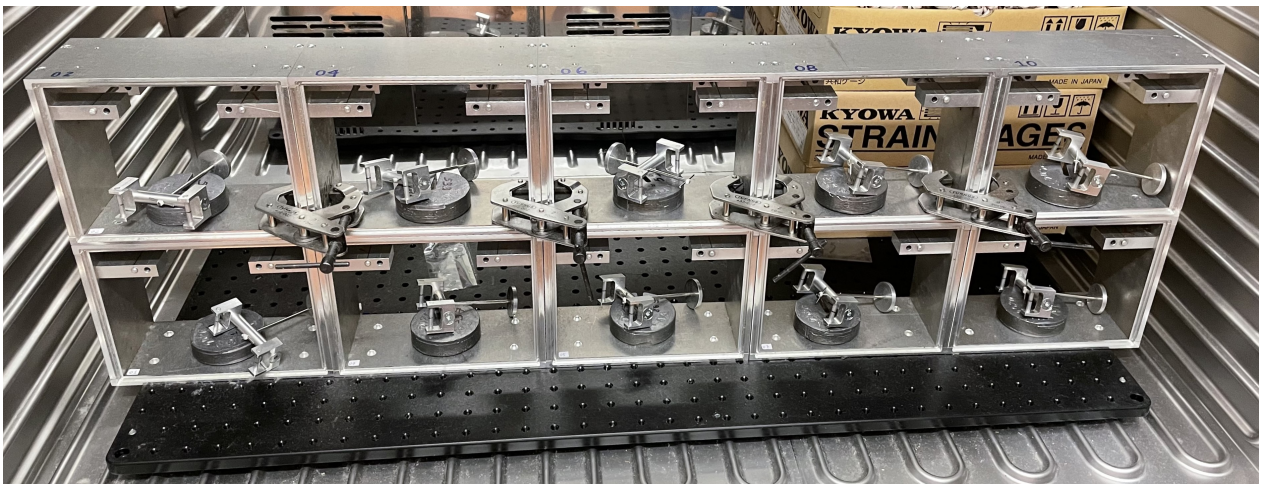

Figure 4.2: Creep boxes in chamber before installing the specimens. The boxes are connected by C–clamps and fixed at the bottom of the chamber.

4.1.2 Loading of the specimens

The stress σ (MPa) and compliance J (GPa^{-1}) values can be calculated by the equation 4.1 and 4.2. In the equation 4.1, P (N) is load, L (mm) is the distance between the 2 outer supports, l (mm) is the distance between the 2 inner loading points, b (mm) is the width of the specimen, h (mm) is the thickness of the specimen. Compliance is equal to the reciprocal of the elastic modulus (equation 4.2). ε is strain measured.

$$\sigma = \frac{3P(L-l)}{2bh^2} \tag{4.1}$$

$$J = \frac{1}{E} = \frac{\varepsilon}{\sigma} \tag{4.2}$$

There were 10 sets of creep boxes, including mass supports and lead blocks. Each element of a single box has the same number to ensure the total weight for each box. Table 4.1 presents information on the dimensions and weight applied for each creep box. The values of outer span (L) and inner span (l) would be substituted according to the number of each test instrument. The load (P) value is the sum of the weight of the load support and lead block. In this study, the average stress calculated from equation 4.1 for 4–point bending test is 10.52 MPa (± 3.05 MPa).

Table 4.1: Creep boxes information

	Box	Support		Lead block
Number	L (mm)	l (mm)	weight (g)	weight (g)
01	110.170	59.80	50.6264	599
02	110.135	59.78	50.7198	599
03	110.160	59.97	50.2902	597
04	110.245	59.82	50.5986	599
05	110.075	59.89	50.0854	598
06	110.240	59.85	50.7452	599
07	109.860	59.90	50.7614	595
08	110.190	59.88	50.8241	598
09	110.285	59.86	50.7188	599
10	110.225	60.00	49.8522	597

4.1.3 Testing environment

In this study, the entire creep tests were conducted in a climatic chamber Memmert HPP750 with a fixed temperature setting of 20 °C and a relative humidity of 85%. The result of Matar (2003) gives us a good example of how the relative humidity affects the creep behavior as shown in figure 4.3. The x-axis is time in logarithm. The y-axis is relative creep, i.e. $\varepsilon(t)$ divided by initial strain. The numerical marks on the line are relative humidity in percent. It indicates that the relative humidity enlarge the delayed deformation, especially for longer duration. According to Morlier (1994), several studies have compared the effect of temperature on wood creep, and the author's conclusions are shown in the figure 4.4. Higher temperatures can make the

creep behavior more pronounced, but considering the variations shown in the figure, we cannot say that this effect is strong. Indeed, an increase in environment temperature leads to a reduction of the moisture content of specimens. At low moisture content, the viscoelastic behavior of wood will be reduced. This would be the opposite of what we would expect: a harsher environment for the wood structure. Therefore, to reach the condition of class 3 in NFEN14081-1 (2016), we accelerated the creep behavior by increasing the relative humidity but not the temperature.

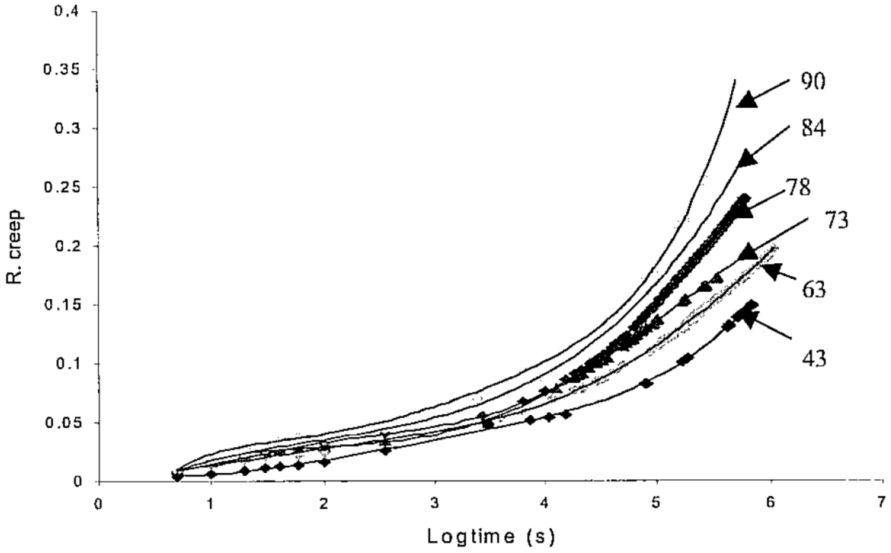

Figure 4.3: Relative creep values at different testing relative humidity (Matar, 2003)

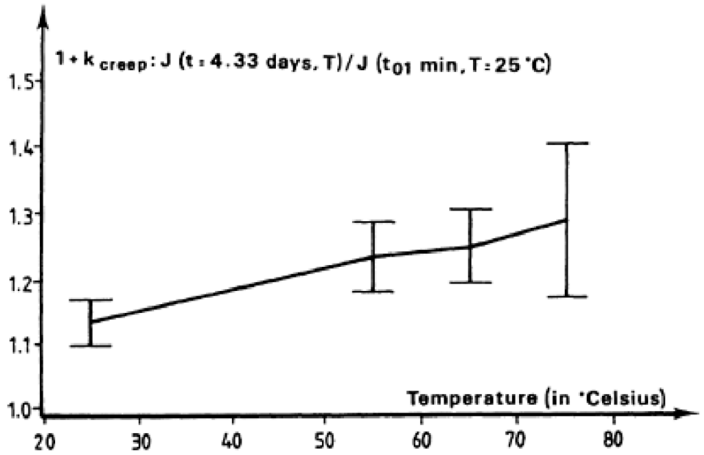

Figure 4.4: Creep behavior at different testing temperature. (Morlier, 1994)

4.1.4 Measurement of strain

Strain is measured with gauges following the procedure:

1. Find the center points on both sides of the specimen along the centerline of the length and width.
2. At the center of both sides of the specimen, paste two strain gauges the parallel to the length.

3. The strain gauges used in this study were KYOWA KFGS-5-120-C1-11 and pasted with cyanoacrylate glue.

After the first series of creep tests, we found an unexpected rise in both creep strain and longitudinal hygroscopic strain. Therefore, we performed correction tests to check this situation. It has been suggested that the drying of the glue absorbs moisture from the nearby environment, including the wooden specimens, which could cause a change in the moisture content in the strain gauge area, resulting in an increase in strain. Therefore, after the strain gauges are glued, the specimens are left in the climate chamber for 1 day before loading. However, there was still an increase in hygroscopic strain between 1 hour after loading and 1 day. We supposed that this phenomenon is due to the opening of the chamber to hang the weight, this is negligible on creep strain.

An additional item to control is the time between installation of the wires of strain gauges and loading. Even if the whole experimental system is in the climate chamber, the opening of the door causes a change in the relative humidity of the chamber. The time necessary to install the wires of strain gauges takes than loading, and is done with the door opened. Therefore, after the installation of the strain gauge wires, the specimens stay in the chamber for 1 hour before loading.

4.1.5 Loading process

Due to the design of the creep boxes, the entire loading process was divided into two steps, which require the control of intermediate times. The first step is to slide the specimen through the load support and into the creep box. This subjects the specimen to a weight of approximately 50 g of the load support. Then, the lead block is hung on the load support. The time between the two loading steps was controlled to be within 1 minute. Ideally, all the weight is loaded on the specimen in a very short time, almost instantaneously. In reality, this was difficult to achieve because the box were in a climate chamber with limited access. Also, the specimens needed to be aligned with the 6 markers. Therefore, it was necessary to set up the specimen as first step and then load the lead block, but we could not have a perfect instantaneous loading.

4.1.6 Data acquisition and strain calculation

The strain gauge wires are connected to the TDS-120 data logger. The strain values for each channel are collected by the machine approximately every 5 seconds. The data logger is connected to a PC with a surface LabVIEW to collect the data and save it as a text file. In this text file, the time of the data logger, the time of the PC and the strain gauges values for each channel are recorded.

In the original data, the collected values were the strain value on the surface of both sides of the specimens. In a bending test, we have the compression strain on the upper side of the samples defined as ε^{-}, and the

tensile strain on the lower side defined as ε^+. Figure 4.5 shows the calculation of strain value at the center of the specimen (ε_c) which is the creep strain, and the hygroscopic strain (ε_{hy}) which is due to swelling or shrinkage. If there is no changing of the moisture content in wood, $-\varepsilon^-$, ε^+ and ε_c would be the same. The hygroscopic strain is uniformed within the specimen, so when there is a change of moisture content, the hygroscopic strain is cumulative with both ε^- and ε^+. In this situation, $\varepsilon^+ = \varepsilon_c + \varepsilon_{hy}$ and $\varepsilon^- = -\varepsilon_c + \varepsilon_{hy}$. By the strain gauges and data logger, we can have $-\varepsilon^-$ and ε^+ directly, so ε_c and ε_{hy} are calculated by equation 4.3 and 4.4 below (Montero, 2011).

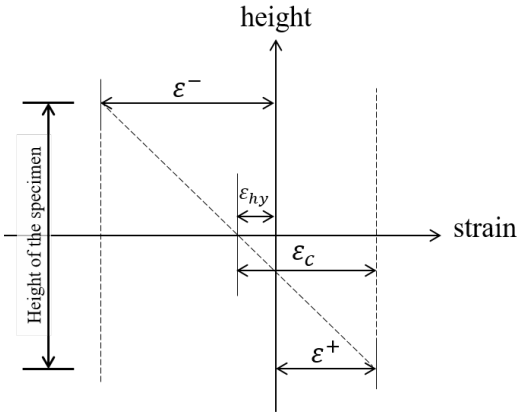

Figure 4.5: Calculation of creep strain and hygroscopic strain (Montero, 2011).

$$\varepsilon_{hy} = \frac{\varepsilon^+ + \varepsilon^-}{2} \tag{4.3}$$

$$\varepsilon_c = \frac{\varepsilon^+ - \varepsilon^-}{2} \tag{4.4}$$

4.1.7 Loading time

We had to decide on the loading time, which had to be short enough to allow for a large number of tests, but long enough to achieve the relevant creep deformation. According to Montero and Gril (2016), the relative creep compliance against the elapsed time is shown in figure 4.6. This result was obtained on spruce with close specimen dimensions, 4-point bending loading conditions, and 25 °C temperature. The viscoelastic creep measurements were made with a duration of 1 week and therefore extrapolated with 3 different predictive models for 50 years magnitude estimation. It shows a turning point of the curves at 10^6 seconds, so ≈ 11.5 days. This means that we can use these measurements to decide on the model and predict further behavior. Therefore, in this study, the creep test was carried out with a nominal duration of 10 days in order to reach the turning point, to have more repetitions of the experimental phases and to take advantage of the calendar weekend.

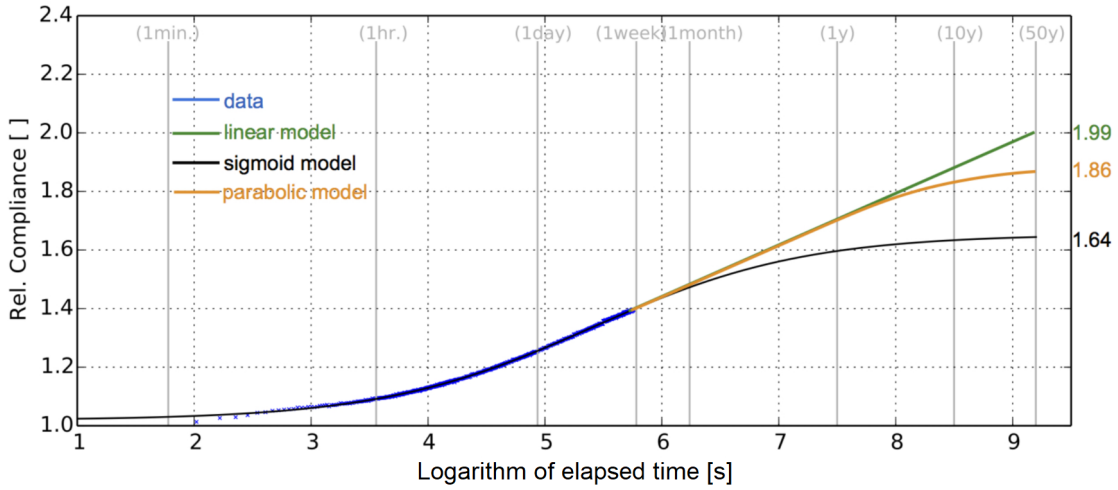

Figure 4.6: Relative compliance of 1 week creep test data at moisture content = 26% and predictive models toward 50 years (Montero and Gril, 2016).

4.2 Creep test result

4.2.1 Initial point value

Since the loading process is not instantaneous, the initial point value has to be defined. Figure 4.7 shows the experimental data of specimen P042 as an example to present the method to calculate the initial time and strain value. In this study, the starting time of the creep curve is defined as the midpoint of the loading process, called t_0. That is, the time value of beginning of loading process plus the time value of end of loading process divided by 2. The strain value at t_0 was calculated by extrapolation, as shown in figure 4.7. The data from the 10^{th} data point, which corresponds to a loading time of about 1 minute, to the 110^{th} data point, which corresponds to a loading time of about 10 minutes, including 100 test data points in sum, were used as extrapolation lines for linear regression calculations. Observing the data curve before loading for 1 minute, there were still some noises and the values were not stable, so we took the data point that was loaded more than 1 minute. To calculate the regression line, it is necessary to include enough data point but less affected by creep behavior, 100 data points were included, and it has been loaded for about 10 minutes. After getting the function of linear regression, which is the red dashed line shown in the figure 4.7, t_0 was substituted into the equation of linear regression, then we can have the ε_0 value. So, the strain value at t_0 was used as ε_0, representing the elastic behavior of the material (red dots in figure 4.7).

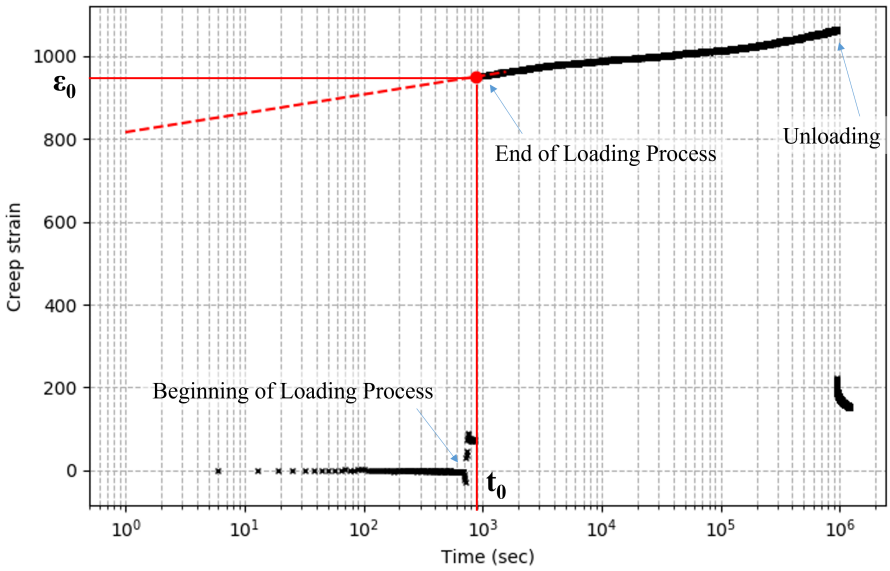

Figure 4.7: Calculating starting point by extrapolation.

4.2.2 Original experimental data

Two types of test are performed:

- 1 species, 1 variable factor (density, specific modulus, or delta Ono), loading for 10 days: it is called for example: poplar test density group.
- 4 species, with close specific modulus (15.5 GPa and 22 GPa) and large variance of density.

The raw creep test data, including creep strain and hygroscopic strain during 10 days of loading, are shown below from figure 4.8 to 4.11. For each figure, both creep strain (ε_c) and hygroscopic strain (ε_{hy}) in $\mu\varepsilon$ are potted against time (second) in logarithmic scale for each species. For the first test of Douglas fir for density group, we had 8 creep boxes. Starting with the poplar test for the density group shown in figure 4.8 (b), we had 10 creep chambers tested simultaneously. The curves of hygroscopic strain show that most of the specimens have a rise period of between 1 hour and 1 day. Even though we adjusted the experimental procedure to try to reduce the humidity variation in the climatic chamber, it was not completely stable. Figure 4.10 (c) shows the drop in hygroscopic strain at day 8, as the machine ran out of water. It causes a jump in creep strain. Figure 4.11 (a) shows that the hygroscopic strain curve of specimen C020 exceeds all other curves, but the reason for this is not clear. This could be caused by an operational error.

In the creep strain results, there are some discontinuous curves, for example in figure 4.8 (d), the creep strain of Oak in density group. Observing all the curves, the discontinuous jumps are always raising and not explained by hygroscopic strain values. Figure 4.12 gives the evaluation of creep test data for each sample: the discontinuous data marked as orange, the valid data marked as green, and the untested specimens marked as white. We had a total of 382 specimens and 137 specimens were tested. The numbers starting from D are Douglas fir specimens, P is poplar specimens, H is beech specimens, and C is oak specimens. Discontinuous test results will not be included in the modeling process. Only valid data marked as green will be considered in the model.

We can see that 32 oak specimens were tested, but 20 specimens had discontinuous curves. Reviewing the size data of the specimens in figure 3.8 (e) and (f), the oak specimens are thinner than the other specimens. Figure 4.13 shows the distribution of specimen sizes with the discontinuity of the data. The blue part in the figures is the sample with normal creep curve, and the orange part is the sample with discontinuous data. The length is a constant value in the 4–point bending, determined by the creep box. In these figures, width, thickness, density, modulus of elasticity, specific modulus and delta Ono at RH=85% are considered. As we can see in figure 4.13(b), the specimens with discontinuous data are more numerous for thickness below 1.6 mm. The other factors do not show a clear trend. Therefore, this is an effect caused by the processing of the specimens and needs more attention, especially thickness.

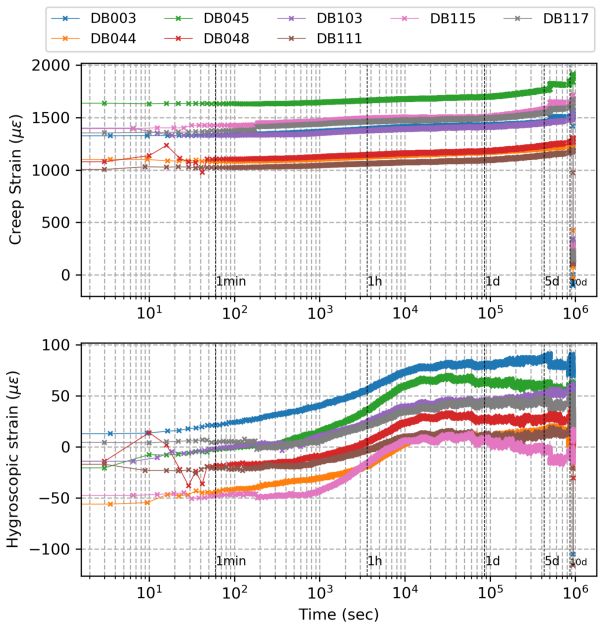

(a) Douglas fir

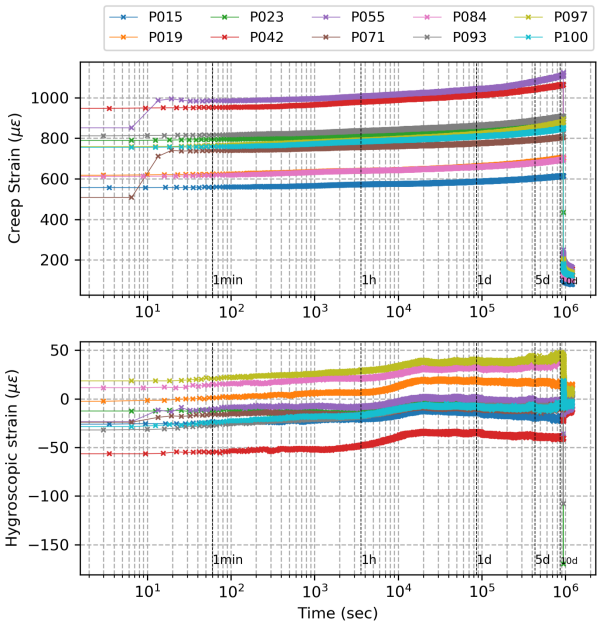

(b) Poplar

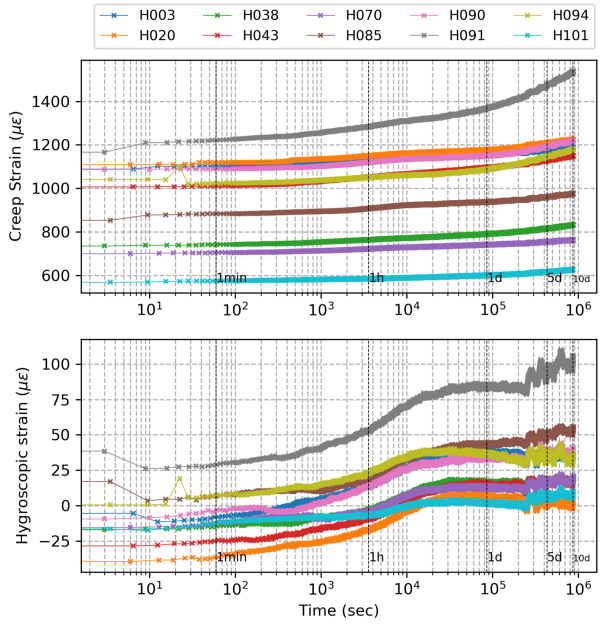

(c) Beech

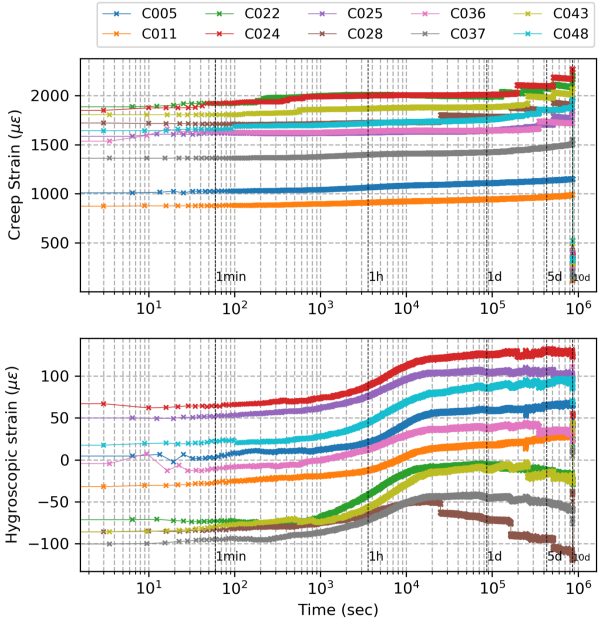

(d) Oak

Figure 4.8: Creep test results, separated into creep strain (ε_c, $\mu\varepsilon$) and hygroscopic strain (ε_{hy}, $\mu\varepsilon$) of density group for each species.

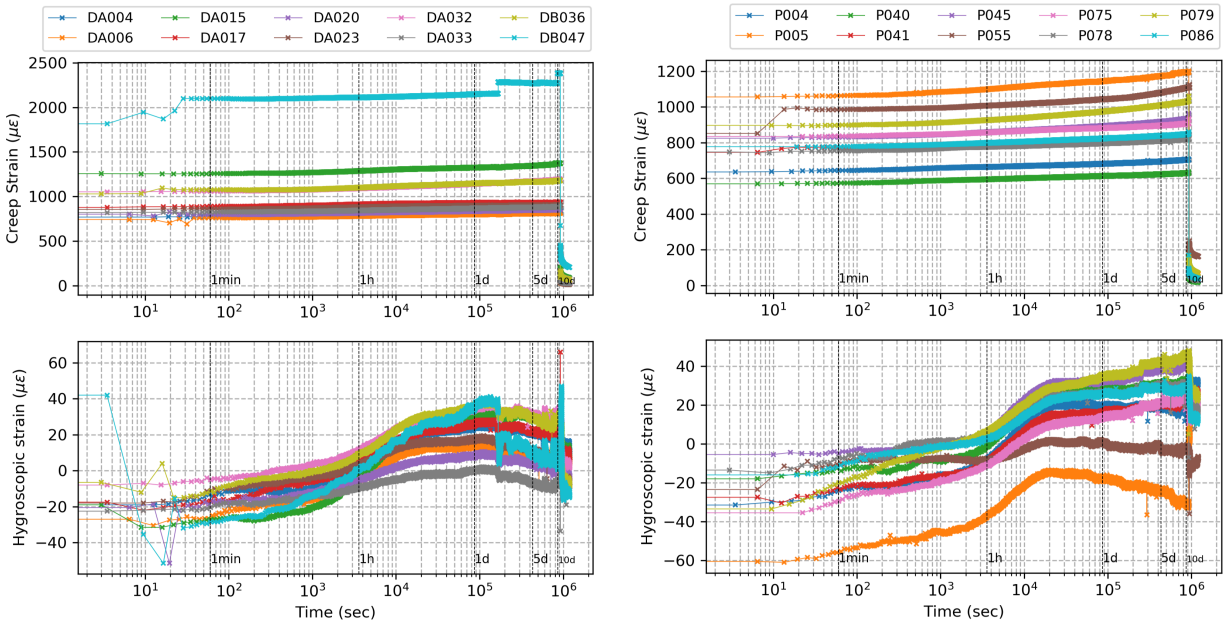

(a) Douglas fir

(b) Poplar

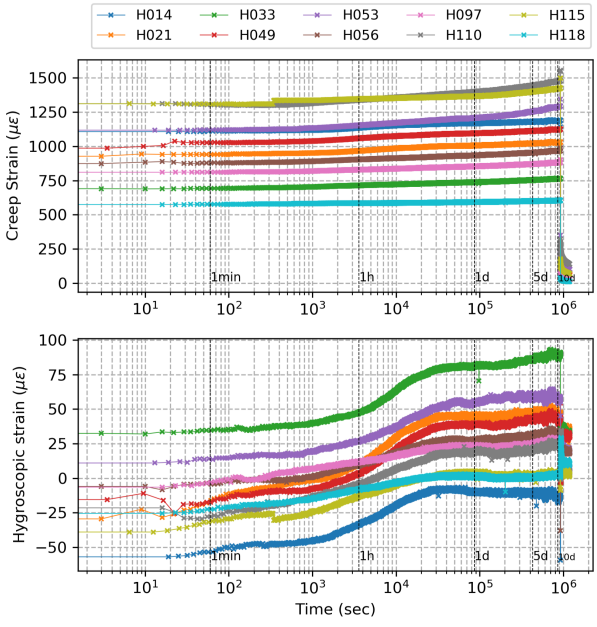

(c) Beech

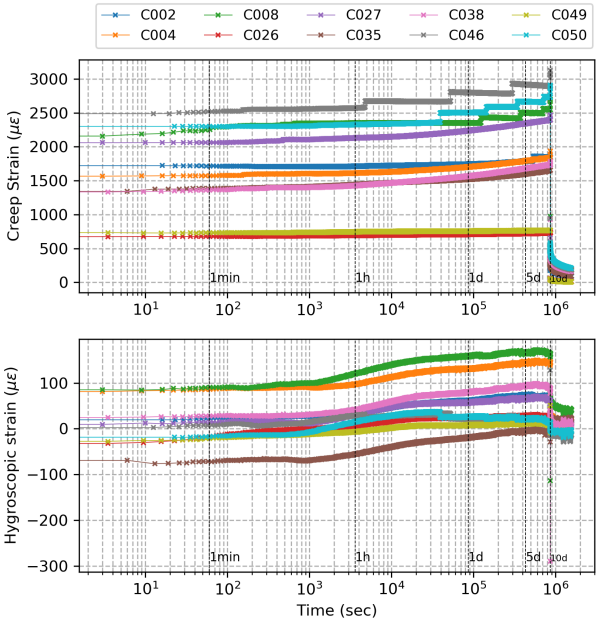

(d) Oak

Figure 4.9: Creep test results, separated into creep strain (ε_c, $\mu\varepsilon$) and hygroscopic strain (ε_{hy}, $\mu\varepsilon$) of specific modulus group for each species.

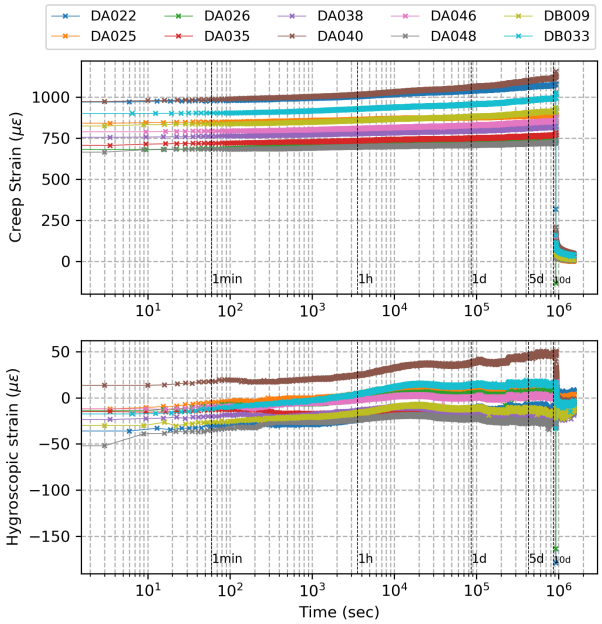

(a) Douglas fir

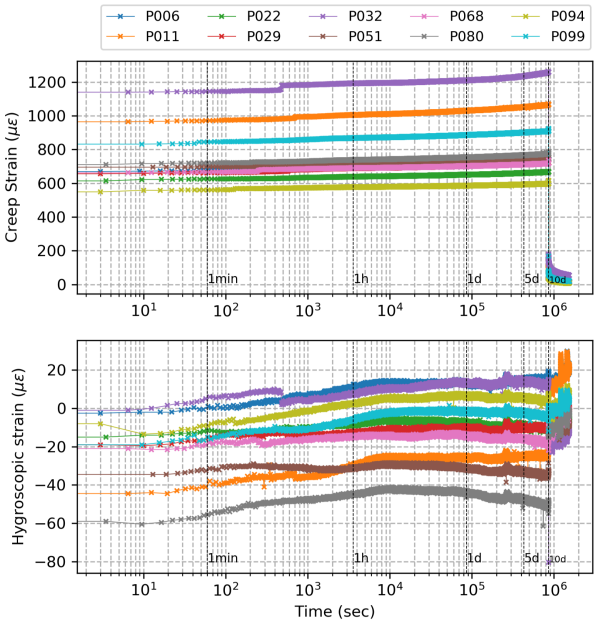

(b) Poplar

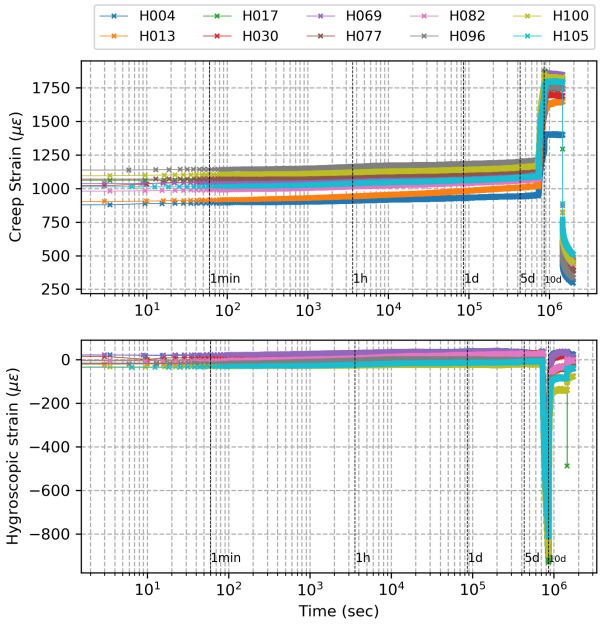

(c) Beech

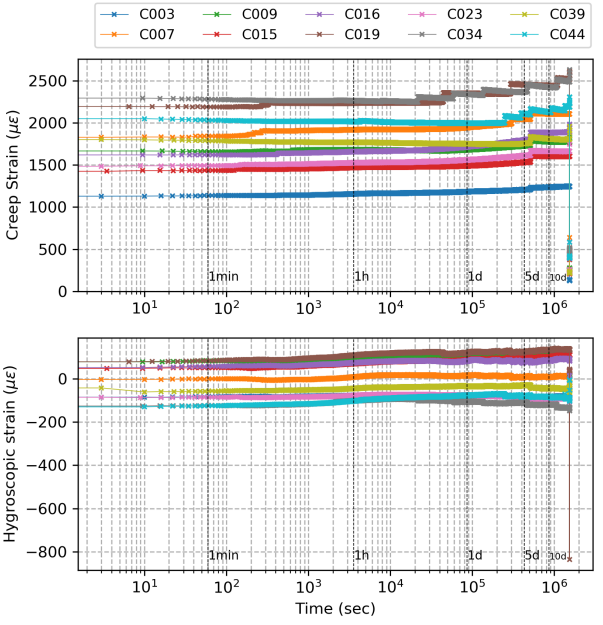

(d) Oak

Figure 4.10: Creep test results, separated into creep strain (ε_c, $\mu\varepsilon$) and hygroscopic strain (ε_{hy}, $\mu\varepsilon$) of delta Ono group for each species.

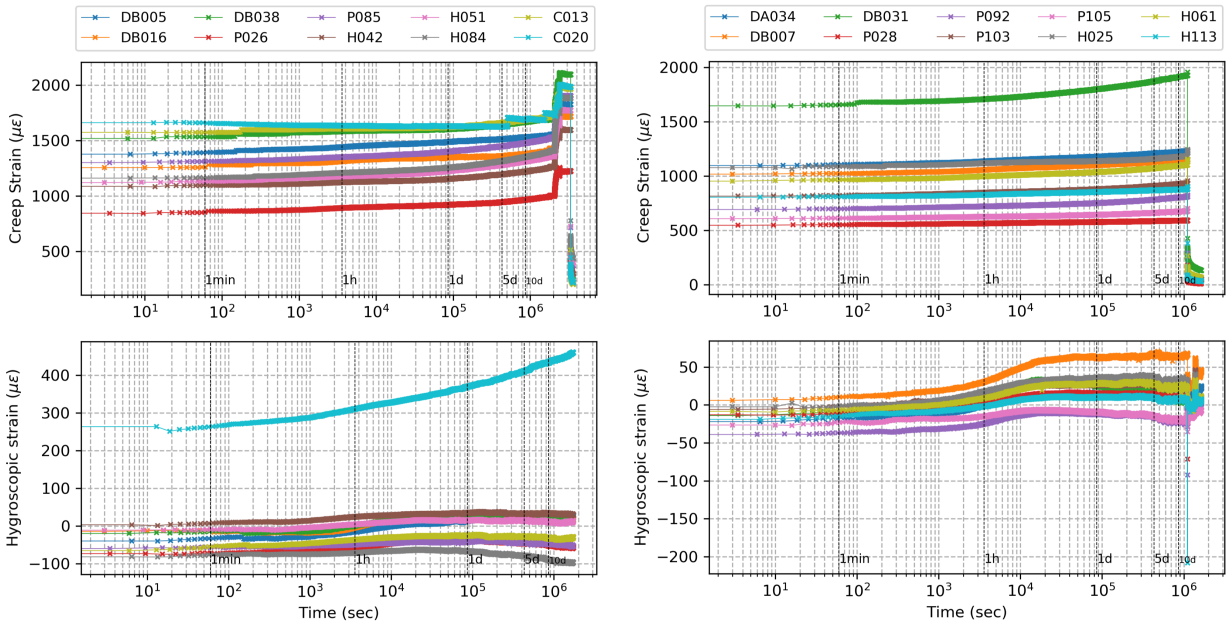

(a) Specific modulus = 15.5

(b) Specific modulus = 22

Figure 4.11: Creep test result of the group with close specific modulus, mix species.

DA001	DA026	DB001	DB026	DB101	P001	P026	P051	P076	P101	H003	H032	H061	H087	H112	C002	C027
DA002	DA027	DB002	DB027	DB102	P002	P027	P052	P077	P102	H004	H033	H062	H088	H113	C003	C028
DA003	DA028	DB003	DB028	DB103	P003	P028	P053	P078	P103	H005	H034	H063	H089	H114	C004	C029
DA004	DA029	DB004	DB029	DB104	P004	P029	P054	P079	P104	H006	H035	H064	H090	H115	C005	C030
DA005	DA030	DB005	DB030	DB105	P005	P030	P055	P080	P105	H007	H037	H065	H091	H116	C006	C031
DA006	DA031	DB006	DB031	DB106	P006	P031	P056	P081		H008	H038	H066	H092	H117	C007	C032
DA007	DA032	DB007	DB032	DB107	P007	P032	P057	P082		H010	H039	H067	H093	H118	C008	C033
DA008	DA033	DB008	DB033	DB108	P008	P033	P058	P083		H011	H040	H068	H094	H119	C009	C034
DA009	DA034	DB009	DB034	DB110	P009	P034	P059	P084		H013	H041	H069	H095	H120	C010	C035
DA010	DA035	DB010	DB035	DB111	P010	P035	P060	P085		H014	H042	H070	H096		C011	C036
DA011	DA036	DB011	DB036	DB112	P011	P036	P061	P086		H015	H043	H071	H097		C012	C037
DA012	DA037	DB012	DB037	DB113	P012	P037	P062	P087		H017	H045	H073	H098		C013	C038
DA013	DA038	DB013	DB038	DB114	P013	P038	P063	P088		H018	H046	H074	H099		C014	C039
DA014	DA039	DB014	DB039	DB115	P014	P039	P064	P089		H020	H047	H075	H100		C015	C040
DA015	DA040	DB015	DB040	DB116	P015	P040	P065	P090		H021	H048	H076	H101		C016	C041
DA016	DA041	DB016	DB041	DB117	P016	P041	P066	P091		H022	H049	H077	H102		C017	C042
DA017	DA042	DB017	DB042	DB118	P017	P042	P067	P092		H023	H050	H078	H103		C018	C043
DA018	DA043	DB018	DB043	DB119	P018	P043	P068	P093		H024	H051	H079	H104		C019	C044
DA019	DA044	DB019	DB044	DB120	P019	P044	P069	P094		H025	H052	H080	H105		C020	C045
DA020	DA045	DB020	DB045		P020	P045	P070	P095		H026	H053	H081	H106		C021	C046
DA021	DA046	DB021	DB046		P021	P046	P071	P096		H027	H055	H082	H107		C022	C047
DA022	DA047	DB022	DB047		P022	P047	P072	P097		H028	H056	H083	H108		C023	C048
DA023	DA048	DB023	DB048		P023	P048	P073	P098		H029	H058	H084	H109		C024	C049
DA024	DA049	DB024	DB049		P024	P049	P074	P099		H030	H059	H085	H110		C025	C050
DA025	DA050	DB025	DB050		P025	P050	P075	P100		H031	H060	H086	H111		C026	

Figure 4.12: Sample condition after creep tests. Green: valid data; Orange: discontinuous data; White: untested specimens

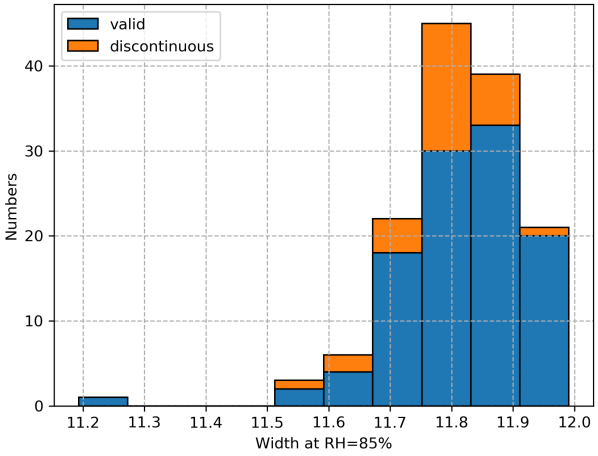

(a)

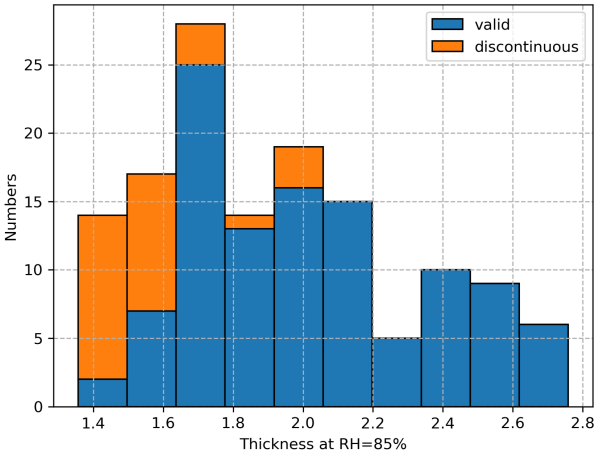

(b)

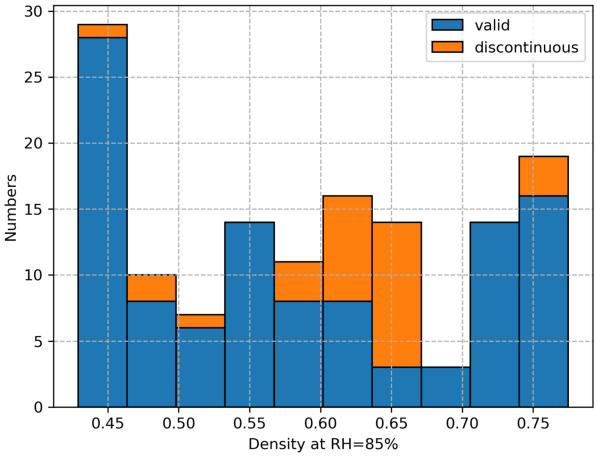

(c)

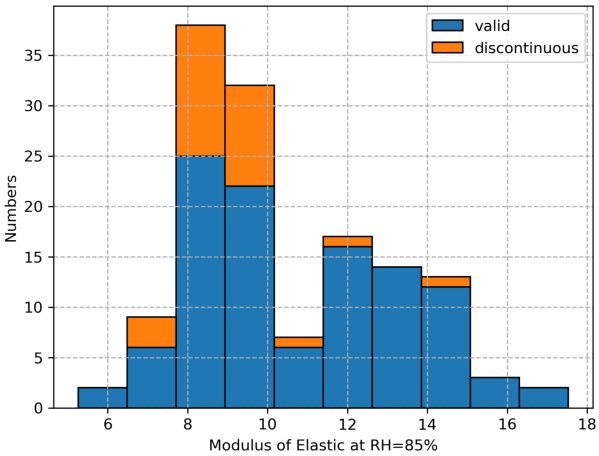

(d)

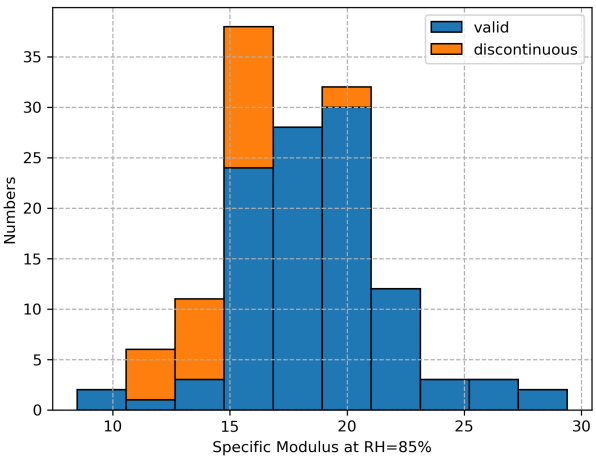

(e)

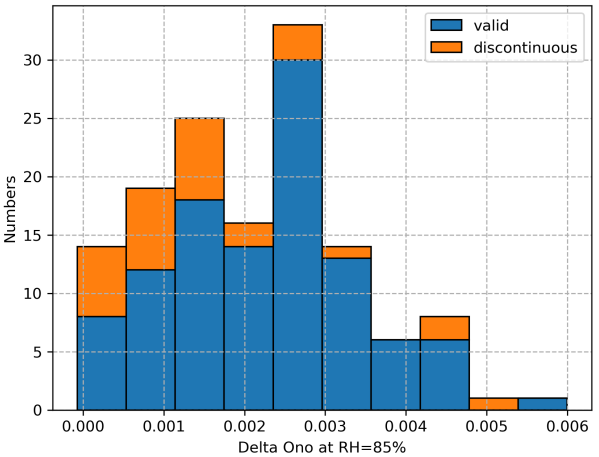

(f)

Figure 4.13: Distribution of the specimens with discontinuous data

4.2.3 Creep compliance

Creep strain (ε_c) is calculated by equation 4.4, and then compliance is calculated from creep strain by equation 4.1 and 4.2, and plotted against time (seconds in logarithmic scale) in figure 4.14 to 4.17. Since the shape of the specimen is somewhat different, calculations of compliance will help to reduce the effect of cross-section and the variation in stress.

Figure 4.14 shows the total compliance for group density and for each species. We selected specimens with different densities and other similar characteristics for testing. All curves were grouped by species, except for a few extreme values that may have been caused by human error. Figure 4.17 shows the two "individual" tests, where the specimens were chosen with close modulus specific and large variance of density, it also shows the similar tendency as previously. This trend presents that the density is highly correlate to species.

Figure 4.15 shows the total creep compliance result of the specific modulus group. In these 4 tests, the samples have a large variance in specific modulus and the variance of other factors is minimized. The curves are more spread out within the same species. However, the variance between species is not present. It symbolizes that the specific modulus, which is highly correlated with the MFA, has a stronger variance within the species and is less correlated with the species.

Figure 4.16 shows the results for specimens with different delta Ono values and minimized the variance of other factors. Delta Ono coefficients indicate the extractive content of the specimens, but the species used in this study had very little extractive material to show differences.

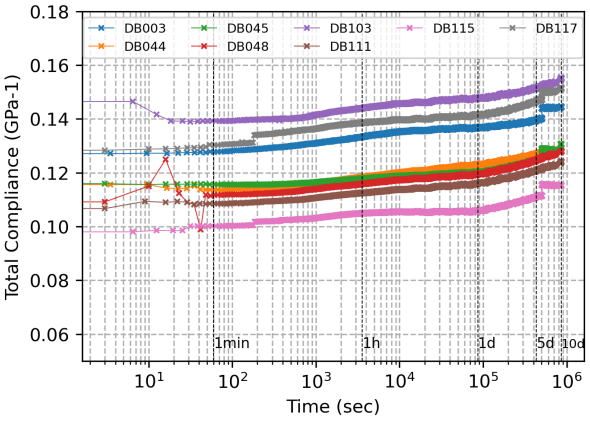

(a) Douglas fir

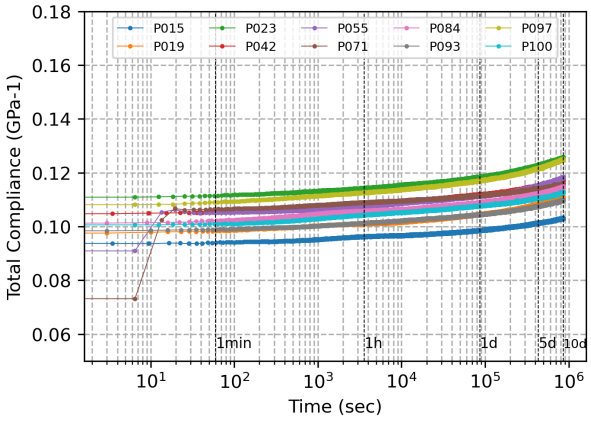

(b) Poplar

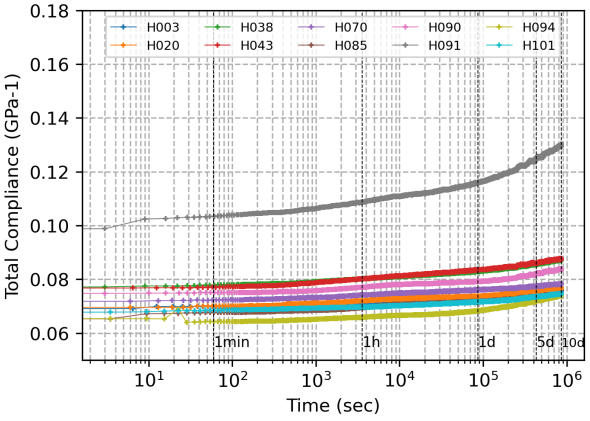

(c) Beech

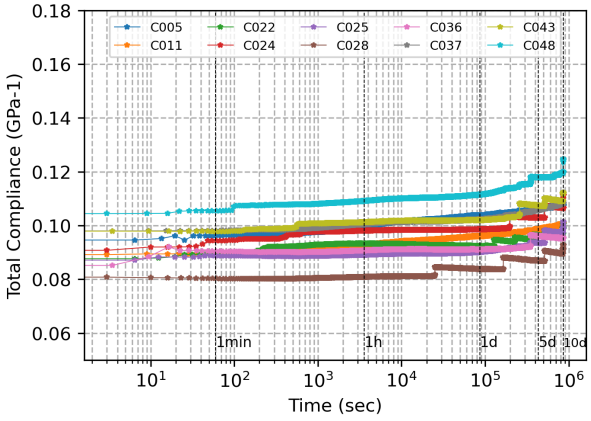

(d) Oak

Figure 4.14: Creep compliance (GPa) against time (sec) of density group for each species.

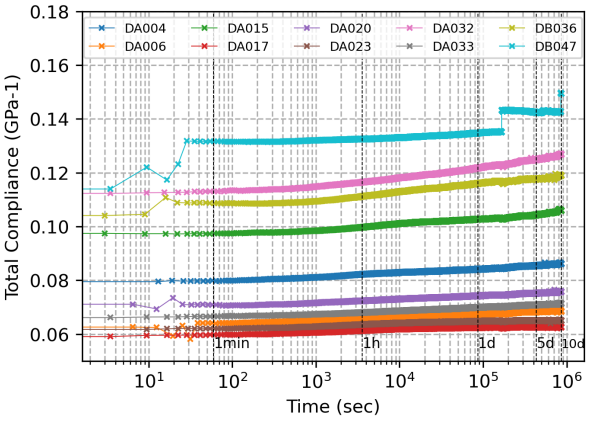

(a) Douglas fir

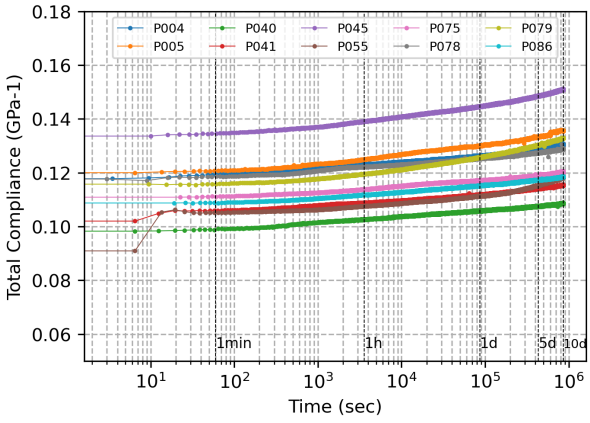

(b) Poplar

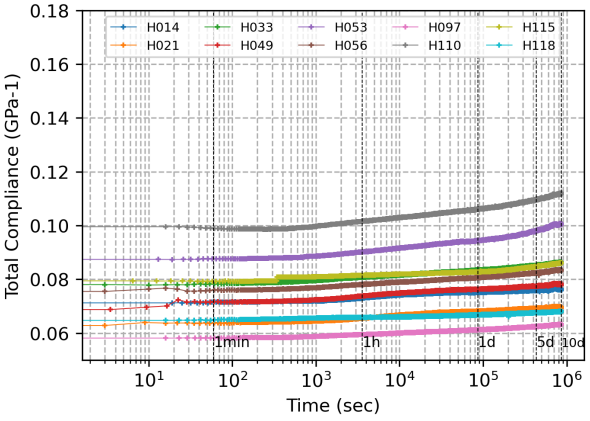

(c) Beech

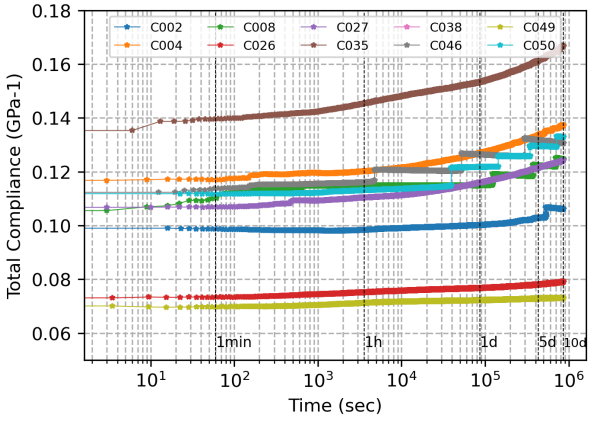

(d) Oak

Figure 4.15: Creep compliance (GPa) against time (sec) of specific modulus group for each species.

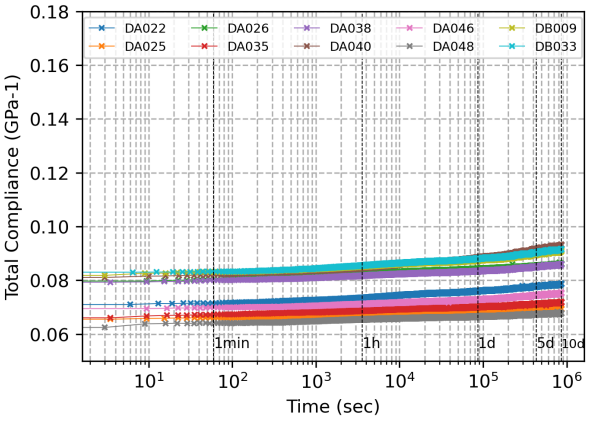

(a) Douglas fir

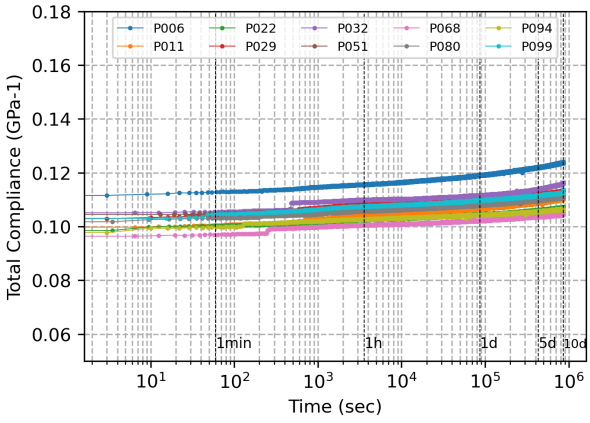

(b) Poplar

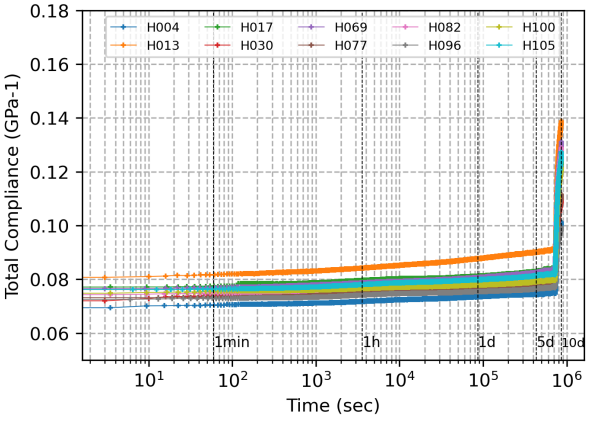

(c) Beech

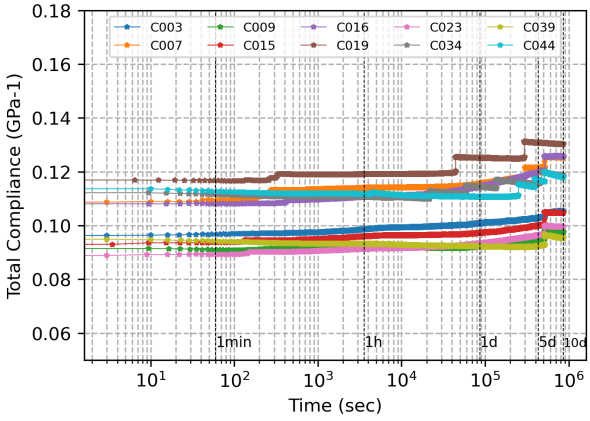

(d) Oak

Figure 4.16: Creep compliance (GPa) against time (sec) of delta Ono group for each species.

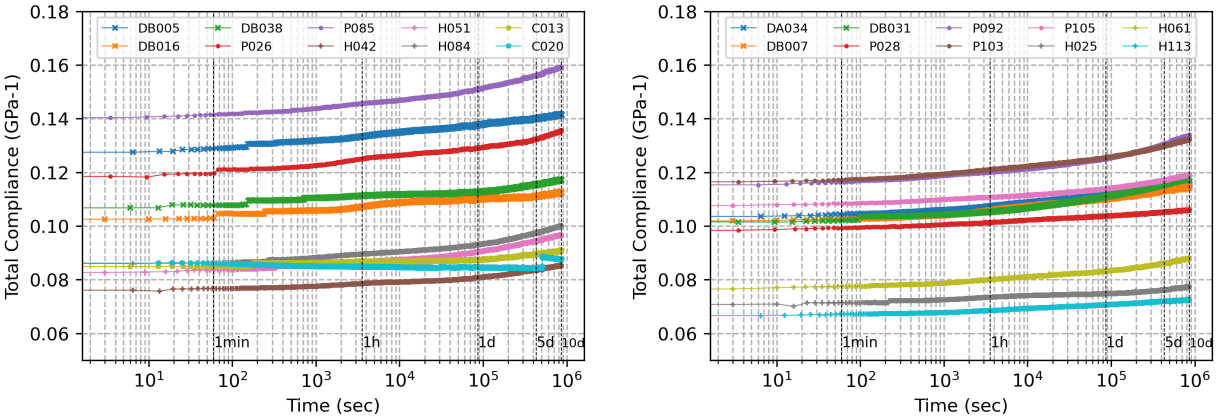

(a) Specific modulus = 15.5

(b) Specific modulus = 22

Figure 4.17: Creep compliance of the group with close specific modulus

4.3 Data Analysis

4.3.1 Elastic behavior

Elastic properties, usually in the form of modulus of elasticity in bending tests, can be calculated from creep curves initial strain value ε_0 and stress. ε_0 is calculated by extrapolation, which has been mentioned in section 4.2.1, and can be considered as elastic strain of 4–point bending test. Therefore, we can take the compliance value calculated from ε_0 as the initial compliance J_0. Figure 4.18 shows the relationship between the reciprocal of initial compliance J_0 and the dynamic Young's modulus E' from vibration test. There is a good proportional relationship between these two factors. It shows a high coefficient of correlation (R^2) which is closed to 1. With this result, we can be sure that the experiments of vibration test and 4–point bending tests are reliable.

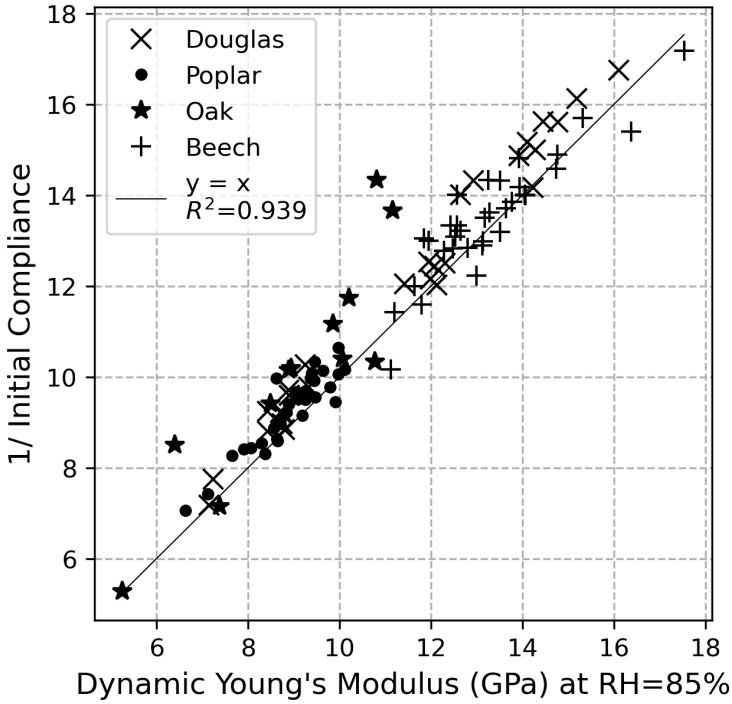

Figure 4.18: Relationship between dynamic Young's modulus and initial compliance (J_0)

4.3.2 Observation of creep compliance against the predictors

In order to understand the creep behavior against time, seven time points were selected, including t_0, the 1^{st} minute (t_{1m}), the 1^{st} hour (t_{1h}), the 1^{st} day (t_{1d}), the 5^{th} day (t_{5d}), the 7^{th} day (t_{7d}), and the 10^{th} day (t_{10d}). Compliance for each time is extracted against each factor to analyze the correlation with density, modulus of elasticity, specific modulus, and delta Ono value. Taking figure 4.19 (a) as an example, the J_0 values are the initial compliance, i.e. the compliance at the time t_0. They are collected from each of the test result curves shown in figure 4.14 to 4.17. The compliance values at t_0 are extracted and plotted against the density of the specimen to see the effect of density on the creep behavior at t_0. Similarly, the compliance at different time points is extracted and plotted against the potential predictors. The data are fitted by linear regression on double logarithms diagram with confidence region and prediction band. 95% confidence region presents the range of linear regression slope in the 95 percent confidence range. 95% prediction band represents that 95% of the

The figure 4.19 shows the correlation between density and compliance at different time points in double logarithm plot. The overall relationship is linear, with a decrease in absolute value of slope and coefficient of determination (R^2). Figure 4.20 shows the relationship between E' which is measured by vibration test and compliance at different time points in double logarithm plot. In this case, as in figure 4.20 (a), the compliance is the reciprocal of the dynamic Young's modulus. The graph shows a strong linear relationship. There are some extreme values may cause by the experimental error. However, they still present a linear correlation with R^2 close to 1. Comparing the absolute value of slope in figure 4.20, it increases with time. In figure 4.20 (a) and (b) plots the initial compliance and the compliance at the 1^{st} minute against dynamic Young's modulus, the absolute values of slope are about 0.945. These two figures present the elastic (and approximately elastic) behavior parts. Figures 4.20 (c) to (f) show the relationship between the compliance value which have been loaded for a period of time and dynamic Young's modulus. Because the compliance values increase during the creep experimental process, the absolute values of slope increase, but it still has a strong proportional relationship. However, this phenomenon is not significant. This means that the elastic behavior part accounts for a high percentage of the compliance in the 10–day creep test results, so it is necessary to separate these two different behaviors in the modeling. Figure 4.21 shows the relationship between specific modulus and compliance. Since the specific modulus has a strong relationship with grain angle and microfibril angle, it can be considered as a characteristic of the fiber. We can see that there is a negative trend between specific modulus and compliance at all–time points, and the absolute value of slope increases with time. Delta Ono is an indicator of extractive content in wood. Figure 4.22 shows the correlation between compliance and delta Ono values. In this study, we were not able to find a direct relationship between these two factors. Therefore, it is presumed that the delta Ono value does not influence the time–dependent behavior in this study.

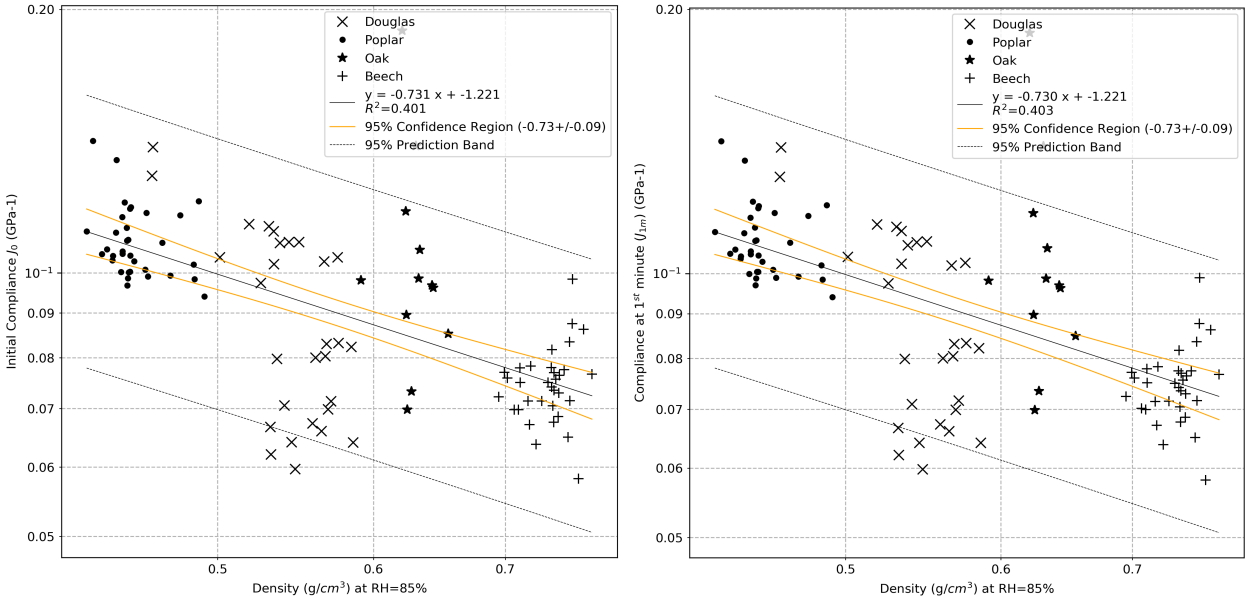

(a) J_0

(b) J_{1m}

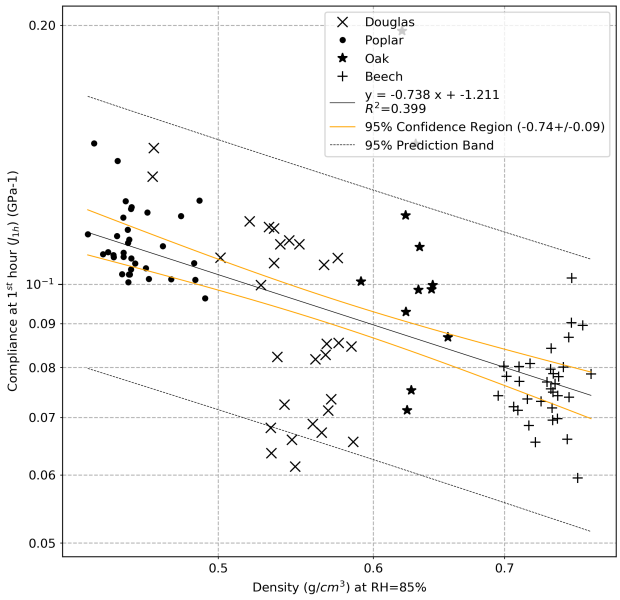

(c) J_{1h}

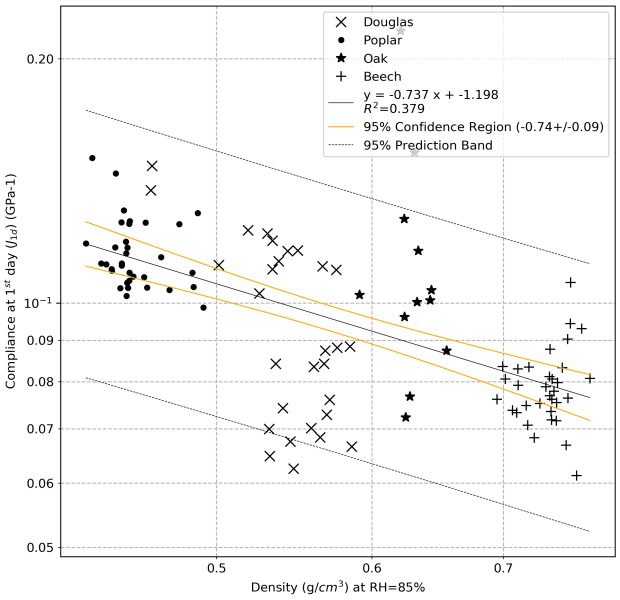

(d) J_{1d}

Figure 4.19: Correlation between density at RH=85% and compliance. (a) initial compliance J_0. (b) compliance at 1^{st} minute J_{1m}. (c) compliance at 1^{st} hour J_{1h}. (d) compliance at 1^{st} day J_{1d}.

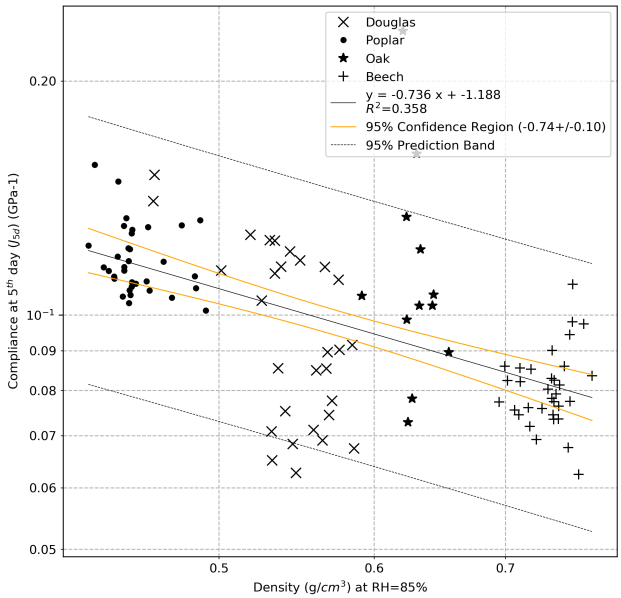

(e) J_{5d}

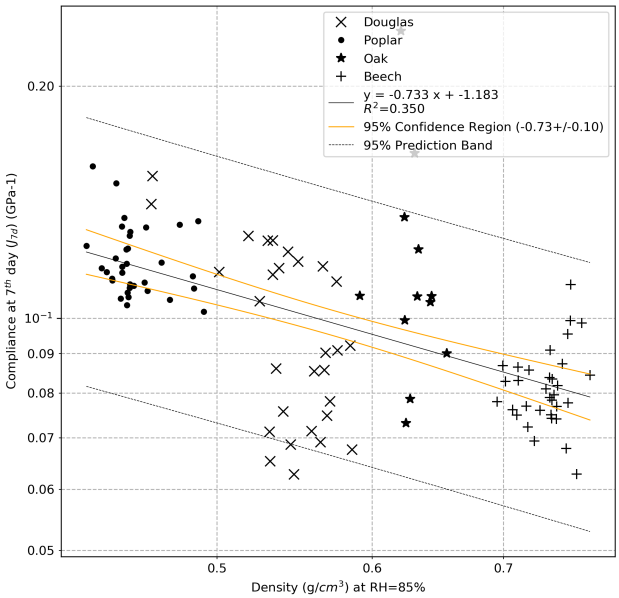

(f) J_{7d}

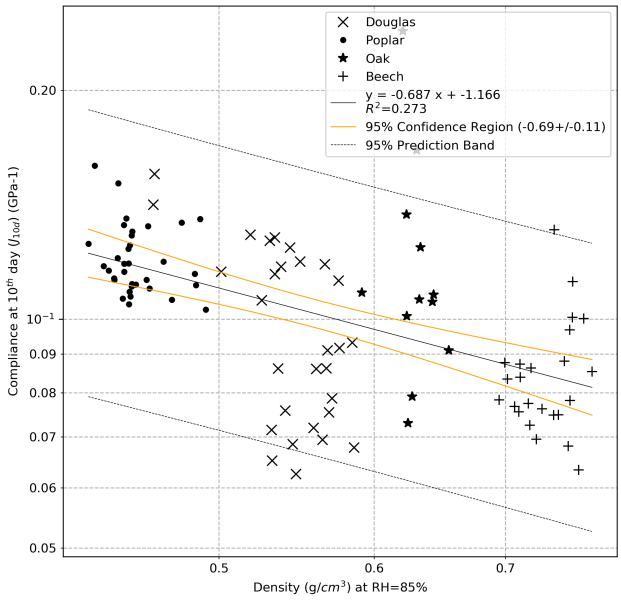

(g) J_{10d}

Figure 4.19: Correlation between density and compliance (continued). (e) compliance at 5^{th} day J_{5d}. (f) compliance at 7^{th} day J_{7d}. (g) compliance at 10^{th} day J_{10d}.

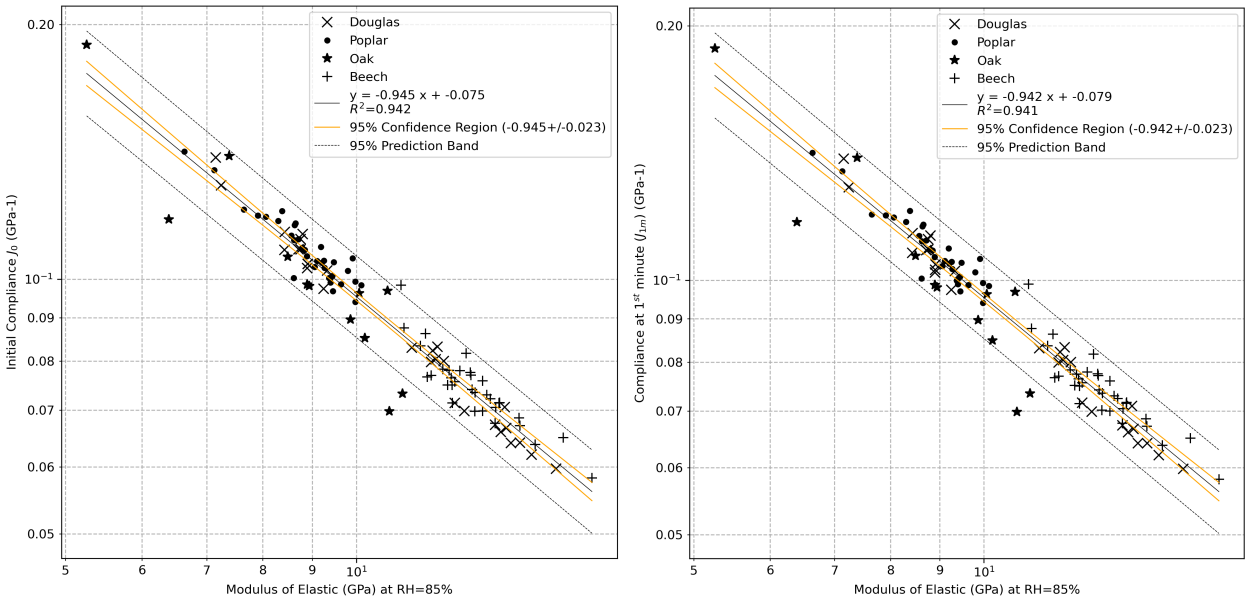

(a) J_0

(b) J_{1m}

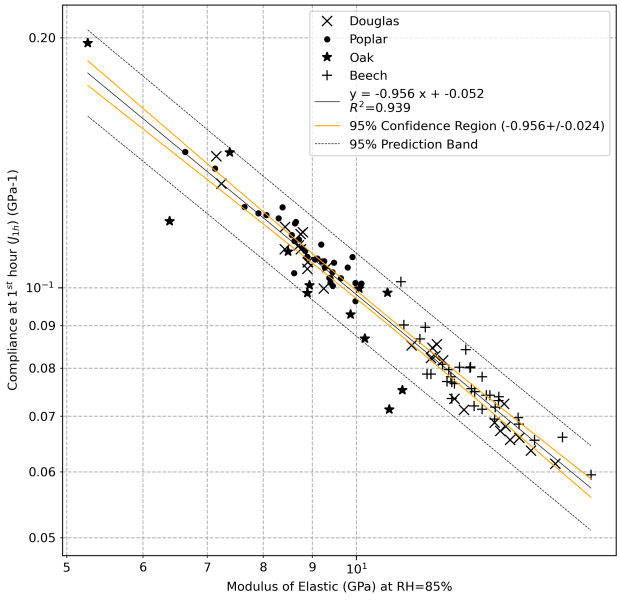

(c) J_{1h}

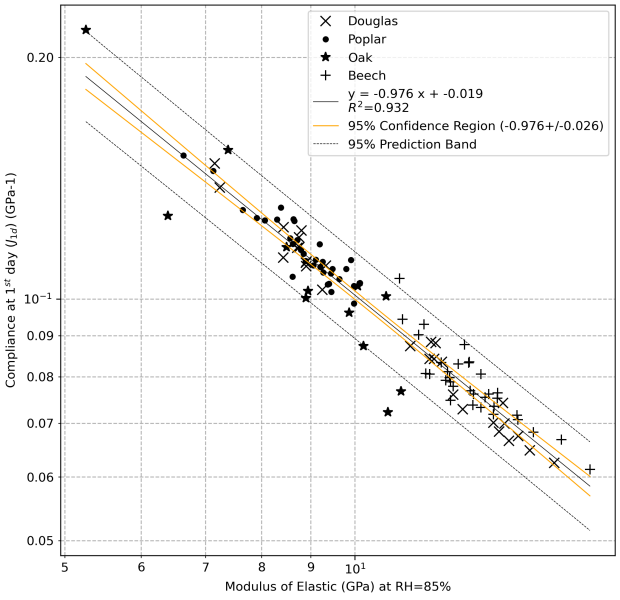

(d) J_{1d}

Figure 4.20: Correlation between dynamic Young's modulus and compliance. (a) initial compliance J_0. (b) compliance at 1^{st} minute J_{1m}. (c) compliance at 1^{st} hour J_{1h}. (d) compliance at 1^{st} day J_{1d}.

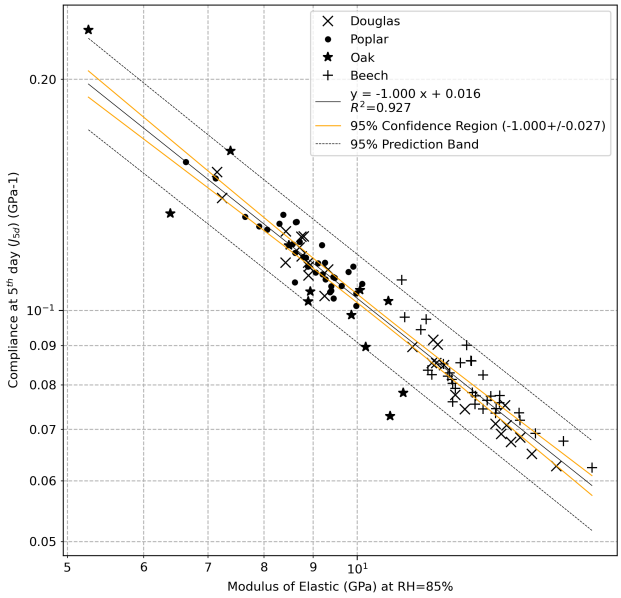

(e) J_{5d}

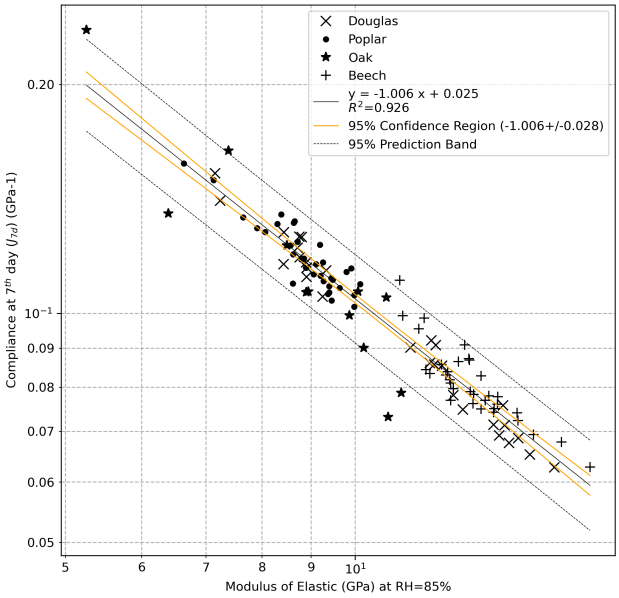

(f) J_{7d}

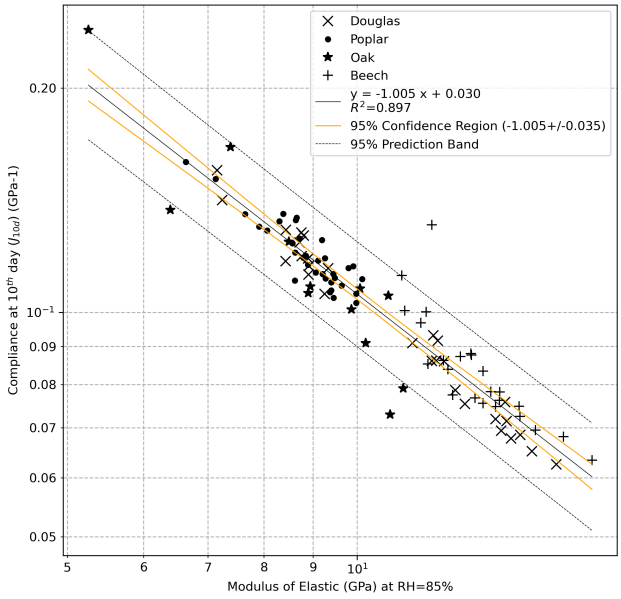

(g) J_{10d}

Figure 4.20: Correlation between dynamic Young's modulus and compliance (continued). (e) compliance at 5^{th} day J_{5d}. (f) compliance at 7^{th} day J_{7d}. (g) compliance at 10^{th} day J_{10d}.

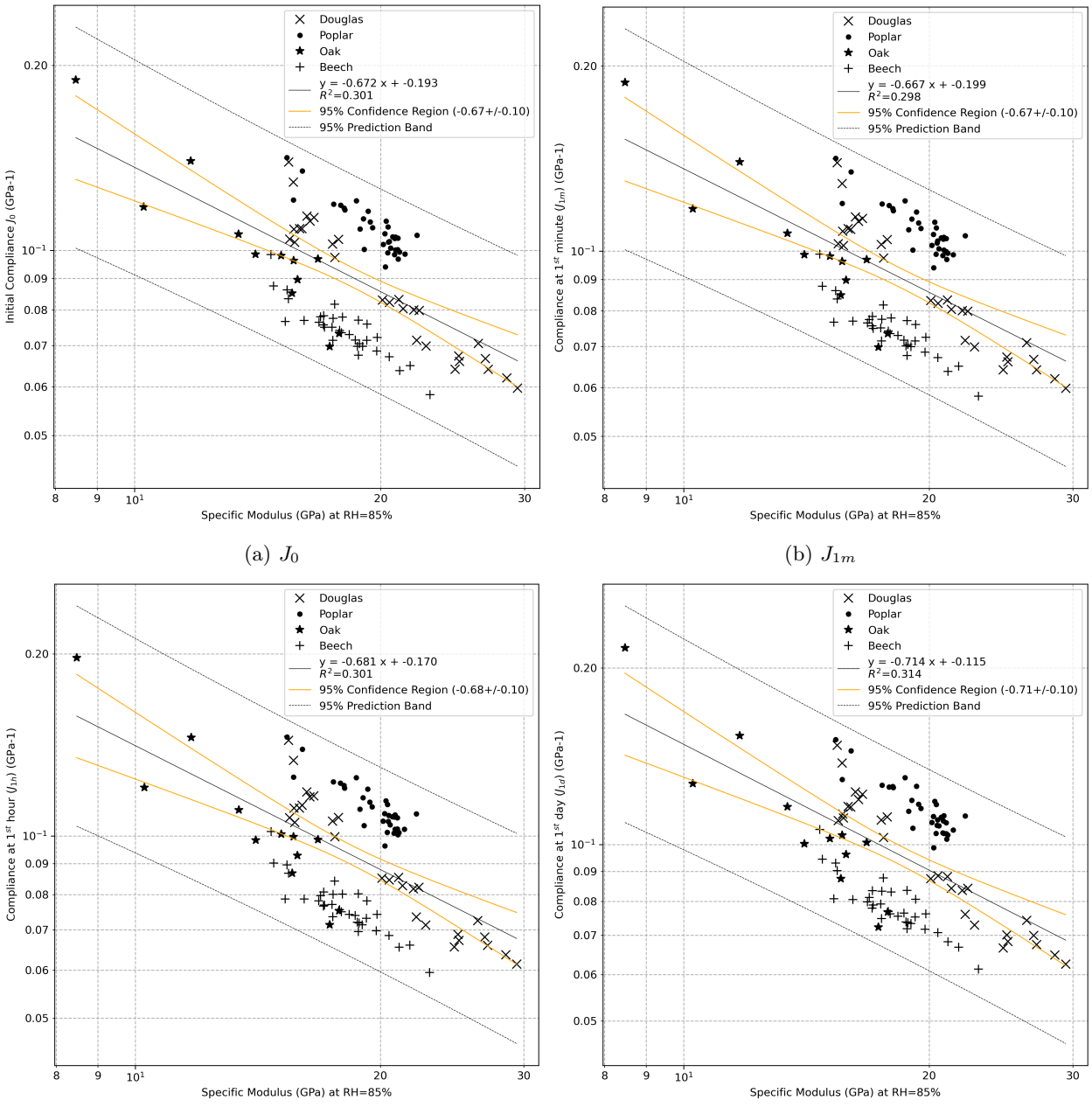

(a) J_0 (b) J_{1m}

(c) J_{1h} (d) J_{1d}

Figure 4.21: Correlation between specific modulus and compliance. (a) initial compliance J_0. (b) compliance at 1^{st} minute J_{1m}. (c) compliance at 1^{st} hour J_{1h}. (d) compliance at 1^{st} day J_{1d}.

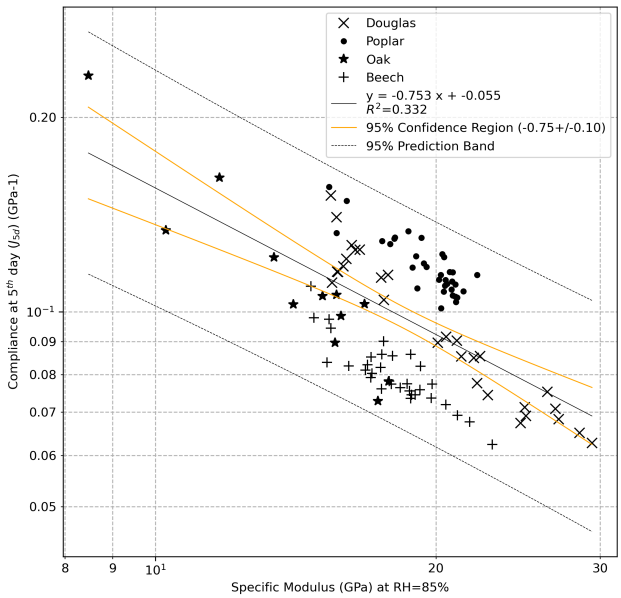

(e) J_{5d}

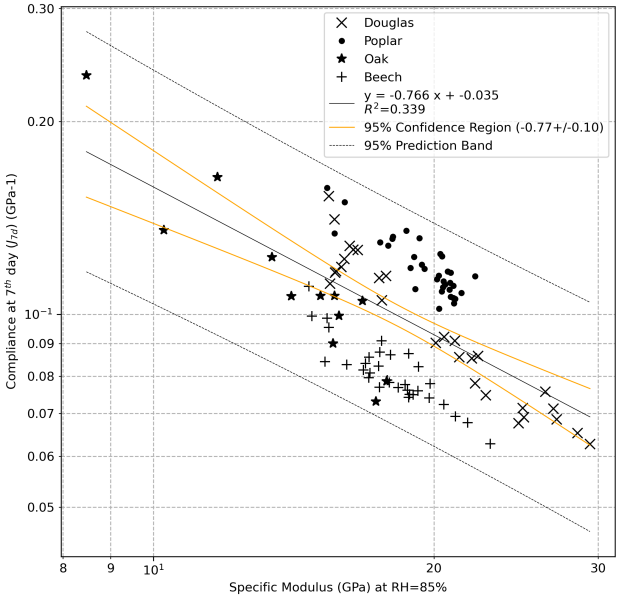

(f) J_{7d}

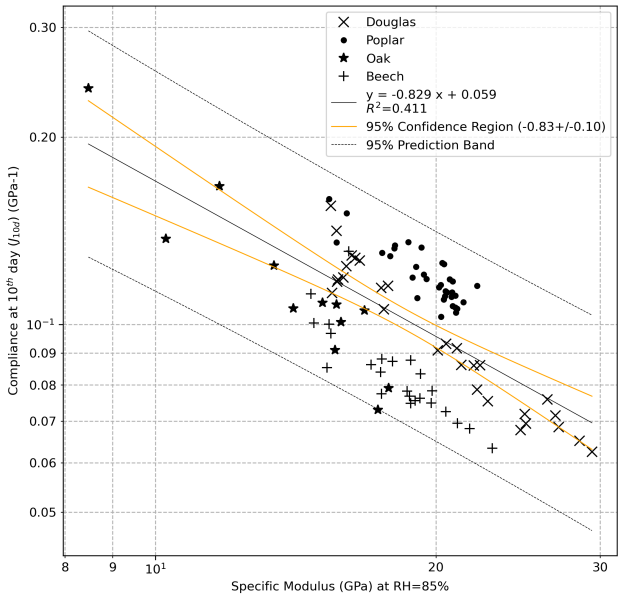

(g) J_{10d}

Figure 4.21: Correlation between specific modulus and compliance (continued). (e) compliance at 5^{th} day J_{5d}. (f) compliance at 7^{th} day J_{7d}. (g) compliance at 10^{th} day J_{10d}.

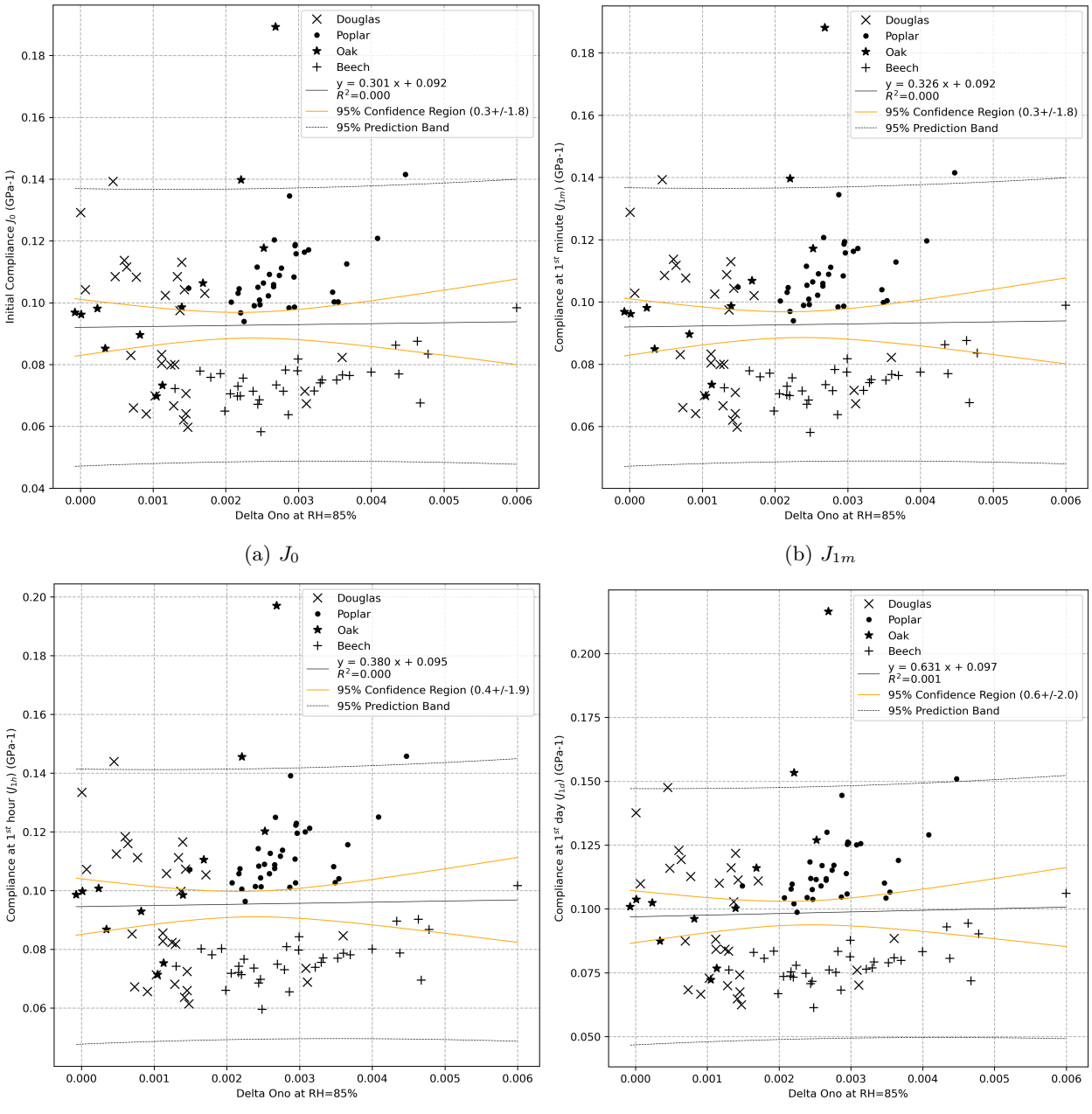

(a) J_0 (b) J_{1m}

(c) J_{1h} (d) J_{1d}

Figure 4.22: Correlation between delta Ono value and compliance. (a) initial compliance J_0. (b) compliance at 1^{st} minute J_{1m}. (c) compliance at 1^{st} hour J_{1h}. (d) compliance at 1^{st} day J_{1d}.

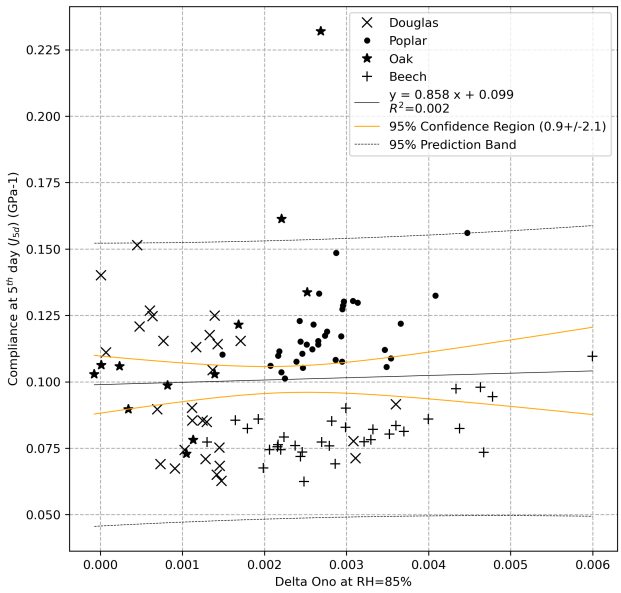

(e) J_{5d}

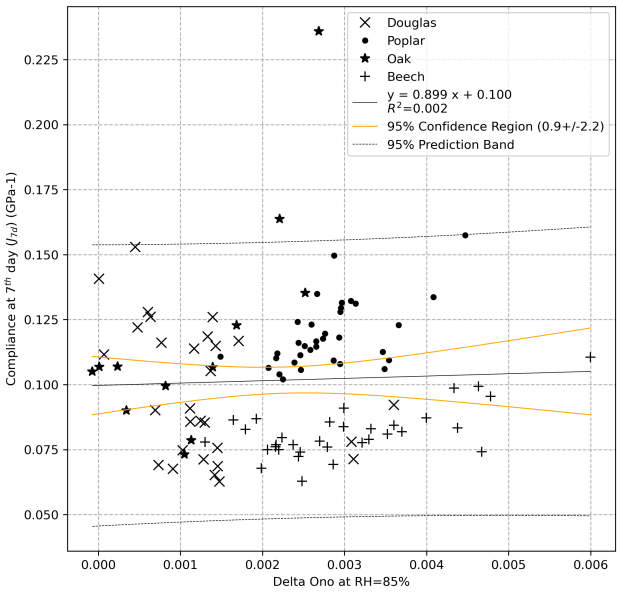

(f) J_{7d}

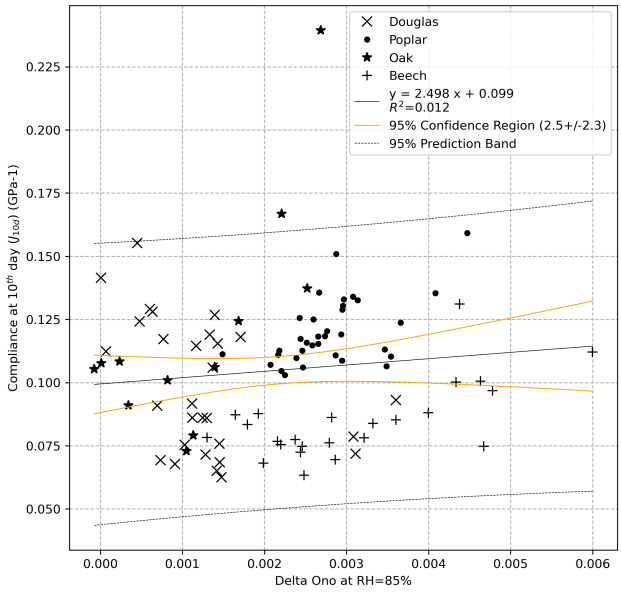

(g) J_{10d}

Figure 4.22: Correlation between delta Ono value and compliance (continued). (e) compliance at 5^{th} day J_{5d}. (f) compliance at 7^{th} day J_{7d}. (g) compliance at 10^{th} day J_{10d}.

4.4 Summary

One issue to consider in the creep test results of this study is the size of the specimen. Wood is a very stiff material. To achieve stress levels, the load applied to the specimen is greater than the weight of the specimen. When testing small specimens, there will be more noise. However, thin specimens are more affected by noise, so there will be some discontinuities in the data.

Some difference between the potential predictors can be found from the curves after calculating the test results in conformity. The result of density group shows that this parameter is affected by the species. On the other hand, the result of the specific modulus group shows the variability within the species. However, there is no clear trend in the Delta Ono group.

Comparing the two types of elastic data obtained from the vibration test and the static test, the dynamic elastic modulus is highly correlated with the reciprocal of the initial compliance. Therefore, the results of the vibration test and the static test are reliable.

To identify the potential predictors, several time points were extracted and plotted against the predictor. There were 4 factors (density, specific modulus, modulus of elastic and Delta Ono) that were discussed and compared. The result shows that the density effect is between species and the specific modulus effect is within species. Modulus of elastic is highly correlated with initial compliance. It also shows that the elastic behavior takes a high proportion of the compliance value. It is necessary to saprate and extract the time dependent part. The Delta Ono value has no clear trend in this study. As a result, density and specific modulus are selected as predictors, and delayed compliance calculation is required to extract the creep behavior.

Chapter 5

Modeling

5.1 General model of creep behavior

The mechanical behavior of materials can usually be divided into elastic and viscous behavior. Most materials exhibit these two behaviors in different proportions, and their behavior can be simulated with rheological models based on springs and dashpots. Hooke's spring is a symbol of purely elastic behavior: the deformation (strain,ε) is proportional to the stress and remains constant when a constant load is applied (figure 5.1 a). E is the elastic coefficient of spring. It can be represented as $\sigma = E \times \varepsilon$. On the other hand, Newtonian dashpot presents the purely viscous behavior as figure 5.1 (b). In that case, the stress is proportional to the derivative of the strain against time. For a constant loading, deformation increases linearly with time. The dashpot is characterized by a viscosity. The relationship can be present as $\sigma = \mu \times \ d\varepsilon/dt$. The deformation on the dashpot is unrecoverable, so the deformation value stays constant after unloading.

(a) Hooke's spring (b) Newtonian dashpot

Figure 5.1: Spring and dashpot elements (Bodig and Jayne, 1982).

There are 2 basic combinations to represent viscoelastic behavior (figure 5.2). A spring and a dashpot connected in series is a Maxwell body, and the another one with two elements connected in parallel is a Kelvin body.

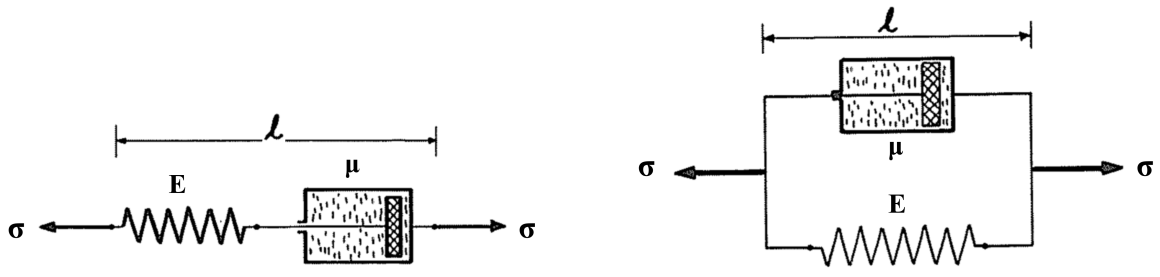

(a) Maxwell body (b) Kelvin body

Figure 5.2: The two basic combinations representing viscoelastic behavior (Bodig and Jayne, 1982).

In the Maxwell's body, the spring and the dashpot are subjected to the same stress (σ). That is, the stress on the spring (σ_S) and the stress on the dashpot (σ_D) are both equal to the stress on the system ($\sigma = \sigma_S = \sigma_D$). The total strain is the sum of the two parts ($\varepsilon = \varepsilon_S + \varepsilon_D$). The spring reacts immediately, then the deformation of dashpot performs with time. After unloading, the spring part recovers, but the dashpot part remains. Both two processes perform by the two units are linear. The spring part shows the linear relationship between load and deformation, with the slope being the elastic modulus of the spring. The dashpot part shows the linear relationship after differentiation. The total strain is the sum of the two units (equation 5.1. The correlation between time and stress or strain is shown in figure 5.3(Banks et al., 2011).

$$\frac{d\varepsilon}{dt} = \frac{1}{E}\frac{d\sigma}{dt} + \frac{\sigma}{\mu} \tag{5.1}$$

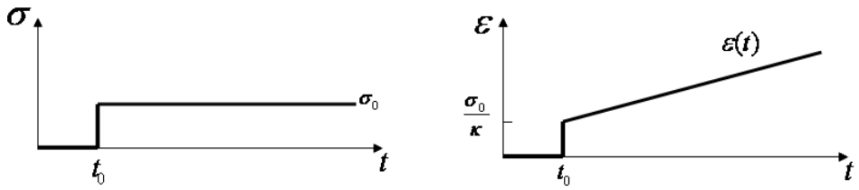

Figure 5.3: Creep function of Maxwell model (Banks et al., 2011).

In the Kelvin body, the 2 elements have the same deformation and jointly support the stress. That is, the total strain is equal to the elastic and viscous strain ($\varepsilon = \varepsilon_S = \varepsilon_D$). The two elements support the total stress together shown in equation 5.2. When a load is applied, as the dashpot is connected in parallel, the deformation doesn't change immediately, but is controlled by time. The deformation recovers after unloading due to the spring. The correlation between time and stress or strain is shown in figure 5.4(Banks et al., 2011).

$$\sigma = E\varepsilon + \mu\frac{d\varepsilon}{dt} \tag{5.2}$$

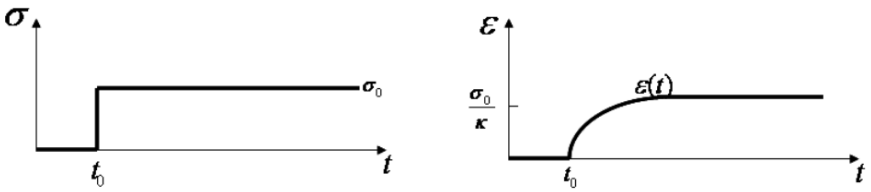

Figure 5.4: Creep function of Kelvin model (Banks et al., 2011).

5.2 Observation of delayed compliance

As previously mentioned in Section 4.4, it is necessary to separate the effect of the elastic behavior from the time-dependent behavior. Therefore, delayed compliance is defined as the measured compliance minus the initial compliance, which is considered elastic behavior. Figure 5.5 takes specimen P06 as an example, shows the calculation way of delayed compliance at 7^{th} day.

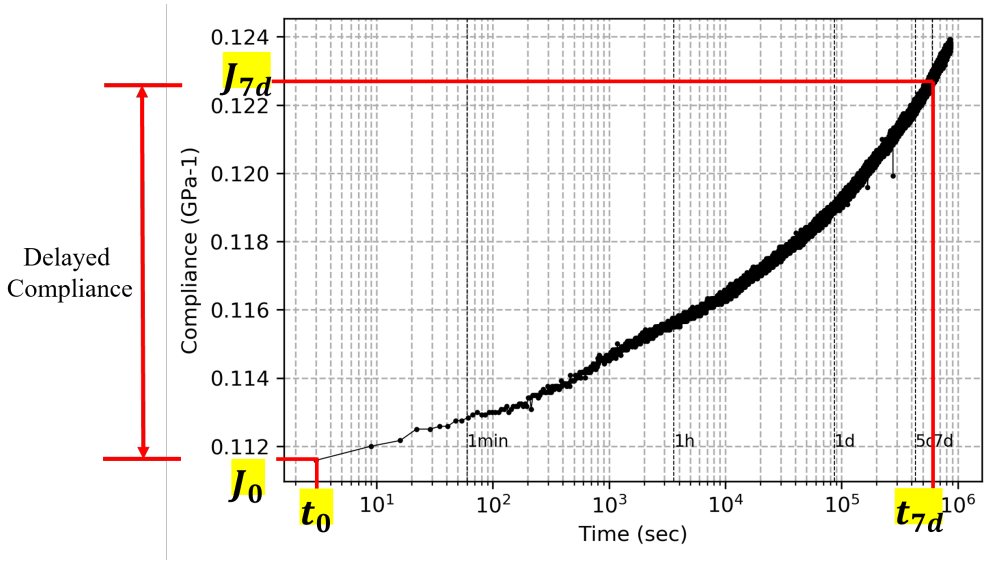

Figure 5.5: Calculation of delayed compliance

Figure 5.6 shows the creep curves after being calculated as delayed compliance. The distribution of curves for each species is similar. It shows little variability between species. However, the variability within species is shown by the range of the curves. It presents that: in the case of this study, time–dependent behavior is more influenced by the within–species factor than by the between–species factor.

There are 2 potential predictors mentioned in section 4.4: density and specific modulus. They are also the cellular level factors that can be measured macroscopically. Considering the cellular behavior, the key assumption of this study is shown in figure 5.7. There are two possibilities for causing creep at the cellular level. The first one is the increased deformation of the cell wall. This means that creep behavior occurs at the microfibril scale or smaller. It could be a reorganization of microfibrils and/or a deformation of the amorphous regions of the cellulose or the amorphous matrix of hemicellulose and lignin. The second one is the creep deformation due to the sliding between the cells. In this case, the deformation of the specimen is caused by the movement between cells. These observations lead to the model shown in figure 5.7. The spring represents the elastic behavior, while the 2–Kelvin bodies represent the delayed deformation : Kelvin body ① stands for the behavior of the cell wall, Kelvin body ② represents the sliding between cells.

According to the assumption, the density is the first parameter considered. Density represents the porosity of wood. Assuming that the deformation occurs only at the cell wall and there is no intercellular slippage, the stiffness of the material would be directly affected by the porosity per unit volume, i.e. the density. The

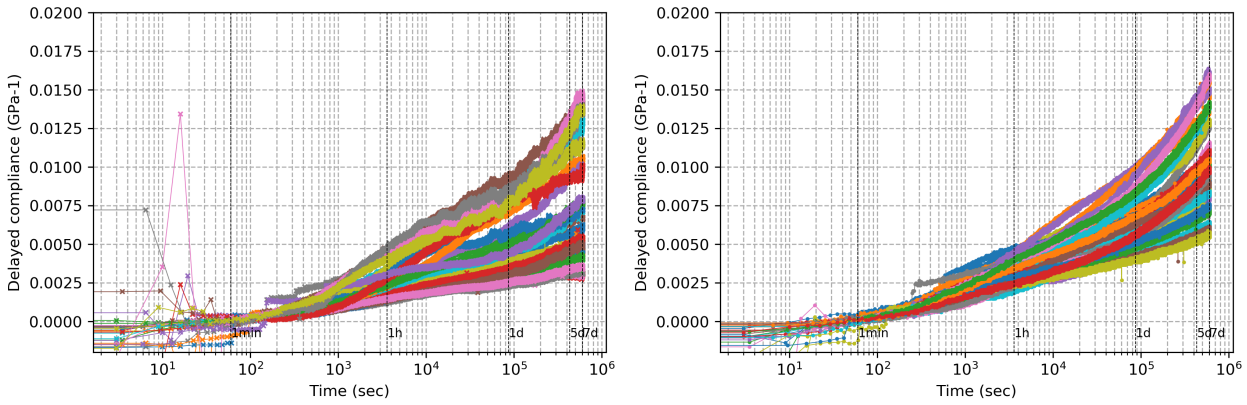

(a) Douglas fir

(b) Poplar

(c) Beech

(d) Oak

Figure 5.6: Delayed compliance results

relationship between the compliance and the density can be present as equation 5.3. In this case, the "a" value would be -1. On the other hand, if the intercellular slippage were eliminated, the creep behavior would be independent of density, the "a" value would be close to zero.

$$\log J = a \times \log \rho + b \tag{5.3}$$

The figure 5.8 shows the relationship between the delayed compliance and the density of the specimens at different time steps. There is a negative proportional relationship from figure 5.8 (a) to (e). It indicates that the assumption is valid. However, this correlation was not significant. All data were grouped by species and divided into 4 groups. We could not find a clear trend within species because the specimens don't cover a wide range of densities. In figure 5.8 (f), the slope of the graph is much flatter. This could be caused by the experimental problem mentioned in Chapter 4: during the test, the humidity of the experimental environment changed on the 8^{th} day. Therefore, these data sets are not considered in figure 5.8 (f). This makes a part of the data with relatively high density missing, resulting in inaccuracy.

From the linear regression result in figure 5.8, the slope varies with time, which is presented in figure 5.9. Considering the delayed compliance of $J_{1m} - J_0$ without sufficient response time and the small number of data points for the delayed compliance of $J_{10d} - J_0$, the other data have a good linear relationship with the

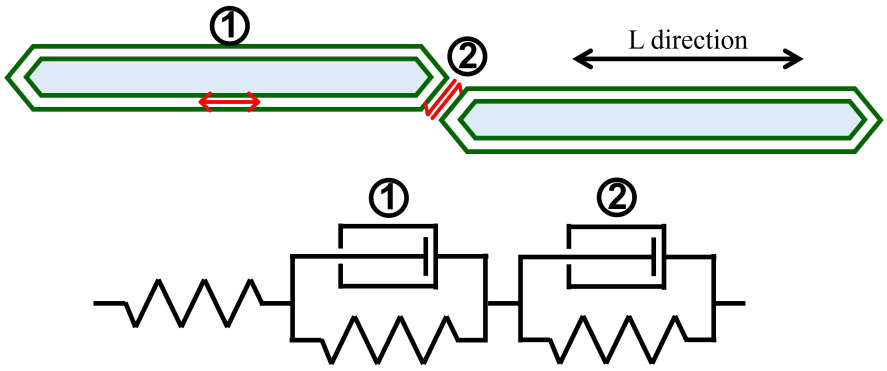

Figure 5.7: Assumptions of creep behavior in the cell scale : deformation of the cell wall (1) and sliding between cells (2), proposition of a model to represent both phenomena.

logarithm of time (seconds) (figure 5.9 b). Figure 5.9 shows that the slope of the regression decreases with time, which indicates that the effect of density is smaller when the loading time is longer.

To understand the changes in behavior over time, the relationship between compliance differences and density is shown in figure 5.10. The difference of compliance is defined as compliance at time t minus time $t-1$, that is, $J_{1m}-J_0$, $J_{1h}-J_{1m}$, $J_{1d}-J_{1h}$, $J_{5d}-J_{1d}$, $J_{7d}-J_{5d}$, and $J_{10d}-J_{7d}$. The slopes in figures 5.10 (a) to (d) are close to -1, among them, the slope in figure 5.10 (b) is the largest. After the 5^{th} day of loading in figure 5.10 (e), the slope is relatively flat. Comparing the regression result in figure 5.10 (c) and (d), they have similar slopes, but the loading times are very different. This means that after 1 day of loading, the effect of density is lower, and therefore it takes 5 times longer to reach the same increment of compliance. With this observation, we believe that the creep behavior can be divided into two phases after 1^{st} days of loading.

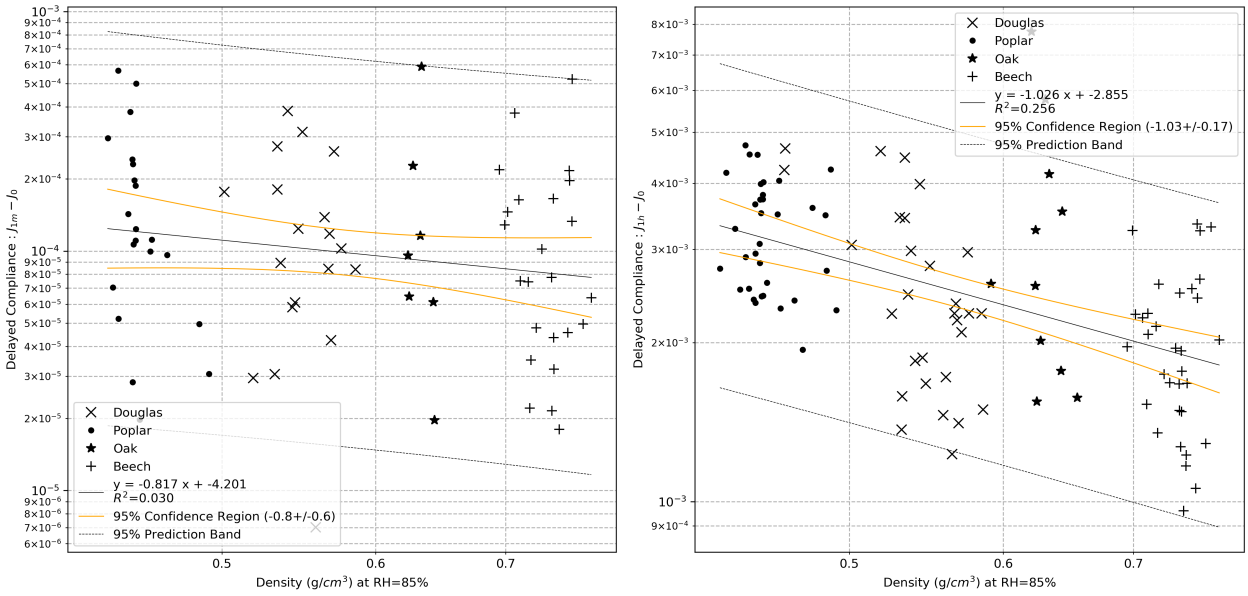

(a) $J_{1m} - J_0$

(b) $J_{1h} - J_0$

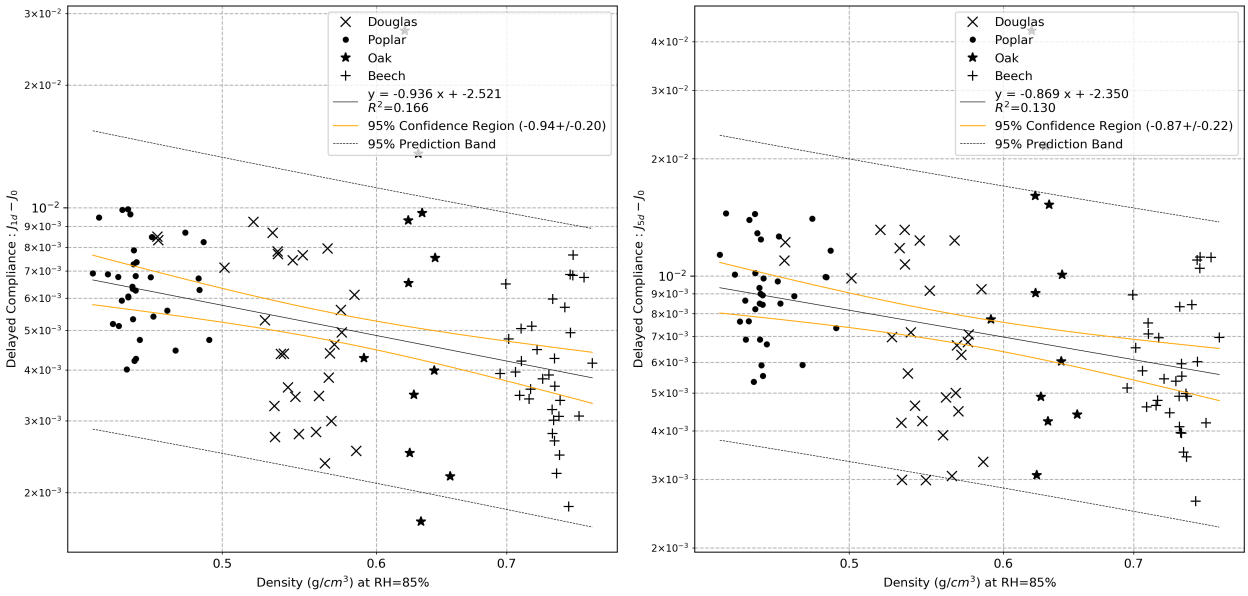

(c) $J_{1d} - J_0$

(d) $J_{5d} - J_0$

Figure 5.8: Correlation between delayed compliance and density. (a) Compliance at 1^{st} minute minus initial compliance. (b) Compliance at 1^{st} hour minus initial compliance. (c) Compliance at 1^{st} day minus initial compliance. (d) Compliance at 5^{th} day minus initial compliance.

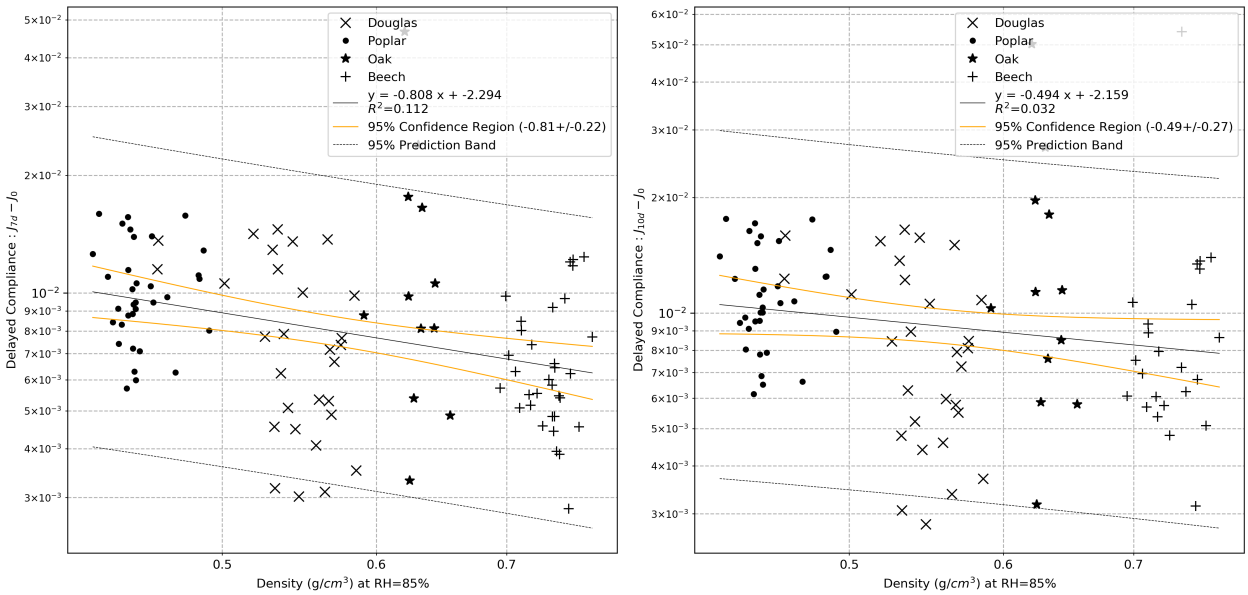

(e) $J_{7d} - J_0$ (f) $J_{10d} - J_0$

Figure 5.8: Correlation between delayed compliance and density (Continue). (e) Compliance at 7^{th} day minus initial compliance. (f) Compliance at 10^{th} day minus initial compliance.

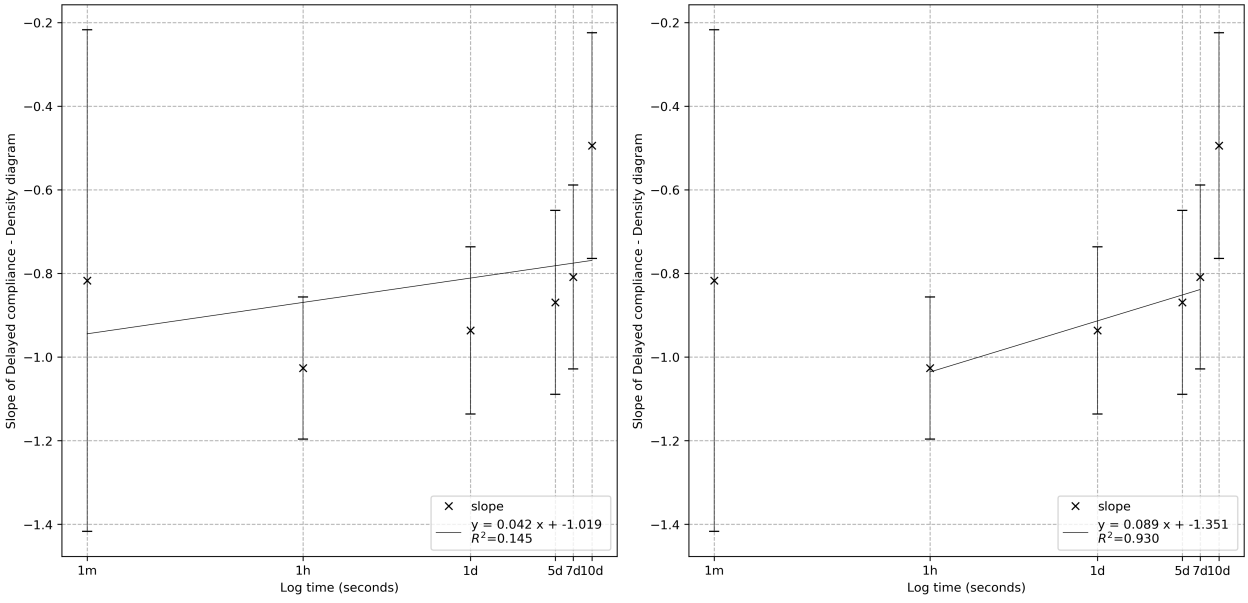

(a) (b)

Figure 5.9: Regression slope of delayed compliance and density. (a) The linear regression result from $J_{1m} - J_0$ to $J_{10d} - J_0$. (b) The linear regression result from $J_{1h} - J_0$ to $J_{7d} - J_0$.

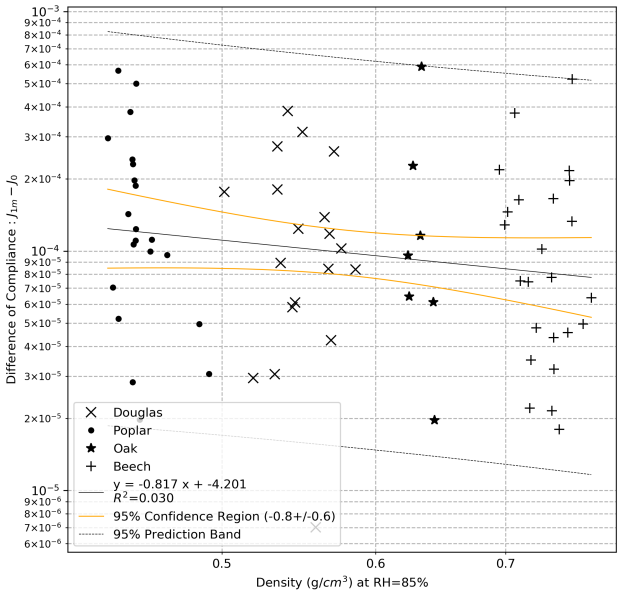

(a) $J_{1m} - J_0$

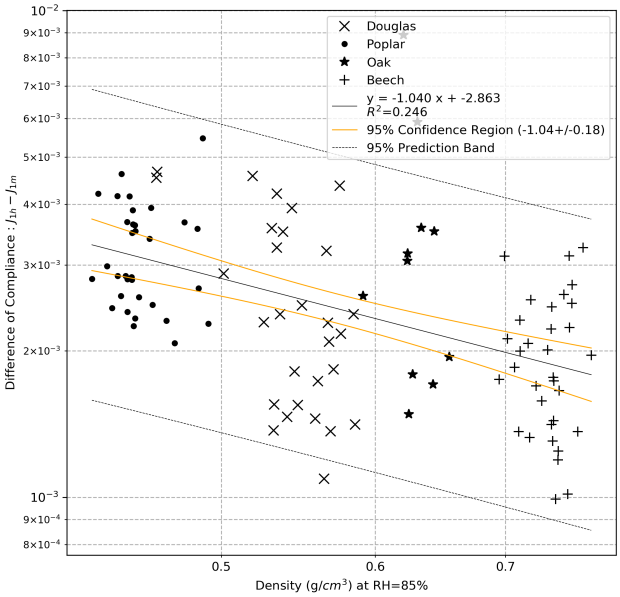

(b) $J_{1h} - J_{1m}$

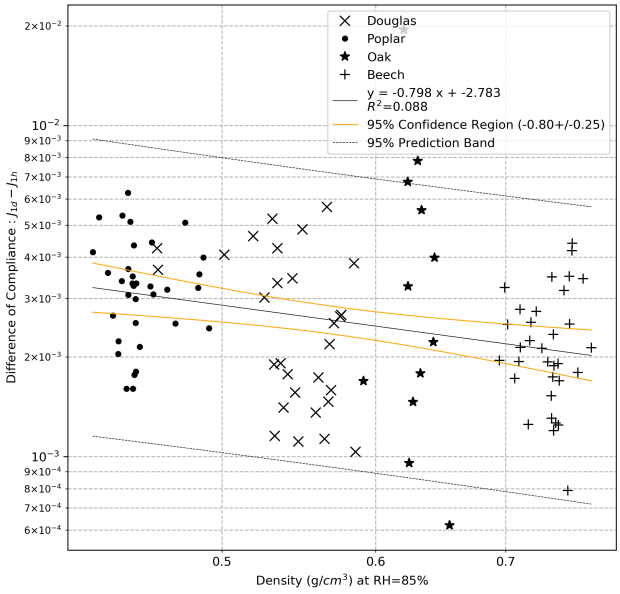

(c) $J_{1d} - J_{1h}$

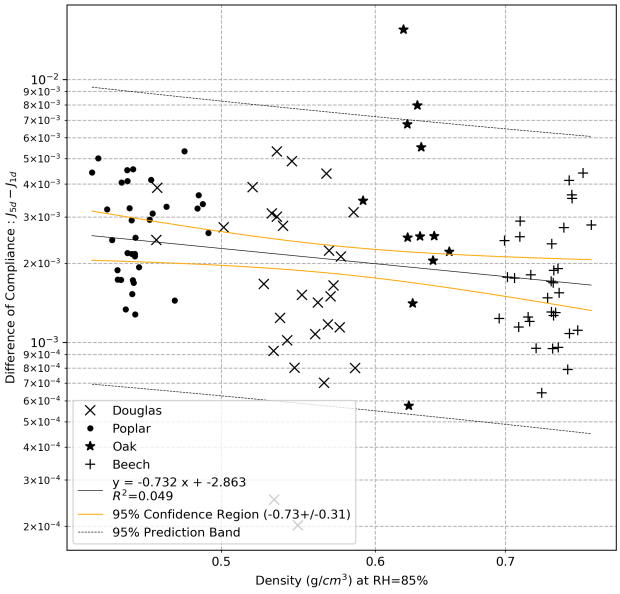

(d) $J_{5d} - J_{1d}$

Figure 5.10: Correlation between differences of compliance and density. (a) Compliance at 1^{st} minute minus initial compliance. (b) Compliance at 1^{st} hour minus 1^{st} minute. (c) Compliance at 1^{st} day minus 1^{st} hour. (d) Compliance at 5^{th} day minus 1^{st} day.

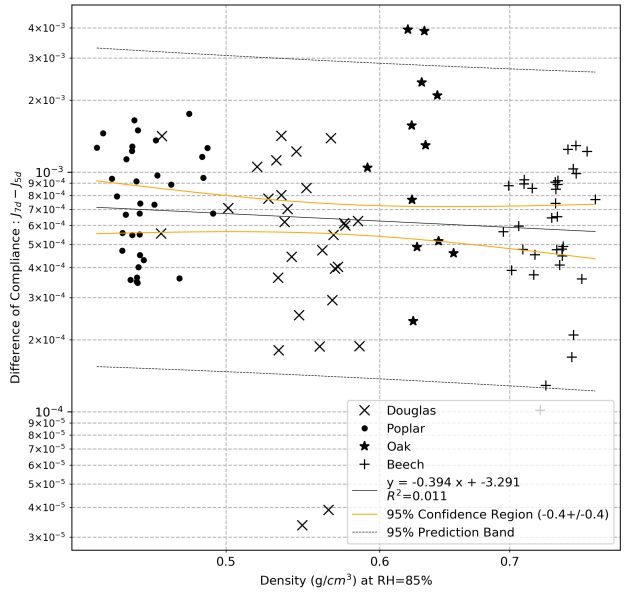

(e) $J_{7d} - J_{5d}$

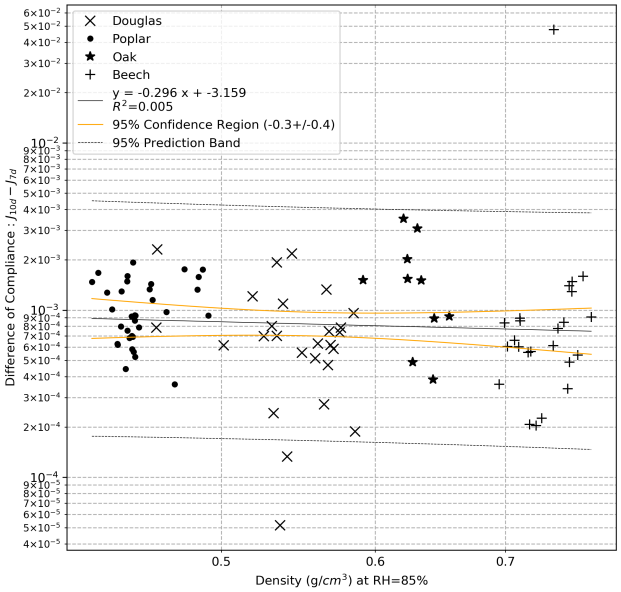

(f) $J_{10d} - J_{7d}$

Figure 5.10: Correlation between difference of compliance and density (Continue). (e) Compliance at 7^{th} day minus 5^{th} day. (f) Compliance at 10^{th} day minus 7^{th} day.

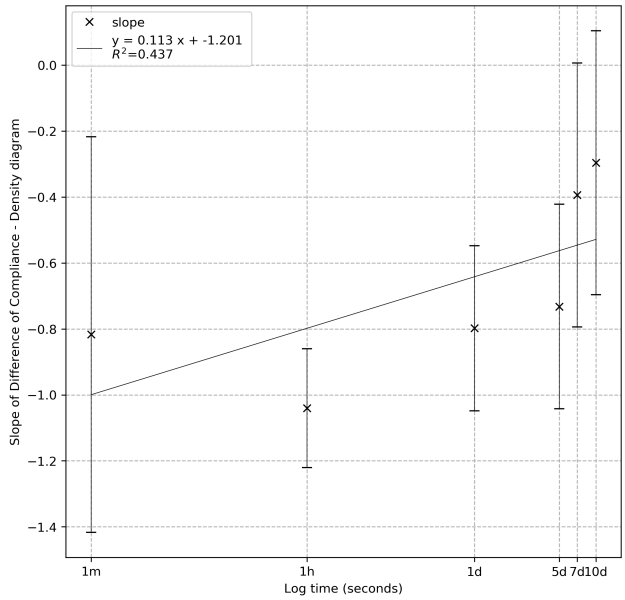

(a)

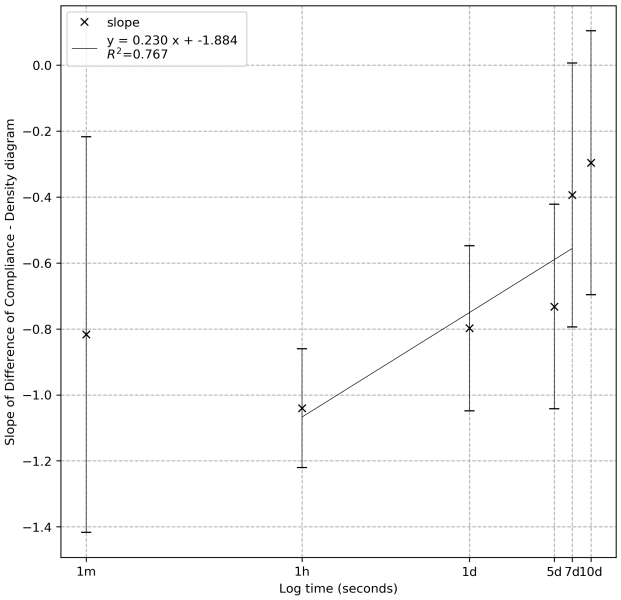

(b)

Figure 5.11: Regression slope of difference of compliance and density. (a) The linear regression result from $J_{1m} - J_0$ to $J_{10d} - J_{7d}$. (b) The linear regression result from $J_{1h} - J_{1m}$ to $J_{7d} - J_{5d}$.

5.3 Two–mechanism model

According to the observation in section 5.2, the assumption is proven: the creep behavior takes place at the cell wall. In addition, the effect of the density changes with time. The first possibility is that the entire creep process involves more than one stage. Figure 5.12 shows the creep curve, which can be divided into three stages based on the slope of the curve (Bodig and Jayne, 1982). During primary creep, the rate of deformation gradually decreases to zero, then it comes to secondary creep. The creep rate remains zero during secondary creep, but the deformation increases continuously. When the creep rate begins to increase, this is the beginning of tertiary creep. Figure 5.13 (a) shows the slope of the experimental creep curves in this study, and (b) shows the slope value in double–log plot. The exact point where the slope is zero cannot be found in the experimental data.

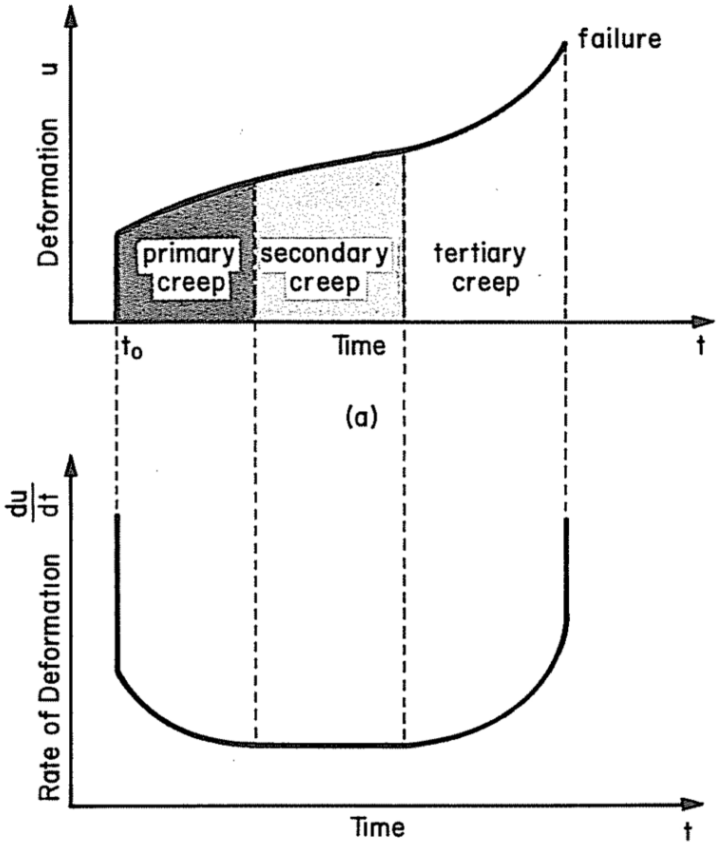

Figure 5.12: Schematic representation of the deformation and rate of deformation during the creep process showing 3 steps : primary, secondary and tertiary creep (Bodig and Jayne, 1982).

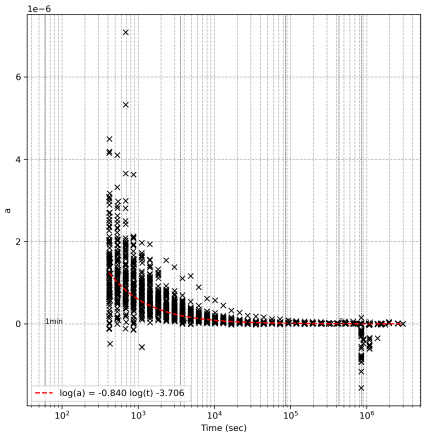

(a) Slope of compliance-time diagram.

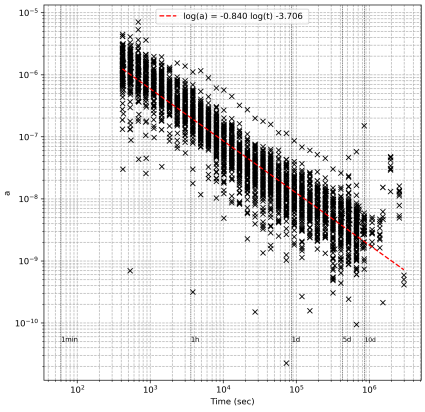

(b) Slope of compliance-time diagram in double logarithm plot.

Figure 5.13: Experimental curves.

In Matar (2003) it is mentioned that primary creep will be completed within 1 to 2 days after loading and will enter the secondary creep process. There is no zero point when considering the diagram of Bodig and Jayne (1982). Thus, refer to the definition in Matar (2003) and to have a practical separation point, primary creep in this study was defined from the time of loading to the end of the 1^{st} day, which present the short–term creep behavior, and the creep process after the 1^{st} day was defined as secondary creep, which presents the mid–term creep behavior (figure 5.14). In addition, to have most curves credible, we have chosen the range between the initial time to the 7^{th} days for analysis and modeling.

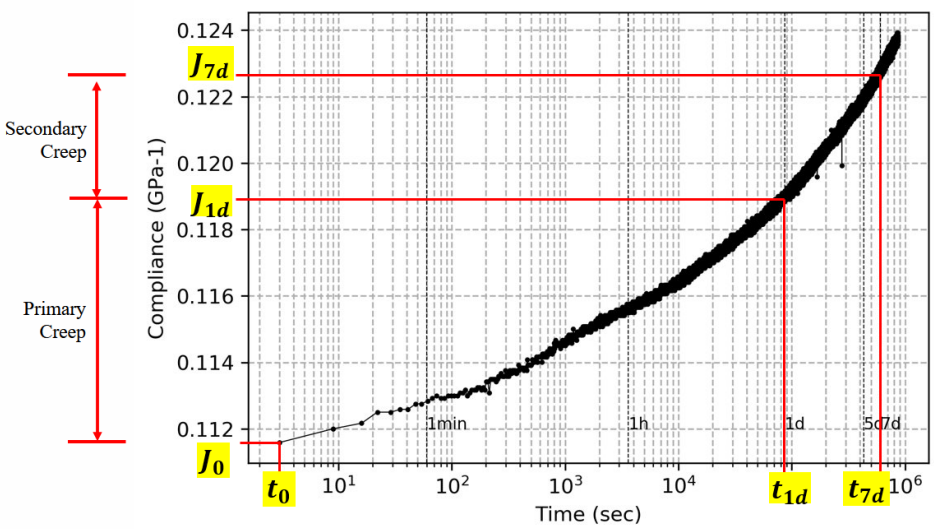

Figure 5.14: Primary and secondary creep calculation scheme for experimental data.

5.3.1 Potential predictor analysis: Density

Figure 5.15 shows the relationship between delayed compliance and density on double logarithm plots. According to the key assumption presented by equation 5.3, equation 5.4 shows the relationship between delayed compliance at different stages and density. The slope in figure 5.15 (a) remains in the inversely proportional range, it is close to -1. However, the slope in figure 5.15 (b) is not -1. This shows that the density effect changes with time and that there are other possible factors affecting the creep behavior.

$$\log(J_m - J_n) = a \times \log \rho + b \tag{5.4}$$

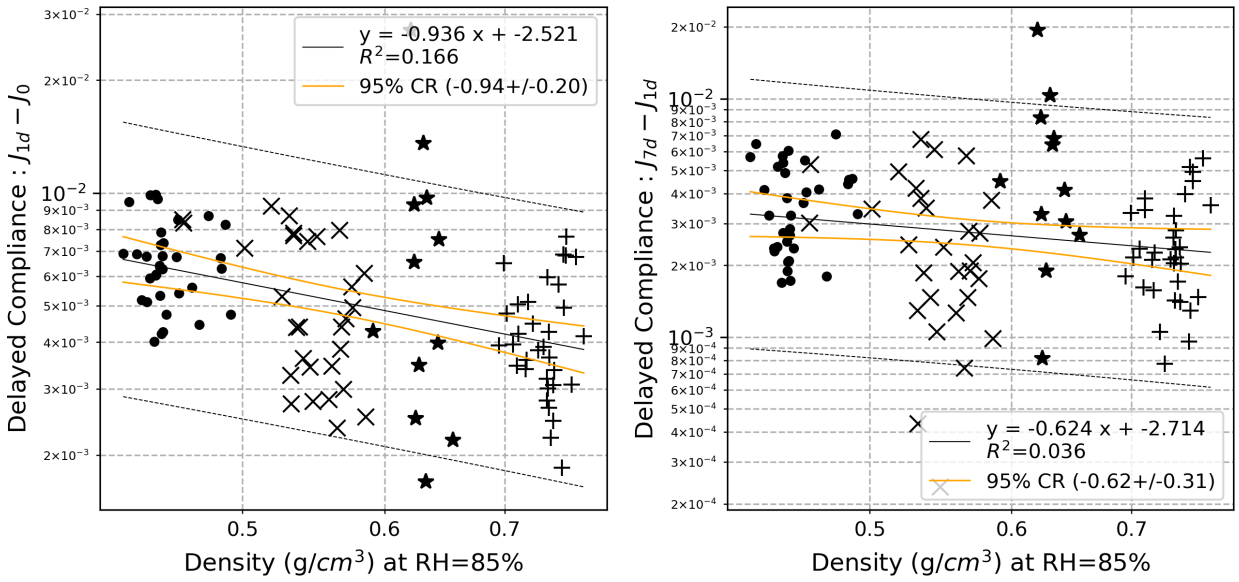

(a) (b)

Figure 5.15: The relation between delayed compliance and density. (a) primary creep (b) secondary creep. ×: Douglas fir, •: Poplar, ⋆: Oak, +: Beech, ——: 95% confidence region (CR), - - - -: 95% prediction band

To remove the density effect in delayed compliance, specific compliance is defined. In section 5.3.1, it was mentioned that there is an inverse proportional relationship between delayed compliance and density. Therefore, the value of "a" in equation 5.4 can be given as -1, and we can have equation 5.5. Moving the density from the right to the left side of the equation, multiplies the delayed compliance by the density, and this value is defined as the specific compliance (equation 5.6).

Figure 5.16 shows the relationship between specific compliance and density. The absolute value of the slope and the value of R^2 are decreased. Thus, it can be considered that the density effect is removed.

$$\log(J_m - J_n) = -\log\rho + b \tag{5.5}$$

$$\log((J_m - J_n) \times \rho) = b \tag{5.6}$$

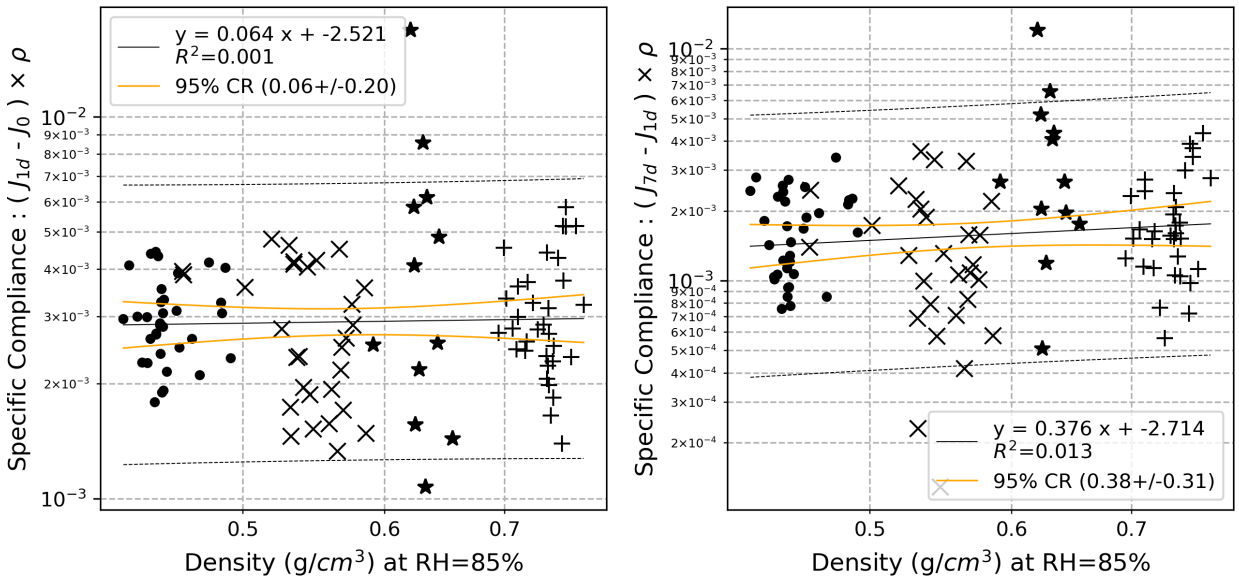

(a) (b)

Figure 5.16: The relation between specific compliance and density. (a) primary creep (b) secondary creep. ×: Douglas fir, •: Poplar, ⋆: Oak, +: Beech, ——: 95% confidence region (CR), - - - -: 95% prediction band

5.3.2 Potential predictor analysis: Specific modulus

The specific modulus is a factor that strongly correlates with the microfibril angles that represent the wood microstructure. It is also the second potential predictor mentioned in section 4.4. Figure 5.17 shows the relationship between specific compliance and specific modulus. Base on equation 5.6, figure 5.17 shows a good linear correlation in double logarithm plot, it can be present in equation 5.7. The regression result shows that the specific modulus effect is stronger on secondary creep than primary creep because the absolute slope of secondary creep is higher than primary creep. This also means that the effect of specific modulus increases with time.

$$\log((J_m - J_n) \times \rho) = c \log E_s + d \tag{5.7}$$

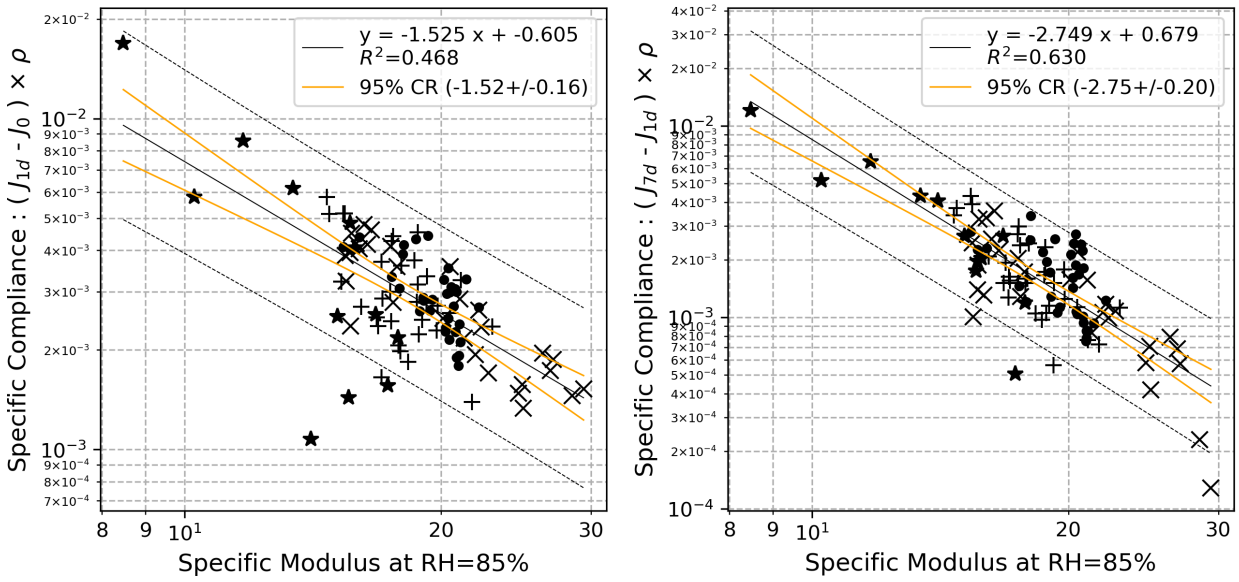

(a) (b)

Figure 5.17: The relation between specific compliance and specific modulus. (a) primary creep (b) secondary creep. ×: Douglas fir, •: Poplar, ⋆: Oak, +: Beech, ——: 95% confidence region (CR), - - - -: 95% prediction band

According to the regression result in figure 5.17, the value absolute of "c" in equation 5.7 can be decided as 1.5 for primary creep and 3 for secondary creep (equation 5.8). Relative compliance can be defined as specific compliance multiplied by specific modulus. However, the "c" value in this study is not -1, this parameter is called adjusted relative compliance. Figure 5.18 shows that the adjusted relative compliance is independent of the specific modulus.

$$\log((J_m - J_n) \times \rho \times E_s^c) = d \tag{5.8}$$

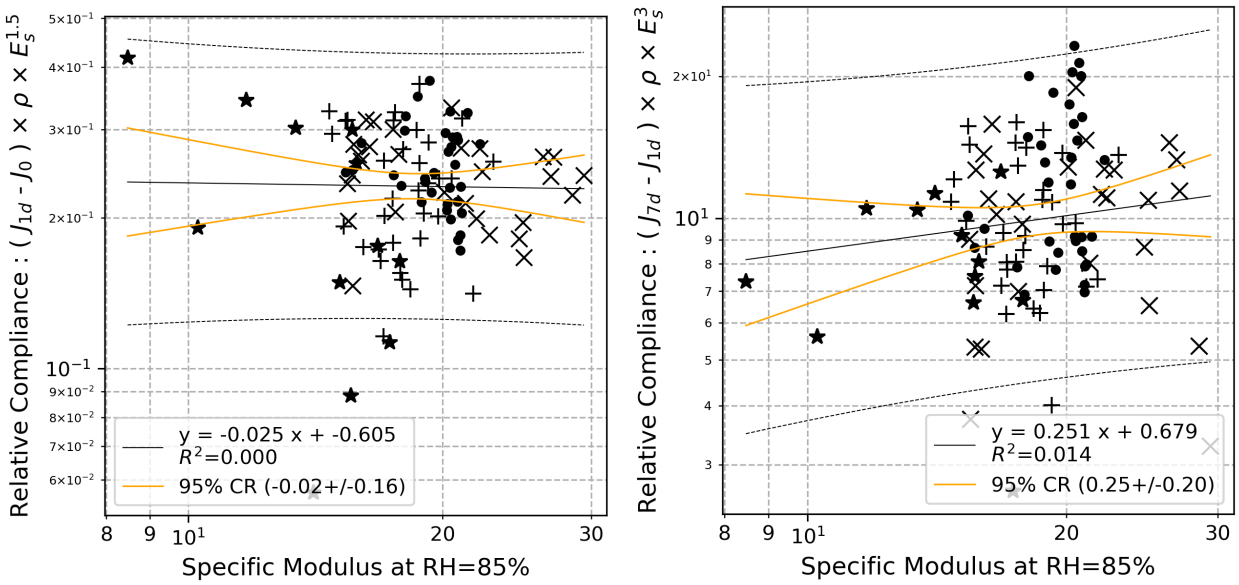

(a) (b)

Figure 5.18: The relation between adjusted relative compliance and specific modulus. (a) primary creep (b) secondary creep. ×: Douglas fir, •: Poplar, ⋆: Oak, +: Beech, ——: 95% confidence region (CR), - - - -: 95% prediction band

5.3.3 Comprehensive analysis: Creep factor

Considering the result in section 5.3.1 and 5.3.2, the creep factor can be defined as equation 5.9 which may be linearly correlated with delayed compliance. It is validated in figure 5.19. Creep factors for both primary and secondary creep have good predictability with high R^2.

$$\log(J_m - J_n) = \frac{d}{\rho \times E_s^c} \tag{5.9}$$

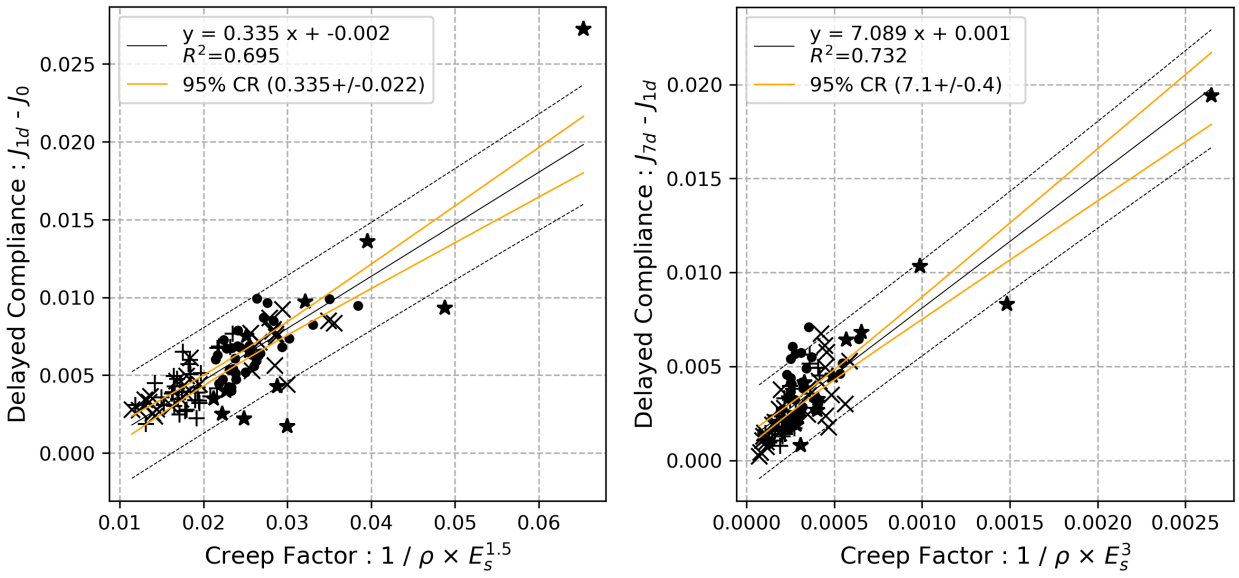

(a) (b)

Figure 5.19: The relation between delayed compliance and creep factor. (a) primary creep (b) secondary creep. ×: Douglas fir, •: Poplar, ⋆: Oak, +: Beech, ——: 95% confidence region (CR), - - - -: 95% prediction band

5.3.4 Summary of two–mechanism model

In the observation and the two–mechanism model, the creep behavior can be separated into primary and secondary creep after 1 day of loading. The delayed compliance in both stages is proportional to density, so we can say that the creep behavior happens on the cell wall. However, the correlation between delayed compliance of secondary creep and density is weaker than primary creep, so the creep behavior might be transferred from the cell wall to the inter–cell wall or happens at other place. The effect of specific modulus is more important in the secondary creep, it means that the role of MFA is increasing with loading time. Yet, this tendency is not that obvious. We would like to know the changing process of creep behavior during the loading time so that we tried the discrete compliance model.

5.4 Discrete compliance model

To understand the more precisely the creep behavior at different times, the second model that has been tried is the discrete compliance model (figure 5.20). This model is based on a combination of Kelvin bodies. It is suggested that the whole creep curve can be constructed from 5 curves that come from the Kelvin body. The compliance can be represented as a function of time according to equation 5.10.

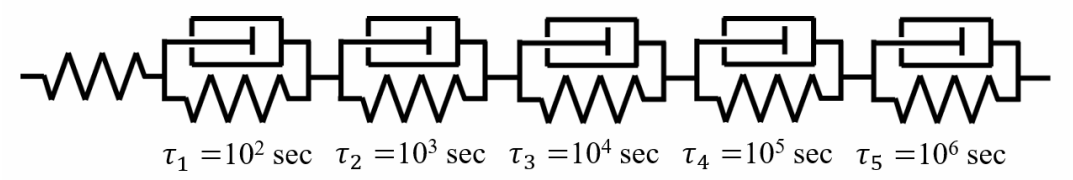

Figure 5.20: Discrete compliance model.

$$J(t) = J_0 + \sum J_i(t) = J_0 + \sum J^*i \times (1 - e^{-t/\tau_i}) \tag{5.10}$$

τ is the characteristic time of the Kelvin bodies, which decides the central position of the curve on the timeline. The whole creep compliance can be represented by the sum of each compliance. That is, the creep behavior model can be constructed by Kelvin bodies connected in series. The behavior of each Kelvin body is represented by $J_i(t)$, which is equal to $J^*i \times (1 - e^{-t/\tau_i})$. J_i stands for the compliance value for the Kelvin body n°i. The discrete model leads to a discretization of tau_i every decade in logarithmic scale. In this study, the model was constructed by 5 Kelvin bodies connect in series, so log τ_i values were given as 2, 3, 4, 5, 6. τ_i values were given as 100, 1000, 10000, 100000, and 1000000 seconds.

The t value in equation 5.10 is time, and the time values were calculated from the logarithm of t which was set between 2 and 5.8 every 0.1. The experimental data were collected every 5 seconds. The data at the time point of the list t was collected for modeling. We can also have the delayed compliance value calculated by $J_i(t)$ at the time points in list t. The sum of $J_i(t)$ is the estimated result of delayed compliance. Figure 5.21 shows the modeling process. The specimen DA046 is taken as an example. The red points in the figures are the experimental data. The modeling values of the $J_i(t)$ are shown in figure 5.21 (a). The fitting result is the sum of the $J_i(t)$, which is shown in figure 5.21 (b).

The model was calculated by Excel solver. J^*i are the variable values which are found by the solver. The error value is the sum of the square of the difference between experimental data and $\Sigma J_i(t)$. The goal of the solver is to find the values i–of J^*i that minimize the error value for a single specimen. The creep behavior can be described by the function $J^*i \times (1 - e^{-t/\tau_i})$, where $(1 - e^{-t/\tau_i})$ represents the role of time in this process, while J^*i represents the predictor that can be used to estimate the creep behavior. The potential predictors are density and specific modulus, which may be found to be correlated with J^*i.

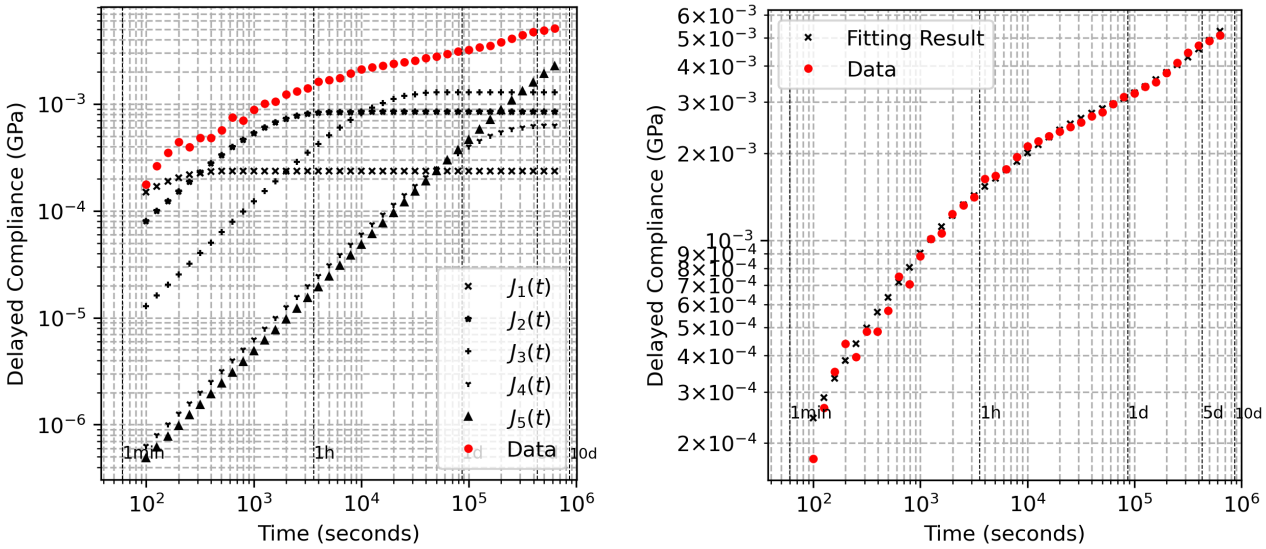

(a) (b)

Figure 5.21: Fitting process of compliance model for specimen DA046. (a) Black dotted lines are the curves from $J_1(t)$ to $J_5(t)$. Red dotted line is the experimental data of DA046. (b) Black dotted line is the fitting result, which is the sum of $J_1(t)$ to $J_5(t)$.

After calculating $\Sigma J_i(t)$ for all the specimens, correlation between J^*i and density, specific modulus is shown in figure 5.23 and 5.25. The slope of J^*i against density and specific modulus is plotted in figure 5.23 (f) and 5.25 (f) to enhance the effect of these factors on the parameters of modeling.

Compared to the two–mechanism model in section 5.3, the discrete compliance model divides the creep curve equally into 5 parts and smoothes the values by the model. $\Sigma J_i(t)$ is the delayed compliance value. J^*i is the creep factor at the characteristic time τ_i, which can be correlated with density and specific modulus. To determine the relationship between J^*i and the predictors, the linear regression is calculated in the double-log plot. It is expected that there is a trend in the slope of the linear regression result.

5.4.1 Correlation between J^*i and density

Figure 5.23 shows the relationship between J_i and density and the slope of density against J^*i shows in figure 5.22. In figure 5.23 shows that the distribution of data is grouped by the species because it is sorted by density. The R^2 values are low. The trend is weak between density and J^*i.

Figure 5.22 shows that the density effect change with time. The absolute value of the slope of the density vs. J^*i decrease with time. It means that the density effect decreases with time, which presents the same trend as the two-mechanism model.

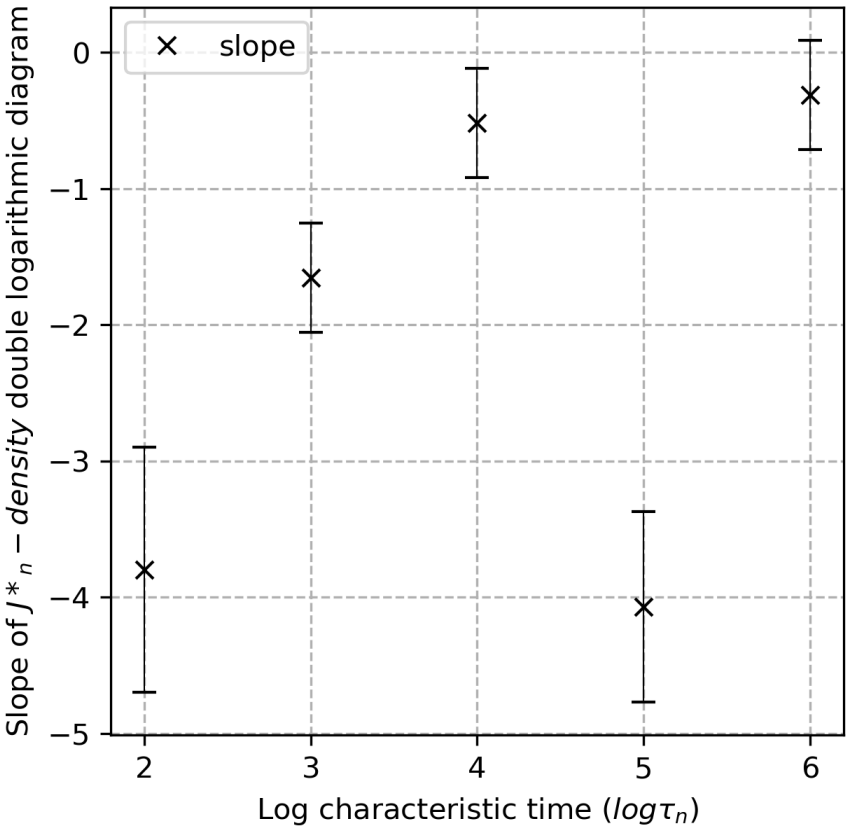

Figure 5.22: Linear regression result of J_i and density

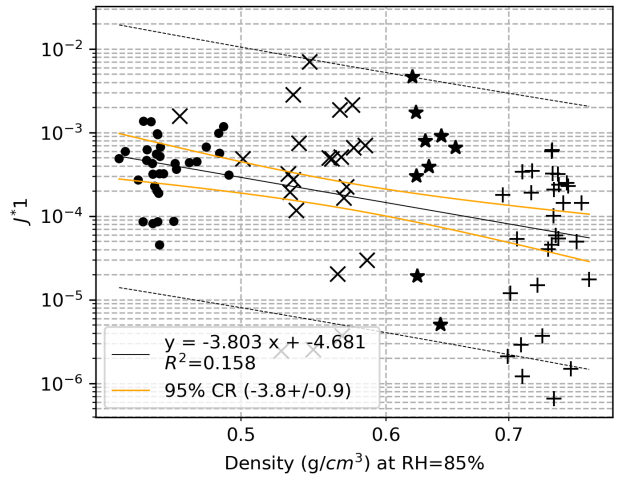

(a)

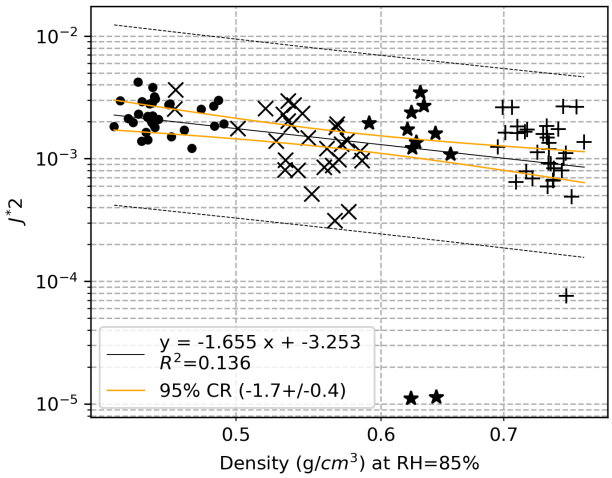

(b)

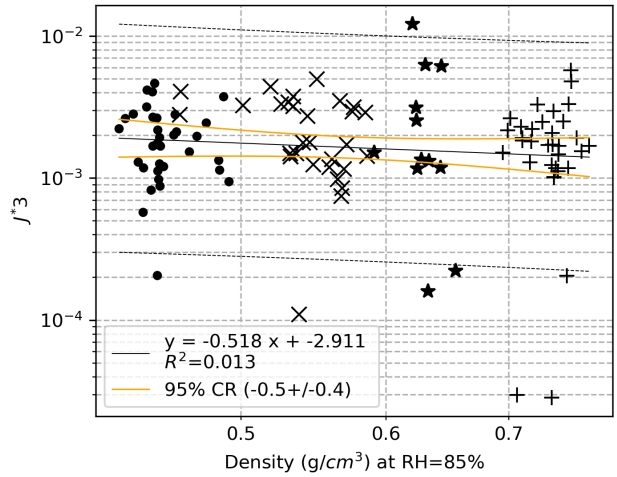

(c)

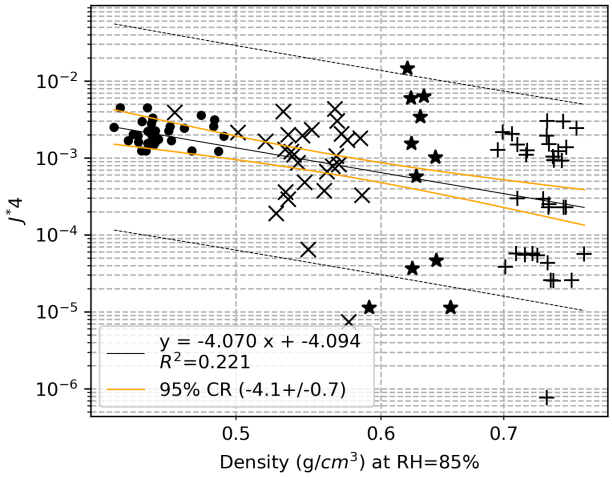

(d)

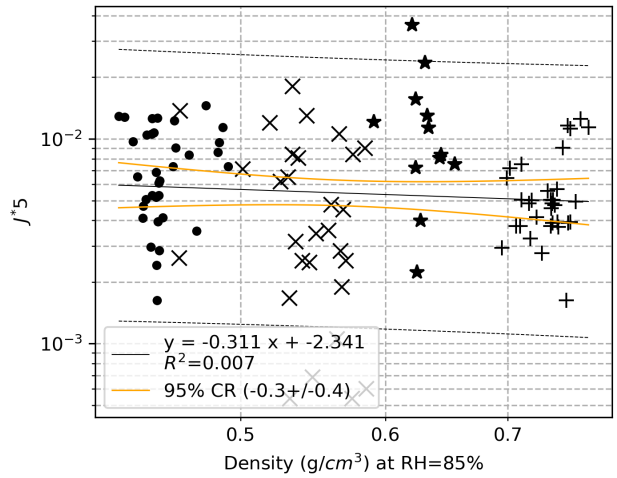

(e)

Figure 5.23: Relationship between J^*i and density. (a) Correlation between J^*1 and density. (b) Correlation between J^*2 and density. (c) Correlation between J^*3 and density. (d) Correlation between J^*4 and density. (e) Correlation between J^*5 and density. ×: Douglas fir, •: Poplar, ⋆: Oak, +: Beech, ——: 95% confidence region (CR), - - - -: 95% prediction band

5.4.2 Correlation between J^*i and specific modulus

Figure 5.25 shows the correlation between J^*i calculated by the model and specific modulus, and figure 5.24 shows the relationship between the slope of the regression result and time. The result in figure 5.25 shows a weak linear trend between J^*i and specific modulus. The data is less grouped by species. Figure 5.24 shows that the slope of the regression result changes over time. There is an increasing trend on the graph. This may mean that the effect of specific modulus increases with time. For the medium to long term behavior, it plays a more important role than density.

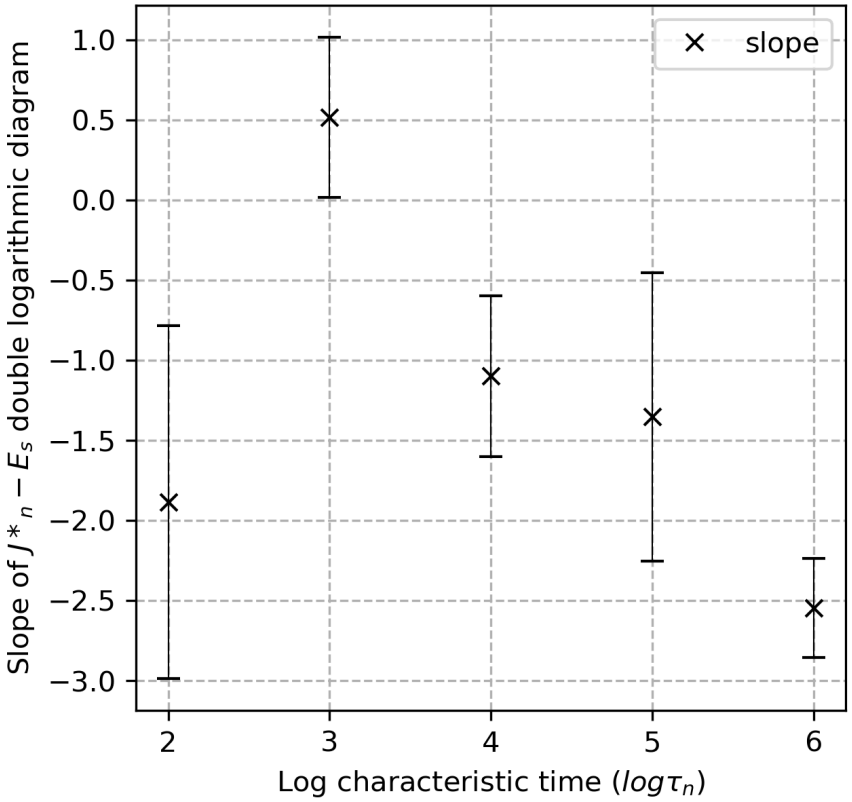

Figure 5.24: Linear regression result of J_i and specific modulus (E_s)

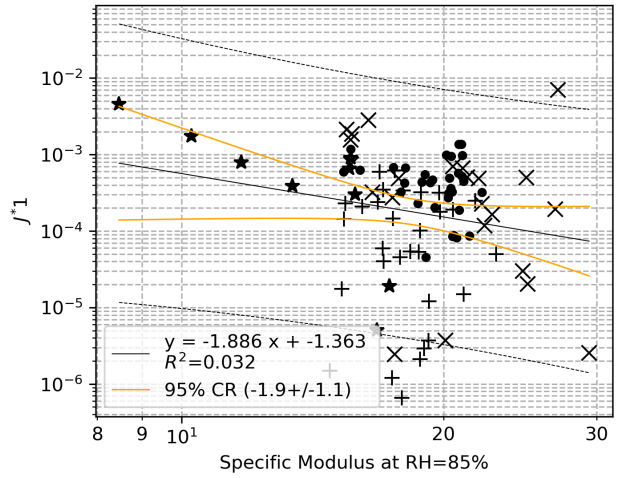

(a)

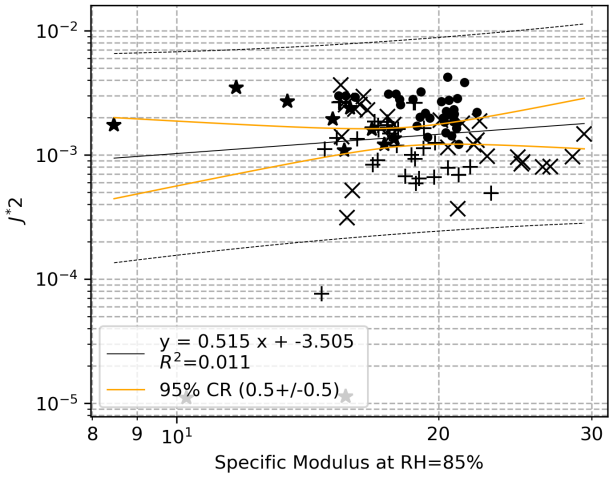

(b)

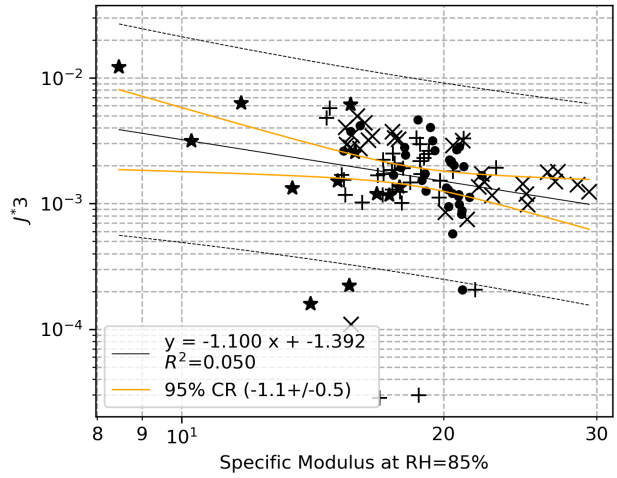

(c)

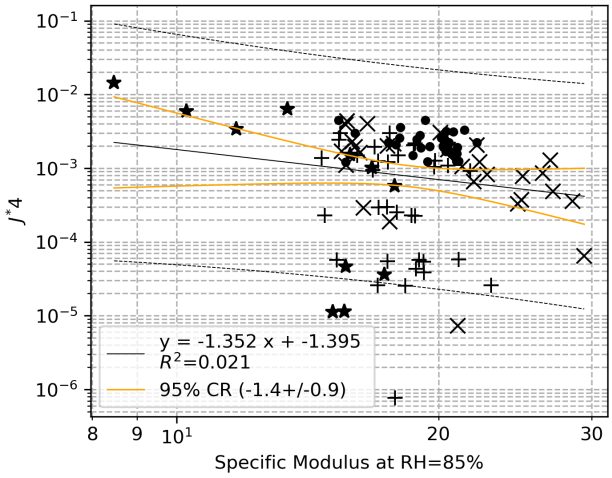

(d)

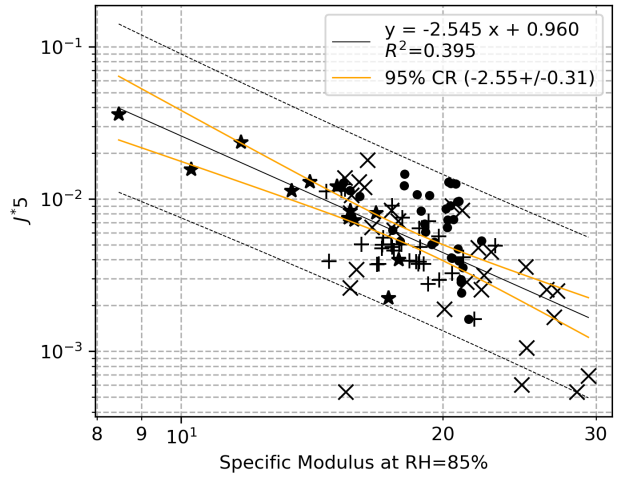

(e)

Figure 5.25: Relationship between J^*i and density. (a) Correlation between J^*1 and density. (b) Correlation between J^*2 and density. (c) Correlation between J^*3 and density. (d) Correlation between J^*4 and density. (e) Correlation between J^*5 and density. ×: Douglas fir, •: Poplar, ⋆: Oak, +: Beech, ——: 95% confidence region (CR), - - - -: 95% prediction band

5.4.3 Summary of discrete compliance model

In the discrete compliance model, we tried to minimize the noise and error in the experiment by fitting the curve rather than by chosing the value of the data at the time points τ_i. If there is a clear correlation between J^*i and the characteristic of the specimens, J^*i can be estimated by a function of specimen characteristic, the function $J(t)$ can be constructed directly by the parameters of density, specific modulus or other wood physical properties. However, the tendency of J^*i and density or specific modulus is not that clear. It is possible to find a function of time to estimate the effect of density and specific modulus (figure 5.26). This function can be used to define J^*i and then the creep curve $J(t)$ can be determined.

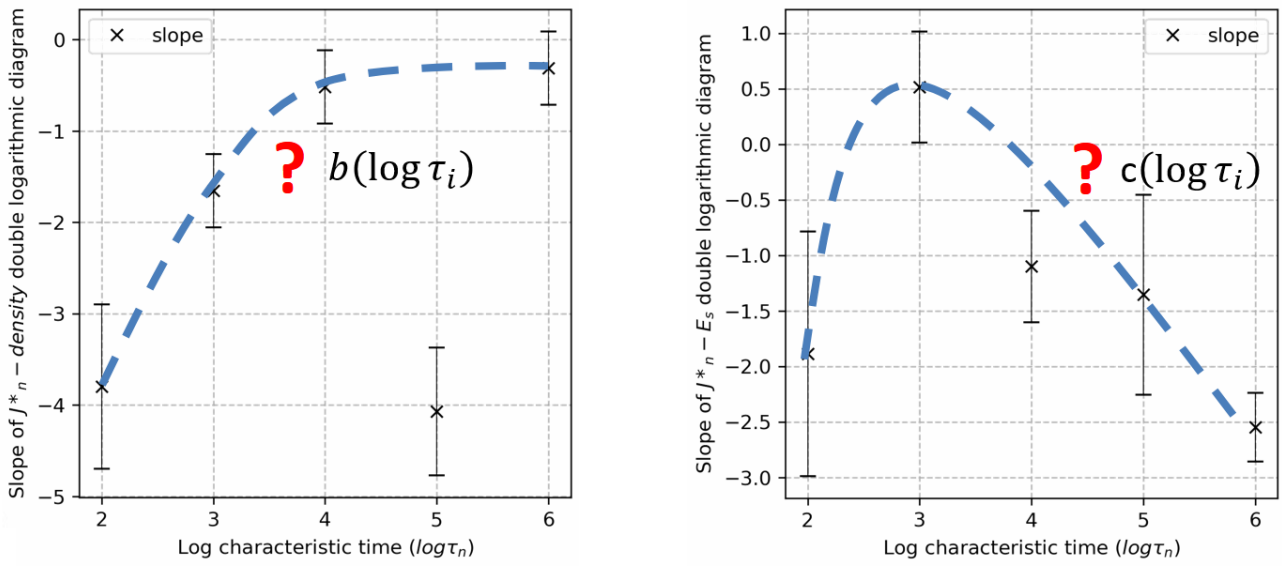

(a) (b)

Figure 5.26: Possible predicted function of J^*i

5.5 Multiple regression model

In the discrete compliance model, we tried to find J^*i value by the experimental data directly. The entire creep curve is divided into 5 parts in this model. The result indicates that it is likely to excite a function of time to represent the effect of predictors. The multiple regression model divides the entire curve into infinite characteristic time (figure 5.27).

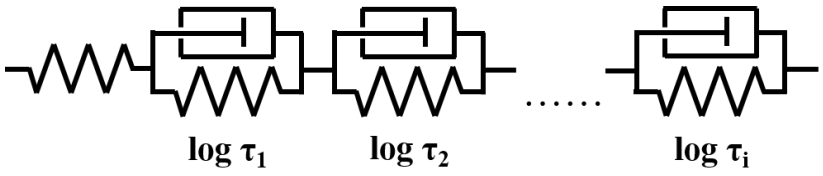

Figure 5.27: Multiple regression model

Equation 5.11 shows the main idea for the creep model based on equation 5.10. Total compliance (J) is the sum of initial compliance (J_0) and J^*i. Total compliance is related to time (t), density of specimens (ρ), and specific modulus (E_s). The sum $\sum J^*i \times (1 - e^{-t/\tau_i})$ represents the time-dependent behavior. J^*i is the function of density, specific modulus, and characteristic time (τ_i). If J^*i could be calculated by the mechanical properties of specimens, the whole creep curve could be constructed and be predicted by the mechanical test.

The function used to fit J^*i is shown as equation 5.12. As the observation in previous sections, delayed compliance has linear correlation with density and specific modulus in double logarithm plot. Considering equation 5.9, delayed compliance can be fitted by the function of density and specific modulus. Thus, the function of J^*i is expressed as $a \times \rho^b \times E_s^c$. In addition, in the result of discrete compliance model (figure 5.26), we can see that the slope of J^*i against density or specific modulus has a weak tendency with time. So, τ_i is taken into account in the function of J^*i and a, b and c are functions of τ_i. Each parameter is defined as a polynomial function of τ_i based on the observation that the slope of the double logarithm plot changes with time.

$$J(t, \rho, E_s) = J_0 + \sum_i J^*i(\rho, E_s, \tau_i) \times (1 - e^{-t/\tau_i}) \tag{5.11}$$

$$J^*i(\rho, E_s, \tau_i) = a(\log \tau_i) \times (\frac{\rho}{\rho_0})^{b(\log \tau_i)} \times (\frac{E_s}{E_{s0}})^{c(\log \tau_i)} \tag{5.12}$$

$$a(\log \tau_i) = i_a + s_a \times \log \tau_i + q_a \times (\log \tau_i)^2 + c_a \times (\log \tau_i)^3 \tag{5.13}$$

$$b(\log \tau_i) = i_b + s_b \times \log \tau_i + q_b \times (\log \tau_i)^2 \tag{5.14}$$

$$c(\log \tau_i) = i_c + s_c \times \log \tau_i + q_c \times (\log \tau_i)^2 \tag{5.15}$$

The fitting of the model was calculated by the Excel solver. A series of $\log \tau_i$ value was given manually as an isometric series from 2 to 5.5 every 0.1. The parameters a, b, and c are the function of τ and there are 10 parameters in the three functions which would be found by the solver (equation 5.13 to 5.15).

The functions a, b, and c are substituted into the function of J^*i (equation 5.12). Among them, ρ_0 and E_{s0} are the mean value of the matrix. In this study, ρ_0 is 0.6 and E_{s0} is 22.

By the equation 5.12, we can have the J^*i at the time τ and substituted into equation 5.11. The sum of all the J^*i is the curve of delayed compliance.

The criterion of this model is the average error value of all the specimens. By the model, we can have the fitting value for each specimen at each τ (J_{model}). As well as experimental data, we sorted the value at each τ for fitting process (J_{data}). The error value of each specimen is calculated by equation 5.16, and then we can have the average error value.

$$\frac{\sqrt{(J_{model}i - J_{data}i)^2}}{\frac{\sum J_{data}i}{n}} \tag{5.16}$$

The objective of the solver is to minimize the average error of all the specimens, and the variables are i, s, q, and c in the equation 5.13, 5.14, and 5.15. There are 10 variables in sum. In the end, we can have the best parameters which can fit all the data in this study and construct the fitting curves by the characteristic of each specimen. The best fitting parameters are shown in table 5.1, and the fitting curves of each sample are shown in appendix A.

Substituting the parameters in table 5.1 into the equation 5.14 and 5.15, the curves of $b(\log \tau_i)$ and $c(\log \tau_i)$ are shown in figure 5.28. The Y values of $b(\log \tau_i)$ and $c(\log \tau_i)$ mean the linear regression slope in double logarithm plot of J^*i and density and specific modulus.

Comparing the curve $b(\log \tau_i)$ with the regression result of linear model in figure 5.23 (f), the starting value of multiple regression model is closer to the observation of delayed compliance in figure 5.8. Both of them show the upward trend, that is, the slopes of double logarithm plot of density and delayed compliance get slower, closer to zero, with time. It represents that the effect of density decreases with time. It is possible that the position in which the creep behavior takes place is shifted. At the same time, the curve $c(\log \tau_i)$ shows higher similarity with the result in figure 5.25 (f). The slope of double logarithm plot decrease with time stands for the effect of specific modulus increase. We could say that the MFA plays an important role in the long-term creep behavior, and the effect is more pronounce when the loading time is longer. It shows the possibility of the creep behavior transferring to the intercellular space and therefore the influence of MFA improves.

Table 5.1: Best fitting parameters of multiple regression model.

	i	s	q	c
$a(\log \tau_i)$	1.3013E-06	3.1331E-06	7.9299E-06	-3.88E-08
$b(\log \tau_i)$	-1.039901	-0.4530212	0.08035558	
$c(\log \tau_i)$	-1.459376	0.27712181	-0.0634186	
Error	31.9%			

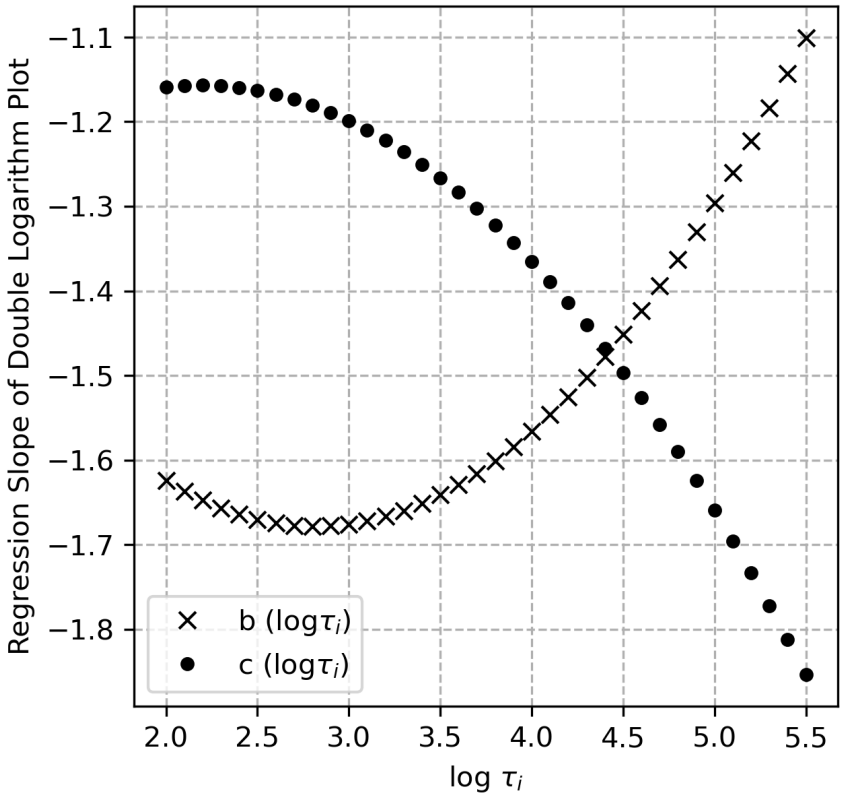

Figure 5.28: Fitting result of $b(\log \tau_i)$ and $c(\log \tau_i)$.

5.6 Summary

The first observation of creep test data show that it is necessary to separate the delayed behavior and elastic behavior in the model. The delayed compliance was defined for modeling. In addition, the effect of density decreases with time. Therefore, the assumed is that the model needs to be separated into two parts as primary and secondary creep.

In the two–mechanism model, the creep curve is separated into primary and secondary creep from loading for 1 day. From the starting of loading to loading for 24 hours was defined as primary creep part, and after that was defined as secondary creep part. Density and specific modulus are considered in the model. The effect of the factors shows the difference between primary and secondary creep. Looking at this phenomenon, we could say that the creep behavior takes place at the cell wall at the primary stage and transfer to intercellular space at the secondary stage.

To understand better the transfer process, the discrete compliance model was designed. A $\log \tau$ isometric series was given which present the Kelvin bodies at different timescale. We can see the changing process of the correlation between the J^*i and density, specific modulus.

Therefore, the multiple regression model is based on assuming that the changing process of regression results can be fitted by the polynomial functions. 10 parameters were found for the three functions, which present time functions of density and specific modulus effects. By this model, the creep behavior can be estimated by the material properties and also shows that the creep behavior of wood starts from the deformation of cell wall, then transfer to other mechanism.

Chapter 6

Conclusions

The aim of this study is to understand the mechanisms of wood creep behavior and to find the main predictors. Compared to other structural materials such as metals or concrete, wood has more different levels of structure and is also highly anisotropic. The mechanical properties of wood are influenced by the different levels of structure, from the angle of microfibrils, which are smaller than the cellular level, to the level of grain, which is visible to the naked eye. All of these properties are determined by the species, the growing environment, the age of the tree, the part of the tree in which it is grown and how it is processed. When we discuss creep behavior, the time factor is taken into account. That is, the loading and environmental history plus the viscoelastic properties of the material will together determine the overall behavior of the material. This is why many studies have shown that it is not possible to develop a general creep theory formulation for all kinds of materials. Materials and test conditions need to be limited, and we can only have specific theories under these conditions.

From the database of this study, we can observe a great variability in this field. The strong anisotropy of wood also makes the influence of the test method more obvious. From the process of categorizing and comparing the data, we can observe that the factors are strongly interacting with each other.

In this study, the use of small clear wood was able to control the macroscopic material properties and reduce its variability. The sampling and analysis process is based on density, specific modulus and delta Ono values. Density corresponds to material properties larger than cellular scale. Specific modulus corresponds to the property of the material that is smaller than the cellular scale, which is the microfibril angle or the grain angle. Delta Ono value corresponds to the chemical property, such as extractive content. Through vibration tests, we can obtain the specific modulus and delta Ono values as predictors of creep behavior. This makes it possible to relate material properties between different time scales. The 10-days 4-point bending creep test was conducted in a climatic chamber to eliminate environmental effects. The creep test results are ideally affected only by the nature of the material at the cellular scale.

The most important assumption of the model in this study is that if delayed compliance is proportional to density, then creep behavior occurs only at the cell wall. It is proved in the linear model. However, we also observed that the magnitude of the effect of these factors on creep behaviors changed over time. Through the fitting compliance model, we find the compliance parameter values at specific time points. This trend is not completely linear. Therefore, in the multiple regression model, we assume that the relationship between creep

parameters and time is a polynomial function, which shows the degree of influence of material properties on the creep behavior change with time. The fitting results show that the effect of density decreases with time, while the effect of specific modulus increases. From this, we can infer that the creep behavior of wood starts with the deformation of the cell walls and then shifts to the intercellular space, which is related to the MFA and the grain angle and is presented by the specific modulus.

The final model of this study remains empirical. It is fitted by experimental results, and there is still space for discussion, and corrections will be required with different experimental operating conditions. In addition, the hypotheses in this study need to be confirmed by more precise experiments in order to better understand the transfer mechanism of the forces on the material during the whole process of creep behavior.

The method in the study is based on only four species in a specific temperature and humidity environment and should be extended to several weeks or months to provide more reliable results. Also, we focused on small clear wood, and we can upgrade to timber elements (with grain variations, knots, small cracks, etc.) for more realistic results, or even use a digital monitoring system for structural elements on real building elements. However, the selection of tree species for a construction project is often previously determined by the price of lumber or the company used to carry it out. In addition, in the European standard, a single prediction factor k_def is provided to estimate long-term deflection (one value for all large wood materials of any species and only 3 values for each service class) and the results presented may lead to propose a more specific approach, for example, linked to strength classes of softwoods and hardwoods, each class being classified by density (NFEN388, 2009). Damping measurements could be linked to verification testing of sawn timber element to provide the end–user information on long-term deformation potential, e.g. for CE certification of sawn timber tested in the production line.

References

H. Abe and R. Funada. The orientation of cellulose microfibrils in the cell walls of tracheids in conifers. *Iawa Journal*, 26(2):161–174, 2005.

L. D. Armstrong and R. S. T. Kingston. Effect of moisture changes on creep in wood. *Nature*, 1960.

R. Astley, K. Stol, and J. Harrington. Modelling the elastic properties of softwood. *Holz als Roh-und Werkstoff*, 56(1):43–50, 1998.

H. T. Banks, S. Hu, and Z. R. Kenz. A brief review of elasticity and viscoelasticity for solids. *Advances in Applied Mathematics and Mechanics*, 3(1):1–51, 2011.

Z. P. Bazant and S. Baweja. Creep and shrinkage prediction model for analysis and design of concrete structures: Model b3. *ACI Special Publications*, 194:1–84, 2000.

J. F. Bell. Experimental solid mechanics in the nineteenth century. *Experimental mechanics*, 29(2):157–165, 1989.

J. Betten. *Creep Mechanics*. Springer-Verlag Berlin Heidelberg, Berlin, Heidelberg, third edition edition, 2008. ISBN 9783540850502. 10.1007/978-3-540-85051-9.

N. Bhatnagar. Kriechen von holz bei zugbeanspruchung in faserrichtung. *Holz als Roh-und Werkstoff*, 22(8): 296–299, 1964.

H. J. Blaß and C. Sandhaas. *Timber engineering-principles for design*. KIT Scientific Publishing, 2017.

J. Bodig and B. A. Jayne. *Mechanics of wood and wood composites*. Van Nostrand Reinhold, New York, 1982.

L. Brancheriau and H. Baillères. Natural vibration analysis of clear wooden beams: a theoretical review. *Wood Science and Technology*, 36(4):347–365, 2002.

L. Brancheriau, C. Kouchade, and I. Brémaud. Internal friction measurement of tropical species by various acoustic methods. *Journal of Wood Science*, 56(5):371–379, 2010.

I. Brémaud, Y. El Kaïm, D. Guibal, K. Minato, B. Thibaut, and J. Gril. Characterisation and categorisation of the diversity in viscoelastic vibrational properties between 98 wood types. *Annals of Forest Science*, 69 (3):373–386, 2012. ISSN 1286-4560. 10.1007/s13595-011-0166-z.

I. Brémaud, J. Ruelle, A. Thibaut, and B. Thibaut. Changes in viscoelastic vibrational properties between compression and normal wood: roles of microfibril angle and of lignin. *Holzforschung*, 67(1):75–85, 2013. ISSN 0018-3830. 10.1515/hf-2011-0186.

Brian H. Bond. *Development of Tension and Compression Creep Model for Wood using the Time-Temperature Superposition Principle*. Publication, Virginia Tech, 1993.

V. Bucur and P. A. Martin. *Delamination in wood, wood products and wood-based composites*. Springer, 2011.

CIRAD. The main technological characteristics of 245 tropical wood species, 2017. URL https://tropix.cirad.fr/en/fiches-disponibles.

D. P. Delmer and Y. Amor. Cellulose biosynthesis. *The plant cell*, 7(7):987, 1995.

C. Dong, S. Zhang, J. Wang, and Y. H. Chui. Static bending creep properties of furfurylated poplar wood. *Construction and Building Materials*, 269(5):121308, 2021. ISSN 09500618. 10.1016/j.conbuildmat.2020.121308.

A. Foudjet and C. Bremond. Creep of four tropical hardwoods from cameroon. *Wood Science and Technology*, 23(4):335–341, 1989.

E. Fukada. The vibrational properties of wood i. *Journal of the Physical Society of Japan*, 5(5):321–327, 1950.

E. Fukada. The vibrational properties of wood. ii. *Journal of the Physical Society of Japan*, 6(6):417–421, 1951.

E. J. Gibson. Creep of wood: Role of water and effect of a changing moisture content. *Nature*, 1965.

R. Gnanaharan and J. Haygreen. Comparison of the creep behavior of a basswood waferboard to that of solid wood. *Wood and Fiber Science*, pages 155–170, 1979.

G. Granello and A. Palermo. Creep in timber: Research overview and comparison between code provisions. *New Zeland Timber Design Journal*, 2019.

P. Grossman and R. Kingston. *Some Aspects of the Rheological Behaviour of Wood*. Commonwealth Scientific and Industrial Research Organization, 1963.

P. U. A. Grossman and R. S. T. Kingston. Creep and stress relaxation in wood during bending. *Australian Journal of Applied Science*, 1954.

R. M. Guedes. *Creep and fatigue in polymer matrix composites*. Woodhead Publishing, 2011.

D. Guitard. *Mécanique du matériau bois et composites*. Cépaduès, 1987.

J. J. Harrington. *Hierarchical modelling of softwood hygro-elastic properties*. Publication, University of Canterbury, 2002.

M. Harrington. Schematische darstellung des hierarchischen aufbaus der nadelbäume. *Graphische Gestaltung durch Mark Harrington. University of Canterbury. Online verfügbar unter http://www. mpikg. mpg. de/8782/research_ report_ 393531*, 1996.

T. Hayashi. Xyloglucans in the primary cell wall. *Annual review of plant biology*, 40(1):139–168, 1989.

S. Hering and P. Niemz. Moisture-dependent, viscoelastic creep of european beech wood in longitudinal direction. *European Journal of Wood and Wood Products*, 70(5):667–670, 2012. ISSN 0018-3768. 10.1007/s00107-012-0600-4.

A. Hermawan and N. Fujimoto. Viscoelastic creep behavior of surface- and inner-layers of sugi boxed-heart timber under various temperatures. *Journal of Wood Science*, 65(1):350, 2019. ISSN 1435-0211. 10.1186/s10086-019-1836-y.

S. M. Holzer, J. R. Loferski, and D. A. Dillard. A review of creep in wood concepts relevant to develop long-term behavior predictions for wood structures. *Wood and Fiber Science*, 21(4):376–392, 1989.

D. N.-S. Hon and N. Shiraishi. *Wood and cellulosic chemistry, revised, and expanded*. CRC press, 2000.

R. J. Hoyle, M. C. Griffith, and R. Y. Itani. Primary creep in douglas-fir beams of commercial size and quality. *Wood and Fiber Science*, pages 300–314, 1985.

H. Huang, S. Mojumder, D. Suarez, A. Al Amin, M. Fleming, and W. K. Liu. Knowledge database creation for design of polymer matrix composite. *Computational Materials Science*, 214:111703, 2022.

M. H. Hubler, R. Wendner, and Z. P. Bažant. Comprehensive database for concrete creep and shrinkage: Analysis and recommendations for testing and recording. *ACI Materials Journal*, 112(2), 2015. ISSN 0889-325X. 10.14359/51687452.

D. G. Hunt. Linearity and non-linearity in mechano-sorptive creep of softwood in compression and bending. *Wood science and technology*, 23(4):323–333, 1989.

InsideWood. Inside wood, 2004. URL https://insidewood.lib.ncsu.edu/welcome.

F. Karlsruhe. Icsd - the world's largest database for completely identified inorganic crystal structures, 1913. URL https://icsd.products.fiz-karlsruhe.de/.

A. Kataoka and T. Ono. The relation of experimental factors to vibration and the measuring values of dynamic mechanical properties of wood 1. *Journal of the Japan Wood Research Society (Japanese)*, 1975.

Y. Kataoka, H. Saiki, and M. Fujita. Arrangement and superimposition of cellulose microfibrils in the secondary walls of coniferous tracheids. *Journal of the Japan Wood Research Society (Japanese)*, 1992.

Y. Kojima and H. Yamamoto. Effect of microfibril angle on the longitudinal tensile creep behavior of wood. *Journal of Wood Science*, 50(4):301–306, 2004. ISSN 1435-0211. 10.1007/s10086-003-0565-3.

F. Kollmann. Über unterschiede im rheologischen verhalten von holz und holzwerkstoffen bei querdruckbelastung. *Forschung auf dem Gebiet des Ingenieurwesens A*, 23(1):49–54, 1957.

F. F. P. Kollmann and W. A. Côté. *Principles Of Wood Science And Technology*. Springer, 1968.

P. Langbour, S. Paradis, and B. Thibaut. Description of the cirad wood collection in montpellier, france, representing eight thousand identified species. *BOIS & FORETS DES TROPIQUES*, 339:7–16, 2019.

G.-L. Leclerc and C. de Buffon. Experiences sur la force du bois. *Mémoires de mathématique et de physique*, pages 453–467, 1740.

T. Liu. Creep of wood under a large span of loads in constant and varying environments. *Holz als Roh-und werkstoff*, 51(6):400–405, 1993.

Y. Liu, T. Zhao, W. Ju, and S. Shi. Materials discovery and design using machine learning. *Journal of Materiomics*, 3(3):159–177, 2017.

S. B. Maidin, I. Campbell, and E. Pei. Development of a design feature database to support design for additive manufacturing. *Assembly Automation*, 2012.

A. Mårtensson. Mechano-sorptive effects in wooden material. *Wood Science and Technology*, 28(6):437–449, 1994.

A. Matar. *The mechano sorptive creep of softwood in bending*. PhD thesis, South Bank University, 2003.

E. Meier. The wood database, 2008. URL `https://www.wood-database.com/`.

W. Moliński and J. Raczkowski. Creep of wood in bending and non-symmetrical moistening. *Holz als Roh-und Werkstoff*, 46(12):457–460, 1988.

C. Montero. *Caractérisation du comportement viscoélastique asymptotique du bois*. Publication, Université de Montpellier, 2011.

C. Montero and J. Gril. Comparison between wood hygromechanical description and deformation modification factors of eurocode 5. In *World Congress of Timber Engineering (WCTE 2016)*, 2016.

V. Moosavi, H. K. Eslam, B. Bazyar, A. Najafi, and M. Talaeepoor. Bending creep behavior of hornbeam wood. *Drvna industrija*, 67(4):341–350, 2016. ISSN 00126772. 10.5552/drind.2016.1609.

P. Morlier. *Creep in Timber Structures*. E and F Spon, 1994.

T. Nakai and P. Grossman. Deflection of wood under intermittent loading. *Wood Science and Technology*, 17(1):55–67, 1983.

NFEN14081-1. Structures en bois - Bois de structure à section rectangulaire classé pour sa résistance - Partie 1 : Exigences générales. Standard, AFNOR, France, Apr. 2016.

NFEN388. Structures en bois - Classes de resistance. Standard, AFNOR, France, Dec. 2009.

T. Nilsson and R. Rowell. Historical wood – structure and properties. *Journal of Cultural Heritage*, 13(3): S5–S9, 2012. ISSN 12962074. 10.1016/j.culher.2012.03.016.

C. Norris and W. J. Kommers. Plastic flow (creep) properties of two yellow birch plywood plates under constant shear stress. *Report of United States Department of Agriculture Forest Service*, 1960.

T. Ono and M. Norimoto. Study on young's modulus and internal friction of wood in relation to the evaluation of wood for musical instruments. *Japanese journal of Applied physics*, 22(4R):611, 1983.

T. Ono and M. Norimoto. On physical criteria for the selection of wood for soundboards of musical instruments. *Rheologica Acta*, 23(6):652–656, 1984.

T. Ozyhar, S. Hering, and P. Niemz. Moisture-dependent orthotropic tension-compression asymmetry of wood. *Holzforschung*, 67(4):395–404, 2013. ISSN 0018-3830. 10.1515/hf-2012-0089.

V. Pittet. *Etude expérimentale des couplages mécanosorptifs dans le bois soumis à variations hygrométriques contrôlées sous chargements de longue durée*. Publication, EPFL, 1996.

C. Popescu, C. Vasile, M. Popescu, G. Singurel, V. Popa, and B. Munteanu. Analytical methods for lignin characterization. ii. spectroscopic studies. *Cellulose chemistry and technology*, 40(8):597, 2006.

C. Richter. *Wood Characteristics*. Springer International Publishing, Cham, 2015. ISBN 978-3-319-07421-4. 10.1007/978-3-319-07422-1.

A. Rusinko and K. Rusinko. *Plasticity and creep of metals*. Springer Science & Business Media, 2011.

A. P. Schniewind. Recent progress in the study of the rheology of wood. *Wood Science and Technology*, 2(3): 188–206, 1968.

A. P. Schniewind and J. Barrett. Wood as a linear orthotropic viscoelastic material. *Wood Science and Technology*, 6(1):43–57, 1972.

F. H. Schweingruber and A. Börner. *The plant stem: a microscopic aspect*. Springer, 2018.

R. Shmulsky and P. D. Jones. *Forest products and wood science: An introduction*. Wiley-Blackwell, Chichester West Sussex U.K. and Ames Iowa, 6th ed. edition, 2011. ISBN 081382074X.

V. I. Slivker. *Mechanics of structural elements: Theory and applications*. Foundations of engineering mechanics. Springer, Berlin and New York, 2007. ISBN 3540447180.

N. Sun and C. E. Frazier. Time/temperature equivalence in the dry wood creep response. *Holzforschung*, 2007.

A. Temesgen, S. Singh, and T. Pankaj. Modeling of creep deformation of a transversely isotropic rotating disc with a shaft having variable density and subjected to a thermal gradient. *Thermal Science and Engineering Progress*, 20:100745, 2020.

J. Tissaoui. *Effects of long-term creep on the integrity of modern wood structures*. Publication, Virginia Tech, 1996.

D. Tong, S. A. Brown, D. Corr, and G. Cusatis. Wood creep data collection and unbiased parameter identification of compliance functions. *Holzforschung*, 74(11):1011–1020, 2020.

TRADA. The timber research and development association, 1934. URL https://www.trada.co.uk/.

N. W. Tschoegl. *The phenomenological theory of linear viscoelastic behavior: an introduction*. Springer Science & Business Media, 2012.

USDA Forest Service. *Wood Handbook: Wood as an Engineering Material*. USDA Forest Service, 2021.

M. Varnier. *Comportement thermo-hygro-mécanique différé des feuillus: des sciences du bois à l'ingénierie*. Publication, Université de Limoges, 2019.

J. Vobolis and M. Aleksiejunas. Investigation of wood mechanical properties by the resonance vibration method. *Mater Sci*, 9(1):139–43, 2003.

E. Wheeler. Insidewood - a web resource for hardwood anatomy. *IAWA Journal*, 32(2):199–211, 2011.

A. C. Wiedenhoeft and R. B. Miller. Structure and function of wood. *Handbook of wood chemistry and wood composites*, pages 9–33, 2005.

R. L. Youngs. *The perpendicular-to-grain mechanical properties of red oak as related to temperature, moisture content, and time*. Publication, Yale University, 1957.

D. Zagorac, H. Müller, S. Ruehl, J. Zagorac, and S. Rehme. Recent developments in the inorganic crystal structure database: theoretical crystal structure data and related features. *Journal of applied crystallography*, 52(5):918–925, 2019.

Appendix A

Multiple Regression Model Fitting Result

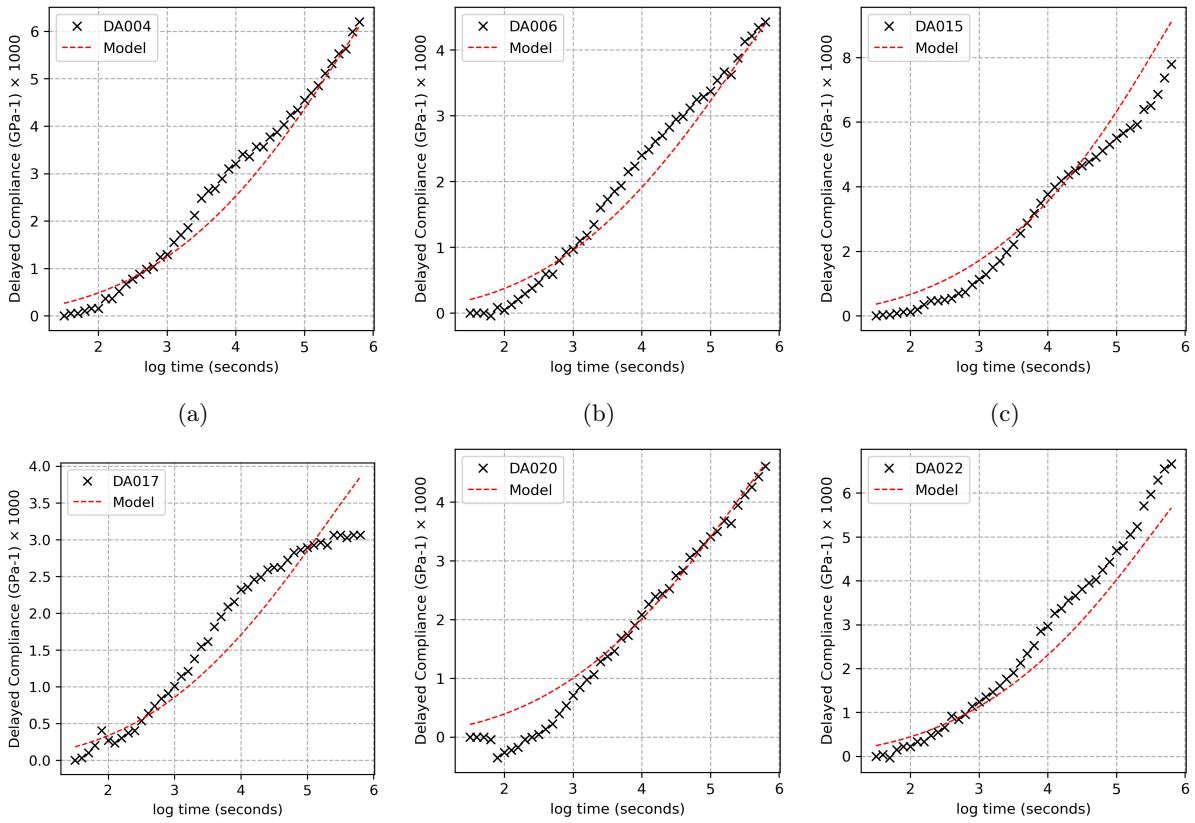

Figure A.1: Multiple regression model fitting results of Douglas fir.

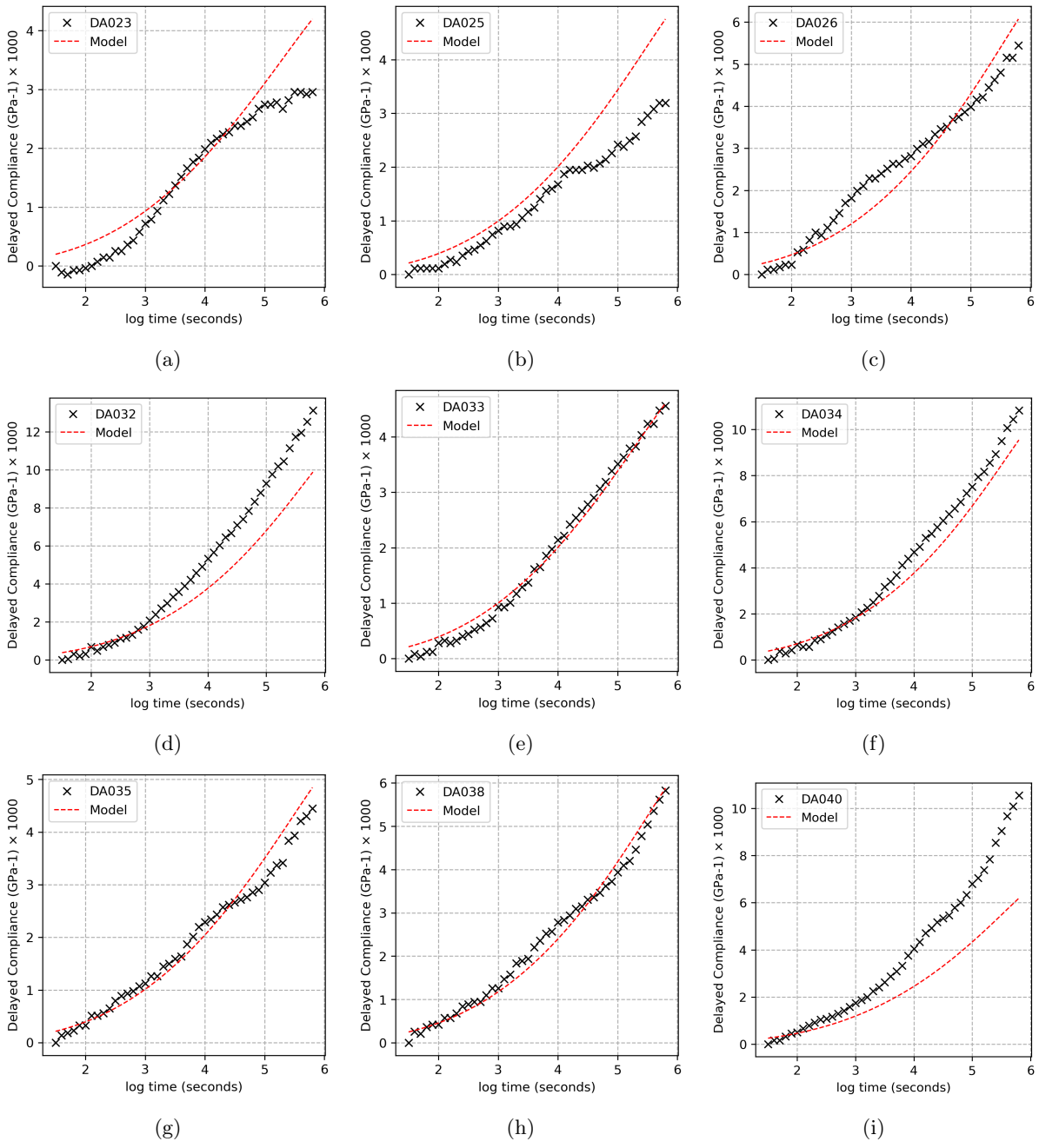

Figure A.2: Multiple regression model fitting results of Douglas fir (Continue).

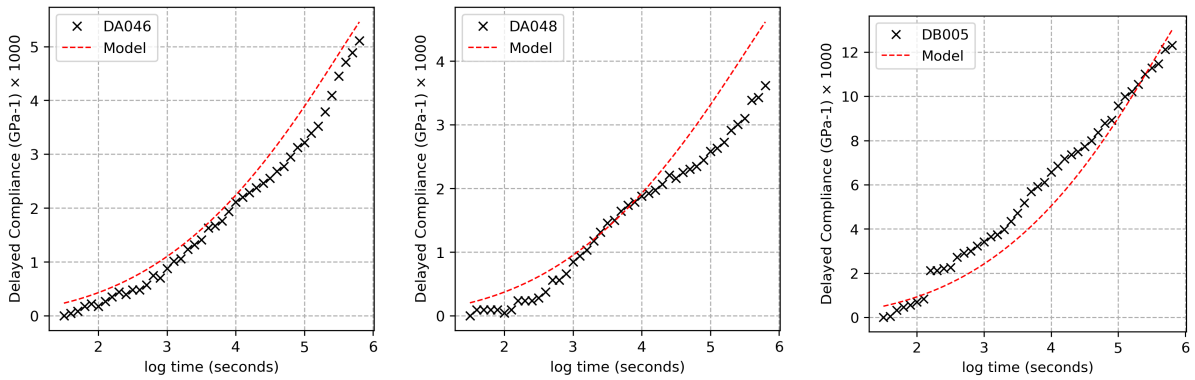

(a)

(b)

(c)

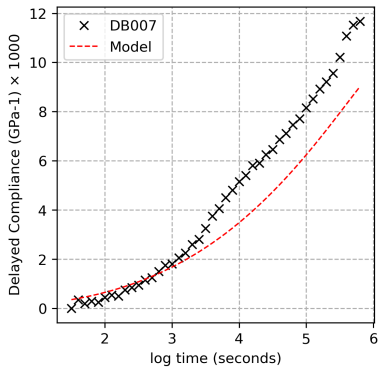

(d)

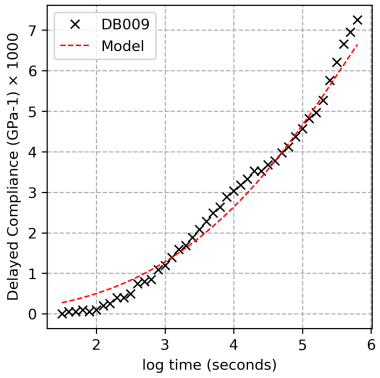

(e)

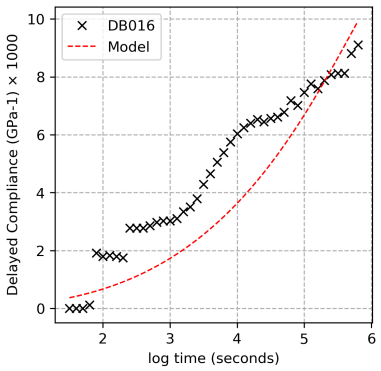

(f)

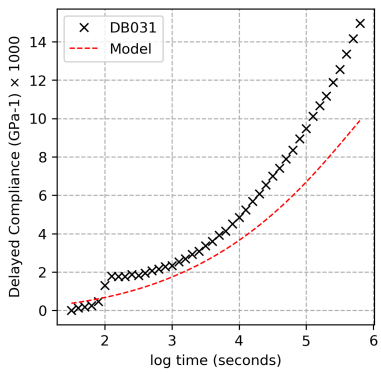

(g)

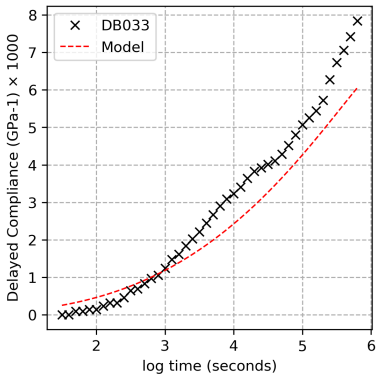

(h)

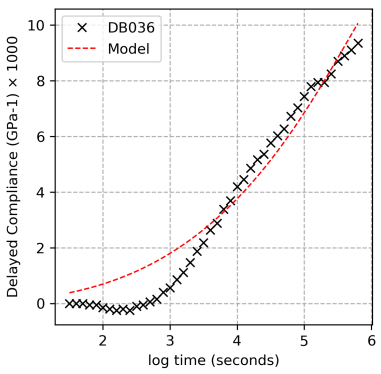

(i)

Figure A.3: Multiple regression model fitting results of Douglas fir (Continue)

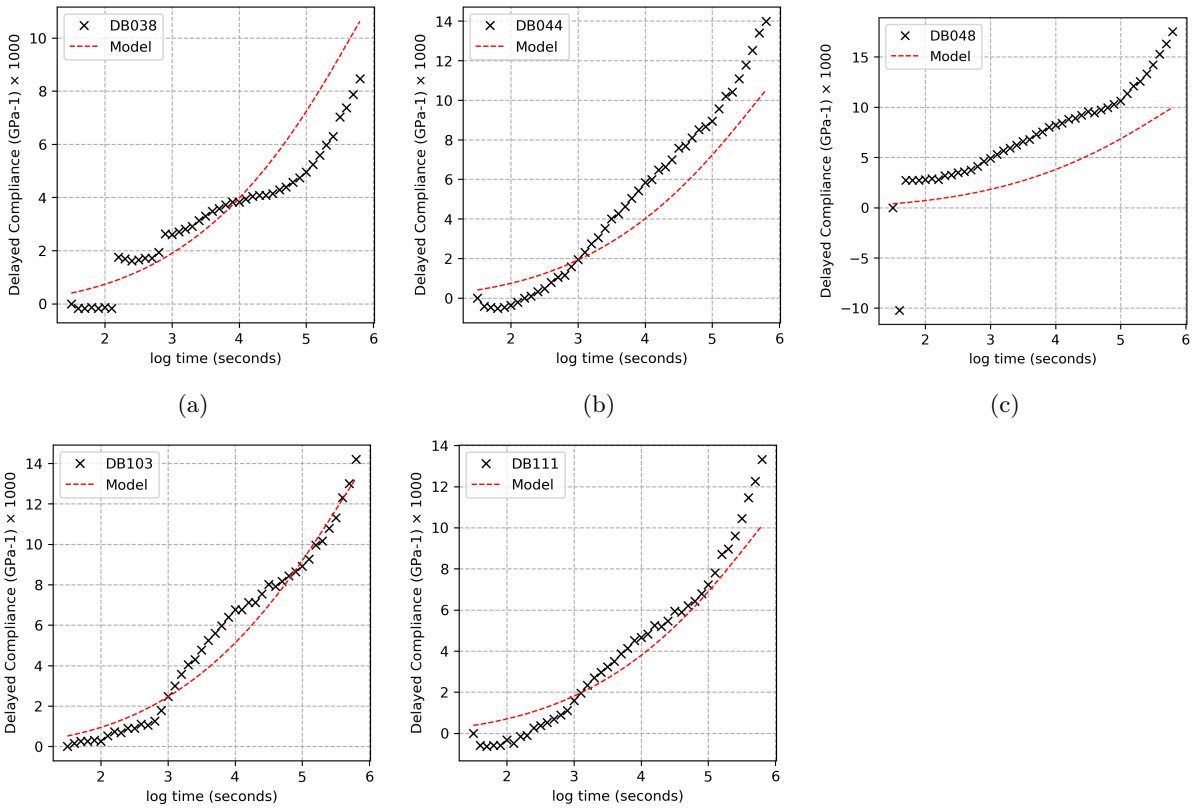

Figure A.4: Multiple regression model fitting results of Douglas fir (Continue).

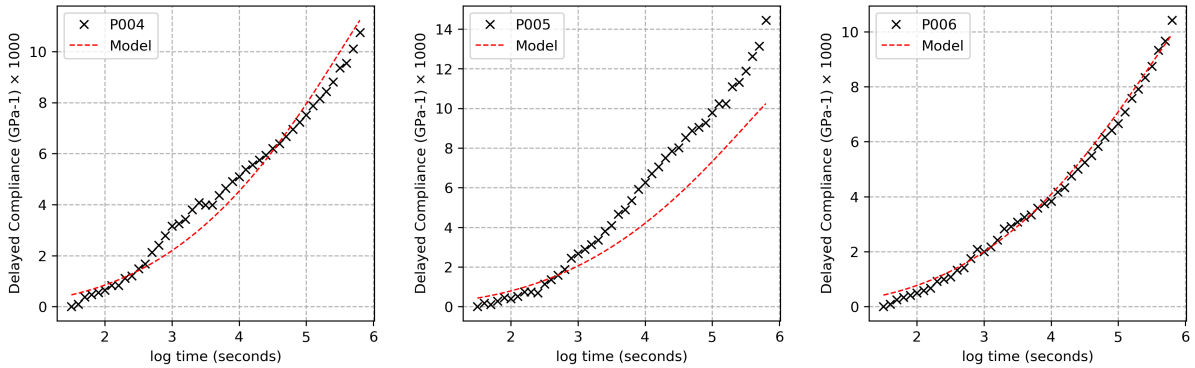

(a)

(b)

(c)

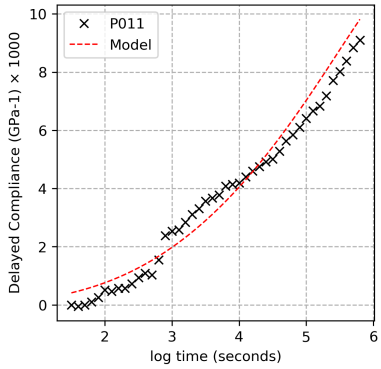

(d)

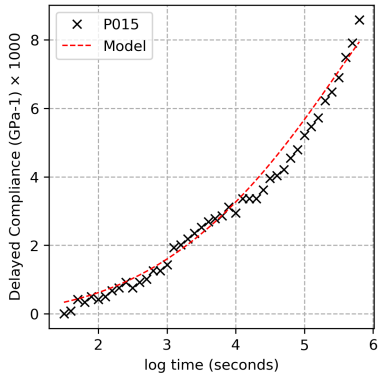

(e)

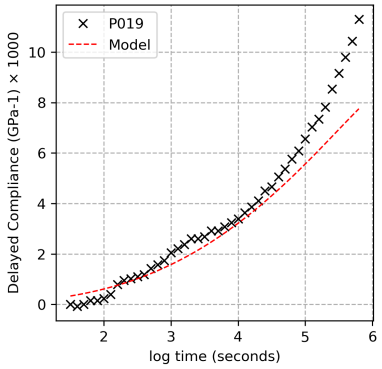

(f)

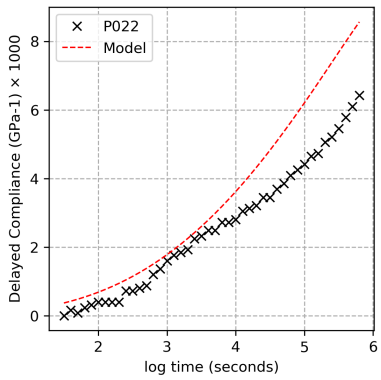

(g)

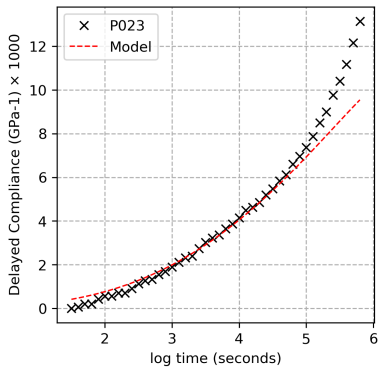

(h)

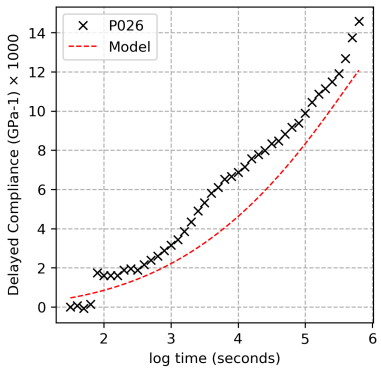

(i)

Figure A.5: Multiple regression model fitting results of Poplar.

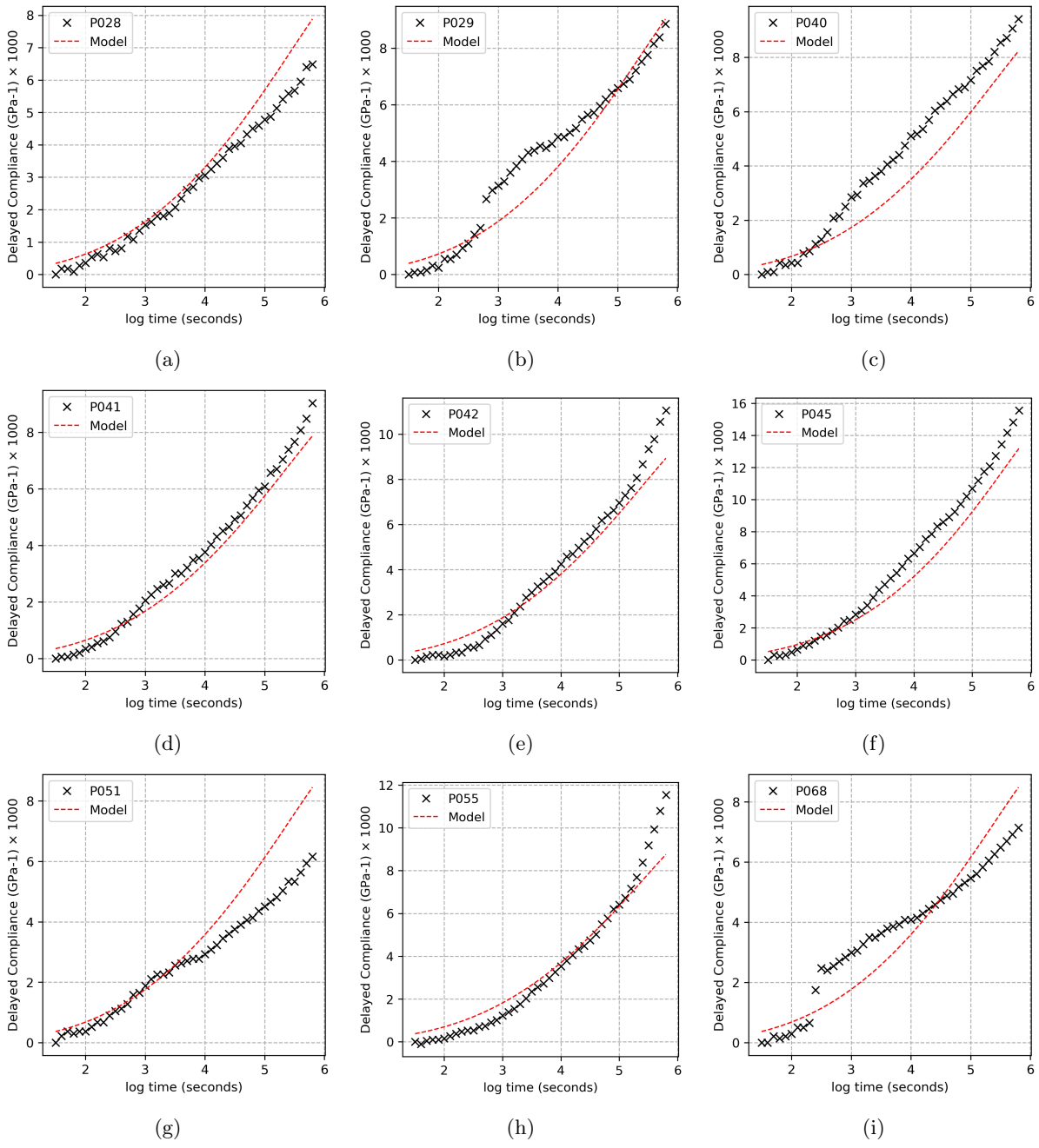

Figure A.6: Multiple regression model fitting results of Poplar (Continue).

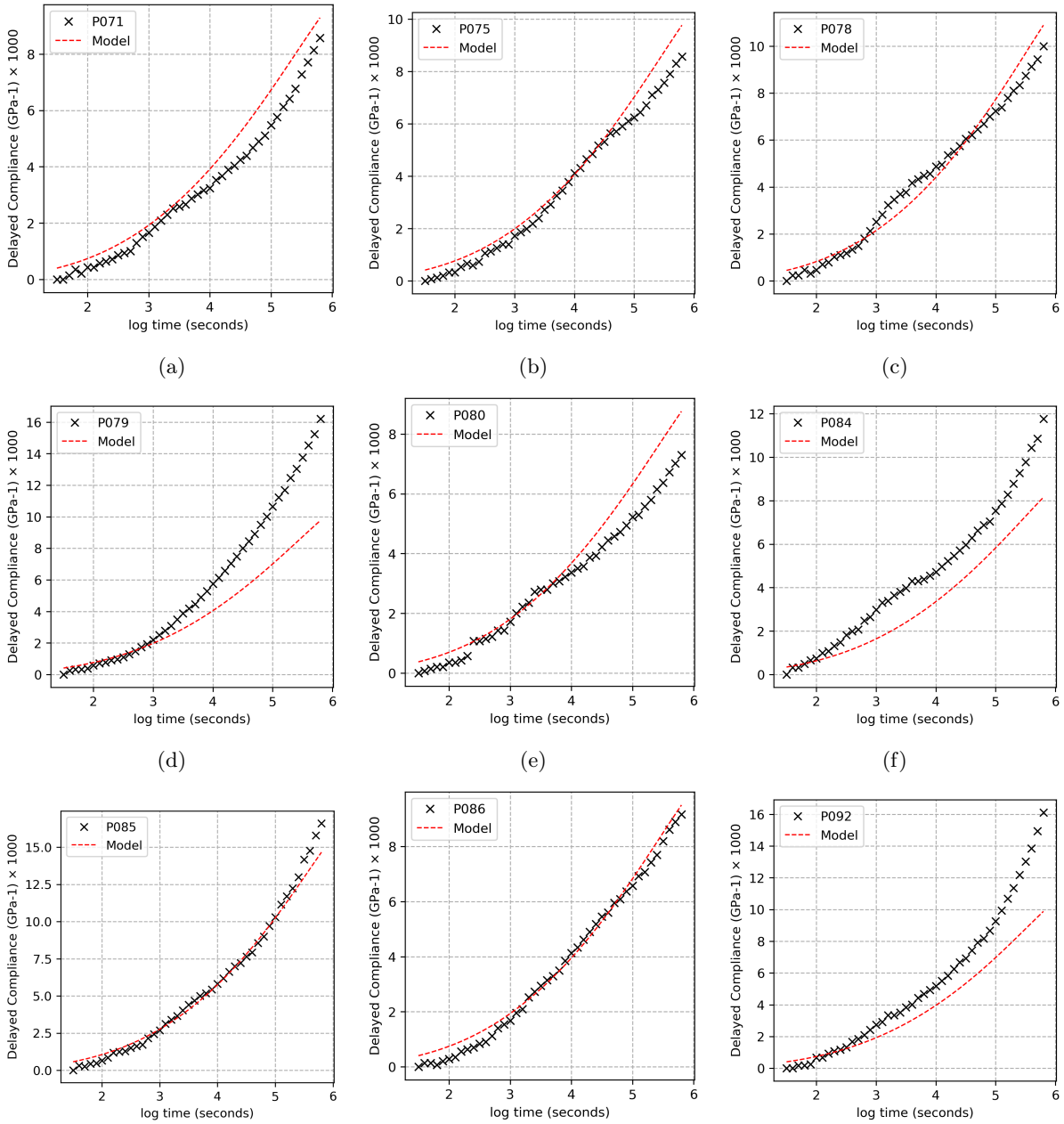

Figure A.7: Multiple regression model fitting results of Poplar (Continue).

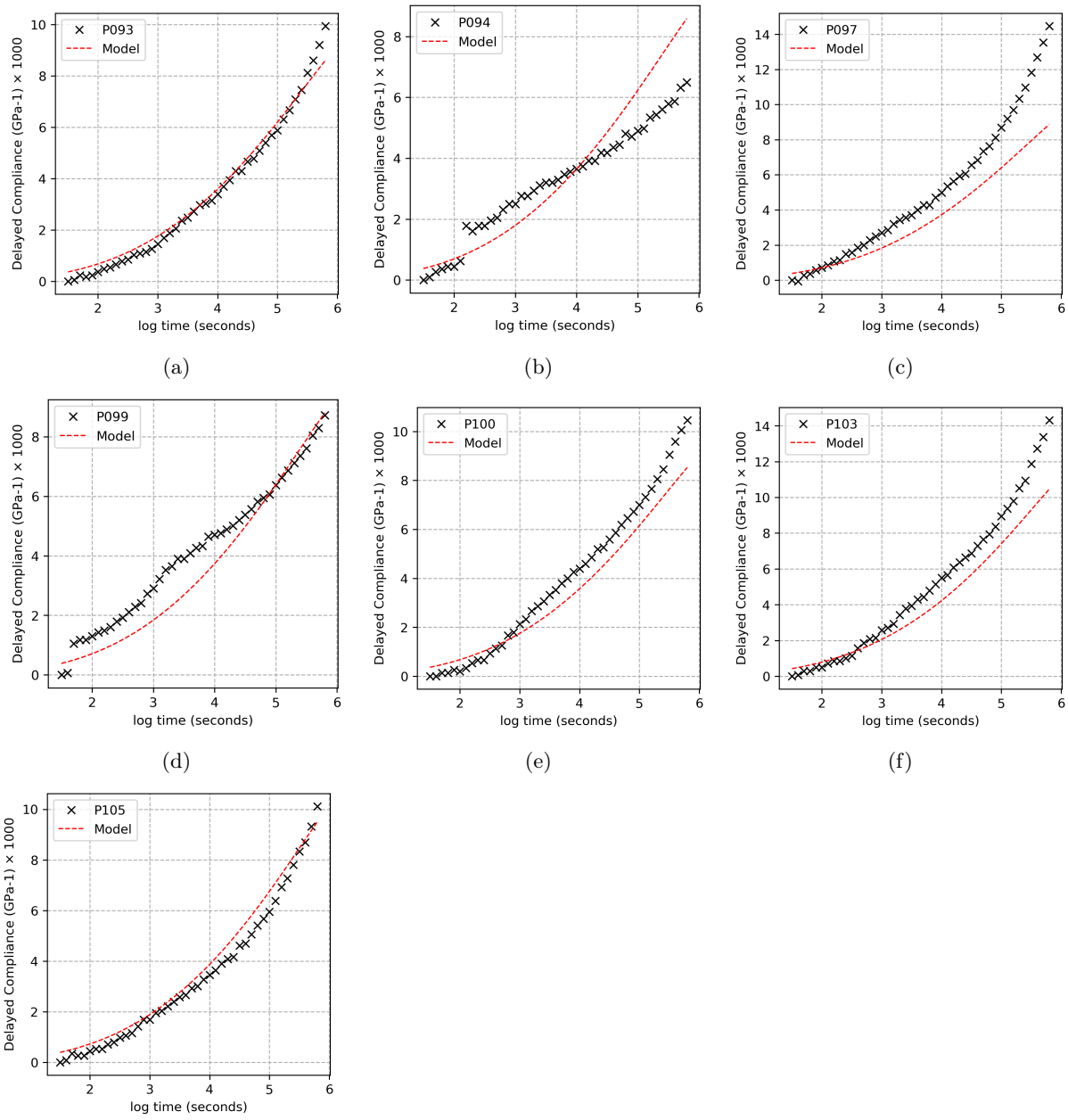

Figure A.8: Multiple regression model fitting results of Poplar (Continue).

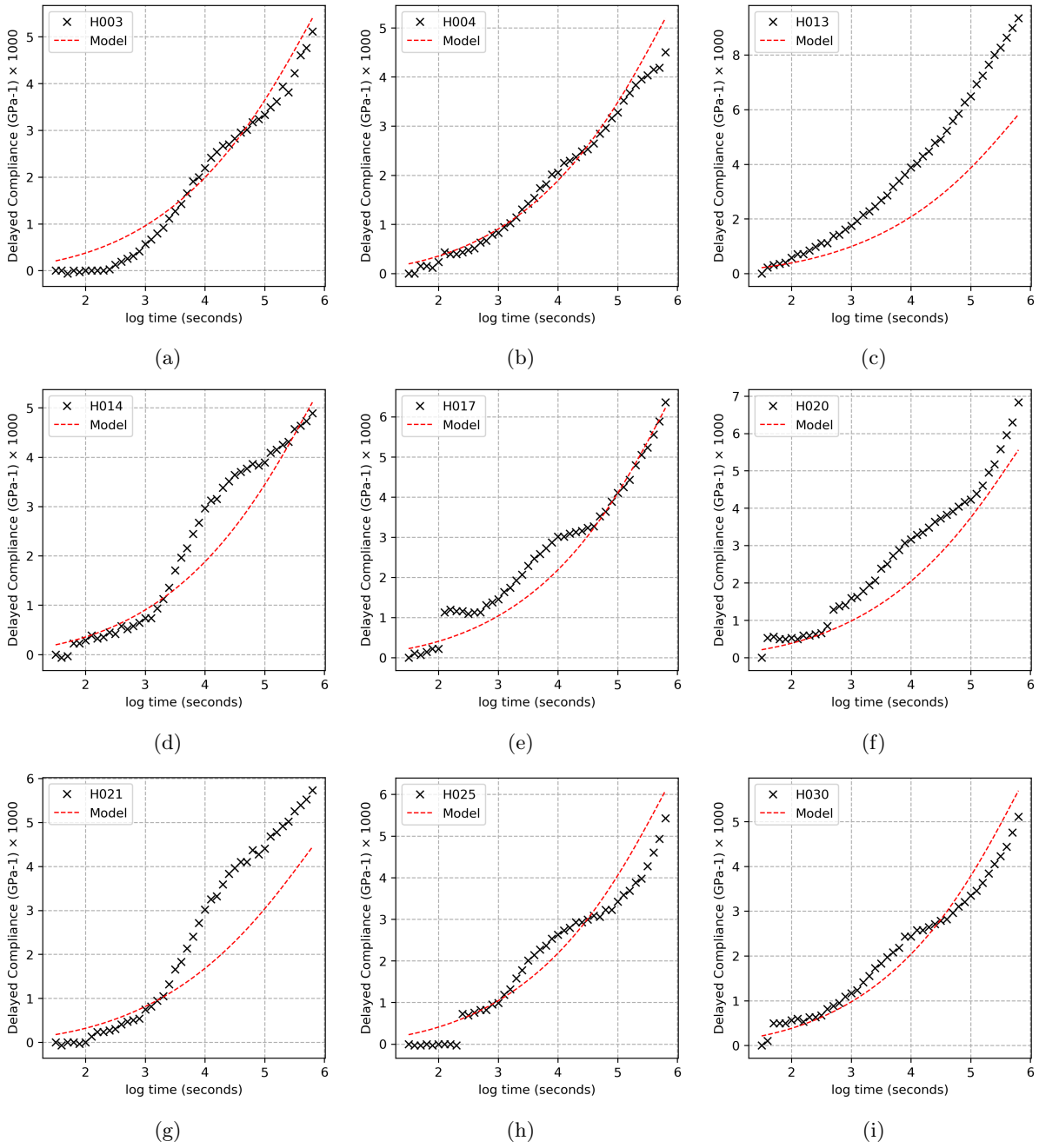

Figure A.9: Multiple regression model fitting results of Beech.

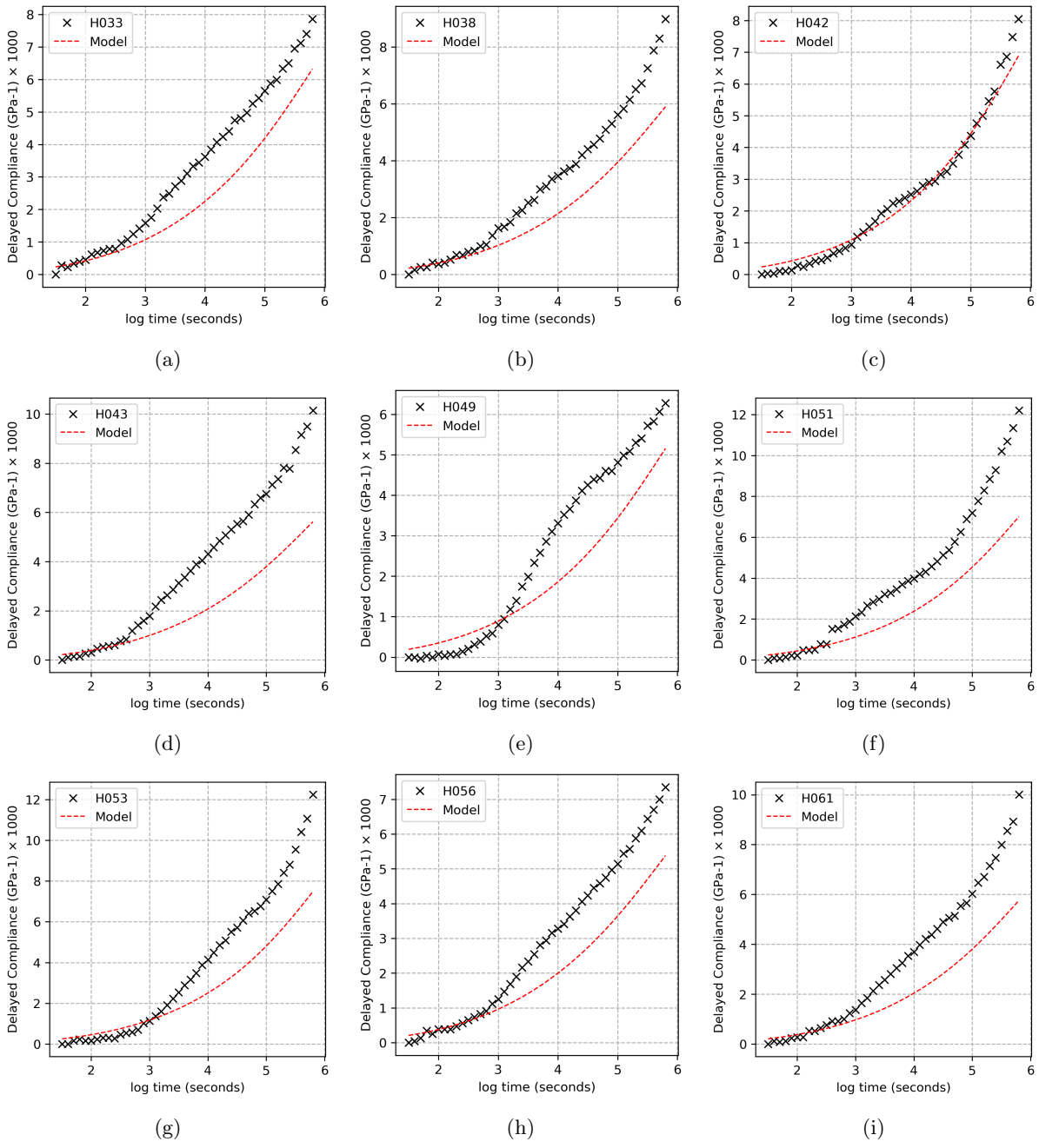

Figure A.10: Multiple regression model fitting results of Beech (Continue).

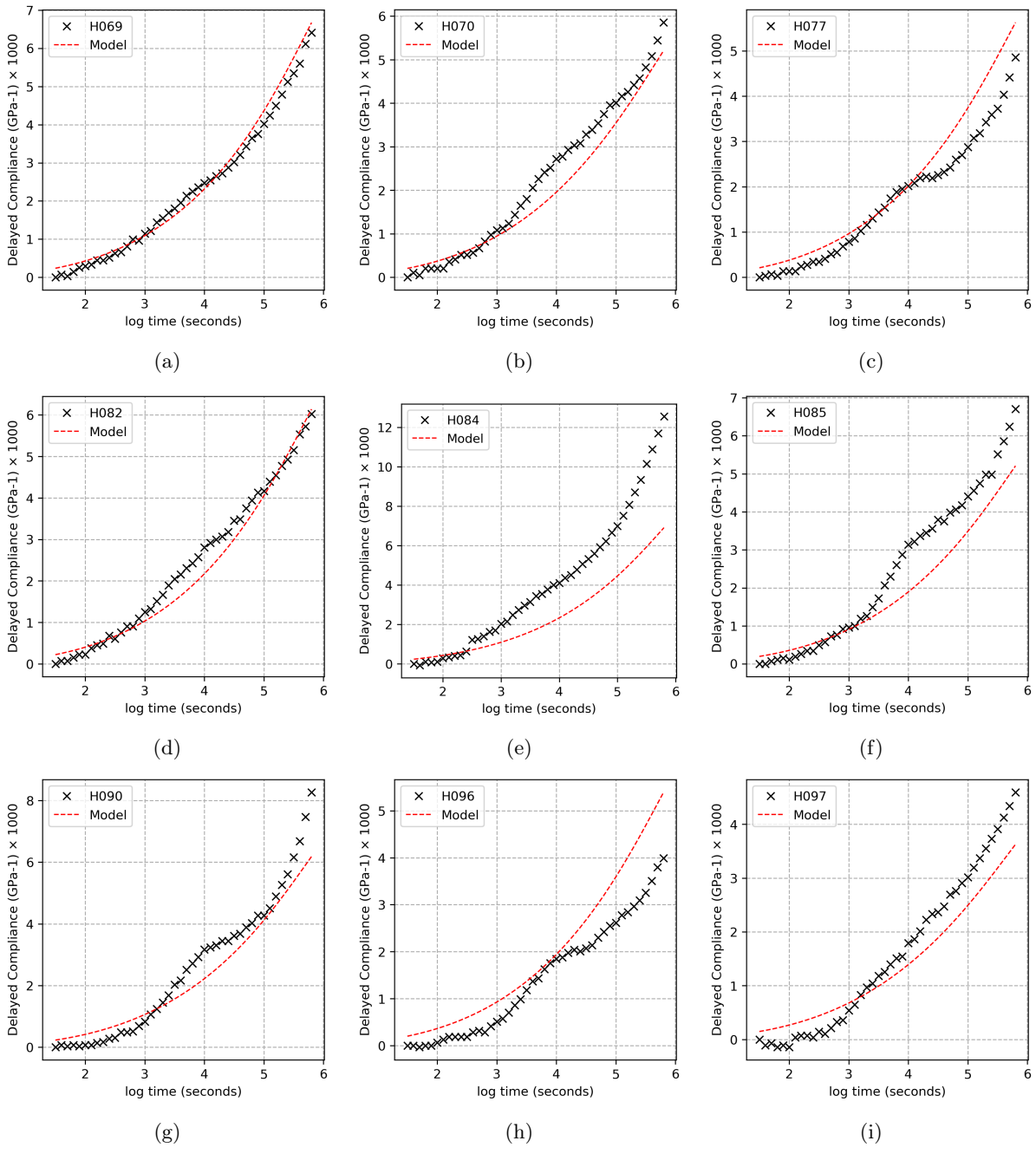

Figure A.11: Multiple regression model fitting results of Beech (Continue).

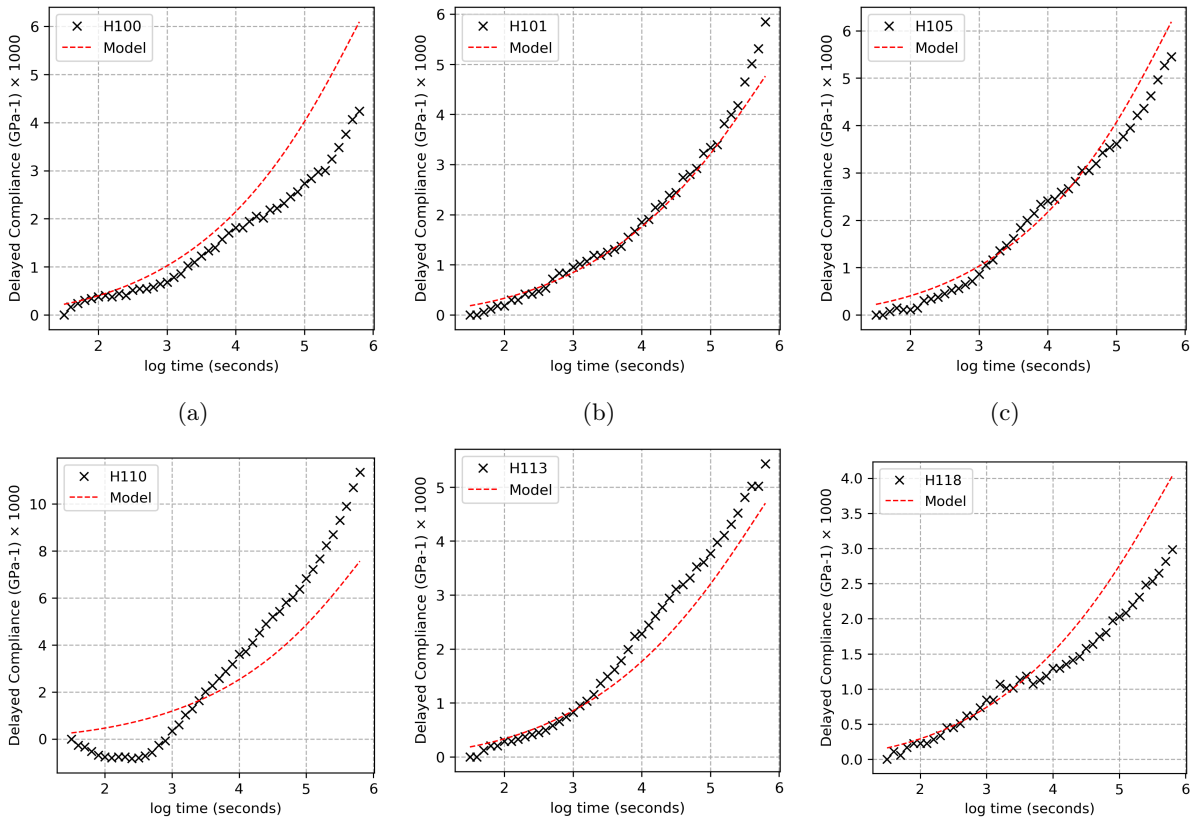

Figure A.12: Multiple regression model fitting results of Beech (Continue).

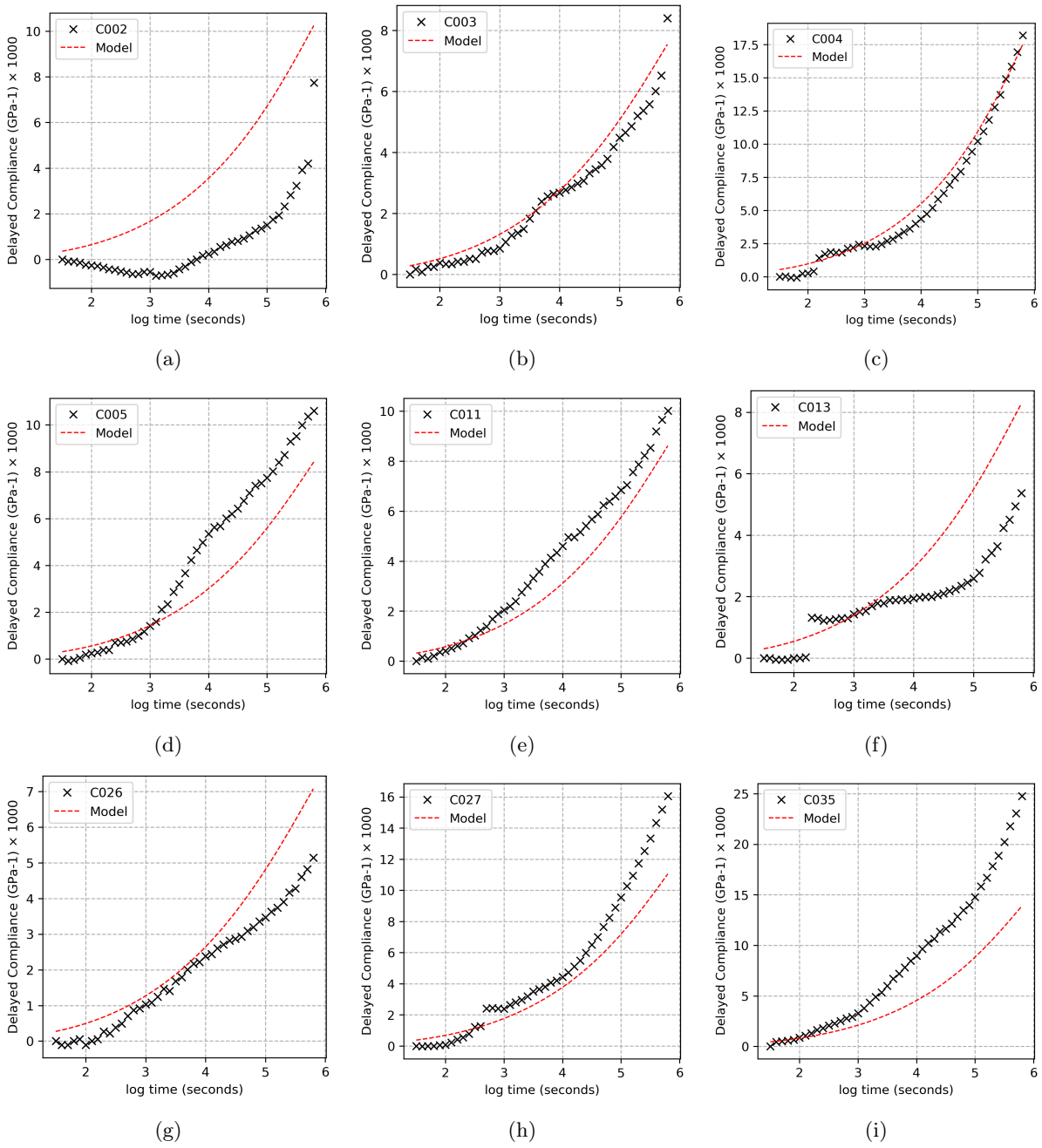

Figure A.13: Multiple regression model fitting results of Oak.

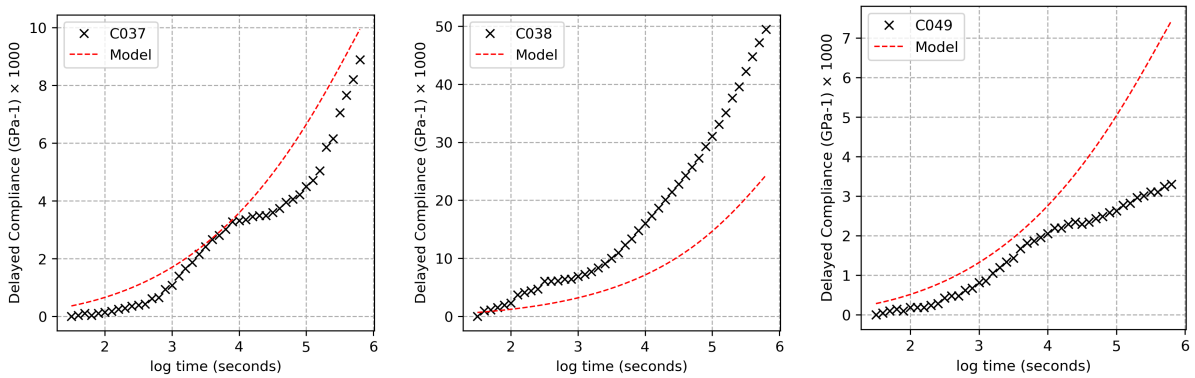

(a) (b) (c)

Figure A.14: Multiple regression model fitting results of Oak (Continue).

Résumé Long

Le bois est utilisé comme matériau de construction depuis des temps très anciens. Tous les matériaux structurels doivent faire face aux défis du temps et du climat. Le comportement de fluage est un phénomène mécanique où la déformation augmente avec le temps, à niveau de chargement constant. Lorsque le fluage atteint les limites mécaniques du matériau (en déformation ou en contrainte), la rupture apparaît. La première observation scientifique du comportement de fluage du bois a été publiée par Armstrong au début des années 1950. Depuis lors, des études successives ont été menées sur différentes essences et différentes méthodes d'essai. Jusqu'à ces dernières années, il n'y a toujours pas de théorie claire sur le mécanisme du comportement de fluage du bois.

L'étude présentée dans ce manuscrit a commencé par un aperçu du matériau bois et la construction d'une base de données sur le fluage du bois qui présente une synthèse des méthodes et des résultats des essais de fluage de la littérature.

Nous avons constaté qu'il y a une grande variabilité sur la condition de l'environnement d'essai et la présentation de donnée. Pour la condition de l'environnement d'essai, ils peuvent généralement être divisé comme trois types : la condition non contrôlée, l'environnement cyclique et l'environnement constant. Même pour les essais en environnement constant, les auteurs observent des paramètres de fluage différent et présentent les résultats de façon très variable. Pour pouvoir comparer les données de littératures, toutes les données étaient recalculées comme complaisance et le temps en second. Les informations des essais étaient organisée dans une méta donnée et donnent avec la courbe du fluage par « Key number ». Nous avons constaté que la première chose qu'affect fortement le fluage du bois est l'angle du fil. Il existe aussi une certaine variabilité dans le comportement du matériau en raison des différentes méthodes expérimentales utilisées. L'environnement d'essai est un facteur variable, mais nous ne pouvons pas encore trouver une tendance claire dans la base de données. Selon le résultat de la base de données, nous avons choisi l'expérience du fluage en flexion 4 point avec une température de 20 degrés et une humidité relative 85% pour comparer uniquement l'effet de la caractéristique des matériaux sur fluage du bois.

Dans les travaux réalisés pendant cette thèse, 4 essences ont été testées : le douglas, le peuplier, le hêtre européen et le chêne européen. Nous avons choisi l'essai de flexion 4 points pour les mesures en fluage et l'essai de vibration pour caractériser les propriétés mécaniques, ainsi que les mesures physiques de densité et de dimensions. Les échantillons sont de petite taille (150 mm dans le sens des fibres), pour éviter les défauts du bois.

L'angle du fil global et local ont été mesurés par le logiciel « ImageJ » à partir de la photo scannée. Dans le résultat, la valeur moyenne de L'angle de fil local absolue est plus grand que l'angle de fil global,

car il existe du fil courbé sur les échantillons. Pour éliminer l'effet de l'ange de fil, nous avons sélectionné les échantillons avec un angle de fil plus petit que 5 dégréés.

Une série de 10 jours d'essais de fluage en flexion 4 points a été réalisée sur la base des essais de vibration et d'un échantillonnage réalisé préalablement. Le dispositif d'essai de vibration a été conçu au LMGC depuis plusieurs années sur la base d'un système développé dans les laboratoires du bois japonais. Le test de vibration permet de mesurer le module spécifique, qui est fortement corrélé à l'angle des microfibrilles et le coefficient d'amortissement, pour avoir une compréhension générale des caractéristiques mécaniques des échantillons. La masse volumique, le module spécifique, le coefficient d'amortissement, le coefficient de gonflement en volume et l'angle de grain des échantillons ont été mesurés et considérés dans l'échantillonnage. La stratégie d'échantillonnage a été conçue pour choisir une propriété spécifique comme variable et contrôler la variance d'autres propriétés, pour que le résultat du test puisse se concentrer sur l'effet d'une propriété donnée. Ainsi, l'influence de chaque propriété est testée séparément des autres afin de déterminer les indicateurs prédictifs du fluage. Il y avait 108 échantillons étaient choisis pour l'essai du fluage (les cercles rouges dans Fig. 1).

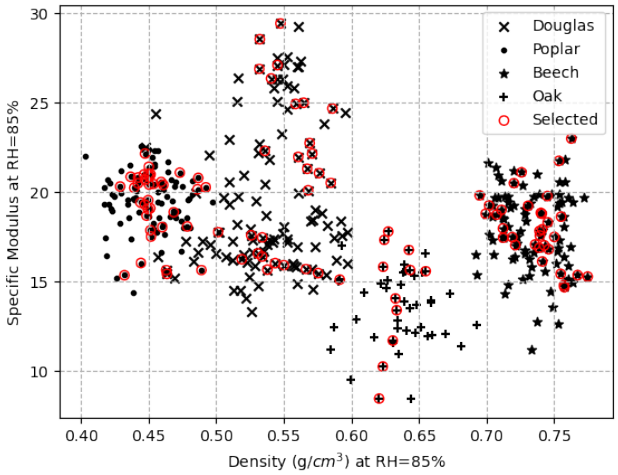

Figure 1: les résultat d'echantillonage

Les échantillons ont été stabilisés à une température de 20 °C et à une humidité relative de 85% avant d'être soumis à l'essai de fluage en flexion 4 points. Une charge de 650 g (10,52 MPa) a été appliquée en flexion 4 points pendant 10 jours. Cent-huit échantillons ont été testés et analysés dans la modélisation.

Pour collecter les données pendant l'expérience, il y a deux jauges sont collées sur les deux surfaces d'échantillon. La déformation axiale peut être calculée par la somme des déformations. La déformation de flexion peut être calculée par la différence des déformations qui est égal à la déformation du fluage.

Dans les résultats d'essai du fluage, nous avons constaté que l'effet de la densité est entre les essences, l'effet du module spécifique est au sein des essences. Par conséquent, nous avons choisi la densité et module spécifique comme prédicteurs. Pour avoir les plus courbes crédibles, nous avons choisi la plage de la complaisance initiale à la complaisance au 7ème jour de la courbe pour la modélisation. Cependant, il n'y a pas de grande différence entre les résultats de la compliance initiale et la complaisance au 7ème jour parce que la déformation

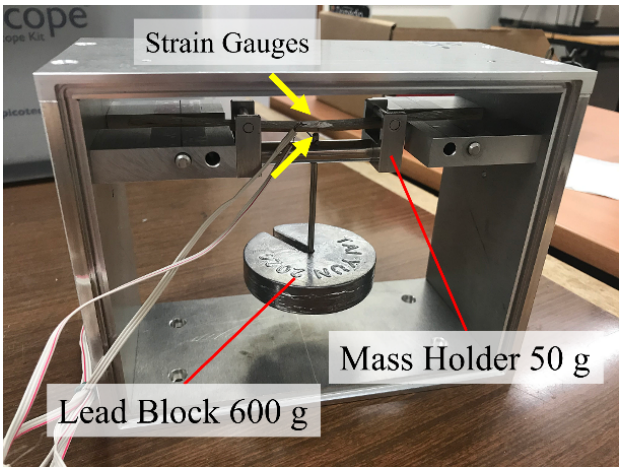

(a)

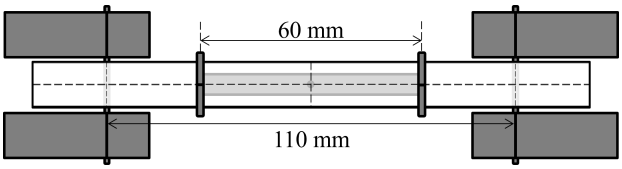

(b)

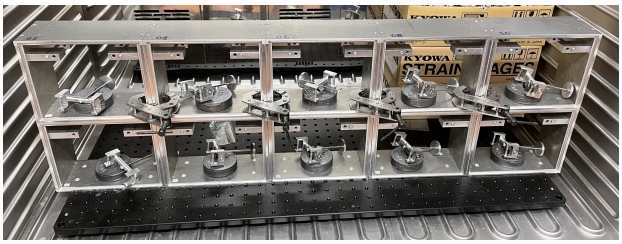

(c)

Figure 2: Système d'expérience

instantanée qui est due au comportement élastique est toujours la partie principale de la déformation totale. Nous avons donc calculé la complaisance différée qui est la complaisance observée moins la complaisance initiale, pour ne voir que le comportement du fluage.

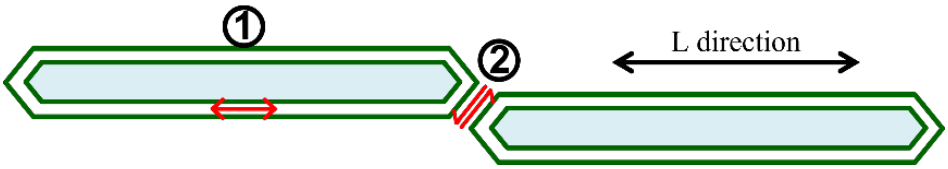

Figure 3: L'hypothèse principale

$$\log J = a \log \rho + b \tag{1}$$

L'hypothèse principale dans cette étude sur mécanisme du fluage du bois est : il y a 2 sources possibles du comportement en fluage : la déformation de la paroi cellulaire ou le glissement intercellulaire (Fig. 3). Si le comportement du fluage se produit uniquement dans la paroi, alors il serait inversement proportionnel à la densité. En effet, la rigidité du matériau est influencée par la porosité. La densité plus élevée signifie moins de porosités, un matériau plus rigide et moins de déformations. Dans ce cas, la valeur « a » dans l'équation 1 sera -1. Mais, s'il y a un glissement intercellulaire, alors le comportement du fluage serait indépendant de la densité. Dans ce cas, la valeur « a » sera à propos de 0. Nous avons constaté un résultat presque inversement proportionnel entre le fluage et la densité, donc le fluage serait lié à la déformation de la paroi. Pour faire disparaitre l'effet de la densité, nous avons calculé la complaisance spécifique qui est la complaisance différée multipliée par la densité. Nous avons constaté que le module spécifique est linéairement lié à la complaisance spécifique.

Le modèle de comportement de fluage représenté par une fonction exponentielle du temps (Eq.2). La complaisance différée peut être représentée par une série d'éléments de Kelvin, et les paramètres des éléments (ressorts et amortisseurs) sont calculés numériquement par comparaison avec les données expérimentales.

Cette étude se concentre sur la relation entre les paramètres d'ajustement du modèle et les caractéristiques des échantillons mesurées expérimentalement. Trois modèles sont présentés pour estimer les paramètres d'ajustement de la fonction de fluage.

$$J(t, \rho, E_s) = J_0 + \sum J^*i(t, \rho, E_s) \times (1 - e^{-t/\tau_i}) \tag{2}$$

Dans le premier modèle, nous avons divisé la courbe du fluage comme deux parties : court terme et moyenne terme. Nous avons constaté que la relation entre les facteurs et le comportement du fluage est différent dans les deux stades différents. Ça veut dire l'effet de la densité et le module spécifique change avec le temps. Par conséquent, nous avons divisé le modèle comme plus d'éléments de Kelvin de trouver la tendance (Fig.4), et nous proposons la fonction J^*i dans l'équation 2 soit la fonction de la densité, le module spécifique et le temps comme l'équation 3.

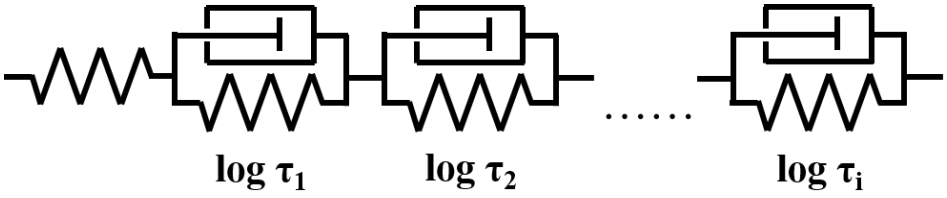

Figure 4: Modèle du fluage avec de nombreux éléments Kelvin

$$J^*i(\rho, E_s, \tau_i) = a(\log \tau_i) \times (\frac{\rho}{\rho_0})^{b(\log \tau_i)} \times (\frac{E_s}{E_{s0}})^{c(\log \tau_i)} \tag{3}$$

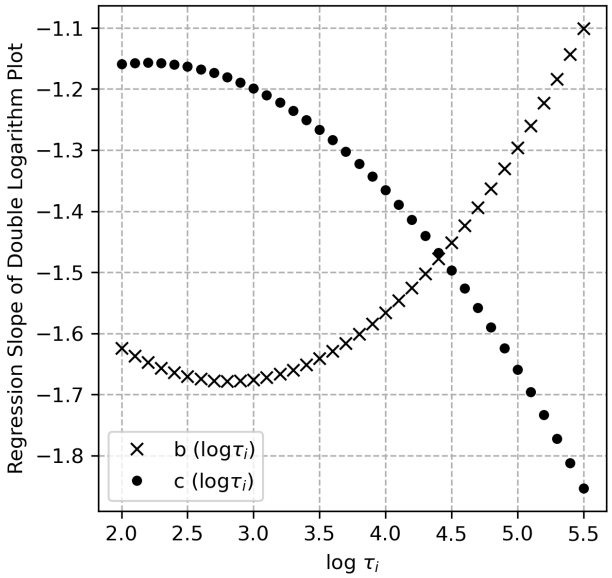

Figure 5: Le resultat de modelisation

La modélisation suggère que le comportement en fluage du bois se produit dans la paroi cellulaire plutôt que par glissement au niveau de la zone intercellulaire. Les résultats de la modélisation permettent de simuler les évolutions des mécanismes dans le temps. L'effet de la densité diminue avec le temps de chargement, et

l'effet du module spécifique augmente. Cela signifie que la déformation est transférée de la paroi cellulaire à d'autres structures du bois, et que l'effet de l'angle des microfibrilles augmente pendant le processus de chargement. Cette étude souligne l'importance de la microstructure sur le comportement rhéologique. La microstructure du bois est influencée par l'âge de l'arbre, l'environnement et les conditions de croissance, ainsi que par les extractibles du bois. Les résultats de cette étude fournissent des propriétés matérielles à considérer dans l'évaluation du classement mécanique des matériaux de construction.

Nous pensons que cette étude pourra aider pour améliorer les normes de calcul des structures en bois comme l'Eurocode 5, on peut avoir un calcul standard du comportement différé qui serait utile pour la construction bois. C'est important à notre époque avec la construction des immeubles de grande hauteur, ou encore des ouvrages publics de grandes portées. De plus, les modèles actuels sont établis à partir l'épicéa. Avec un modèle indépendant des essences, cela peut élargir le choix des essences en construction en adéquation avec les ressources disponibles et mieux gérer la longévité des bois d'œuvres.

Mots clés : Bois ; Comportement différé ; Modélisation ; Rhéologie ; Expérimental ; Longévité